The Lattice Dynamics and Thermal Properties Of Nanostructures

S. P. Hepplestone

March 16, 2007

Declaration

The Lattice Dynamics and Thermal Properties of Nanostructures.

Submitted by Steven Paul Hepplestone, to the University of Exeter as a thesis for the degree of Doctor of Philosophy in Physics, November 2006.

I certify that all material in this thesis which is not my own work has been identified and that no material has previously been submitted and approved for the award of a degree by this or any other University.

.....

S. P. Hepplestone

Acknowledgements

This Thesis and its contents would not be possible except for several friends and colleagues who have come to know during the past few years. Each person I mention below has been responsible for keeping me sane, helping me along the way, making me tea, and many other things which are too numerous to mention and apologies to those I forget (though most know what my memory for names is like). Without further ado I would like to thank the following (in alphabetical order):

Kenton Arkill, Timothy Atherton, John Birkette, Catherine Blake, Allison Carrol, Katawut, Gareth Cole, Marie Dunkerley, Elizabeth Darnill, Matthew Eames, John Hale, Luke Hounsome, John Inkson, Paul Steven Keatley, Tristan Kershaw, Sam Ladak, Ray Mahdon, Hazel Northcote, Kate Northing, David O'Farrell, Andy Peat, Martin Smith, Leigh Shelford, Jamie Thompson, Gemma Winter, Shemiah Weekes, all my friends from Diss and everyone I have forgotten to mention.

Lastly, three people deserve a special mention, the first is my supervisor and friend Prof. G. P. Srivastava. Without G. P. this thesis would not be here. It is for all the patience, help and wisdom that G.P. has given me and his support both as a supervisor and as friend that I am very thankful for and pass on a huge amount of gratitude. I also wish to thank my family, whose support I have been able to count on everyday during my PhD, both during the good and hard times. My kindest thanks and gratitude.

Thank you all.

Steven

Abstract

In this Thesis, the physics of phonons in silicon nanostructures and carbon nanotubes has been discussed. The fundamental quantity, the phonon dispersion curves, which are necessary for considering any thermal property, have been obtained. The phonon dispersion relation results for nanostructures of various sizes have been discussed and the effects of dimensionality on their lattice dynamics has been presented. Based upon these phonon dispersion relations, the specific heat capacity of carbon nanotubes has been calculated. The change over from one-dimensional behaviour to two-dimensional behaviour has been explained and a relationship for this occurence, which is dependent on the nanotube size and temperature, has been expressed. Using the dispersion relations obtained in this Thesis, detailed calculations of the lifetime of phonon modes in nanostructures have been performed using an approach based on Fermi's Golden Rule. The lifetime of the low-lying zone-center optical modes has been calculated and shown to be comparable with that of bulk acoustic modes. Hence, it has been shown that these modes must be included for accurate calculations of the lifetime of phonon modes undergoing phonon-phonon interactions. Upon this basis the lifetime of phonon modes in carbon nanotubes were calculated and this lifetime has been shown to be of the order of nanoseconds. A correct one-dimensional model was described for the carbon nanotube, which considered the important angular momentum conditions which limit phonon-phonon interactions that had not been noted before. This model was adapted using Debye dispersion relations to provide analytic expressions for the relaxation rate of phonon modes. This analytic expression was shown to be in good agreement with numerical calculations based upon fully dispersive phonon dispersion relations. It is shown that the thermal conductivity is linearly dependent on temperature for between 75 K and 225 K. It was also shown that mass-defect scattering has substantially less effect in one-dimensional systems than in three-dimensional systems. Using the theory for boundary scattering, the reason for the vast number of different theoretical results is described as being a result of the ballistic free-path distance, L_0. These results are expected to be of great use to anyone who is researching into the theory or applications of nanotubes or semiconducting nanostructures.

Contents

List of Figures

List of Tables

List of Publications

Chapter 3

- S. P. Hepplestone and G. P. Srivastava, *The lattice dynamics of rectangular silicon nanowires*, Phys Stat sol (c), **1**, 2617 (2004).
- S. P. Hepplestone and G. P. Srivastava, *The lattice dynamics of ultrasmall silicon nanostructures*, Appl. Phys. Lett. **87**, 231906 (2005); Virtual. J. Nanoscale Sci. Technol. **12**, 24 (2005)*.
- S. P. Hepplestone and G. P. Srivastava, *The lattice dynamics of silicon nanostructures*, Nanotechnology **17**, 3288 (2006).

Chapter 4

- S. P. Hepplestone, A. M. Ciavarella, C. Janke and G. P. Srivastava, *Size and temperature dependence of the specific heat capacity of carbon nanotubes*, Surf. Sci. **600**, 3633 (2006).

Chapter 5

- S. P. Hepplestone and G. P. Srivastava, *The intrinsic lifetime of low-frequency zone-centre phonon modes in silicon nanowires and carbon nanotubes*, Appl. Surf. Sci. **252**, 7726 (2006).
- S. P. Hepplestone and G. P. Srivastava, *Phonon-phonon interactions in single-wall carbon nanotubes*, Phys. Rev. B, **74**, 165420 (2006); Virtual. J. Nanoscale Sci. Technol. **9**, 85 (2006)*.
- S. P. Hepplestone and G. P. Srivastava, *Frequency and Temperature Dependence of Anharmonic Phonon Relaxation Rate in Carbon Nanotubes*, (Submitted to Institute of Physics Conference Proceedings).

*Traditionally, these papers are only cited from their source journal, i.e Appl. Phys. Lett. and Phys. Rev. B. Here, however, all instantances where these papers may be found have been cited.

Chapter 1

Introduction

"Thermodynamics is a funny subject. The first time you go through it, you don't understand it at all. The second time you go through it, you think you understand it, except for one or two small points. The third time you go through it, you know you don't understand it, but by that time you are so used to it, it doesn't bother you any more."

Arnold Sommerfeld, (December 5, 1868 - April 26, 1951)

1.1 A short history of matter and thermodynamics

Since early antiquity, mankind has been fascinated with the behaviour of matter. Questions such as what it is made of, why unsupported objects drop to the ground, why various materials have different properties, and other, more difficult topics have been the subject of considerable human endeavour for many thousands of years and will probably remain so for many hundreds more. As time has passed, several theories have been proposed and developed to explain matter's characteristics and behaviour. Of these theories, some have proved to be highly accurate and some have proved to be fallacy. It was not until the seventeenth century, in what many

refer to as the the scientific revolution, that science was born in the form which would evolve into what we recognise today. It is also from this period that the term scientist arose. Many of the ideas which were commonly accepted before the seventeenth century and had originated with Greek scholars such as Aristotle, under went rigorous scientific testing, and were found to be highly inaccurate or completely unfounded. This led to the development of what many refer to now as scientific method and also to the beginnings of physics. Galileo, and then Newton are said to mark the beginning of this age where such rigorous testing and investigation of materials and their properties would become the standard practise until this day. Both of these two men were interested in the way matter interacted, and set out to test and understand the classical theories of the Greeks, which led both of them to propose new theories about matter's interactions and properties.

After these two notable figures, the birth of thermodynamics is said to have begun with the German scientist Otto von Guericke who, like Newton and Galileo, wished to test the Greek theories. In particular, Guericke wanted to test Aristotle's belief that "Nature abhors a vacuum." In 1650 Guericke designed and built the first vacuum pump, which was to prove vital to early experimental developments. After this, several physicists (such as R. Hooke and R. Boyle) improved and used the vacuum pump design to analyse the characteristics of gases and propose simple theories regarding their behaviour. This led to the eventual development of the ideal gas laws. These simple experiments and more led Bernoulli [1] to suggest the conservation of energy and beginnings of the kinetic theory. Whilst other theories were to be developed and proposed over the coming century (such as the phlogiston and caloric theories in the 18th century) the kinetic theory was to have a lasting influence and gain eventual acceptance.

This period also marked the beginnings of the creation and application of the electronic circuit. Whilst historically speaking earlier devices were created, it was in 1745 that electronics, electricity and its components became the subject of scientific endeavour with the invention of the capacitor by Ewald Georg von Kleist. This was followed in the next year by the more famous Leyden Jar. Other components were also developed in the coming century, and the beginnings of what would become the

electrical circuit started to dawn.

Historically, the 1800's saw the kinetic theory being adopted and accepted by the scientific establishment as a whole and the fundamental laws of thermodynamics were suggested and developed. It was during this period that Boltzmann developed the famous equation which bares his name to this day and the beginnings of statistical physics appeared. The theories of thermodynamics and solid state physics grew and, in 1907, Einstein [2] applied the new, developing field of quantum mechanics to explain the specific heat capacity of an object by suggesting that particles acted as simple harmonic oscillators in solids. This was to be followed by the famous Debye [3] model in 1912 for specific heat capacity where the first concepts of a phonon (that is a quantum of vibration) was introduced. As quantum mechanics took form, Einstein and Bose proposed for bosons, and consequently phonons, the Bose-Einstein distribution as an improvement to the now familiar and accepted Boltzmann function.

The latter half of the twentieth century saw the field of electronics reaching maturity and the development of the theories of lattice dynamics and thermal conductivity, based upon quantum and statistical physics, occurring simultaneously. These theories were used to explain the latest physical applications that were being created such as the newly invented transistor. As the electronics and computers were improved and refined, heat management and thermal issues within these systems became increasingly important. This was because as the components decreased in size, their power and hence their heat production (per kilogram) increased. Because of this, the thermal properties of materials have become more critical with each decrease in size. The last decade has seen these components reach the nanoscale regime. In this regime, quantum effects dominate and new and interesting physical properties and behaviour are observed. These features enable the creation of devices not possible on a macroscopic scale such as quasi-two dimensional, one-dimensional and zero-dimensional systems. These systems have their properties strongly effected by the role of phonons and their interactions due to the small scale and reduced dimensions. Also, the thermal properties of such systems are different from their bulk (three-dimensional) counterparts due to the high degree of quantisation they

offer. Materials like these, have been suggested to possess possibly the highest thermal conductivities for any material known and other interesting features in their vibrational and thermal behaviour.

1.2 Outline

This thesis explores and explains the lattice dynamics and thermal properties of several fundamental nanostructures. A particular emphasis is placed upon two one-dimensional systems: the carbon nanotube and the silicon nanowire. The changes in the thermal and vibrational characteristics and properties of these systems with changes in size, temperature and other variables are examined using different theoretical techniques. These theories are used to explain the thermal and vibrational features of these structures and as well as available experimental results.

In the remainder of this chapter, nanostructures are defined and some of their interesting and unique physical properties are described. In Chapter 2 the experimental techniques for producing such nanosystems, and methods for analysing their structure are detailed. Also, experimental procedures for measuring the vibrational features and thermal properties of these systems are explained and the results available from these experiments are shown. In Chapter 3 the history of the theory of lattice dynamics and continuum models for phonon dispersion relations is described in brief. The presented theory is explained and the results of calculations for several different nanostructures are discussed. The effects of dimensionality on lattice dynamics are particularly emphasised and focused. Chapter 4 presents the theory of specific heat capacity of solids and the theory behind it. This theory is then applied to carbon nanotubes. This chapter presents the results of calculations based upon the theory presented. Chapter 5 introduces the theory of phonon-phonon interaction and the history of its development. This is followed by the results for the calculation of the lifetime of phonon modes undergoing three-phonon scattering processes, with both numerical and analytic schemes being adopted. Chapter 6 presents the history and theory of thermal conductivity for bulk and one-dimensional systems. It is applied

to nanotubes and results are obtained and discussed based upon these calculations. Chapter 7 presents the conclusions and summarises the results presented in previous chapters. It also presents suggestions for future research and where further investigation maybe needed. Finally this chapter presents the concluding statements to this thesis.

1.3 What are nanostructures?

Nanostructures are defined as any material which has one or more dimensions which are measured on the the scale of nanometers. This definition has been applied for structures that have a confining dimension ranging from 600 nm in size to structures which are only one or two atoms in size (less than a nanometer). These structures vary widely in form and can consist of slabs [4], wires [5], dots [6], rings [7], tubes [8], hollow spheres [9] and more. The definition also does not distinguish between stand alone nanostructures and nanostructures which are attached to a larger system such as a substrate. To cover all the many varied forms of nanostructures is an almost impossible task, so the discussion will be limited to those which are considered the more fundamental and/or important structures for future developments.

1.3.1 Nanotubes

Among the first nanostructures to be discovered were carbon nanotubes, though their is much contention as to the initial date of their discovery [10, 11, 12]. However, in 1991 Iijima [11] was amongst the first to described the structure of carbon nanotubes and this timely publication is regarded by many as to when they started to draw attention from the scientific community at large. Since then, researchers have established that these tubes have several novel properties that make them potentially very useful in many different fields of physics and electronics. Single-wall carbon nanotubes [13] consist of a sheet of carbon atoms rolled up into a tube. These tubes range in diameter from 0.7 nm to 2.0 nm. Figure 1.1 shows an example of a single-wall nanotube of radius 0.6875 nm. There also exists multi-wall

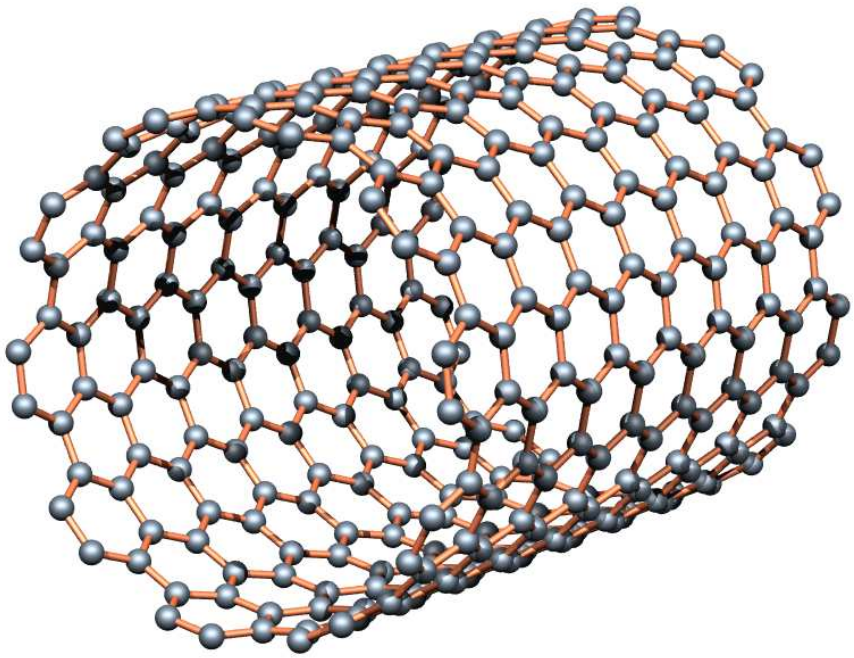

Figure 1.1: A section of a (10,10) carbon nanotube. The spheres represent carbon atoms. The joining lines represent the bonds between atoms.

nanotubes, which consist either of several tubes within each other, the *Russian doll* effect, or a single continuous sheet rolled up several times, the *Parchment* effect. A particular case of the multi-wall nanotube which is also studied is the double wall nanotube [14], which consists of a smaller nanotube contained within a larger tube. Since these first carbon nanotubes, other materials have also been found to form nanotubes such as aluminium nitride [15], boron nitride [16] and silicon [17, 18, 19]. As carbon nanotubes have a diameter of the order of nanometers in size, these structures can be considered as one dimensional because they have two degrees of confinement and one degree of freedom. They also, like most quasi one-dimensional structures, have a large aspect ratio of the length to the diameter; most tubes show: $[(\text{length/diameter}) > 10^4]$.

Single-wall nanotubes are classified into two categories: chiral and achiral. An achiral nanotube is symmorphic and has a mirror image which is identical to the original structure. Conversely, a chiral nanotube's mirror image cannot be superimposed upon the original structure, but does exhibit spiral symmetry. The chiral nanotube consists of two special cases: the armchair and zig-zag nanotubes. The

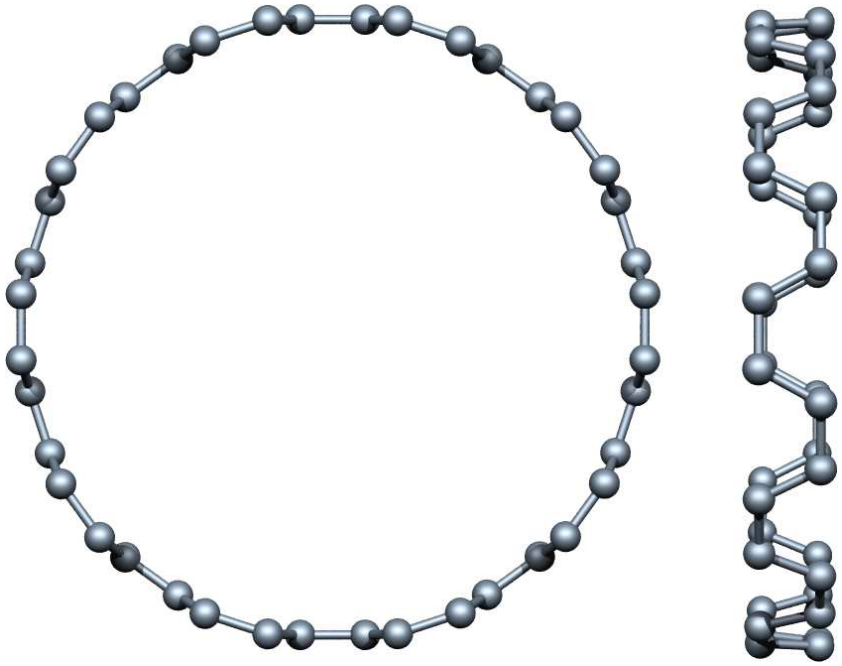

Figure 1.2: The unit cell of a (10,10) carbon nanotube shown from two different angles. The spheres represent carbon atoms. The joining lines represent the bonds between atoms within the unit cell.

descriptive terms armchair and zig-zag arise from the shape of the cross-sectional ring of a carbon nanotube. Figures 1.1 and 1.2 help illustrate this for the (10,10) armchair nanotube.

In order to define a nanotube, one must first define graphene, which is a two dimensional sheet of carbon atoms arranged in a hexagonal grid. The two primitive lattice vectors of graphene, shown in Fig. 1.3, are defined as:

$$\mathbf{a_1} = \Big\{\frac{\sqrt{3}}{2}a_{gr}, \frac{a_{gr}}{2}, 0\Big\}, \tag{1.1}$$

$$\mathbf{a_2} = \Big\{\frac{\sqrt{3}}{2}a_{gr}, -\frac{a_{gr}}{2}, 0\Big\}, \tag{1.2}$$

and

$$a_{gr} = \sqrt{3}a_{c-c}, \tag{1.3}$$

where $a_{gr}(= 2.46$ Å) is the lattice constant of two-dimensional graphite (i.e. graphene) and $a_{c-c}(= 1.42$ Å) is the nearest neighbour bond length in graphite.

For a single-wall carbon nanotube the structure is defined by the chiral vector $\mathbf{C_h}$, which is shown in Fig. 1.3. The chiral vector is defined in terms of the lattice vectors $\mathbf{a_1}$ and $\mathbf{a_2}$ by the relation:

$$\mathbf{C_h} = n_1\mathbf{a_1} + n_2\mathbf{a_2} \equiv (n_1, n_2), \tag{1.4}$$

where n_1 and n_2 are integers, and $0 \leq |n_2| \leq n_1$. The chiral vector is the vector which is perpendicular to the nanotubes axis and represents the two points which would join if a sheet of graphene were rolled up to form the corresponding nanotube. The chiral vector can be used to define all the different types of nanotubes. The armchair case corresponds to when $n_1 = n_2 = n$, or $\mathbf{C_h} = (n, n)$, and when $n_1 = n$ and $n_2 = 0$, or $\mathbf{C_h} = (n, 0)$ corresponds to the zig-zag nanotube. The other combinations of n_1 and n_2 correspond to achiral nanotubes (i.e. $n_1 \neq n_2 \neq 0$).

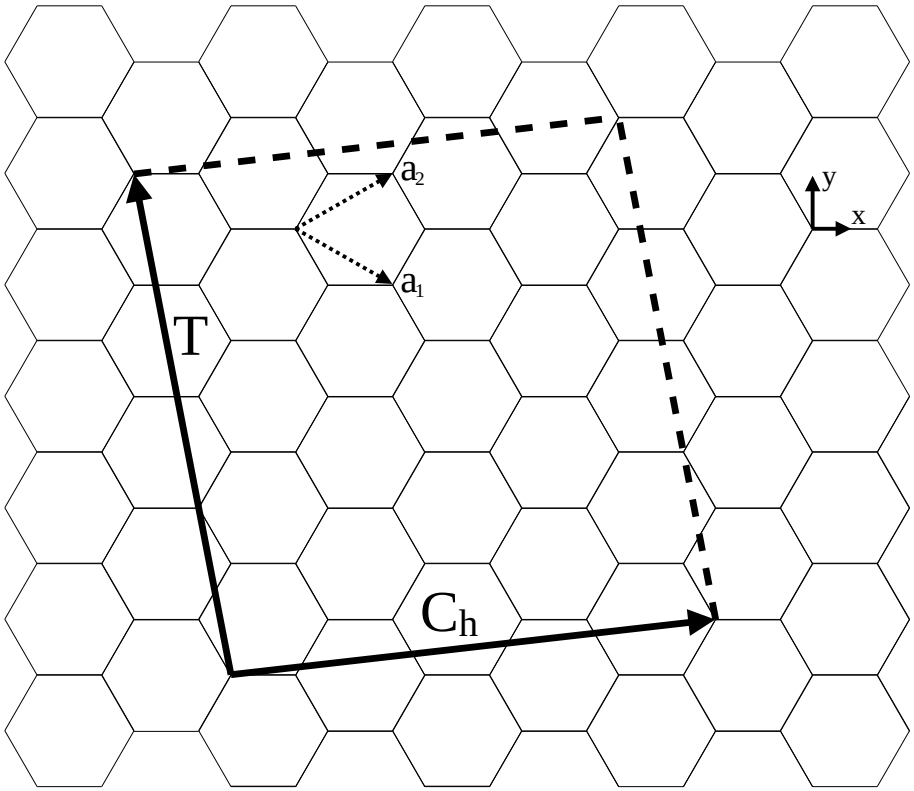

Figure 1.3: An illustration of the structure of graphene. Carbon atoms occupy the apexes of each hexagon. The following vectors are displayed: the primitive lattice vectors, $\mathbf{a}_1$ and $\mathbf{a}_2$; the chiral vector $\mathbf{C}_h$; the translation vector $\mathbf{T}$; the x-y axis.

From Eq. (1.4), it is possible to calculate the radius (R) of the nanotube. This is because the magnitude of the chiral vector is equal to the circumference of the

nanotube or $|\mathbf{C_h}| = 2\pi R$. Hence:

$$R = \frac{a_{gr}}{2\pi}\sqrt{n_1^2 + n_2^2 + n_1 n_2}. \tag{1.5}$$

This equation shows for (n, n) armchair nanotubes that $R = \sqrt{3}a_{gr}n/(2\pi)$ and $R = a_{gr}n/(2\pi)$ for $(n, 0)$ zig-zag nanotubes. Hence when discussing the size of a single wall nanotube, it is common to refer to the indices (n_1, n_2) instead of a specific radius (as $R \propto n$ for the armchair and zigzag nanotubes).

The translation vector $\mathbf{T}$ is defined as the vector along the tube's propagation axis such that $\mathbf{T}.\mathbf{C_h} = 0$. This vector is shown in Fig. 1.3. It is defined as:

$$\mathbf{T} = t_1\mathbf{a_1} + t_2\mathbf{a_2}, \tag{1.6}$$

where t_1 and t_2 are related to the integers n_1 and n_2 by:

$$t_1 = \frac{n_1 + 2n_2}{d_R}, \quad t_2 = -\frac{2n_1 + n_2}{d_R}, \tag{1.7}$$

where d_R is greatest common denominator of both terms.

The number of atoms per unit cell or the number of hexagons per unit cell (which is half the number of atoms) may be obtained easily from $\mathbf{C_h}$ and $\mathbf{T}$. From the definitions of $\mathbf{C_h}$ and $\mathbf{T}$ the total area is $|\mathbf{C_h}\wedge\mathbf{T}|$, as can be readily observed from Fig. 1.3. Hence the total number of atoms per unit cell is:

$$N = \frac{|\mathbf{C_h}\wedge\mathbf{T}|}{|\mathbf{a_1}\wedge\mathbf{a_2}|} = \frac{4(n_1^2 + n_2^2 + n_1 n_2)}{d_R}. \tag{1.8}$$

For (n, n) and $(n, 0)$ nanotubes, it is easy to show $N = 4n$.

Figure 1.2 shows the unit cell of a (10,10) carbon nanotube. The unit cell for a (10,10) nanotube contains forty atoms. The chiral vector for a (10,10) armchair nanotube is defined as $\mathbf{C_h} = 10\mathbf{a_1} + 10\mathbf{a_2}$ and the translation vector as $\mathbf{T} = \mathbf{a_1} - \mathbf{a_2}$.

1.3.2 Fullerenes

Carbon nanoballs, which are more commonly known as buckminsterfullerenes or buckyballs, were first reported in 1985 [9, 21] and these consisted of a sphere of

atoms. Since then, buckyballs of different sizes (due to differing numbers of atoms) have been discovered and synthesised. Buckyballs consist of a hollow sphere of sixty carbon atoms which are arranged into a series of connecting pentagons and hexagons. Of these, the C_{60} molecule is the smallest such structure where the pattern of pentagons and hexagons can be arranged so that the pentagons do not touch each other, though other arrangements are possible. An example of a pure fullerene is shown in Fig. 1.4. In reality, fullerene's are very difficult to obtain in isolated pure form as the production process for C_{60} normally creates C_{70} and other compounds. Only recently have techniques for the purification of C_{60} on a kilogram scale been achieved [22].

Fullerenes have been the subject of much investigation since their discovery and several different applications have been suggested and shown. The use of fullerenes as light-activated antimicrobial agents has been reported [23], among other medical applications, but it has also recently been reported [24] that fullerenes may be dangerous to organisms as they can cause damage to the brain tissues. Buckyballs have also been shown to undergo Youngs slit diffraction [25] which has made them one of the largest objects to demonstrate these effects.

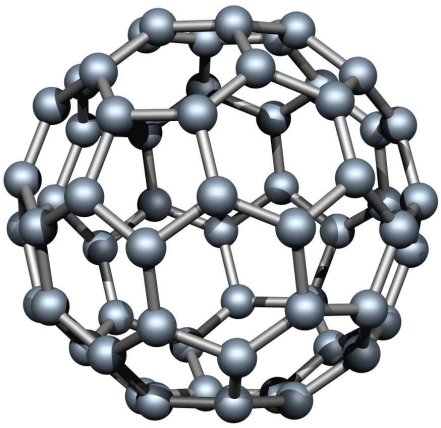

Figure 1.4: A C_{60} molecule. The spheres represent carbon atoms. The joining lines represent the bonds between atoms.

1.3.3 Bulk Semiconductors

Semiconductor nanostructures have a similar internal structure to that of bulk counterparts, thus it is prudent to define these systems first. Many bulk semiconductors have the zinc-blende or diamond type structure [26]. These structures consist of the face-centered cubic lattice and a two atom basis. The face-centered cubic's primitive lattice vectors are defined as

$$\mathbf{a}_1 = \frac{a}{2}(1,1,0),$$

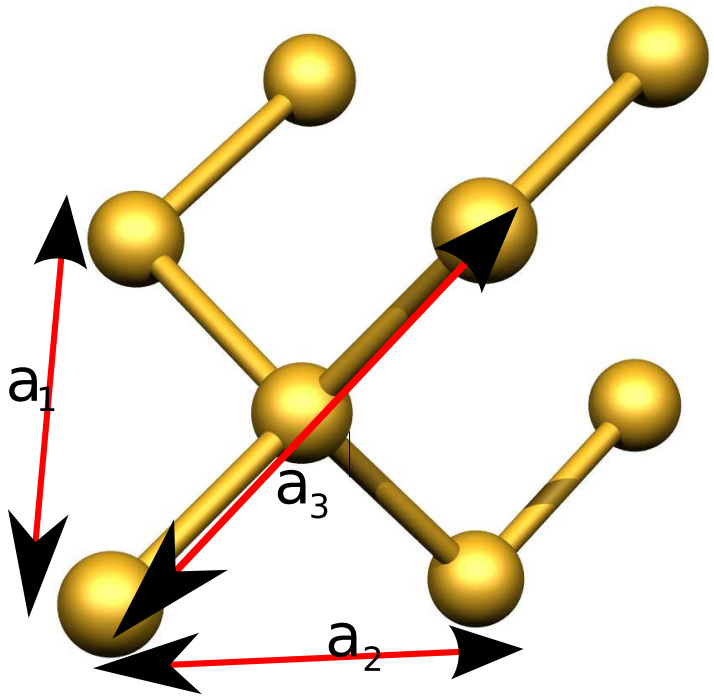

Figure 1.5: A ball and stick model showing the eight atoms which are contained (partially) within the conventional unit cell for diamond type structures. The spheres represent silicon or diamond atoms. The joining lines represent the bonds within the unit cell between atoms. Also shown are three vectors indicating the three primitive lattice vectors $\mathbf{a_1}$, $\mathbf{a_2}$ and $\mathbf{a_3}$.

$$\begin{aligned} \mathbf{a}_2 &= \frac{a}{2}(1,0,1), \\ \mathbf{a}_3 &= \frac{a}{2}(0,1,1), \end{aligned} \tag{1.9}$$

where a is the cubic lattice constant.

For silicon, diamond and germanium, the basis set consists of two identical atoms with their relative co-ordinates defined as

$$\begin{aligned} \mathbf{b}_1 &= (0,0,0), \\ \mathbf{b}_2 &= \frac{a}{4}(1,1,1). \end{aligned} \tag{1.10}$$

From these expressions the position of any atom within the structure may be found.

It is also from these that the Brillouin zone, or momentum space is defined. See Appendix A for more details.

An example of the diamond structure is shown in Fig. 1.5. Many IV-IV and III-V compounds form the diamond or zincblende style structure such as silicon, diamond, germanium, gallium arsenide and gallium nitride. In these bulk structures, each atom is tetrahedrally bonded to its four nearest neighbours (via sp^3 bonds). The diamond-type structure (which is only the IV-IV type) is also characterised by a centre of inversion located at the midpoint between the two atoms within the basis. For further details on these structures and their definitions see Ref. [27].

1.3.4 Nanowires

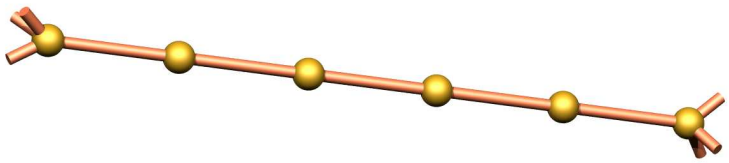

Figure 1.6: A ball and stick model showing a typical gold atomic chain nanowire. The spheres represent the gold atoms and the joining lines represent the bonds.

Nanowires can come in two forms; stand-alone or placed (or grown) upon a substrate. Stand-alone nanowires of various different structures have been studied and suggested. These can range from a chain of gold atoms [28] to larger structures which have several thousand atoms across the diameter of the nanowire. Two types of stand-alone nanowire are discussed here: nanowires which consist of a chain of atoms (the gold atom nanowire) and semiconductor nanowires.

A chain of atoms nanowire is literally a series of atoms linked in a "daisy" chain. An example of a single chain nanowire can be seen in Fig. 1.6. These can consist of either a single chain of atoms, or a set of parallel chains which are weakly connected. These chains of atoms are normally connected at both ends (illustrated) to an external system due to the manufacture of these devices. Often, one end will be attached to

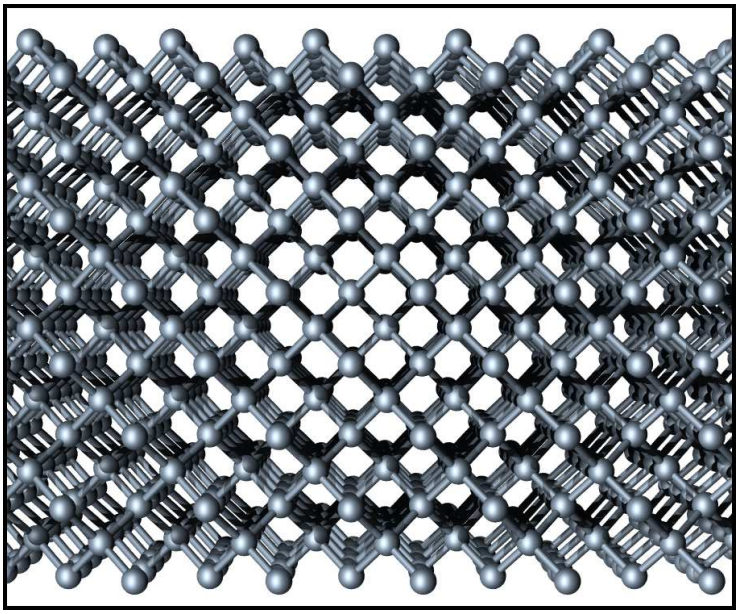

Figure 1.7: A ball and stick model showing a typical section of an silicon nanowire of dimensions 1.629 nm × 1.629 nm. The spheres represent the silicon atoms and the joining lines represent the bonds.

an atomic force microscope tip and the other to a substrate.

Nanowires formed from silicon [29, 30, 31] semiconductors are an alternate to chains of atoms and are attractive to the electronics industry due to the familiarity and popularity that silicon has gained over the last half a century. Nanowires have also been formed from other semiconductors such as germanium [32] and gallium arsenide [33], but these have not attracted as much attention in academia or commerce as silicon. It has been observed [34] that silicon nanowires show an internal structure of the same form as bulk silicon. Typical nanowires grown have diameters ranging from 10 nm to hundreds of nanometers and lengths in excess of 1 μm such that their aspect ratio is (Length/diameter)$> 10^3$. Most real semiconductor nanowires grown are covered in an amorphous layer of oxide which varies from 1 nm to several nanometers in thickness. However, recent techniques have been developed for using hydrogen termination [35, 36] to "clean" the surface of silicon substrates and it is feasible that these methods may be applied to silicon nanowires to reduce surface defect effects and the amorphous coating for practical applications.

An example of a clean silicon nanowire of dimensions 1.629 nm × 1.629 nm is shown

in Fig. 1.7. The wire shown has a square cross-section. This cross section (of the nanowire) is perpendicular to the direction of propagation, and provides a practical method for defining the shape and size of different nanowires. These cross-sectional areas can be rectangular, square, circular or irregular in appearance.

For defining silicon nanowires and modelling their properties, the simplest approach is to consider a square nanowire of dimensions d nm by d nm by L_0 nm where d is the confining dimension of the nanostructure (the width) and L_0 is the total length of the nanostructure (in this case the wire). These *theoretical* nanowires have the same structure as that of bulk silicon and are considered grown in the (100) direction.

Nanowires grown or placed on a substrate have been observed in many forms, two of which are the single chain (or ultra-thin) wires and thicker wires upon substrate. The thinner of these tend to be characterised by wires which consist of only a few atoms in cross-section area. These atoms tend to form along the surface of substrate along preferential bond sites such as surface dimers or atomic ridges. They also are normally only one or two atoms high and not many exceed four atoms in width. Such wires' behaviour is dominated by their interaction with the substrate and their structure is determined by this interaction.

The second type of nanowire grown on a substrate is much larger and consists of a second material formed in lines (via a variety of mechanisms) with a large cross sectional area which consists of up to ten thousand atoms. Such wires are often characterised by having structural form similar to their bulk counterparts except at the interface between the wire and the substrate. Nanowires of this size placed upon a substrate have properties which are determined by both their rough surfaces and that of the substrates. These substrates also show impure surfaces which have step defects and are often oxidised.

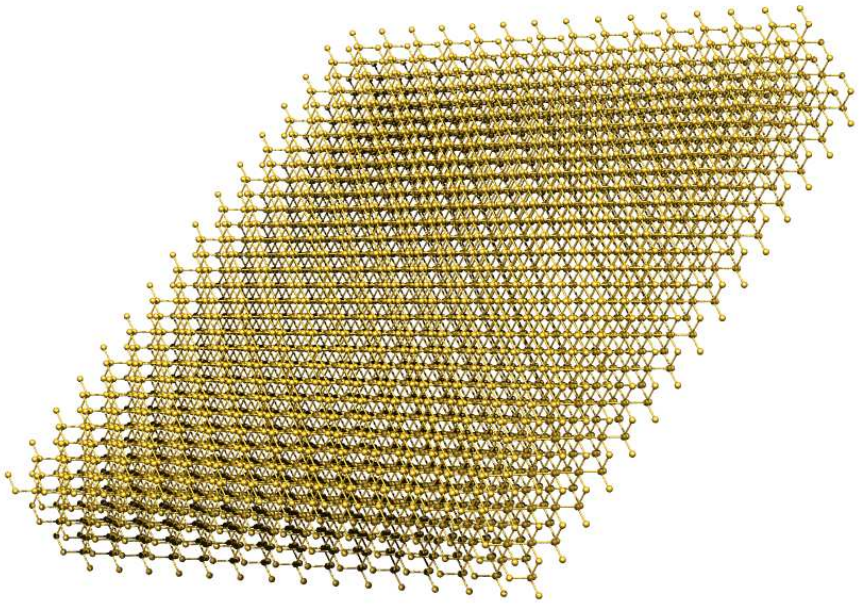

Figure 1.8: A ball and stick model showing a typical section of a silicon nanoslab which is 1.629 nm thick. The spheres represent the silicon atoms and the joining lines represent the bonds.

1.3.5 Nanoslabs

Thin two-dimensional structures have been studied extensively in the last three decades, be they of the form of a two-dimensional electron gas, a thin film, or an ultra thin suspended layer. These structures have two dimensions which are of the order of microns or above and one dimension of the scale of hundreds of nanometers or less. In experiment, two-dimensional stand-alone structures are rarely observed as these are very difficult to produce currently. However, thin layers of silicon have been grown upon an insulator [37] with a silicon oxide barrier between the two systems to enable study of the two-dimensional material's properties. Stand-alone nanoslabs are, conversely, very common in theoretical work [38, 39, 40]. This is because in order to model phenomena such as surface relaxation [41, 42], atomic absorbtion [43] and dimer tilting [44] a large slab of material is required to simulate a bulk substrate. However, often due to computational limitations these slabs often have a thickness of less than a hundred atoms, which means they are of the order of nanometers in thickness. Hence it is expected that nanoslabs properties become rapidly more

bulk-like with increasing thickness and will show less unique quantisation effects than their corresponding one- or zero-dimensional counterparts.

Similar to defining nanowires, and for later comparison a nanoslab is considered to have dimensions d nm by L_0 nm by L_0 nm where d is the confining width of the nanostructure (the width) and $L_0 \times L_0$ is the total surface area of the nanoslab A_0. These theoretical nanoslabs, like the nanowires, have the same structure as that of bulk silicon and are considered grown in the [100] direction.

1.3.6 Nanodots

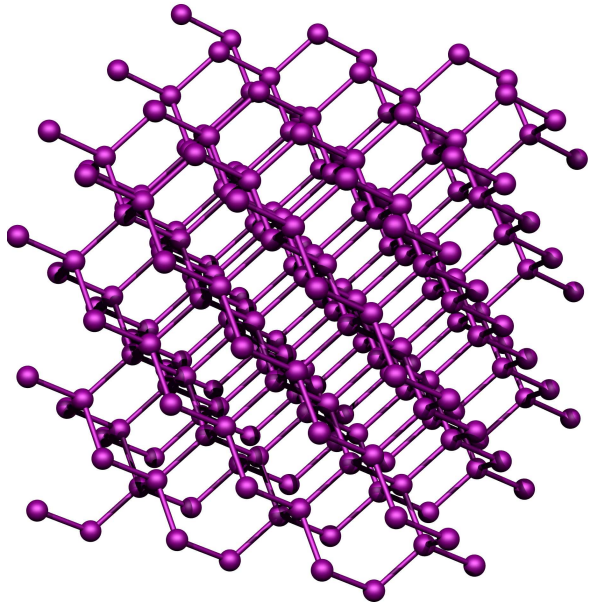

Figure 1.9: A ball and stick model showing a typical silicon nanodot of dimensions 1.629 nm $\times$ 1.629 nm $\times$ 1.629 nm. The spheres represent the silicon atoms and the joining lines represent the bonds.

The final type of nanostructure to be considered are those which are confined in all three dimensions; nanodots or zero-dimensional structures. These nanodots have volumes of the order of $(\text{nm})^3$. These systems are unusual as it is almost impossible to create stand-alone structures. This is not an unsurprising result as such structures must either be suspended (or embedded) in a medium or placed upon a surface in order to be of practical use or to have their properties measured. Nanodots can

consist of a cluster of atoms (such as gold nanodots) or a more ordered structure such as silicon nanodots. Clusters of atoms such as gold have been observed [45] and these are similar to the the gold nanowires, and clusters of other materials have also been manufactured [46]. Silicon nanodots, like the nanoslab and nanowire have atomic structure similar to bulk silicon, with each of the atoms forming tetrahedral bonds. These nanodots are often manufactured either upon a substrate's surface [47] or within an embedding material such as amorphous silicon [6]. As such, these system are not true zero-dimensional as they are heavily dominated by their interaction with either the embedding material, which means no true confinement in any of the three dimensions; or the substrate, which means confinement properties in one direction are altered substantially.

To define silicon nanodot structures, they are considered to have a bulk silicon like structure and have dimensions d nm by d nm by d nm, where d is the confining length of the nanostructure (the width). A stand-alone nanodot of confining width $d = 1.629$ nm is shown in Fig. 1.9. These theoretical nanodots, like the nanowires and nanoslabs mentioned previously, have the same structure as that of bulk silicon and are considered grown in the (100) direction.

1.3.7 Nanostructures Upon Substrate

Lastly, whilst these structures have been described earlier, it is possible to conceive the possibility of placing a nanowire on one of the two surfaces of a nanoslab in order to model a silicon nanowire (or nanodot) grown upon a silicon substrate. This structure is defined using two parameters d_1 and d_2. A nanowire upon a silicon substrate is considered to have dimensions d_1 nm by d_1 nm by L_0 nm and placed upon a substrate with thickness d_2 nm and area A_0. This theoretical structure, like its predecessors, has the same structure as that of bulk silicon and are considered grown in the (100) direction.

1.4 Interesting Properties Of Nanostructures

Nanostructures exhibit several exciting and unusual properties due to their tiny size. Within these scales of nanometers, many features that cannot be observed in bulk such as quantisation and integer current flow, are readily observed. To provide a flavour for such properties some of the characteristics of particular nanostructures are described below. The following sections are by no means exhaustive and are simply to introduce a few of the reasons why nanostructures have attracted so much interest in the last decade.

1.4.1 Electronic and optical properties

Nanostructures, due to their small size, show different electronic properties from their bulk counter parts. In particular, silicon nanostructures and carbon nanotubes show several changes from their bulk equivalents.

A nanotube's electronic properties are determined from its structure and hence, these properties are heavily dependent on the tube's chiral number (n_1, n_2). For carbon nanotubes, the chiral number determines whether a tube is metallic or semiconducting and for nitride nanotubes, the chiral number determines the size of the band gap. If, for a carbon nanotube, the chiral number is shown to obey the relation $(n_2 + 2n_1) = 3i$ where i is an integer, then the tube is metallic. However, if a carbon nanotube does not obey this relation then the tube is semiconducting with a band gap between 0.0 eV and 3.0 eV. This bandgap is inversely proportional to the tube's diameter. This is readily explained using the electron energy dispersion curves of graphene, which can be simply obtained from a tight binding method [13]. By applying a technique known as zone-folding, the electron dispersion curves of a carbon nanotube are approximately obtained from graphene. This results in the one-dimensional energy dispersion relations of a nanotube being cross sections of those for a two-dimensional graphene-type structure. *Ab initio* calculations of the electronic structure of carbon nanotubes have shown this relatively simple model to be reasonably accurate [48, 49].

One of the results of this behaviour in carbon nanotubes is the appearance of a plasmon mode which has an energy between 5 eV and 7 eV independent of chirality [50]. This mode is a result of the π-bonds on nanotube's surface and a divergence in the electronic density of states near the band edge. This plasmon shows strong optical properties under electron emission loss spectroscopy and shows the common heritage of all tubes; the graphene sheet. Calculations have also revealed higher energy plasmons, but these have weaker optical properties.

Quantised current flow was first observed experimentally in 1997 by Tans *et al.* [51] in single-wall nanotubes and later confirmed by Bezryadin *et al.* [52]. Nanotubes, due to their unique structure are expected to act as quantum wires. Multi-wall tubes have been shown to have two-dimensional behaviour [53], but single wall carbon nanotubes show quantised step like current flow. Similar behaviour has also been observed in the gold chain nanowire [28], and this is characteristic of a one-dimensional system. However, due to the contacts resistance, which is greater than the quantum resistance within the tube, Coulomb charging occurs as the capacitance of the tube/wire is very small. This leads to the Coulomb blockade effect and the electron pump [54]. This shows that quantised conductance can be expected in most one-dimensional conducting materials, even if they have a very different basic structure, and is a key feature of such systems.

Electronic properties of silicon nanowires also substantially change in character from their corresponding bulk counterpart and some have been shown to have direct bandgaps [55]. These structures may also be metallic or semi-metallic if the surface is clean and allowed to relax [56, 57] and have also been joined with carbon nanotubes to form a heterojunction [58]. Such devices and applications are still in their infancy, with reproducibility and purity being key factors in experimental and theoretical investigations.

Also of interest in nanostructures is the highest optically active vibrational mode, which can be detected via Raman scattering [6, 59, 60]. This mode is highly affected by the confining dimension(s) of the nanostructure and thus, Raman scattering measurements are believed to provide a vital technique for the characterisation of

the size of the nanostructures.

1.4.2 Magnetic Properties

Nanostructures show interesting magnetic properties. A thin sheet of material grown between two larger materials can be used to form a tunnel junction [61, 62]. A current flow across a tunnel junction is dependent on the spin of the charge carriers and the thickness of the barrier. As the barrier is, in-effect, a two-dimensional nanoslab joining two separate systems, the reduced size enables electrons to tunnel through the material from one side to the other.

Carbon nanotubes have also been shown to be able to perform electron spin transport [63]. As long as the two contacts are comparatively close (< 100 nm), nanotubes show clear hysteretic switching in the magnetoresistance, providing the basis for a single-wall nanotube spin transistor.

1.4.3 Thermal Properties

Nanostructures show some very attractive and promising thermal properties which are dramatically different from their bulk counterparts. Some nanostructures have shown thermal conductivity which is much greater than their bulk counterparts (such as carbon nanotubes) [64], whilst others display thermal conductivity much lower than bulk samples (such as silicon nanowires) [65]. Due to the increased density of components on processor chips, these factors are becoming increasingly important in the field of heat management. Without effective methods for reducing the heat build up in such components, electronic error due to electron-phonon interaction and lattice distortion increases and this renders these components redundant. The heat build up within the aforementioned future electronic components needs to be understood in both the individual systems, as well as the combined systems for device manufacture.

The electronic applications also emphasise a second feature which changes in nanos-

tructures, the specific heat capacity [66]. It was predicted early on that the temperature dependence for structures of reduced quantisation would be different from that of bulk materials. In particular, the change in specific heat capacity in nanotubes and nanowires, with temperature, is expected to show a change from one dimensional behaviour to two- (three-)dimensional, in the case of nanotubes (nanowires).

Chapter 4 and 5 provides greater detail of the behaviour of these properties. In particular, theoretical models which enable an understanding of how the factors of size and temperature affect the specific heat capacity of these structures.

1.4.4 Vibrational Properties

In order to understand the thermal properties of a semi-conducting structure, one must first understand the vibrational features. Theoretical calculations of the vibrational characteristics of a structure are usually carried out by two methods: atomistic lattice dynamical calculations [67] and continuum lattice dynamical calculations [3]. The theory of atomistic calculations is based upon an approach to evaluate the relationship between atomic vibrations, phonon momentum (or wave-vector) and phonon energy (or frequency). This can be done via *ab initio* techniques or phenomenological methods; the latter being where the forces between atoms are approximated. Continuum theories treat the structure as a continuous medium, smearing out the individual atomic structure. Whilst continuum techniques are generally only applicable to the low energy ranges (the acoustic branches) and long wave-length regions of the Brillouin zone (the zone centre), these techniques are often more able to yield useful analytic expressions. Also, the dominating contributors to the thermal properties of a material usually are the phonon acoustic branches.

For nanostructures, all these methods have been used with varying degrees of success for different materials and generally most techniques produce qualitatively similar results. Several new features are observed in the vibrational features of nanostructures and these are described in more detail in Chapter 3. Here, two new features are mentioned as these are common to all nanostructures.

The first feature is the appearance of a new low-lying vibrational mode near the zone centre which has energy comparative to the zone edge frequency of the acoustic modes [68]. This new phonon branch, which is referred to here as the σ branch, with zone centre frequency ω_σ, has a large non-zero group velocity (unlike other higher optical modes in bulk) and is a direct result of quantisation within these structures.

The second feature which is observed in both nanowires and nanotubes is the appearance of a fourth acoustic mode. Normally, for bulk materials, there are three acoustic modes, the longitudinal (LA) and two transverse modes (TA). In nanotubes, these three modes exist and as well as a fourth mode known as the twist mode (WA). This is a result of the "twisting" degree of freedom available to the nanowire which is not normally available to bulk objects. In nanowires, the four acoustic branches are the dilatational, the doubly degenerate flexural and the torsional [69]. These four branches in these nanostructures are expected to have a major effect on the thermal properties of these structures.

In Chapter 3, a more detailed description is given of the history of calculation of vibrational modes and their theory, and how these theories have been applied to bulk systems and nanostructures. Both the atomistic lattice dynamical approach and the continuum lattice dynamical approach are used to calculate the phonon dispersion relations of various silicon nanostructures and carbon nanotubes.

1.5 Summary

In this chapter an introduction to the history of solid state, thermal and vibrational physics was provided, followed by an outline of the thesis. The concept of nanostructures and what they are was introduced. The carbon nanotube is defined in terms of its chiral vector (n_1, n_2) and the nanoslab, wire and dot are defined in terms of their confining width d. Also, silicon nanowires of thickness d_1, placed upon an ultrathin substrates of thickness d_2 were defined. Properties such as the electronic, optical and magnetic properties of particular nanostructures were described. Lastly, the thermal and vibration features of nanostructures were briefly discussed. In the

next chapter, experimental techniques for creating these structures and measuring their vibrational and thermal properties are discussed. Examples of data from experiments are shown to set the context for the theoretical work in the following chapters.

Chapter 2

Experimental Methods

The true method of knowledge is experiment.

William Blake, All Religions are One, 1788

2.1 Introduction

The previous chapter introduced nanostructures and some of their interesting properties. It also defined key terms which are used to describe nanostructures and introduced the focus of this thesis, their thermal and vibrational properties. This chapter presents the experimental data, research and techniques for the creation and study of these nanotstructures, with an emphasis on the study of their vibrational and thermal properties. In the first section of this chapter, the fabrication techniques used to produce the various nanostructures described previously are detailed and explained. Examples from several groups of the different methods used to manufacture nanostructures are given and some of their results are presented. The second section describes methods that are used to perform Raman and neutron scattering measurements, illustrated by experimental examples. Raman and neutron scattering are two of the most important techniques available for nanostructures in developing an understanding of the energy of vibrational modes and also their phonon density of states. In the final section procedures for measuring both the

thermal conductivity and specific heat capacity of nanostructures are discussed and results from experiments are presented.

2.2 Fabricating Nanostructures

As seen in the previous chapter, a wide variety of nanostructures can be realised. Each of these nanostructures can be fabricated using a number of different techniques. Some of these techniques are applicable to more than one nanostructure depending on the conditions applied in the experimental set up, whilst others are unique to that particular structure. Given the wealth of literature available on the subject, the focus presented here is examples of the more common methods which have been suggested and applied for the nanostructures considered within this thesis.

2.2.1 Stand-alone Nanowires

2.2.1.1 Dissolution Method

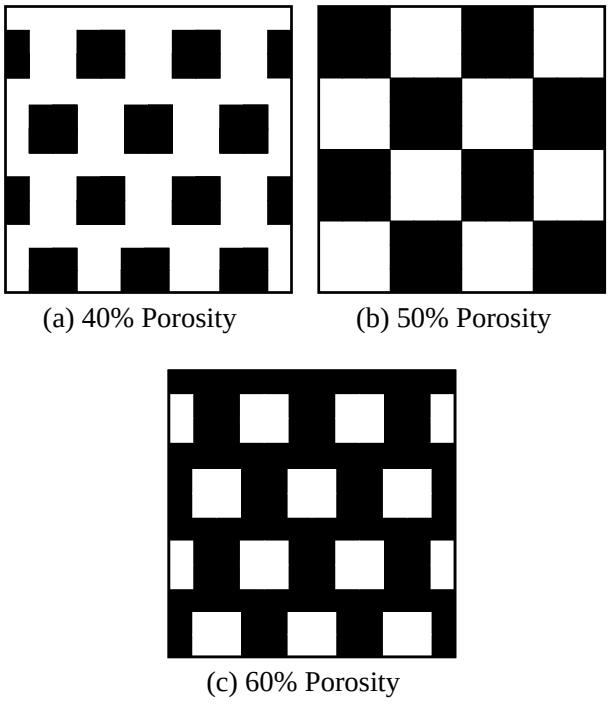

Figure 2.1: A schematic plan of the silicon wafer (white) containing rectangular holes (black). The change in porosity indicates how a silicon nanowire is formed using the dissolution technique.

In 1990, one of the first techniques for producing silicon nanowires was developed by Canham [55]. The method he suggested involved anodising the (100) surface of a silicon wafer. Due to the electronic and structural properties of the silicon material, the anodisation creates a regular array of potential dips across the silicon surface. To the anodised surface, an electro-chemical agent (in this example, Hydro-fluoride-solution) is applied, which preferentially etches the dips, creating pores of various sizes on the surface as shown in Fig. 2.1 (a). Upon further etching, these pores are increased both in size and depth, which eventually leads to them merging at the corners, as shown in Figs. 2.1 (b) and (c). This creates of an array of free-standing wires. To confirm these were nanowires, Canham detected the direct bandgap that these silicon structures produced, a strong indication of nanowire formation. However, these wires were not very long as noted by Canham, and they

are not expected to be uniform, well organised or easy to transfer. Nevertheless, this was among the first methods developed for producing stand-alone silicon nanowires.

2.2.1.2 Vapour-Liquid-Solid Method

Several techniques have been developed since the efforts of Canham, and one of the most common techniques for producing free standing nanowires is the vapour-liquid-solid (VLS) technique [30]. In order to use this method to form a nanowire, the material that the wire will be made from must be dissolved in vapour form into a second liquid at high temperatures. These two materials are carefully chosen so that the combined mixture is a eutectic liquid [27]. This mixture is allowed to cool and, as the eutectic cools, it precipitates the vapor. This precipitant occurs in the form of solid, thin strands, and these will form the future wire. This is due to the high surface tension of the liquid, which minimises the diameter of the wire as it is grown. Because of this, it is important that the liquid has a much lower melting point when compared with the precipitant.

An example of this technique for silicon nanowires was presented by M. Sunkara *et al.* [30]. The method M. Sunkara *et al.* developed to produce nanowires is a low temperature technique. This technique produced a yield of nanowires which ranged in diameter between 6 nm and 50 nm depending the growth conditions.

Sunkara *et al.*'s method utilises atomic-hydrogen mediated gas-phase chemistry and low melting point metals. A silicon substrate is coated with a thin gallium film. The surface is exposed to 1:100 sccm (Standard Cubic Centimeters per Minute) of H_2 in N_2 plasma at 700 Watt microwave power. The gallium is heated and melts. Then, due to the liquids high surface tension, the gallium condenses into droplets that rest on the substrate. This leaves the silicon substrate exposed and the hydrogen plasma etches the exposed silicon surface regions creating silyl radicals. This process then uses the catalytic decomposition of silane or silyl by gallium to form a eutectic mix. This is achieved by the reaction

$$\mathrm{SiH}_{x(g)} + x\mathrm{H}_{(g)} \underset{\rightarrow}{Ga} \mathrm{Ga} - \mathrm{Si}_{(l)} + x\mathrm{H}_{2(g)}. \tag{2.1}$$

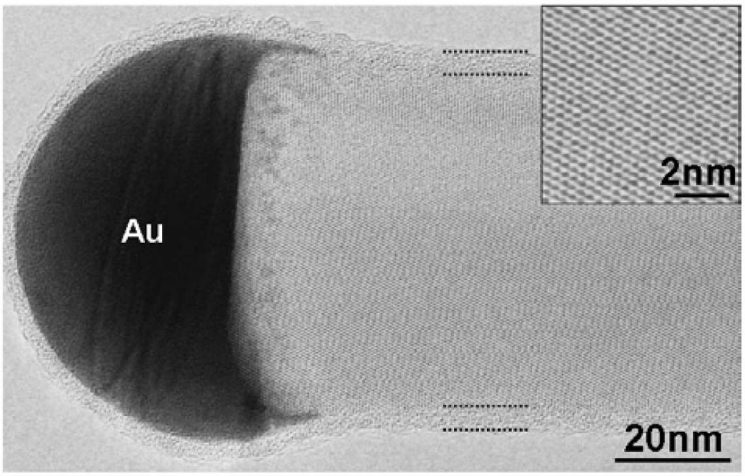

Figure 2.2: Reproduced from Stelzner *et al.* [34]. A High Resolution Tunnelling Electron Microscope photograph of a single crystalline silicon nanowire with a gold nanodot cap. The amorphous shell (dotted lines) and the uniform internal crystalline structure (inset) are shown.

These two materials form a eutectic at very low temperatures and, as the system cools, the silicon precipitates. As described earlier, due to the high surface tension and low silicon atomic percentage in the eutectic mix, the precipitate is most stable when forming solid crystals with diameters in the range of nanometers. Due to the low miscibility and high surface tension, the process ensures that further precipitate forms a continuous wire, which slowly grow out from the droplets and have a diameter of the original precipitant.

These experiments were carried out at various temperatures for a series of different durations and it was found that the length of the wire was proportional to the time of experiment (as one would expect). The nanowires grown with this technique were shown to have a large distribution of diameters ranging from 6 nm to 50 nm, and this was independent of growth time.

Stelzner *et al.* [34] refined the vapour-liquid-solid technique further by implanting a silicon substrate with positive gold ions. This substrate is etched with a HF solution to remove the oxide on the surface. The substrate is inserted into a chamber which is evacuated to a pressure of 1×10^{-6} mbar and the temperature is raised to 850 K for annealing. Once this is completed, the temperature is reduced to 770 K and

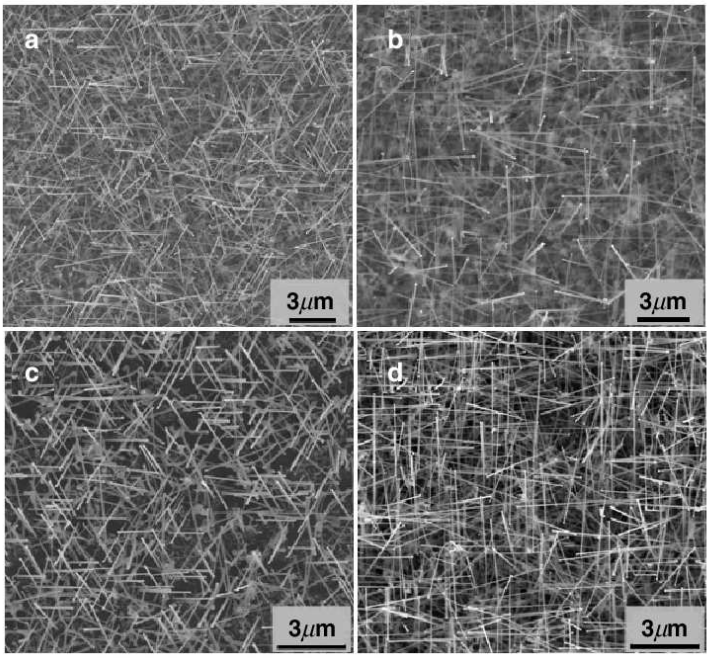

Figure 2.3: Reproduced from Stelzner *et al.* [34]. Scanning Electron Microscope images of silicon nanowire arrays grown on various substrates with [(a) and (b)] or without [(c) and (d)] gold implantation.

a mixture of 20 sccm argon and 4 sccm silane (SiH_4) is introduced at a pressure of 5 mbar for 20 minutes to grow nanowires. The resultant nanowires were shown to have various growth directions ([100], [110] and [111]) with an amorphous outer layer as shown in Fig. 2.2 and are found in a spaghetti-like mixture as shown in Fig. 2.3. The majority of the nanowires are capped with an gold nanodot which has a diameter ranging from 20 nm to 200 nm. This dot determines the diameter of resultant nanowire, meaning that the wire's diameters range from 20 nm to 200 nm as well. This technique was also performed using silver nanodots instead of gold which led to higher quality wires [70].

2.2.1.3 Nanotube Template Method

This technique uses a nanotube as a template to produce a nanowire. It has been used to produce gallium nitride nanowires [71] and several different carbide nanowires such as TiC, NbC, Fe_3C, and SiC [72]. The principle is that a oxide

vapour form of the material is reacted with carbon nanotubes at high temperature to produce a nanowire.

Han *et al.* [71] developed the technique so that it is possible to produce GaN nanowires of various lengths and diameters. For this, they first produced a Ga-Ga_2O_3 powder mixture. This mixture was placed in a crucible and covered with an alumina plate which had 3-5 μm channels cut through it from the upper surface to the lower. Nanotubes were placed on to the aluminium plate as shown in Fig. 2.4. The nanotubes used for this experiment were obtained using the chemical vapour deposition method (See later in section 2.2.4.3). These tubes consisted of multi-wall carbon nanotubes of average diameter of 15 nm. The final experimental set up is shown in Fig. 2.4. From this, the nanorods were produced via the reaction

$$2Ga_2O_{(g)} + C_{nanotubes} + 4NH_3 \rightarrow 4GaN_{nanorods} + H_2O + CO + 5H_{2(g)}. \qquad (2.2)$$

This reaction took place in a furnace with a horizontal quartz tube and constant flowing ammonia atmosphere passing over the carbon nanotubes. The chamber was brought to a pressure of 1 Torr at a temperature of 1173 K for 1 hour. The samples were then removed and exposed to the atmosphere. Examination of the sample after the experiment revealed the nanotubes had transformed into GaN nanorods of diameter 4 nm to 50 nm with lengths of up to 25 μm. The nanorods produced were solid with hexagon wurtzite crystal structure. This contrasted with the hollow tubes which were used to produce them. A similar reaction to this was applied to produce Si_3N_4 nanorods and Han *et al.* suggested that it may be used for other materials as well.

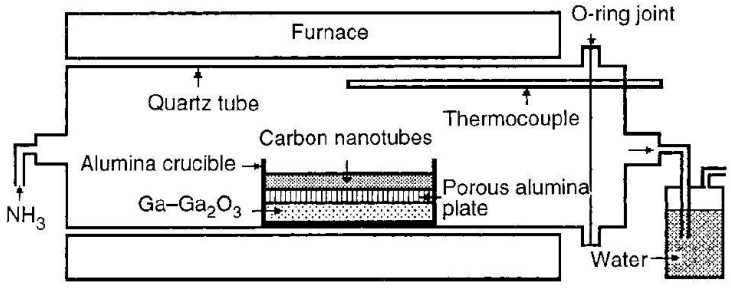

Figure 2.4: Reproduced from Han *et al.* [71]. A schematic diagram of the set up for preparing GaN nanorods.

2.2.1.4 Laser Ablation Technique

The laser ablation technique is a simple method where a sample of material is heated by a high power laser causing it to evaporate. This material is then gathered and mixed into an inert gas which is pumped through the system. This process leads to the growth of nanowires on the wall of the system, which can then be gathered for analysis.

Yu *et al.* [29] have applied this idea to grow silicon nanowires. In their approach, they prepared a target material which consisted of silicon powder mixed with nano-sized nickel and cobalt. This mixture was compressed into a plate, and then placed inside a quartz tube of dimensions 42 mm diameter by 570 mm length. This system was first evacuated to a pressure of 290 mTorr before being degassed by passing a flow of argon at 1123 K for 4 hours, which also heated the sample. After further degassing at 1473 K for 12 hours, the target is ablated by a high-powered laser (4 Watt on a 1 mm $\times$ 3 mm point) at a pressure of 500 Torr and temperature of 1473 K. The argon is passed through the chamber to aid in the deposition of the nanowires.

The properties of the resulting nanowires were found to be dependent on the reaction mechanism. These wires were observed to form two size distributions. The determining factor was whether the catalysts of nickel and cobalt were used. The first size distribution that Yu *et al.* produced was using the catalyst, where the nanowires were shown to have a uniform diameter of 13 ± 3 nm. However, if a catalyst was not used, then diameter distribution was not uniform and varies from 15 nm to 60 nm. These techniques are expected to become useful method for producing silicon nanowires of varying sizes if the catalyst and growth mechanisms can be better understood. The disadvantage of this technique is that the structure of the nanowire consists of a series of grains, which could reduce the mean-free-path of both electrons and phonons due to boundary scattering. This, in turn, would adversely affect their properties.

2.2.2 Nanowires on a Substrate

As described in Chapter 1, there are two broad definitions of nanowires upon a substrate. The first uses individual atoms to form the wire, whilst the other produces much larger wires with bulk internal structure. Several of the latest methods (at the time of writing) for producing both types of structure are presented in Ref. [73].

2.2.2.1 Nanowires by Self Assembly

Nanowires produced by self assembly are systems where the atoms preferentially form wires on a surface, rather than spreading out and forming a thin sheet or a series of islands.

These wires are interesting as it is possible to partially control where they are formed. This can be achieved using mechanical stresses, which are applied externally to the system. These techniques are advantageous as they require no lithography, which is difficult to perform at the nanoscale.

Saif *et al.* [74] in 2003 demonstrated a method to produce nanowires made of nickel deposited on a silicon substrate. Their fabrication technique began with first placing a silicon wafer in a heatable chamber. The silicon wafer was then coated by plasma-enhanced chemical-vapour-deposition (see section 2.2.4.3 for more details) silicon oxide. This oxide contains impurities (OH), which provide compressive stress in the film. The system is annealed at 800 K for 24 hours which leads to the impurities escaping from the film. This creates a tensile stress in the film and causes the film to crack. In order to relieve the stress, this crack cuts through the film and reaches the silicon substrate, creating a wedge-like shape. The crack is then partially filled using electrochemical deposition with nickel. After this, the oxide is removed using wet etching techniques, the surface is then clear, except for the deposited nickel, which forms a series of wires.

The wire's position is controlled by the cracking, which in turn is controlled by the stress. By tuning such parameters, one is able to partially choose the shape,

orientation and density of the nanowires produced.

2.2.2.2 Dangling Bond Technique

One of the first and most important devices that was developed in nanoscience and technology was the scanning tunnelling microscope [75] which was first reported in 1982. It is due to this device and the electron transmission microscope [76] that many of the images of nanostructures have been made possible. This has been vital as it has enabled researchers to confirm and understand nanostructures to a degree that would not have been previously possible. Since 1982, the scanning tunnelling microscope has been adapted for several different tasks, including the manipulation of individual atoms [77].

Hashizume *et al.* [78, 79] have applied this new technique for creating single atom nanowires on a substrate using dangling bonds. Their procedure is as follows: A silicon wafer sample is placed in an ultra-high-vacuum chamber and subjected to resistive heating which leads to substrate temperatures of up to 1530 K. It then undergoes further "outgassing" (the removal of gas from the chamber) at a temperature of 970 K for the period of at least twelve hours. This process enabled Hashizume *et al.* to obtain an atomically clean silicon surface wafer (which they confirmed using scanning tunnelling microscopy). Atomic hydrogen is then injected into the chamber. This chamber is kept at

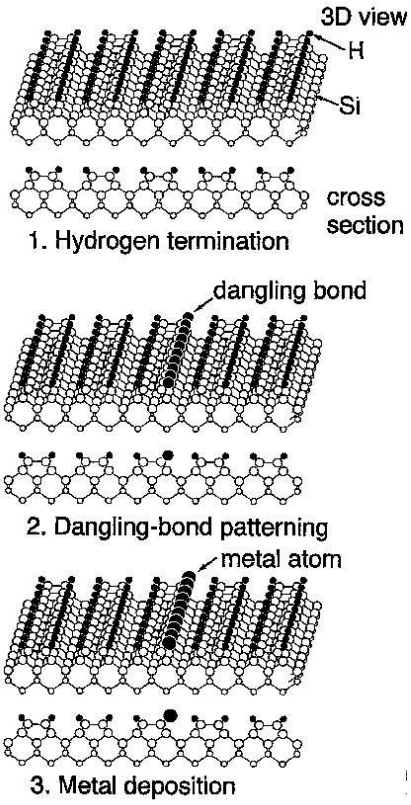

Figure 2.5: Reproduced from Hashizume *et al.* [78]. A schematic showing the method of fabrication of an atomic metal wire on the silicon surface. (1) Hydrogen termination of the surface. (2) Dangling bond fabrication. (3) Gallium atoms joining on bond sites to form a wire.

low pressure of 2×10^{-8} Torr and the wafer is maintained at a temperature ranging from 520 K - 670 K during the process, which takes approximately 10 minutes. Using this technique, the surface of silicon substrate has its dangling bonds and dimers terminated with hydrogen atoms. The surface may then be considered atomically clean and inert.

Depositing gallium on the surface of the system is done using a gallium dispenser, which is made of a tungsten filament and a small amount of gallium. The dispenser is introduced to the chamber in which the system is housed and heated to 870 K - 920 K. This process produces gallium particles, which can then be deposited onto the surface of the substrate. The gallium atoms in the chamber are shown to preferentially adsorb onto the dangling bond sites and impurities.

In order to create atomic wires, one needs to control the dangling bond sites locations. Hashizume *et al.* showed, using electron exposure from the scanning tunnelling tip, that hydrogen atoms can be made to desorb from the surface before gallium is introduced. Thus, by careful control of the tip, patterns of dangling bonds may be formed on the surface. Then gallium atoms can be introduced and these will bond to the dangling bonds. From this nanowire patterns of single atoms can be formed as shown in the schematic shown in Fig. 2.5. This was then confirmed using the scanning tunnelling microscope.

2.2.3 Nanodots

Nanodots, or zero-dimensional structures, are produced either suspended in a medium [6, 80] or upon a substrate. Of these, the former reveals characteristics of stand-alone structures and shows zero-dimensional characteristics whilst the latter shows substantially different properties, which are heavily dependent on the substrate used.

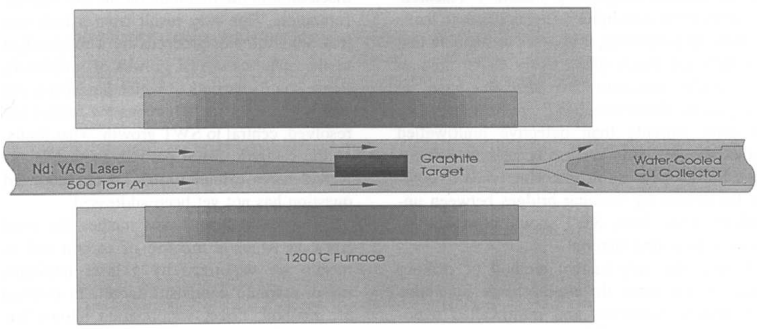

Figure 2.6: Reproduced from Guo *et al.* [82]. A schematic of the oven laser-vaporisation apparatus.

2.2.3.1 Sputtering Technique

Mishra *et al.* [6] show an effective method to produce silicon nanodots embedded in amorphous silicon dioxide is to use the sputtering technique. Sputtering is in essence the ejection of atoms from a target material and the condensation of these atoms onto a substrate. Mishra *et al.* used a sputtering target, which consisted of several small plates of Si/SiO_2 that were 5 mm $\times$ 55 mm in size and placed on a SiO_2 substrate. This target is bombarded by argon ions at 0.1 Torr for 2 hours. The process is largely driven by momentum exchange between the ions and atoms in the material due to collisions. The mechanism of sputtering is relatively simple as when an ion strikes a large cluster of close-packed atoms it can eject one or more of the surface atoms from the target's surface. These ejected atoms then condense onto a substrate material in the chamber which is not the target of the original bombardment. Using this mechanism, several silicon dots can be embedded in a layer of SiO_2.

2.2.4 Carbon Nanotubes

2.2.4.1 Laser Vaporisation Approach

A technique similar to that used to produce silicon nanowires, as described in section 2.2.1.4, can also be applied to carbon nanotubes [13, 81, 82]. The laser va-

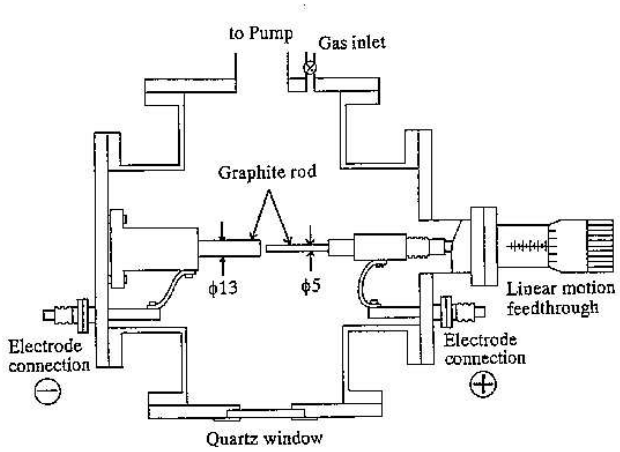

Figure 2.7: Reproduced from Saito *et al.* [84]. A schematic of a carbon arc generator.

porisation technique has been used by several groups with considerable success. A particularly good description of the method has been presented by Gou *et al.* A quartz tube is placed in the centre of a furnace with a graphite target. The graphite target contains 0.6% cobalt and 0.6% nickel alloy within it and it is set up as shown in Fig. 2.6. The system is evacuated to a pressure of 10 mTorr and a high powered laser (300 mJ/pulse) is focused onto a 6 mm - 7 mm diameter spot on the graphite which causes vaporisation. The quartz chamber is filled with argon at a pressure of 500 Torr which flows from the source to the copper collector and the chamber is heated to 1470 K via the furnace. As the material is vapourised it is swept downstream and deposited onto the water cooled copper collector's surface.

The material collected on the copper collector was observed by Gou *et al.* using transmission electron microscopy. They observed the nanotubes to form as mats of ropes, where each rope consisted of a bundle of single-wall nanotubes. These single-wall nanotubes have a diameter distribution that peaks at 1.38 ± 0.02 nm. This peak is close to the ideal $(10, 10)$ nanotube. The spread in distribution of diameters is less within each rope than when comparing different ropes grown under the same growth conditions. It can be clearly seen that the carbon nanotubes within each rope are all aligned to a common axis parallel to the rope.

2.2.4.2 Carbon Arc Method

The carbon arc method [13, 66, 83] is another effective method for large scale production of carbon nanotubes. This technique was first pioneered by Saito *et al.* [13]. The apparatus, as shown in Fig. 2.7, consists of two graphitic rods placed in a reactor. A voltage is applied between two electrodes and a current flows between these two points. This current leads to the creation of various nanotubes on the cathode.

Journet *et al.* [83] used this method to produce large quantities of carbon nanotubes in 1993. In their setup, the negative electrode (cathode) and positive electrode (anode) had diameters of 16 mm and 6 mm respectively and were separated by a gap approximately 1 mm in size. The anode had a small hole drilled into its centre, into which a mixture of graphite powder and the catalysts had been placed (in this case, Y and Ni). The carbon arc is operated in an atmosphere of argon at a pressure of approximately 500 Torr. The argon flows at a rate of 5 to 15 mls^{-1} to sweep through the chamber for cooling purposes. The arc discharge is created when a voltage of 30 eV is placed across the electrodes and a current of 100 A is allowed to flow. Carbon nanotubes are grown on the end of the cathode and, as this process occurs, the anode length decreases. The nanotubes that were grown were single-wall, arranged in ropes and aligned approximately with the direction of the current flow. These tubes tend to be located in the inner region of the apparatus where the temperature is at a maximum (2770 K to 3270 K). Journet *et al.* showed that by applying this technique, tubes of average diameter 1.4 nm were produced in ropes. The diameters of the ropes of tubes were between 5 nm and 20 nm and several grams of nanotubes could be produced.

By varying the catalysts [13] it is possible to prepare multi-wall tubes. Also, by altering the the conditions, Journet *et al.* demonstrated it was possible to vary the average diameter of the carbon nanotubes produced. However, these nanotubes are still usually small in diameter (<1.5 nm) . The smallest they managed to achieve had a peak in its distribution occurring at approximately 0.7 nm.

2.2.4.3 Chemical Vapour Deposition Technique

Vapour grown carbon nanotubes use a similar method to that used to grow carbon fibres [13, 85]. These methods are comparatively simple and effective. Nanoparticles, such as iron particles, are placed into a sealed environment on a substrate, which normally consists of some form of graphite such as a rod. Into this environment, benzene vapour and hydrogen gas are introduced and the system is heated to 1250 K or greater. After one hour under these conditions, nanotubes and nanofibres of both the single and multi-wall kind can be found deposited in the chamber. By varying the injected gas (benzene vapour in this case) it is possible to change what types of tube are grown. Endo *et al.* [85] showed that further heat treatment at temperatures exceeding 2770 K for 10 to 15 minutes can improve the crystallinity and reduce the number of defects within these structures. This method (like the previous) can be fine-tuned to grow different bundles of tubes or fibres, but it has not been shown yet to produce any single tube (multi-wall or single-wall) of a particular chirality. This is a common problem with all the techniques available for growing nanotubes.

2.3 Raman and Neutron Scattering

Whilst several methods for producing nanostructures exist, methods for determining their vibrational characteristics and properties remain relatively few. Raman scattering and neutron scattering are two of the more powerful tools that can be used for discerning the vibrational features of these nanostructures. The former is useful for detecting different phonon modes energy values near the Brillouin zone centre and the latter is useful for examining the phonon density of states in nanomaterials. For nanostructures, these techniques have been refined and enhanced to enable measurements of these nanoscale systems to be carried out.

2.3.1 Raman Scattering

Of the two techniques outlined above, Raman scattering is the more common as it is easier to perform and can be used to identify both the energy of optically active vibrational modes near the zone centre, and the energy of electronic transitions. These measurements normally consist of applying a laser to the target material and collecting the scattered light from the sample using a Raman spectrometer - a spectrometer which detects centimetre scale wavelengths. These spectra are then gathered and analysed.

The principle behind measuring Raman scattering is relatively simple. A high energy monochromatic beam of light (such as a laser beam) is shone onto or projected at the sample. The photons in this beam of light are then scattered by two mechanisms: Raman scattering and Rayleigh scattering [27]. Raman scattering is an inelastic process as the energy of the incident light is different from the reflected light. This is because the resultant photon has either lost (Stokes-Raman scattering) or gained (Anti-Stokes Raman scattering) energy equal to the energy of a vibrational mode (i.e. a phonon). By measuring this change in frequency, one may then calculate the energy of the phonon. However, as the wave-vector of the photon is very much smaller than the Brillouin zone all interactions between it and the phonons must occur near the Brillouin zone centre due to momentum conservation. Momentum conservation also enables one to calculated the polarisation of the phonon which was involved in the scattering as depending on the orientation of the sample and the incident beam, selection rules are created and particular modes are not allowed to interact. In nanostructures this information is less prevalent as the samples tend not to have a uniform orientation, which makes observing photon polarisation (and hence phonons polarisation) impossible as the scattering cannot be linked with the orientation of the crystal structure.

Table 2.1: Reproduced from O'Connel *et al.* [89] A comparison of the radial breathing mode frequency for individualised nanotubes (in solution) and roped samples of different radii.

(n_1, n_2)	Diameter (nm)	ν (solution) (cm^{-1})	ν (roped) (cm^{-1})
(8,0)	0.6350	-	364
(6,4)	0.6921	-	333
(6,5)	0.7573	307	307
(9,1)	0.7573	304	304
(8,3)	0.7819	296	296
(7,5)	0.8290	-	282
(10,2)	0.8841	264	266
(9,4)	0.9156	256	261
(8,6)	0.9658	244	244
(12,1)	0.9948	236	236
(10,5)	1.0503	225	227
(9,7)	1.1029	215	214
(13,2)	1.120	211	213
(12,4)	1.145	206	209
(13,3)	1.170	205	203
(11,6)	1.1856	200	201
(11,7)	1.2477	193	192

2.3.1.1 Raman Scattering in Carbon Nanotubes

Several groups [14, 87, 88, 89, 90] have performed Raman scattering measurements on carbon nanotubes to help increase the understanding of their vibrational modes.

In 2004, O'Connel *et al.* [89] applied Raman spectroscopic techniques to single-wall carbon nanotubes and bundles of single-wall nanotubes in 2004. The objective of their research was to compare the effects that the bundling of nanotubes, when forming ropes, had on their vibrational modes. To perform their experiment, they obtained single-wall nanotubes in bundles (ropes) from Rice University. This is

a common trend in nanotechnology in particular, where one group produces the samples and another characterises them. To prepare the single-wall nanotubes, O'Connel *et al.* suspended the bundles of single-wall tubes in an aqueous solution of sodium sulfate. They then combined, briefly, 1% of the surfactant with 40 mg of nanotube material in 200 ml of water. This mixture underwent high shear mixing for 1 hour and then was ultrasonicated (subjected to high-intensity acoustic energy) at 590 W for 10 minutes. The resultant mixture then underwent centrifuge for four hours at 200,000g (where $g = 9.81$ ms^{-2}) using a swing bucket rotor. The resulting decant was isolated for experiments, having now separated the bundles of tubes into individual tubes. For the bundles of tubes, preparation involved taking 10 mg of solid HiPco nanotubes and suspending them in 10 ml of isopropane. This mixture was then allowed to dry upon a slide.

To obtain the actual measurements, the excitation was performed using a Ti:Sapphire laser which emitted wavelengths between 700 nm and 985 nm. The resulting spectra were collected using a triple monochromator and a charge-coupled device camera. The laser had a power of 15 mW and data was corrected to remove background information such as that of the solution or raw background spectra. O'Connel *et al.* do not elaborate on this however.

One of the modes which was studied in this report was the Radial Breathing mode. This mode, which as mentioned earlier, is a unique mode to nanotubes and is also optically active. This mode is known to have a frequency which lies in the region of 100 cm^{-1} to 400 cm^{-1} for nanotubes of diameter between 0.6 nm and 1.4 nm. O'Connel's results for this mode are shown in Table 2.1. As can be seen, the effect of bundling on nanotubes does not change the breathing mode frequency, but a change in nanotube diameter does. O'Connel *et al.* do note that bundling does effect electronic transitions which are observed in nanotubes.

2.3.1.2 Raman Scattering In Silicon Nanowires

Like nanotubes, nanowires have also attracted considerable attention in Raman spectroscopy [91, 92, 93, 94, 95].

Table 2.2: Reproduced from Li *et al.* [91]. The Raman frequency, and average wire size of the two samples of nanowires measured. Also shown is the full width half maximum (FWHM) of the data.

Sample	Raman frequency (cm^{-1})	Average size (nm)	Grain size (nm)	FWHM (cm^{-1})
Si NW A	504	13	10	23.1
Si NW B	511	20	15	15.6
Bulk Si	520	-	-	2.8

In 1998 Li *et al.* used Raman spectroscopy to measure the energy of the optical modes in silicon nanowires. Their nanowires were grown using the laser ablation technique described in section 2.2.1.4. This method of production allowed them to produce two sets of samples (A and B). In sample A, the nanowires had a relatively uniform diameter of 13 $\pm$ 3 nm whilst those grown in sample B had a diameter distribution of 15 to 60 nm. They also obtained crystalline bulk silicon and amorphous SiO_2 nanowires. The Raman spectra were obtained in the standard method detailed previously, at room temperature. The laser that Li *et al.* used was a He-Ne laser and the Raman signals were measured with a spectrometer that had a spectral resolution of 1.0 cm^{-1}.

From these samples, Li *et al.* obtained the results shown in Table 2.2. They clearly show that as the wires decrease in diameter, the Raman frequency of the highest optical mode is downshifted due to confinement effects. They also showed in [91] that in the amorphous sample, the frequency dropped even further, to 490 cm^{-1}. Lastly, they showed that the peak was asymmetric, which indicates that the wires amorphous coating may have a further effect on the results.

This was expanded upon later by Ding *et al.* [92] who showed clearly that the grain-like structure of the nanowire and the wavelength of the exciting light both affected the shift in the position of this peak. The grain-like structure is shown in Fig. 2.8 and it is suggested that the frequency of the peaks is more grain-like than wire-like. This is explored further in Chapter 3.

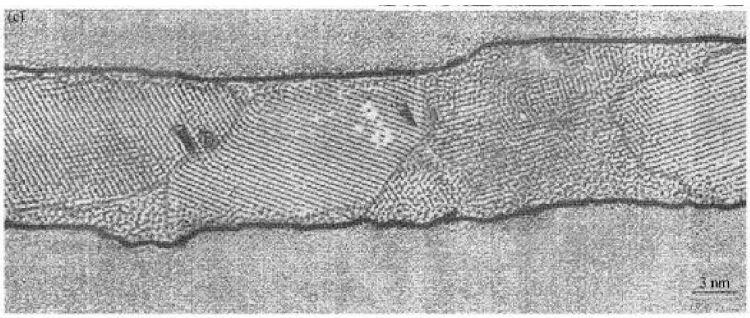

Figure 2.8: Reproduced from Ding *et al.* [92]. A high resolution tunnelling electron microscope image of the silicon nanowire being observed in the Raman measurements.

2.3.1.3 Raman Scattering In Silicon Nanodots

Isolated silicon nanodots are not possible as one requires a mechanism to suspend them. As such most of the research into Raman scattering in silicon [6, 80, 96] (and other nanodots [60, 97, 98]) has the nanodots suspended in an embedding medium (such as silicon dioxide).

In 2002, Mishra *et al.* [6] performed Raman scattering measurements of silicon nanodots embedded in SiO_2. They showed in their results that the annealing duration and temperature (used to create the nanodots embedded in the SiO_2) led to Raman shifts towards higher wavelengths associated with the 525 cm^{-1} maximum of bulk silicon. From this they concluded that the amorphous silicon led to a downshifting of the peak associated with this mode and that increased annealing would improve the quality of the silicon nanodots embedded within the amorphous silicon. They then used photoluminescence results to examine more closely the samples and provide a second method of confirming the nanodots diameter. From the two sets of results, they were able to provide evidence that the embedded silicon does not undergo complete confinement, as expected. The results also confirmed the observations of Li *et al.* [91] that the amorphous coating on nanostructures has an effect on their vibrational properties.

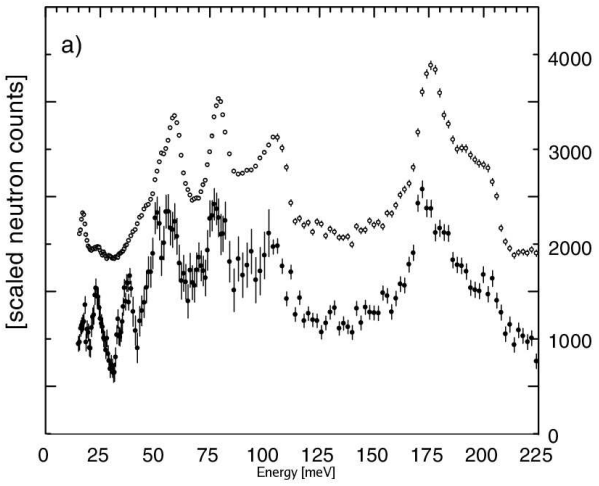

Figure 2.9: Reproduced from Rols *et al.* [99]. The room temperature density of states of a single wall nanotube sample (solid circles) and a graphite sample (hollow circles) using the filter method.

2.3.2 Inelastic Neutron Scattering

Inelastic neutron scattering is a more difficult procedure to undertake as the equipment is expensive and more specialised. However, neutron scattering is very useful for providing information on the structure of the phonon dispersion curves and the phonon density of states. Inelastic neutron scattering is conceptually similar to Raman scattering. There are, however, significant differences. The major difference is that photons interact primarily with the electrons of a sample, whereas neutrons interact with the nuclei. Also, because of their comparatively lower velocities, neutrons are able to react with phonon modes in different segments of the Brillouin zone, which have different momenta. This in turn enables one to build up a picture of the phonon dispersion relations and phonon density of states of the structure.

2.3.2.1 Inelastic neutron scattering in carbon nanotubes

For carbon nanotubes, neutron scattering experiments were undertaken by Rols *et al.* [99] in 2000. They obtained their nanotubes using the laser vaporisation technique outlined in section 2.2.4.1. After obtaining these nanotubes, they used a series of purification techniques to remove the amorphous carbon, residual metals

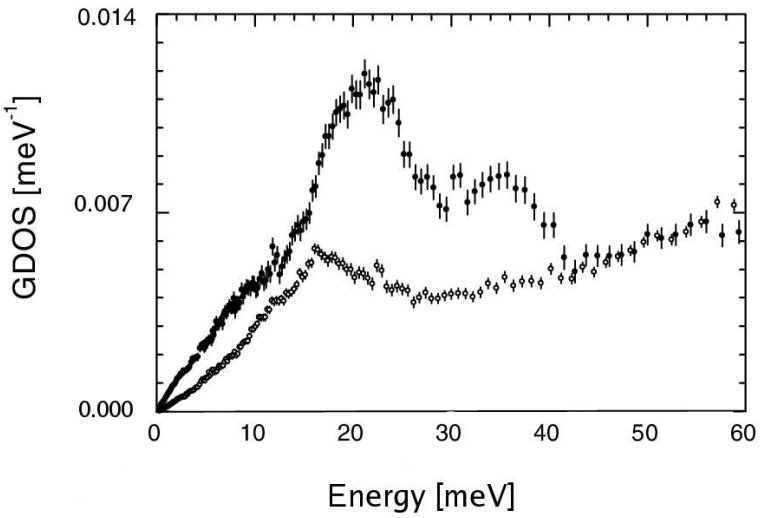

Figure 2.10: Reproduced from Rols *et al.* [99]. The room temperature density of states of a single wall nanotube sample (solid circles) and a graphite sample (hollow circles) using the time in transit method.

and graphitic impurities from the sample as well as the surfactant. They then applied high resolution electron microscopy to characterise the sample. It was found that the sample had a prevalence of bundles of tubes over isolated tubes with very few impurities. The nanotubes measured in the sample were estimated to have mean diameter of 1.4 nm with a standard deviation of $\pm$ 2 nm. This was performed using scanning tunnelling microscopy. For their inelastic neutron scattering measurements, Rols *et al.* used two complementary techniques. For their first method a berylium filter was used which enables results to be detected in the energy range of 20 - 250 meV. The second method applied uses the time-of-flight of the neutron (from the emitter to the detector) from which the scattered neutrons velocity can be calculated. Using these two methods, Rols *et al.* counted the number of scattered neutrons and their energies and were able to build an effective picture of the phonon density of states in the sample.

Figures 2.9 and 2.10 show the results of applying these two measurement techniques. Figure 2.9 shows a comparison of a single wall carbon nanotube and graphite both measured using the filter method. It can be clearly seen that the phonon density-of-states for the tube is substantially different from graphite in the low energy range, but shows similarities in the high energy range. Figure 2.10 also shows a difference

as higher energy radial breathing modes lead to an additional peak not observed in graphite, as expected. It is also of considerable interest that, because these tubes are found in the form of ropes and bundles of tubes, the density of states for the phonon modes is not finite as the energy tends to zero.

2.4 Specific Heat Capacity and Thermal Conductivity

Specific heat capacity and thermal conductivity are two of the most important thermal properties which a material possesses. In nanostructures, measuring these properties has posed several difficulties. This is because ensemble samples of nanostructures have different properties from the isolated case. As seen earlier, techniques have not yet reached the stage where one can manufacture individual nanostructures of reliable and repeatable physical quantities with ease. However, despite these difficulties, progress is being made rapidly and the hope of being able to grow uniform structures and samples of high crystallinity are expected to be realised soon.

2.4.1 Specific Heat Capacity

The specific heat capacity of an object, C_v is defined as

$$C_v(T) = \left(\frac{\delta E}{\delta T}\right)\Bigg|_{V_0} \tag{2.3}$$

where E is the total energy of the system, T is the temperature of the system and V_0 is the volume of the system. The subscript v in C_v declares that the specific heat capacity is measured (or calculated) at constant volume. This originates with the classical expression [100]

$$\Delta H = C_v(T)\Delta T \tag{2.4}$$

where ΔH is the total energy added or removed from the system and $\Delta T (= T_1 - T_2)$ is the change in the temperature. Equation (2.4) holds only when the system does not undergo a phase transition.

2.4.1.1 Specific heat capacity of carbon nanotubes

In order to measure the specific heat capacity C_v of carbon nanotubes, Hone *et al.* [66] prepared carbon nanotubes using the technique described in section 2.2.4.1.

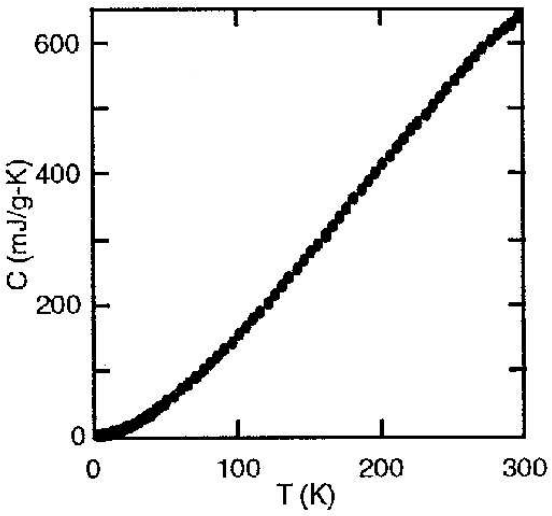

Figure 2.11: Reproduced from Hone *et al.* [66]. The specific heat capacity of a sample of ropes made up of single wall carbon nanotubes.

These tubes were acid-treated to remove catalyst particles and amorphous carbon. These were then filtered, rinsed, dried and tightly folded into two small pellets which were vacuum annealed. After this, the samples were examined using x-ray diffraction to ensure they retained their hexagon crystal structure. To carry out the actual measurements, Hone *et al.* used the Quantum Design Physical Properties Measurement System. The first stage is to measure the specific heat capacity of the stage onto which the sample is mounted, followed by measuring the combined system and subtracting the stage contribution. The principle of the measurement is that the stage and sample with a control puck are first stabilised at an initial temperature. Then using a heater operating at a known power the sample and stage are heated. The system is then allowed to cool to the puck temperature and the time the cooling takes is measured. Then using the *two-tau* model [101] the specific heat capacity is fitted.

Hone *et al.*'s measurements for the specific heat capacity are shown in Fig. 2.11. These measurements show that the specific heat capacity of carbon nanotubes increases with temperature as expected, but the behaviour is different from graphene or graphite. These measurements show clearly that the specific heat of carbon nanotubes does not vary as T^3 as expected in bulk materials. They also observed when

measuring the size of bundles of nanotubes that they had a strong peak in their size distribution near the (10,10) nanotube. This is discussed further in Chapter 4.

2.4.2 Thermal Conductivity

The measurement of the thermal conductivity of a material can be performed by several different methods, but the key feature is measuring the heat flow between two contacts. Connecting one-dimensional nanostructures to these contacts, without the contacts dominating the properties of the system, has been one of the largest difficulties in measuring thermal conductivity and a number of different techniques and methods have been adopted to perform these measurements in carbon nanotubes.

2.4.2.1 Thermal Conductivity of Carbon Nanotubes

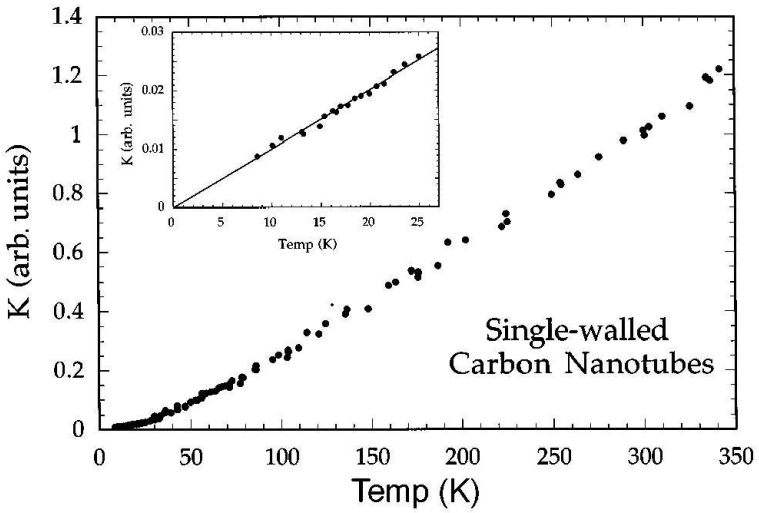

Figure 2.12: Reproduced from Hone *et al.* [102]. The thermal conductivity (in arbitrary units) of a sample of ropes made up of single wall carbon nanotubes.

The thermal conductivity of carbon nanotubes κ_{CNT} is a very important and attractive property. Nanotubes are expected to have thermal conductivities greater than that of diamond (the highest thermal conductor previously known) due to the strong carbon bonding and the high mean freepath. As mentioned in Chapter 1 this has lead to much interest in these structures.

J. Hone *et al.* [102] measured the thermal conductivity of single-wall carbon nanotube mat ensembles in 1998. The carbon nanotubes were prepared using the arc discharge method, as described in section 2.2.4.2. This method yields high-purity carbon mats of tangled nanotubes. Hone *et al.* also used samples prepared using the laser vaporisation technique (described in section 2.2.4.1) and noted similar results.

In order to carry out thermal conductivity measurements, Hone *et al.* mounted the mats in a series of rods made from Constantin. The temperature-dependent thermal conductance of the rods was measured before the sample was added for later comparison, so as to eliminate the rods' contribution. A heater was placed at one end of the Constantin rod to provide heat current to a cold temperature stage. By comparing the temperature drop across the sample and the Constantin rod, it was then possible to calculate the thermal conductivity. The experiment was first run on several known thermal conductivities to test the equipment, before the samples were inserted. After initial measurements, different samples of varying geometry and thermal conductance were measured. These were shown to have the same temperature dependence as the initial sample.

Figure 2.12 shows the results Hone *et al.* observed in their experiment for the temperature range 8 K - 350 K. For the range 40 K to 350 K, the thermal conductivity κ_{CNT} was shown to vary with very little curvature with temperature (i.e. $\frac{\delta^2\kappa}{\delta T^2} \ll 1$). For temperatures of less than 40 K, the thermal conductivity of carbon nanotubes was linear. This early experiment brought to light the expected temperature behaviour of the carbon nanotube, but failed to correctly measure its magnitude. This was due to the measurements being carried out using carbon nanotube mats, which meant that, due to dampening of phonon modes, the magnitude of the thermal conductivity was much less than expected and was only 35 $\mathrm{Wm^{-1}K^{-1}}$ at room temperature.

This was to be corrected later in 2001 when Kim *et al.* [103] fabricated a device which enabled them to measure the thermal conduction of an individual multi-wall carbon nanotube suspended between two islands. To carry out these measurements, Kim *et al.* fabricated two silicon nitride islands suspended on two silicon nitride

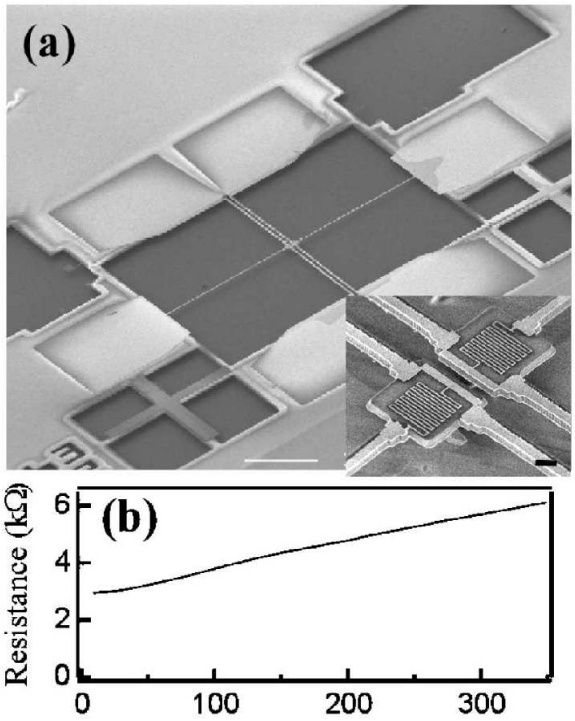

Figure 2.13: Reproduced from Kim *et al.* [103]. (a) A scanning electron microscopy image of two silicon nitride islands suspended by three silicon nitride legs. Inset: Enlarged image of the islands showing the platinum resistors. (b) The measured variation of the resistance of a platinum resistor with temperature.

beams. By applying electron beam and photo-lithography they were able to design and fabricate two coiled platinum resistors on these islands, as shown in Fig. 2.13 (a). As can be seen from Fig. 2.13 (b), the resistance of each of these islands varies with temperature and hence this acts like a thermometer for measuring the temperature of each island. A carbon nanotube, produced using the arc technique described in section 2.2.4.2, was placed using a scanning tunnelling microscope [104] across the two islands as shown in the inset in Fig. 2.14. This was achieved using a similar technique to that described in section 2.2.2.2.

Figure 2.14 shows the results of Kim *et al.* for a multi-wall nanotube of diameter 14 nm with a bridge length of 2.5 μm. The results show the thermal conductance of the nanotube increases by several orders of magnitude as the temperature is raised from 7 K to 300 K. At temperatures greater than this, the thermal conductance decreases. To calculate the thermal conductivity, Kim *et al.* ignore the effect of the

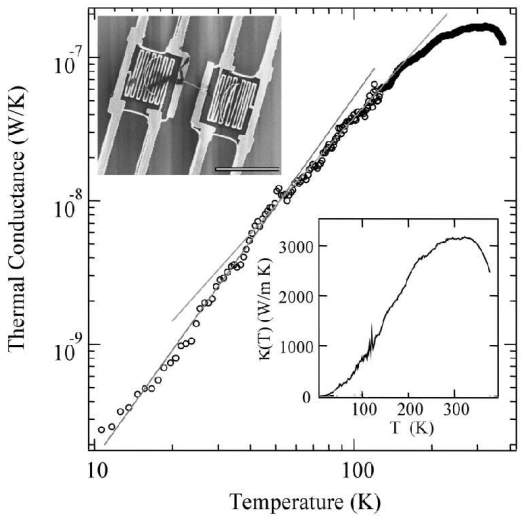

Figure 2.14: Reproduced from Kim *et al.* [103]. The measured thermal conductance of an individual multi-wall carbon nanotube of diameter 14 nm. Lower inset: The thermal conductivity of an individual multi-wall carbon nanotube. Upper inset: A scanning electron microscopy image of the suspended islands with an individual multi-wall nanotube placed upon them.

contact between the tube and the resistor and use the relation $\kappa_{CNT} = \Sigma_{CNT}/L_0$ where Σ_{CNT} is the conductance of the nanotube and L_0 is the length of the tube. It is important to note that neglecting the effect of tube-resistor contact means that the measured values of κ_{CNT} are underestimates. This shows that carbon nanotubes can have thermal conductivities of at least 3000 $\mathrm{Wm^{-1}K^{-1}}$ at room temperature and suggests that they are the best heat conductors known.

2.5 Summary

In this chapter several experimental techniques regarding nanostructures and their thermal and vibrational properties have been described. In section 2.2 several different methods for producing nanodots, nanotubes and nanowires were presented. The results presented here, from other groups, show that such devices are feasible to produce, but also described some of the problems associated with their fabrication. It can also be seen from this section that there are several different and diverse forms of nanostructures and that steady progress is being made in their manipulation and application.

In section 2.3 two methods for measuring these nanostructures vibrational properties (Raman scattering and inelastic neutron scattering) were presented. Here emphasis was given to two important vibrational modes associated with nanostructures; the highest vibrational mode and the breathing mode, with the latter being of particular importance to nanotubes. These modes will be explored in more detail in Chapter 3 and their behaviour as a function of nanostructure size explained.

Finally, methods for measuring both the specific heat capacity and the thermal conduction of carbon nanotubes were presented in section 2.4. These show that nanostructures have some unique thermal properties which are quite unlike their bulk counterparts. These properties will be examined and explained using theoretical models in Chapters 4, 5 and 6.

In order to understand these key characteristics of the thermal properties of nanostructures, one must have a good knowledge of the phonon dispersion relations. In the following chapter the theory of lattice dynamics and phonon dispersion relations for nanostructures will be developed and it will explain several key results that were observed in some of the previous sections, as well as reveal other interesting vibrational features.

Chapter 3

Phonon Modes in Nanostructures

With this salt I am shaking the foundations of the empire.

Mohandas Gandhi, (October 1869 - January 1948)

3.1 Introduction

This chapter begins with an introduction to lattice dynamics and discusses the development of the subject over the last century. An important phenomenological model, the Adiabatic Bond Charge model, is introduced and the basics of its formulation described. The main subject of this chapter, the lattice dynamics of silicon nanostructures, is introduced and the previous background research in this area summarised. The theoretical method for modelling the lattice dynamics of silicon nanostructures is described, using the Adiabatic Bond Charge model as a basis. This is followed by a detailed discussion of the results. Lattice dynamical calculations for silicon nanowires, nanodots, nanoslabs and other structures are presented and summarised. The last section of the chapter describes the lattice dynamics of carbon nanotubes. Analytic expressions for the phonon dispersion relations are derived and the meaning of these expressions discussed. These results are compared and contrasted with silicon nanostructures and the behaviour of key modes is explained. Finally, concluding remarks are presented.

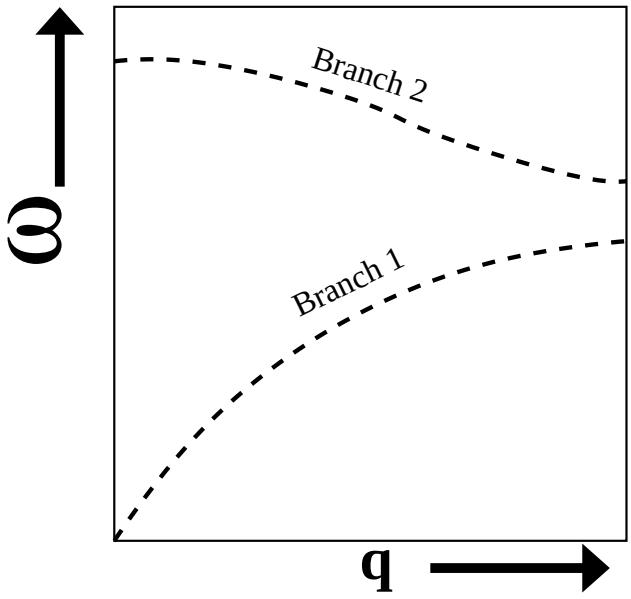

Figure 3.1: An example of phonon dispersion curves for a two atom system with one degree of freedom. As can be seen, each momenta $\mathbf{q}$ has two corresponding possible energies, which are denoted by branch 1 and branch 2.

3.2 What Is Lattice Dynamics?

The concept of a phonon and its properties were first introduced by Debye [3] in 1912. A phonon is defined as a quantum of vibrational energy within a crystal structure. Phonons are considered as a *quasi-particle* with wave vector $\mathbf{q}$ and angular frequency ω_s for atomic vibrational polarisation s. The energy of a phonon mode is $\hbar\omega_s$ and its momentum is $\hbar\mathbf{q}$. Lattice dynamics is the study of the relationship between these two quantities: $\omega = \omega_s(\mathbf{q})$. To solve this problem, one must first use two underlying assumptions for a crystal structure and its interactions:

1. The atoms obey harmonic motion, i.e. they act within the harmonic approximation and energy is conserved.

2. The phonons do not interact with each other or other free particles within the structure.

It is important to elaborate further as it is possible for a phonon with momentum $\mathbf{q}$ to have multiple corresponding energy levels or branches as shown in Fig. 3.1. These branches are the different vibrational polarisations a phonon mode may possess and are denoted by the subscript s. In the case of Fig. 3.1 the possible values for s are 1 and 2. Examples of polarisations can be longitudinal, where atoms oscillate in the direction of wave propagation, and transverse, where atoms oscillate perpendicular to the direction of propagation. The maximum possible number of branches for a bulk atomic model (as opposed to a continuum model which is explained later) is the number of atoms per unit cell N multiplied by the number of degrees of freedom the atoms have (normally three). These branches are divided into two categories: acoustic, and optical. Acoustic branches are defined by the relation $\omega(\mathbf{q} = 0) = 0$ with atoms vibrating in phase and optical branches are defined by the relation $\omega(\mathbf{q} = 0) \neq 0$, with atoms moving out of phase. These definitions can vary. Due to the unique behaviour of phonon modes in low-dimensional systems, these definitions are usually modified. For example, in nanostructures, one can observe mixed modes, which have the vibrational behaviour of both acoustic and optical nature. This will be clarified later in this chapter. For now, to avoid confusion, the definitions stated above are adopted.

To understand how phonon dispersion curves arise, one must first understand the crystal potential and define the atomic co-ordinates. The atomic co-ordinates of a system are defined using the unit cell vector $\mathbf{l}$, and the relative position, $\mathbf{b}$, of the atom within this unit cell. This is the mean position or the equilibrium position of the atom. In reality the bth atom will be located at position $\mathbf{r}(\mathbf{lb})$ at time t as it will be vibrating. Hence the displacement, $\mathbf{u}(\mathbf{lb})$, of atom lb may be written as

$$\begin{aligned} \mathbf{u}(\mathbf{lb}) &= \mathbf{r}(\mathbf{lb}) - (\mathbf{l} + \mathbf{b}) \\ \mathbf{u}(\mathbf{lb}) &= \mathbf{r}(\mathbf{lb}) - \mathbf{x}(\mathbf{lb}), \end{aligned} \tag{3.1}$$

where $\mathbf{x}(\mathbf{lb}) = (\mathbf{l} + \mathbf{b})$. Using this definition, the crystal's potential energy can be expanded as a function of displacement $\mathbf{u}(\mathbf{lb})$ using a Taylor series. Hence

$$V = V_{00} + \sum_i \frac{\delta V}{\delta u_i}\bigg|_0 u_i + \frac{1}{2!}\sum_{i,j} \frac{\delta^2 V}{\delta u_{ij}^2}\bigg|_0 u_i u_j + \frac{1}{3!}\sum_{i,j,k} \frac{\delta^3 V}{\delta u_{ijk}^3}\bigg|_0 u_i u_j u_k + ... \tag{3.2}$$

where i, j and k are the vector indices (i.e. u_i where i=1 corresponds to u_x) and V is the crystal's potential energy. For calculations of lattice dynamics, terms of the third order and higher in Eq. (3.2) are ignored as these are small perturbations on the total energy of the system. The zeroth order term, V_{00}, sets the zero of the potential and hence can be excluded. Lastly, as the system is in equilibrium the first order term must also be ignored as the system has no net velocity. This leaves the second order term V_2 to be considered, where

$$V_2 = \sum_{i,j} \frac{1}{2!} \frac{\delta^2 V}{\delta u_{ij}^2}\bigg|_0 u_i u_j. \tag{3.3}$$

Having defined this term, one needs to understand the form this function takes. Once the form of V_2 is understood, the equations of motion may be set up and a dynamical matrix for the atoms of the system created. By solving this dynamical matrix one may obtain the phonon dispersion relations. Consequently, it is the term in Eq. (3.3) which is key to understanding models of lattice dynamics.

3.2.1 The Development of Lattice Dynamics

The last century has seen the proposal and development of several models to describe the lattice dynamics of covalently bonded materials. These models vary greatly in complexity from simple continuum models to detailed *ab initio* models. Each of these models have different uses and applications in various areas.

The field of lattice dynamics began to take form in 1912 when Debye [3] proposed a simple model known as the elastic isotropic continuum model. In this model the atomic crystal structure was smeared out and treated as a continuous elastic medium. This is the easiest and most simplistic view of a solid semiconductor that may be taken when discussing its vibrational behaviour. It is surprisingly effective for such a simple model and can form a basis in estimating the basic thermal features of a semiconductor. By applying this model, it is possible to relate the elastic constants that describe the semiconductor to the zone-centre group velocities c_s of an acoustic phonon mode $\omega_s(\mathbf{q})$. The dispersion relation Debye obtained for the

frequency of a phonon mode $\omega(\mathbf{q})$ is

$$\omega_s(\mathbf{q}) = c_s|\mathbf{q}|. \tag{3.4}$$

However, this model is a gross approximation and fails completely to consider or describe optical modes.

The next step in the modelling of lattice dynamics was a series of phenomenological force models which built on each previous model, and the development of a few *ab initio* models as well. The latter of these methods, the *ab initio* models, were created in the 1970's and require an accurate and parameterless calculation of microscopic electron response to lattice vibrations. These calculations can be done via a number of different techniques such as the Frozen phonon method [105] and the Planar force constant method [106]. However, *ab initio* calculations of lattice dynamics of nanostructures have only recently become feasible and these are still limited to the smallest and thinnest of structures with only a few atoms in the unit cell. This is due to the lack of translation symmetry in one or more directions which introduces difficulties in modelling the periodic potentials of the crystal structure. In particular, nanowires present a very difficult problem as calculations of the phonon dispersion relations for structures with greater than 100 atoms become nearly impossible within current computational limits. This has led to the use of phenomenological models for modelling nanostructures. These were first developed in 1914 and have been continuously improved and adapted for more advanced structures up until the present day.

An atomistic phenomenological model can be described as a model where interatomic interactions in a crystalline structure are simplified in terms of spring-constant forces. The first and easiest to understand is the simple spring or force constant model [27] where each atom in the lattice is connected by a spring to its nearest neighbour and the equation of motion for the system is solved. This is the essence of the majority of phenomenological models for lattice dynamics. However, unlike the atom and spring model mentioned previously, real atomic structures have multiple forces between different atoms and the force between the atoms varies with the distance the atoms are apart. Also each atom interacts with more than just

its nearest neighbours, but with decreasing strength as the distance between the atoms becomes greater. Generally, in phenomenological models, when this force is considered negligible, then it is discarded. It is with various levels of sophistication that researchers have approached these problems.

The first phenomenological model that was suggested for understanding the lattice dynamics of covalently bonded structures was the Born model [67] in 1914. In his model, Born proposed modelling the interatomic force between nearest neighbours with a central and non-central component. This simple model was later expanded in 1954 to become the Born-von Kármán model [107], which allows for interactions between all atoms in the lattice rather than just the nearest neighbours. The effective crystal potential energy which was proposed for the second order term V_2 (see Eq. (3.3)) was given by

$$V_2 = \frac{1}{2}\sum_{lb}^{p}\sum_{l'b'}^{p}\sum_{i}^{3}\sum_{j}^{3}\Phi_{ij}(\mathbf{lb};\mathbf{l'b'})u_i(\mathbf{lb})u_j(\mathbf{l'b'}), \tag{3.5}$$

where p is the total number of atoms in the entire crystal structure and Φ_{ij} are the force constants between atoms $\mathbf{lb}$ and $\mathbf{l'b'}$. The values of these force constants are considered parameters which are fit according to experimental data for the phonon modes (see section 2.3). In reality this produces an unfeasibly large number of parameters which require fitting and these parameters start to lose physical meaning. Instead an approach is adopted where all atomic interactions within a certain radii of each atom are considered. Outside of this radii their contributions to the final results are considered negligible. Smith [108] in 1948 applied the Born-von Kármán model to the diamond structure, considering only the first and second nearest neighbours. Her results showed good agreement for most phonon modes, though the optical modes were slightly different from experimental Raman results available at the time and the transverse acoustic branch was completely wrong. In 1959, it was shown by Herman [109] that it required consideration up to the sixth nearest neighbour of each atom (and hence over 20 constants!) to fit the phonon dispersion curves of diamond accurately.

The next level of sophistication that was developed was the valence force model [110]. This model expressed the internal energy of the crystal in terms of the position

of the atoms, the bond lengths between the atoms and the angles between those bonds. This model also proved highly accurate and a considerable improvement on the Born-von Kármán model. However, it still required over 10 force constants to accurately reproduce experimental results. Furthermore, in 1966 Keating [111] showed that any phenomenological model must remain invariant under rotational transformations, and this was a failure of the valence force model. This approach enabled Keating to simplify the forces between atoms within the system into three components: the central force between atoms, non-central force between atoms and a bond stretch-stretch force to represent the strength of the tetrahedral bonds. This model required only a few force constant parameters and, whilst not as accurate as some of the models described previously, these force constants could be appreciated in terms of their physical meaning.

These models were to form the basis for Weber in 1976 to propose the adiabatic bond charge model. In this model he considered previous arguments put forth by both Keating and others and also took into account other models which had been proposed in this time period such the shell model [112]. In particular, the effort by several in the field to emphasise that the parameters considered must have a good physical meaning led Weber to develop the adiabatic bond charge model. This model uses only four parameters for diamond-structure (or IV-IV) materials which can all be understood in terms of their clear physical meaning.

3.2.2 Adiabatic Bond Charge Model (BCM)

The adiabatic bond charge (BCM) method was originally developed by Weber [113] in 1976 for studying the lattice dynamics of tetrahedrally bonded bulk group-IV semiconductors such as silicon and diamond. The model was also adapted by Rustagi and Weber for studying III-V semiconductors [114] such as Gallium Arsenide. In Weber's approach, the atom is considered a non-polarisable ion core and a shell of valence electrons. The valence charge density is considered as point charges, called bond charges (bc's), which are located midway (in the IV-IV case) along the tetrahedral bonds between the nearest homopolar neighbours as illustrated in

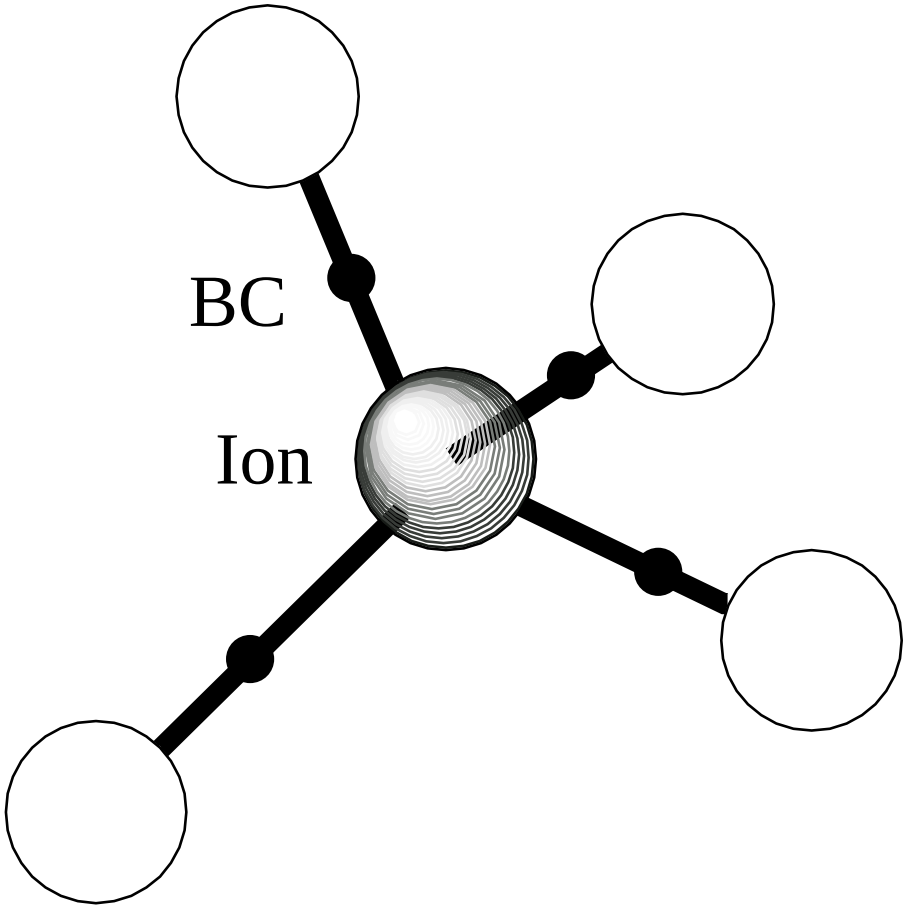

Figure 3.2: A schematic illustrating the concept of bond charges and ions in the adiabatic bond charge model.

Fig. 3.2. These bond charges are allowed to move adiabatically and are assumed to have zero mass. The equations of motion for the ions and their bond charges are evaluated and a dynamical matrix is obtained by considering three types of interaction: (i) Coulomb interaction between all particles within the structure (ion-ion, ion-bc, bc-bc) , which is evaluated using the Ewald summation technique [115], (ii) short range central force interaction acting centrally between nearest neighbours (ion-ion, ion-bc, bc-bc), and (iii) a rotationally invariant Keating type bond bending interaction [111], depending on the bc-ion-bc angle. Once these interactions are taken into account, dispersion relations of the form $\omega = \omega(\mathbf{q}s)$ are obtained for the lattice dynamics of the system. To calculate the phonon dispersion relations, one must understand how the dynamical matrix is constructed and how it is made of these three force components (Coulombic, central, and Keating-type). In Fig. 3.3 the results of calculations for silicon bulk are shown [116]. As can be seen, these

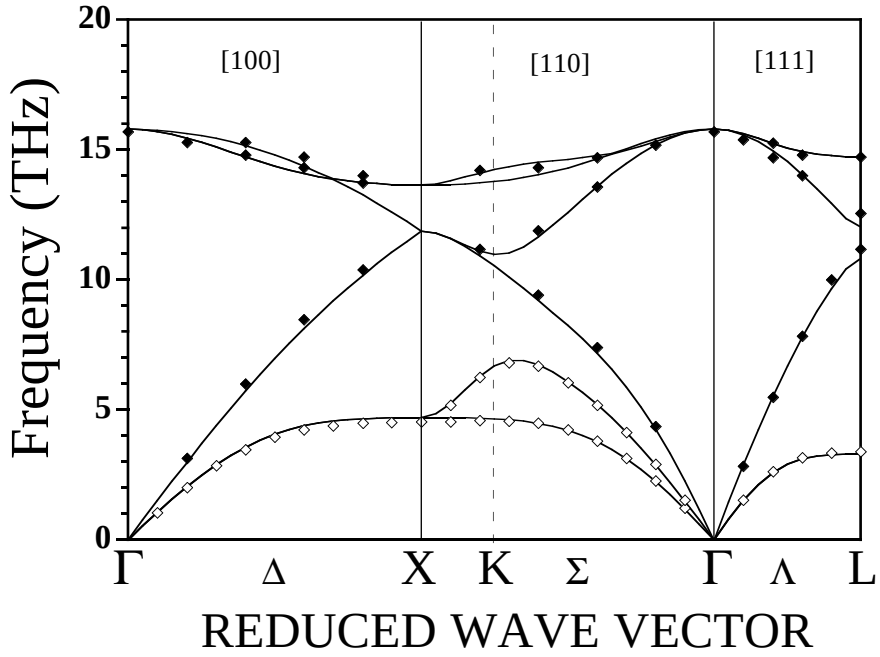

Figure 3.3: The phonon dispersion curves for bulk silicon. The experimental results of Dolling [117] and Nilsson [118] are shown in the dark and light diamonds respectively.

results provide excellent agreement with the experimental results of Dolling [117] and Nilsson [118].

3.2.2.1 The $\mathbb{C}$-Matrix

To create a dynamical matrix, one normally begins with the classical equations of motion for the the atoms within the crystal structure in terms of the interatomic potential and the atomic displacements. It can be seen from Eq. (3.2) that the classical equation of motion may be written as

$$M_b \frac{d^2 u_i(\mathbf{lb})}{dt^2} = -\sum_{l'b'j} \Phi_i j(\mathbf{lb};\mathbf{l'b'}) u_j(\mathbf{l'b'}), \tag{3.6}$$

where M_b is the mass of the the bth atom in the unit cell, t is the time co-ordinate and the other symbols have their usual meanings. To evaluate Eq. (3.6), a trial solution is applied. It is of the form

$$u_i(\mathbf{lb}) = \frac{1}{\sqrt{M_b}} \sum_{\mathbf{q}} U_i(\mathbf{q};\mathbf{b}) \exp[i(\mathbf{q}.\mathbf{x}(\mathbf{lb}) - \omega t)], \tag{3.7}$$

where $U_i(\mathbf{q};\mathbf{b})$ is the amplitude of vibration of the bth atom in the unit cell and a function of the wave-vector $\mathbf{q}$. By applying this relation, Eq. (3.6) becomes

$$\omega^2 e_i(\mathbf{b};\mathbf{qs}) = \sum_{\mathbf{b}'j} \mathbb{C}_{ij}(\mathbf{bb}'|\mathbf{q}) e_j(\mathbf{b}';\mathbf{qs}), \tag{3.8}$$

where the $\mathbb{C}$-matrix has $3N$ eigensolutions with eigenvalues $\omega^2(\mathbf{q}s)$ and eigenvectors $\mathbf{e}(\mathbf{b};\mathbf{q}s)$, and N is the number of atoms per unit cell. The eigenvectors describe the oscillations of the atoms for each vibration mode and $\omega(\mathbf{q}s)$ has its usual meaning. The $\mathbb{C}$-matrix is related to the force constant matrix, Φ, by

$$\mathbb{C}_{ij}(\mathbf{bb}'|\mathbf{q}) = \frac{1}{\sqrt{M_b M_{b'}}} \sum_{\mathbf{l}} \Phi_{ij}(\mathbf{ob};\mathbf{lb}) \exp[-i\mathbf{q}.(\mathbf{x}(\mathbf{0b}) - \mathbf{x}(\mathbf{lb}))]. \tag{3.9}$$

3.2.2.2 $\mathbb{C}$-Matrix in the BCM

In the adiabatic bond charge model, the equations of motion are set up in the same manner as previously, but one must now consider the bond charges as additional particles in the system. These bond charges are positioned midway between each pair of adjacent ions as shown in Fig. 3.2. Hence Eq. (3.8) becomes extended as

$$\mathbb{M}\omega^2 \mathbf{e}_{ion} = \mathbb{C}_{\mathbf{ion-ion}}\mathbf{e}_{ion} + \mathbb{C}_{\mathbf{ion-bc}}\mathbf{e}_{bc}, \tag{3.10}$$

and

$$\mathbb{M}'_{bc}\omega^2 \mathbf{e}_{bc} = \mathbb{C}_{\mathbf{bc-ion}}\mathbf{e}_{ion} + \mathbb{C}_{\mathbf{bc-bc}}\mathbf{e}_{bc}, \tag{3.11}$$

where $\mathbb{M}$ is the ion mass matrix, $\mathbb{M}'_{bc}$ is the bond charge mass matrix and $\mathbf{e}_{ion}$ and $\mathbf{e}_{bc}$ are eigenvectors of the two coupled dynamical equations for ion and bond charge displacement. As mentioned earlier, this is simplified by the adiabatic assumption that $\mathbb{M}'_{bc} = 0$ for all the bond charges. Hence the bond charge eigenvector may be eliminated from Eq. (3.10) by applying Eq. (3.11). Therefore the effective equation of motion becomes

$$\mathbb{M}\omega^2 \mathbf{e}_{ion} = [\mathbb{C}_{ion-ion} - \mathbb{C}_{ion-bc}\mathbb{C}^{-1}_{bc-bc}\mathbb{C}_{bc-ion}]\mathbf{e}_{ion}. \tag{3.12}$$

The full explanation behind the solution of this equation is presented in Appendix B as it is lengthy and complex. Here, a brief description of the procedure is provided, with key equations for the interatomic forces presented.

To solve Eq. (3.12), each of these matrices can be evaluated in terms of Coulombic and non-coulombic components. The repulsive Coulombic force can be summarised by the force constant matrix

$$\Phi_{ij}^{C}(\mathbf{lb};\mathbf{l'b'}) = \frac{n_C Z^2}{\epsilon}\frac{1}{4\pi\epsilon_0}\frac{\delta^2}{\delta x_i \delta x_j}\frac{Q_b Q_{b'}}{r}\bigg|_{\mathbf{r}=\mathbf{x}(\mathbf{lb};\mathbf{l'b'})}, \tag{3.13}$$

with the condition that $(\mathbf{lb}) \neq (\mathbf{l'b'})$. Here, ϵ_0 is the permittivity of free space, Q_b and $Q_{b'}$ are the charge of the bth and b'th atoms respectively, r is the distance between these two atoms, n_C is the product of the charges of the ion and the bond-charges depending on the interaction (so ion-ion = 4, bc-bc = 1 and ion-bc=-2) and $\frac{Z^2}{\epsilon}$ is an adjustable parameter.

The non-coulombic forces consist of two components. The first of these is the central short-range force which is mainly attractive. Its force constant matrix is of the form

$$\Phi_{ij}^{SC}(\mathbf{lb};\mathbf{l'b'}) = \left\{\frac{x_i x_j}{r^2}[\phi''_{bb'}(r) - \frac{1}{r}\phi'(r)] + \frac{\delta_{ij}}{r}\phi'_{bb'}(r)\right\}\bigg|_{\mathbf{x}(\mathbf{lb};\mathbf{l'b'})} \tag{3.14}$$

where $\phi''_{bb'}$ and $\phi'_{bb'}$ are considered parameters (see Appendix B for exact definitions).

A third component is required as the central short range force and coulomb force are still inadequate for describing the lattice dynamics of the system. This third force is the Keating bond bending force [111]. From this, the force constant matrix between ion b and its adjacent bond charge Υ can be constructed;

$$\Phi_{ij}^{K}(b;\Upsilon) = \frac{B_b}{4a_b^2}\sum_{\Upsilon'}(r_j(\Upsilon') - r_j(b))(r_i(\Upsilon) + r_i(\Upsilon') - 2r_i(b)). \tag{3.15}$$

where B_b is an additional adjustable parameter for the crystals structure and

$$a_b^2 = -\mathbf{x_{b\Upsilon}}.\mathbf{x_{b\Upsilon'}} \tag{3.16}$$

where Υ' indicates a summation over the all the adjacent bond charges.

Eqs. (3.13), (3.14), and (3.15) rely on only four adjustable parameters, which all have physical meaning. Hence it is now possible to form the $\mathbb{C}$-matrices in Eq. (3.13) and find the eigensolutions, $\omega^2(\mathbf{q}s)$ and eigenvectors $\mathbf{e}(\mathbf{q}s)$ for the vibrational modes of a bulk system for each value of the wave-vector $\mathbf{q}$.

For further information regarding the adiabatic bond charge model the reader is directed to see Appendix B and also to Ref. [26].

3.3 Lattice Dynamics of Silicon Nanostructures

3.3.1 History

The development of nanostructures has renewed interest in the field of lattice dynamics as the phonon dispersion relations in nanostructures are expected to be significantly different from the bulk due to the confinement and zone-folding effects. Therefore, it is very important to acquire effective knowledge of phonon dispersion relations in nanostructures. This has been done using two approaches, continuum models and phenomenological models. The phenomenological models are considered very useful for the highly accurate information they provide, whilst the advanced continuum models which have been proposed are generally useful for acquiring analytic forms of the phonon dispersion relations.

The continuum models have been employed to explain the phonon dispersion of semiconducting nanostructures since the early nineties when Stroscio *et al.* [68, 119, 120] used various elastic continuum models to investigate the lattice dynamics of the acoustic modes of nanodots, nanoslabs and nanowires (both cylindrical and rectangular). These models differ from the original Debye elastic model in that the system is not considered as a continuous isotropic medium, but has boundaries. For example, when modelling a rectangular nanowire, Stroscio *et al.* treated the nanowire as a continuum bar, which had mass density ρ and dimensions d_1 nm $\times$ d_2 nm. A good discussion and further examples of these models is presented by Stroscio and Dutta [68]. Also, phenomenological models of different sophistications have been employed to describe the phonon dispersion relations in nanostructures since the early eighties. In particular, during the eighties, phenomenological models were concentrated on their application to nanoslabs [121]. It was not until the last decade that calculations began to be performed for nanodots (microcrystals) [122] and nanowires [123]. Of these, nanowires have attracted the most recent interest, but the other structures also present fascinating details.

For nanowires, Stroscio *et al.* [68, 119, 120] used an elastic continuum model to investigate the phonon dispersion of the acoustic modes of both cylindrical and

rectangular nanowires. This approach provided information on one acoustic branch (the dilatational mode) and a qualitative description of phonon dispersion relations in realisable-size quantum dots and wires. Also, this model provided information about a new lowest non-zero zone-centre mode, which is produced due to confinement effects and lies in the upper end of what is considered the acoustic energy range. This mode is a result of zone-folding; that is where a bulk-like acoustic branch is "folded" due to a reduction in the Brillouin zone to form a low-lying non-zero branch. As such, this mode is sometimes referred to as a folded acoustic mode or a low-lying optical mode. For clarity, all branches which do not obey the condition $\omega_s(\mathbf{q} = \mathbf{0}) = 0$ will be called optical. From this point onward, the lowest-lying non-zero zone-centre mode will be referred to have frequency ω_σ at the Brillouin zone centre, and the branch will be referred to as the σ branch.

In 1997 Nishiguchi *et al.* [69] used a variational model to discern the nature of the acoustic modes in nanowires. Using this model, Nishiguchi *et al.* predicted the existence of four acoustic branches and calculated their dispersion relations. However, due to the focused nature of this technique, they were unable to yield a full set of phonon dispersion curves for nanowires. In 2003 Mingo *et al.* [123] used a force constant model with frozen boundary conditions to obtain the full phonon dispersions of an ultrathin nanowire grown in the [110] direction. In a more recent work, Mingo *et al.* [124] used an atomistic Green's function approach, with completely reflective boundaries, to calculate the phonon dispersion of ultrathin wires. These two recent techniques show strong agreement in the optical region of the phonon dispersion curves, but the former technique does not yield the fourth acoustic branch obtained by Nishiguchi *et al.* Thonhauser *et al.* [125] in 2004, used a simple spring and mass model to discuss whether clamped or free standing boundary conditions are appropriate to calculate phonon modes in a nanowire grown in the [111] direction. In this work they concluded that for optical modes it is more appropriate to consider clamped boundary conditions. Their work also confirmed the presence of four acoustic modes obtained in the work of Nishiguchi *et al.* However, this work did not investigate variations of phonon modes with nanowire size, nor did it discuss other confinement effects.

For nanoslabs, long wavelength optical modes were obtained on the basis of a very simple valence force field model in 1980 by Kanellis *et al.* [121]. They showed, using this simple technique, that the optical of the higher optical slab modes is lower than the corresponding bulk case, rising almost exponentially towards the bulk value with increasing slab thickness. In contrast, Jusserand *et al.* [126] suggested using a simple theory based upon the diatomic linear chain model to explain the behaviour of the confined zone-centre highest optical mode in a slab. In their approach, Jusserand *et al.* showed that the highest optical zone-centre mode $\omega_{optical}$ varies as $\omega^2_{optical} - \omega^2_{bulk} \propto 1/d^2$ where d is the thickness of the slab and ω_{bulk} is the frequency of the highest optical mode in the corresponding bulk material. This result was shown to apply to both slabs and superlattices. Nanoslabs are also characterised by the presence of the zone-centre lowest non-zero acoustic mode of frequency ω_σ. The variation of this mode with slab thickness has traditionally been described with Lamb's theory [127, 128].

For nanodots and microcrystals, the variation of confined acoustic and optical modes with the size of the system has been discussed using several theories, without a general consensus being reached. A good review of these variations has recently been presented by Sun *et al.* [129]. Continuum theories have also been applied to nanodots to predict their phonon dispersion, and the variation of the confined modes with the size of the structure. These theories, however, are inapplicable for ultrasmall structures (typically for sizes smaller than 15 Å).

As discussed above, despite some work being carried out, there is in general lack of a comprehensive theory of the lattice dynamics of semiconducting nanostructures. No single technique has been applied to investigate similar features in different nanostructures, making comparison unreliable. More importantly, with existing available methods it is not possible to identify which important features are dependent on dimensionality and which are dependent on the size of the nanostructure, or possibly whether both factors contribute to such features.

3.3.2 Methodology

To model silicon nanostructures, the adiabatic bond charge model, as described in section 3.2.2 and Appendix B was adopted. This approach was applied to five different system types without a change in methodology or introducing new variables or simplifications. These were: three-dimensional bulk (3D) silicon; periodic silicon supercells in the form of quasi-two-dimensional nanoslabs (2D) with thickness d; quasi-one-dimensional nanowires (1D) with dimensions $d \times d$; quasi-zero-dimensional nanodots (0D) with square cross-sections of dimensions $d \times d \times d$; and quasi-one-dimensional nanowires grown upon a quasi-two-dimensional nanoslab. The nanoslab layers are made of Si(001) bi-layers, and the nanowire axis is considered grown along [001] direction. The nanostructures were modelled within the supercell geometry, constructed with an artificial periodic arrangement invoked. Neighbouring nanostructures were separated by a vacuum region large enough to prevent interactions between them, but not over-sized to maximise computational efficiency. Such a scheme has been successfully applied to study the lattice dynamics of semiconductor surfaces (see, e.g. Refs. [26, 130]).

The vacuum region was considered to consist of an embedding material with the same atomic network as the nanostructure, but with atomic mass less than 10^{-6} of a single silicon atom. With this simple consideration the nanostructure retains its unreconstructed geometry at its interface with the vacuum, and the dangling bonds at the surface(s) remain in their bulk positions. Thus the silicon bulk parameters for the adiabatic bond charge model are employed without any alteration. The phonon frequencies due to the embedding material lie far above the frequency regions for bulk materials and nanostructure, due to the low mass of the embedding material and are easily discarded from the analysis of results. The in-plane periodicity for nanoslabs and along-axis periodicity for nanowires avoid the problem of determining complex (imaginary) phonon frequencies which may arise due to a finite length of the system.

The embedding technique, which *almost* mimics the clamped boundary conditions employed by Thonhauser *et al.* is expected to produce a good description of the

physics of atomic vibrations in nanostructures, but would not allow for four acoustic branches obtained for free standing nanowires [69]. The embedding technique is chosen deliberately, as practical considerations of uses of nanostructures mean these structures will be fixed to an additional system (normally a bulk substrate, or in the case of nanowires, suspended and connecting two bulk-like systems), which is expected to prevent the existence of the tortional mode. An ultra-light mass was chosen as opposed to an infinite mass because the latter choice leads to an interference between the vibrational spectral of the embedding medium and the sample. An additional advantage of the ultra-light mass embedding technique is that when the embedding atoms near the surface of the nanostructure are replaced by hydrogen mass, the results obtained were for hydrogenated surfaces.

An optimum amount of the vacuum region was chosen within the computational resources available. For the calculations presented here, all results have been carried out with a vacuum region of 1.086 nm between neighbouring supercells, except for the 3.8 nm $\times$ 3.8 nm nanowire and the 1.62 nm $\times$ 1.62 nm $\times$ 1.62 nm dot, where due to computation limitations (memory constraints) the vacuum was set to be 0.543 nm (i.e. equivalent to the bulk lattice constant). Within the supercell approach outlined above, phonon branches in the direction of confinement exhibit slight dispersive tendencies. This is due to two factors: (i) the *quasi-2D/1D/0D* nature of these systems and (ii) the interaction between neighbouring unit cells. For a vacuum size of 1.086 nm between neighbouring supercells, a maximum inaccuracy of 1 cm^{-1} for optical modes and 10 cm^{-1} for low lying non-zero zone centre modes was estimated. The error is less in the optical region, where maximum inaccuracy for a vacuum of 0.543 nm was 3 cm^{-1}. This is well within experimental errors of measurements of such modes. For example, for a nanowire with a width of $d = 0.543$ nm, vacuum regions of 0.543 nm, 1.629 nm, 3.80 nm produced results for the highest optical mode to be 480.56 cm^{-1}, 477.51 cm^{-1}, and 477.14 cm^{-1} respectively.

The Brillouin zone is discussed in detail in Appendix A. Here, for all the modelled nanostructures the directions Γ-X, Γ-Y and Γ-Z will be considered as the principal symmetry directions in the Brillouin zone. For nanoslabs Γ-X will be considered the direction of confinement. For nanowires the confining directions will be considered

as Γ-X and Γ-Y. For nanodots phonons are confined along all the three symmetry directions. For the nanowire upon a substrate, Γ-Z is the direction of propagation in both the wire and the slab, Γ-Y is considered to be perpendicular to the wire, but parallel to the surface, and Γ-X is the direction perpendicular to the slab and the wire.

The density of states for the nanostructures was calculated using a Brillouin zone sampling method. In this technique, one calculates the corresponding frequencies of the phonon modes for a large sample (1000+) of evenly distributed points from through-out the Brillouin zone. From these results, one can calculate the number of phonon modes that lie within a frequency range and hence approximately calculate the density of states. A small gaussian broadening is applied to the final results to account for missing points within the Brillouin zone.

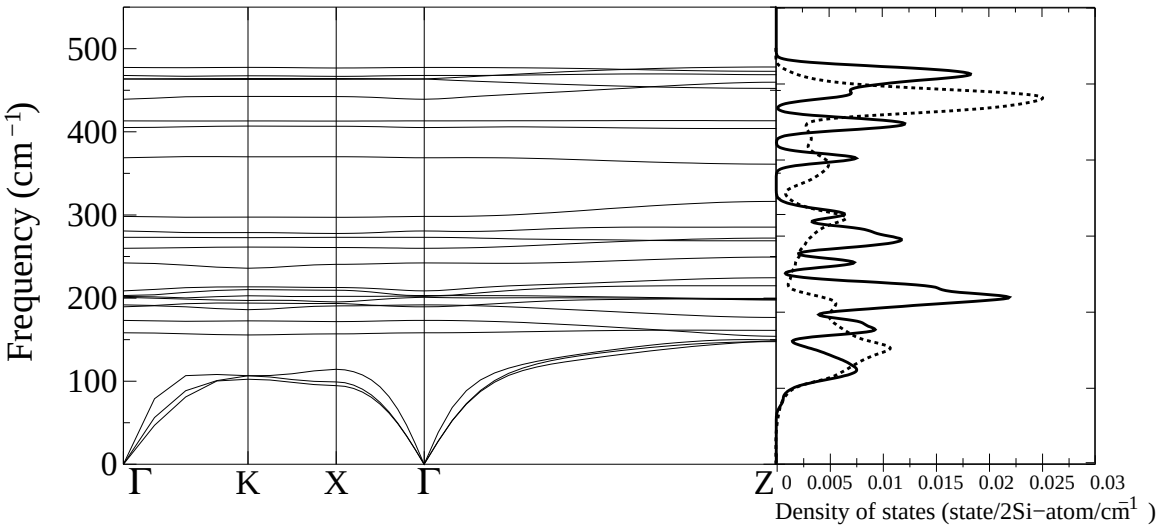

Figure 3.4: The phonon dispersion curves and density of states for a silicon nanowire of cross section 0.543 nm $\times$ 0.543 nm. The $\Gamma - X$ direction is considered to be perpendicular to the direction of propagation of the wire, the $\Gamma - Z$ direction is parallel to the direction of propagation of the wire, and $\Gamma - K$ is along the face diagonal in the Brillouin zone for the wire. Also shown are the density of states for the wire (bold line) and the density of states of bulk silicon (dashed line).

3.3.3 Results of Calculations

3.3.3.1 Stand alone nanowires

Phonon dispersion curves were calculated for stand alone silicon nanowires of cross-section $d \times d$, with d ranging from 0.543 nm (*viz.* $d = a$, the bulk lattice constant) up to 3.801 nm (*viz.* $d = 7a$). In general, two important features were noted in the dispersion curves and density of states curves: folding effects; *i.e.* bulk results folded on to the nanowire Brillouin zone and confinement effects; *i.e.* phonon modes which arise due to reduced dimensionality upon the formation of wires.

As can be observed in Fig. 3.4, the ultrathin nanowire (the thinnest considered - 0.543 nm $\times$ 0.543 nm) shows several unusual and unique properties not seen in thicker nanowires. All the non-acoustic modes are almost flat and dispersionless, even in the direction of propagation, Γ-Z. The acoustic modes have very high group

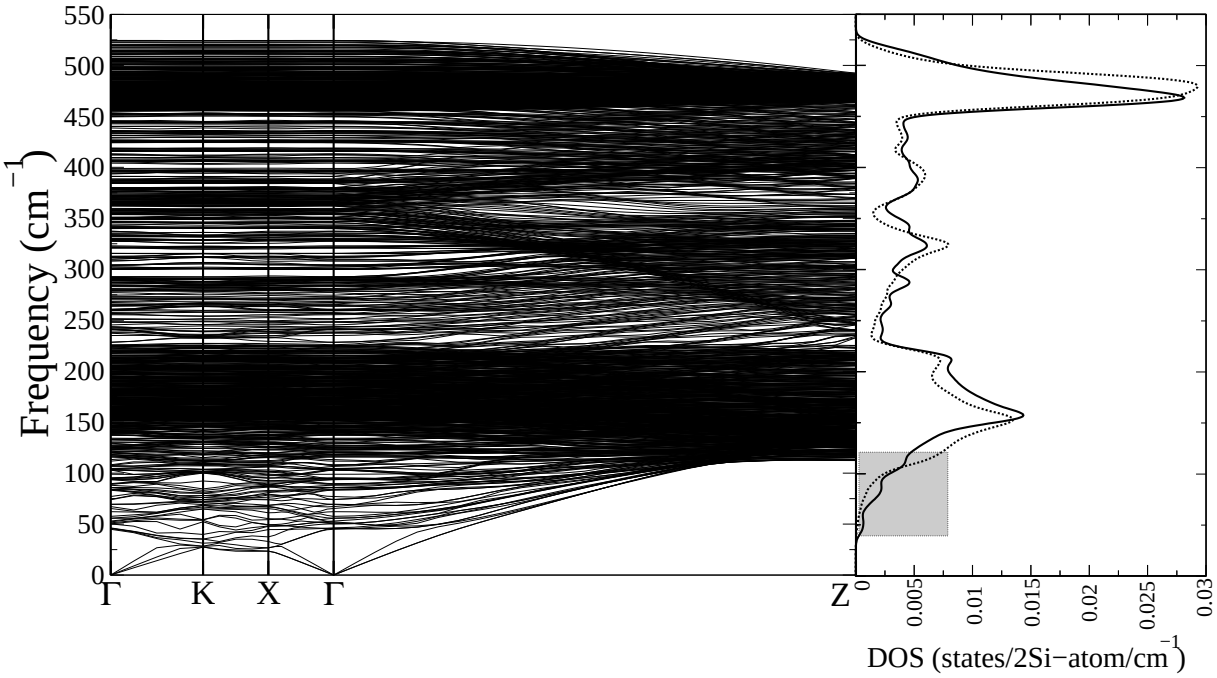

Figure 3.5: The phonon dispersion curves and density of states for a silicon nanowire of cross section 3.8 nm × 3.8 nm. Also shown are the density of states for the wire (bold line) and the density of states of bulk silicon (dashed line).

velocities near the zone centre in the Γ-Z direction, nearly three times greater than the corresponding velocities in bulk silicon. Another feature of note is the appearance of several gaps in the density of states. These gaps are located both within and above the bulk silicon acoustic range. These gaps are also observed in Mingo *et al.*'s recent report [124]. Also, within the density of states there are sharp delta-like peaks, showing that for the thinnest nanowire, strong quantisation effects dominate above all other factors in its phonon dispersion properties. These results show that the ultrathin nanowire is unlike thicker nanowires (as shown in Fig. 3.5) and should be treated as a new material with very different properties.

As the wire thickness increases, the gaps in the density of states decrease rapidly, such that a wire of dimensions greater than 1.08 nm × 1.08 nm has no gaps in its density of states. Figure 3.5 shows clearly that for thickest nanowire considered there are no gaps in the density of states. Also, the peaks broaden and their relative heights change. With increase in the wire thickness the density of states begins to look more like that of bulk silicon. However, as can be clearly seen in the boxed region, in the lower acoustic range the density of states increases in flat steps. This

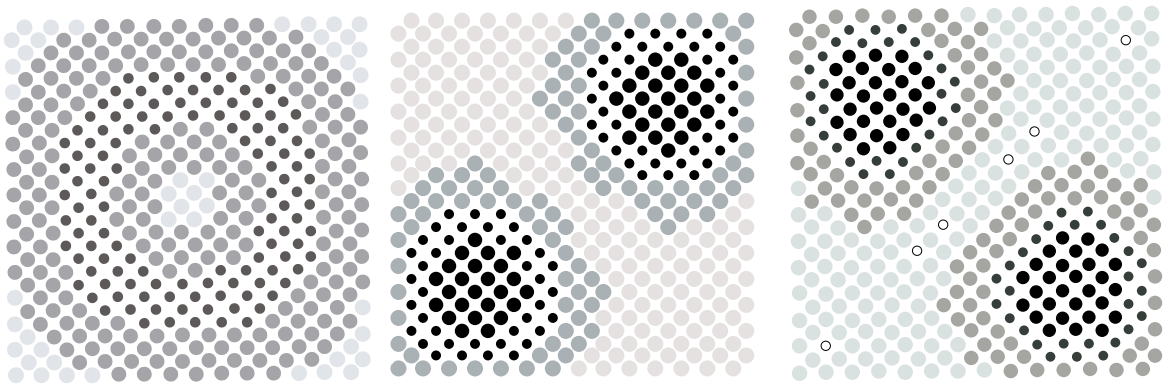

(a) (b) (c)

Figure 3.6: The amplitude of atomic vibration of the three lowest non-zero modes very near the zone-centre for a nanowire of cross section 3.8 nm × 3.8 nm. The darker the atom, the higher its relative amplitude of vibration compared to other atoms: (a) lowest non-zero mode, (b) second lowest non-zero mode, (c) third lowest non-zero mode.

feature is in strong agreement with the prediction of the Debye continuum model prediction corresponding to $\omega \propto q$ and $g(\omega) \propto \omega^0$. The position of the highest lying peak in the density of states shifts gradually upwards with the thickness of the nanowire, tending towards the bulk peak for $d > 3a$. This is illustrated in Fig. 3.5 which shows a bulk-like peak at high energies for the largest nanowire considered. The energy of the highest optical mode is shifted downwards due to quantisation. The trend in the shift of the highest mode is discussed later in section 3.3.3.4. Also, the optical modes slowly become more dispersive in the Γ-Z direction as the wire thickness increases, showing that quantisation is less strong for thicker wires as expected. However, in the directions of confinement, these modes remain almost completely flattened for all thicknesses of the wire considered here, which is very indicative of minimal interaction between nanostructures.

One interesting feature that changes as the wire thickness decreases is the group velocity near the zone centre of the dilatational acoustic mode in the direction of propagation (Γ-Z). For the ultrathin nanowires considered here, the group velocity is much higher than in bulk silicon. With an increase in wire thickness the group

velocity decreases and drops below the longitudinal bulk value. This shows a clear difference from the results obtained from the continuum model [68] which predicts a constant zone-centre group velocity for nanowires, which is much lower than bulk, regardless of thickness. These results clearly show that with an increase in the system size, the group velocity will decrease towards the result obtained from the continuum model.

For thicker wires, lower lying optical branches are no longer flat or dispersionless, but have a non-zero group velocity. For the lowest three optical modes, the amplitudes of atomic vibrations at the zone-centre (or at least very near) are shown in Fig. 3.6 for a nanowire of size 3.8 nm $\times$ 3.8 nm (*i.e.* for $d = 7a$). It can be seen from this figure and also Fig. 3.5 that the upper two of these modes are degenerate in pattern and energy. These three modes are all mixed modes, with partially transverse and partially longitudinal character in atomic vibrations. In particular, the lowest mode is majority transverse-like in its vibrational character and the other two degenerate modes are majority longitudinal-like in character. These modes become increasingly mixed as they change from the Brillouin zone centre (Γ point) to the zone edges (X, Y, and Z). This mixed vibrational behaviour is both in longitudinal and transverse in-character, but also increasingly a mix of the three images presented in Fig. 3.6. The low-lying optical modes in the thinnest nanowire also show mixed polarisation behaviour. Although these low-lying optical modes may play an important role in electron-phonon interaction, the lowest of these, the ω_σ mode, is of particular interest.

Figure 3.7 shows the variation of the energy of this mode with the thickness d of the nanowire. This variation can be expressed as

$$\omega_\sigma = \frac{A}{d^\alpha}, \tag{3.17}$$

where α is equal to $(2/3)\pm0.06$ and the proportionality constant A is estimated as 3.41 nm$^{2/3}$ THz. It can be clearly seen from the results of the continuum model [68] that this theory predicts $\alpha = 1$. This difference is believed to be a result of the simplistic 1D nature of such a model. It can be seen that using the relationship between ω_σ and d in Eq. (3.17) it is straightforward to determine the confining

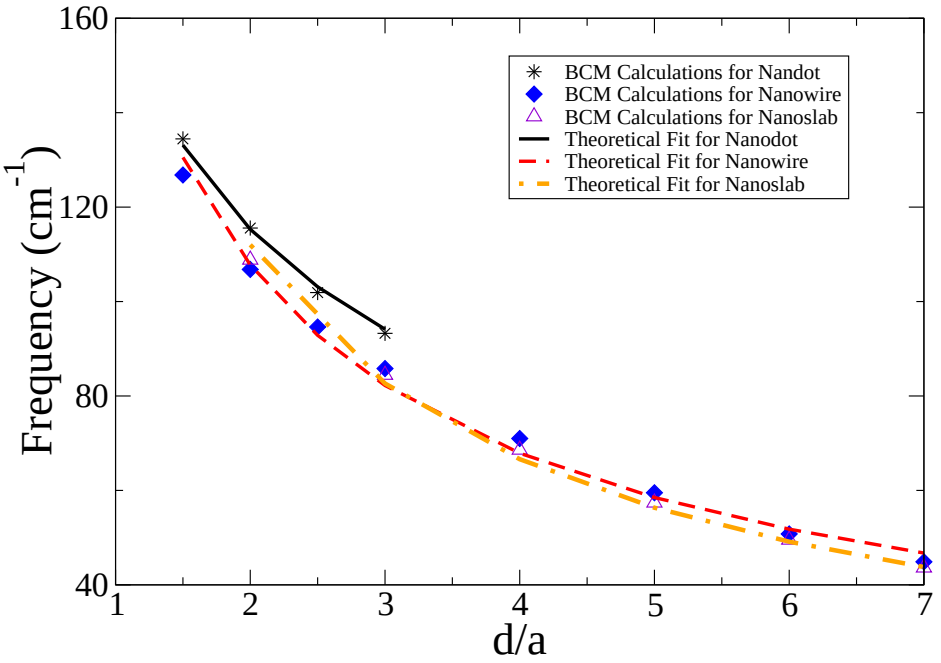

Figure 3.7: The variation of the lowest non-zero mode ω_σ with the size d of the nanostructure.

size of a silicon nanowire from Raman scattering measurements. However, it is important to note that this mode will be lowered by amorphous silicon that coats many wires [124, 131]. Also, it is expected that the shape and morphology of the nanowire will affect this mode.

It is worthwhile and important to compare the value of the ω_σ mode presented here with that obtained by Thonhauser *et al.* [125]. Figure. 3.8 shows the phonon dispersion relations for selected phonon modes for a hexagonal nanowire of approximately 3.5 nm in diameter. The value shown in Fig. 3.8 for the lowest acoustic mode ω_σ is within 1 cm^{-1} of the value obtained for the square nanowire shown in Fig. 3.5. These two results are in excellent agreement and support each other well. It is interesting to also contrast and compare the group-velocity that Thonhauser *et al.* calculate. For their model, they calculate a group velocity of approximately 5.2 kms^{-1} for the transverse acoustic mode and 8.9 kms^{-1} for the longitudinal mode. Again these two results are in good agreement with our calculated values. However, for thinner nanowires (i.e d decreases), Thonhauser *et al.* calculated a decrease in the group velocity, whereas our results show an increase. It is also interesting that for thicker

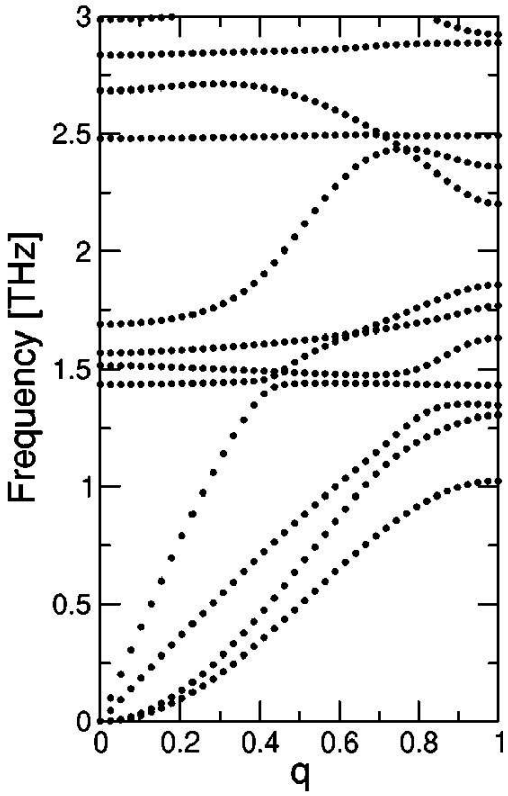

Figure 3.8: Reproduced from Thonhauser *et al.* [125]. Selected phonon dispersion curves for a hexagon silicon nanowire of approximately 3.6 nm diameter.

wires, the results of Thonhauser *et al.* tend to a velocity that is much greater than that predicted from the continuum model (of Stroscio *et al.* [68]) and also greater than the bulk value, where as ours tend towards the continuum model result (as expected) for thicker wires. The reason for this discrepancy may lie in the choice of parameters for Thonhauser's model, which are different from the parameters Thonhauser uses for bulk. However, without experimental verification, it is impossible to clearly state which result is correct. It is the belief of the author that the agreement of the results presented here with the continuum model, which is expected to be valid for nanowires of greater than 5 nm in diameter, indicates that these results are more feasible.

3.3.3.2 Stand alone nanodots and nanoslabs

Vibrational properties of silicon nanodots and nanoslabs share many common features with nanowires, but also show distinct differences. Nanodots offer confinement

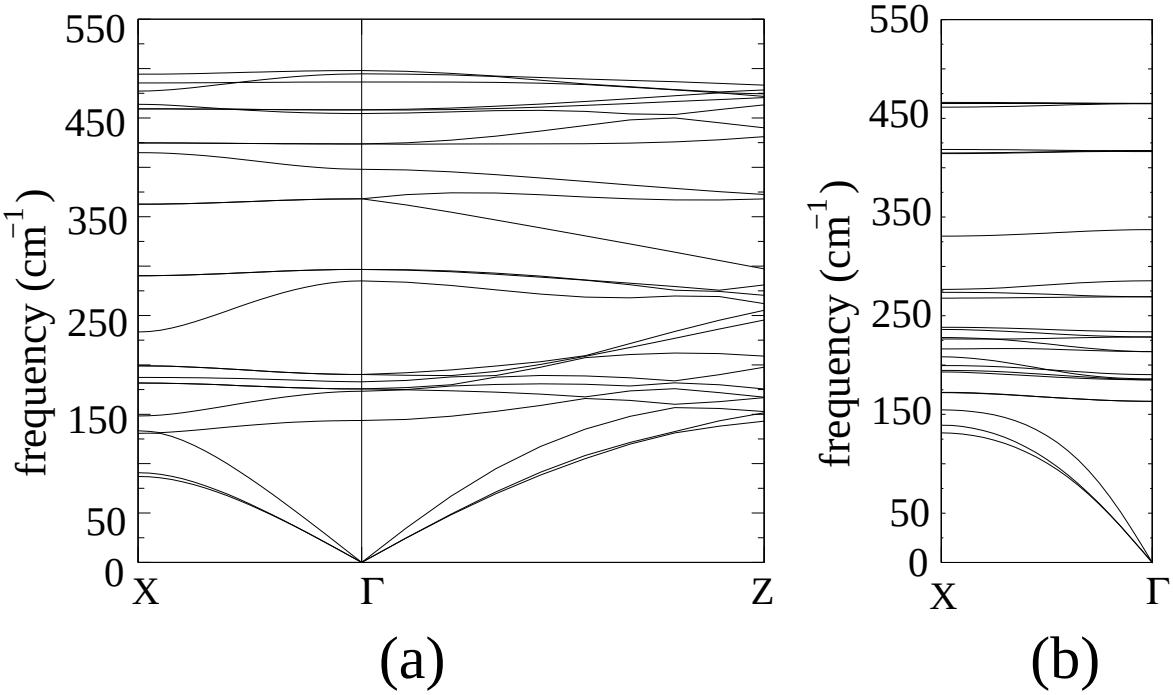

Figure 3.9: The phonon dispersion curves for: **(a)** a silicon nanoslab of thickness 0.543 nm; **(b)** a silicon nanodot of size 0.543 nm × 0.543 nm × 0.543 nm.

in all three directions and, as such, provide no direction of propagation. Indeed for silicon nanodots the phonon dispersion curves are flat and dispersionless in all directions for all sizes considered here (up to $d = 3a = 1.68$ nm in width), as shown in Fig. 3.9 (b). This is similar to what is observed in the directions of confinement for nanowires. In the thinnest silicon nanoslab the phonon branches are flat and dispersionless in the direction of confinement, though not to the same degree as for the thinnest nanowire, as shown in Fig. 3.9 (a). As the size of confinement d increases, it can be seen that the nanodots show much greater flatness in their branches than a nanowire of the same size of confinement. This is not unexpected as there is no direction of propagation for the nanodot, and thus quantisation effects completely dominate. Phonon branches remain rather flat for slab thickness $d = 2a = 1.08$ nm and begin to exhibit dispersive behaviour for thicker slabs. However, unlike the ultrathin nanowire or ultrasmall nanodot, the ultrathin nanoslab does not show flatness in the direction of propagation for many of its branches. This is a direct result of a nanoslab only having one degree of confinement as opposed to the nanowires with two degrees of confinement. Thicker nanoslabs show much less flatness in their branches, even in the direction of confinement as size increases.

One common feature between nanowires, nanodots and nanoslabs is shown in Figs. 3.4 and 3.10. It is the appearance of several gaps in the density of states in the ultrathin nanostructures. There is a single gap in the density of states for silicon nanoslabs, observed near 400 cm^{-1}, whereas for the nanowire there are three clear gaps and for the nanodot there are four clear gaps. The number and width of gaps reduce rapidly as the nanostructure size increases and are thus a unique feature of ultra-small silicon nanostructures. These gaps are observed in the density of states for dots smaller than 1.629 nm $\times$ 1.629 nm $\times$ 1.629 nm in size, and for wires smaller than 1.086 nm $\times$ 1.086 nm. A closer examination of Fig. 3.10 (b) and the highlighted regions in Fig. 3.5 and Fig. 3.10 (c) shows that the density of states in the acoustic region follows the prediction of the Debye continuum model ($g(\omega) \propto \omega$, $g(\omega) \propto \omega^0$, and $g(\omega) \propto \omega^{-1}$ for 2D, 1D and 0D respectively) before becoming bulk-like for much larger systems. This range becomes smaller with increase in the number of degrees of confinement, such that dots become characterised with bulk-like features even for a cubic length of 1.6 nm.

For the ultrathin nanoslab the group velocity of the fastest acoustic mode is higher in the Γ-Z direction than in bulk, as observed for the ultrathin wire. However, similar to the wire, as the slab thickness increases, the group velocity of this mode near the zone centre decreases to below the bulk value. This change-over occurs for the wire at $d = 3$ nm and for the nanoslab at $d = 16.29$ nm. The velocity of this mode in the nanoslab tends to the bulk value for infinite thickness as expected.

The effect of increased quantisation is reflected in the behaviour of the zone-centre lowest non-zero mode ω_σ, as shown in Table 3.1. As the number of degrees of confinement increases, the energy level of ω_σ increases. This is expected as quantisation effects increase from nanoslab (2D) to nanowire (1D) to nanodot (0D) due to the increased number of degrees of confinement. This raises the question regarding the behaviour of this mode as a function of d in these structures. The results of the lattice dynamical calculations show the variation of ω_σ with nanosize in the form in Eq. (3.17) with α equal to $(3/4)\pm0.04$ for nanoslabs and $(1/2)\pm0.08$ for nanodots. An interesting observation is that the exponent α can be expressed as $(4 - N)/(5 - N)$, where N is the number of degrees of confinement. The variation

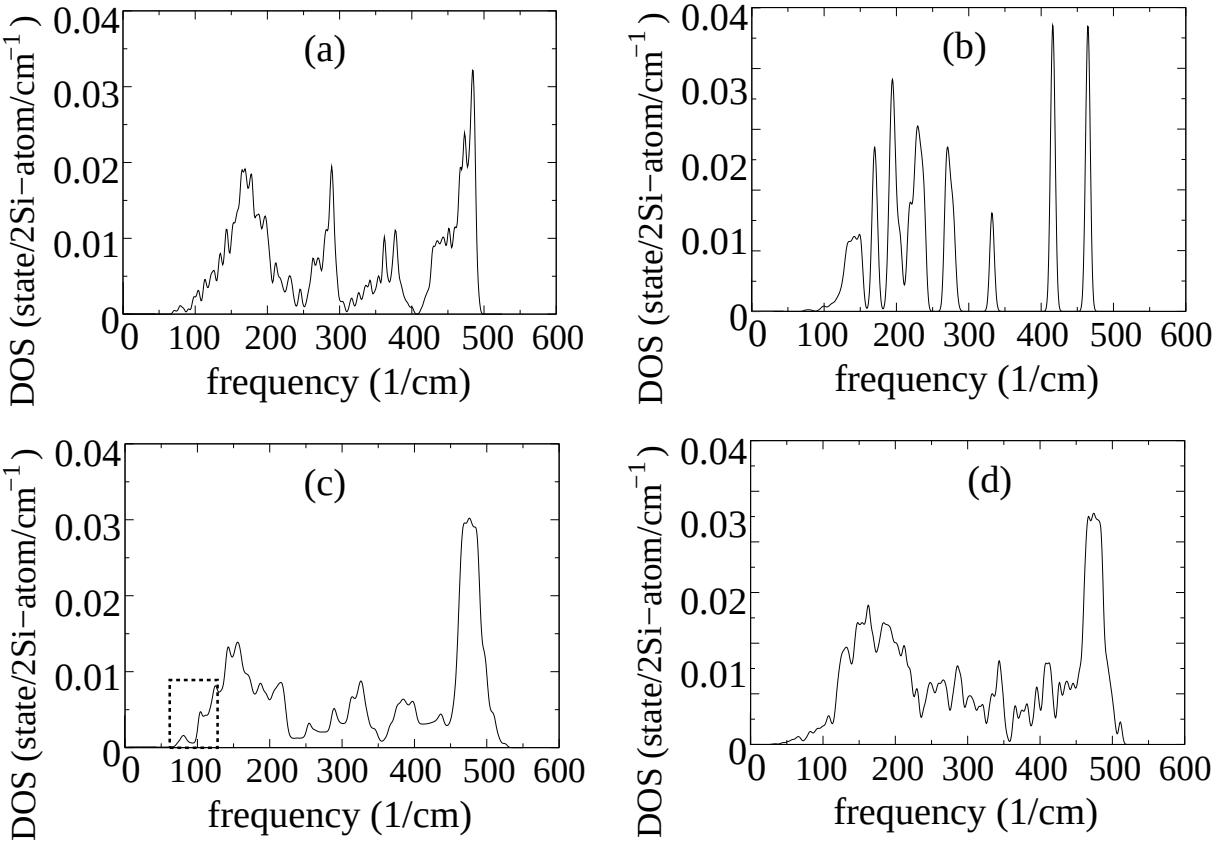

Figure 3.10: The density of states for thin nanoslabs, square nanowires and cubic nanodots of varying size: **(a)** nanoslab 0.543 nm thick, **(b)** nanodot 0.543 nm $\times$ 0.543 nm $\times$ 0.543 nm in volume, **(c)** nanoslab 32.520 nm thick, **(d)** nanodot 1.629 nm $\times$ 1.629 nm $\times$ 1.629 nm in volume. Continuum-like behaviour is highlighted.

Table 3.1: The zone-centre lowest non-zero mode for different sizes and dimensionality of nanostructure.

Dimensionality	Size of confinement, d (nm)	ω_σ (cm^{-1})
2	1.68	84.46
2	1.09	108.84
2	0.54	143.69
1	1.68	80.21
1	1.09	103.46
1	0.54	158.22
0	1.68	91.20
0	1.09	119.94
0	0.54	163.29

of ω_σ with nanosize is shown in Fig. 3.7 where the proportionality constant A is obtained to be 3.57 $nm^{3/4}$ THz for nanoslabs and 3.60 $nm^{1/2}$ THz for nanodots. Again, this equation like Eq. (3.17) can help identify the confining size of a nanostructure. The above expression also agrees with the experimental Raman measurements carried out by Fujii *et al.* [132] presented in section 2.3.1.2 for the lowest non-zero mode after allowing for an appropriate lowering of the frequency due to the interaction with the embedding material in their work. It is interesting to note that these lattice dynamical calculations indicate that the size variation of the ω_σ mode is different from that presented from continuum Lamb theory and this suggests a key difference between atomistic and continuum models.

It is important to note that in the $\Gamma - X$ direction for the silicon nanodot, the acoustic phonon modes still have a clear velocity. This is due to two factors: (i) The repeated periodicity within the supercell technique, which means that each nanodot is located within 2 nm of the next nanodot and (ii) The vacuum's finite mass, which allows for acoustic modes to propagate. As such, within this region the acoustic modes can be considered an artificial construct and disregarded.

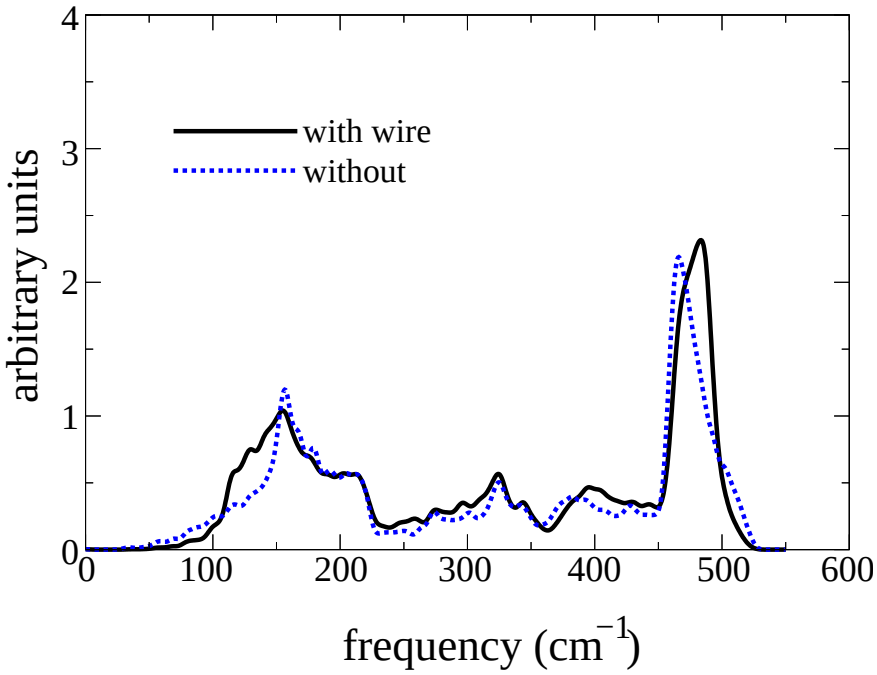

Figure 3.11: The DOS for a silicon nanoslab of thickness 2.715 nm with and without a nanowire of cross section 0.543 nm $\times$ 0.543 nm grown upon it.

3.3.3.3 Nanowires on (001) thin substrate

The first expected feature of nanowires on a substrate when compared to stand alone nanowires is a reduction in the confinement effect on the phonon spectrum. This is found in present calculations and shown in Figs. 3.11 and 3.12. Figure 3.11 shows the density of states of the ultrathin nanowire on a silicon substrate, compared to an identical slab of silicon substrate without the wire. The density of states in the acoustic range (less than 150 cm^{-1}) shows a step like behaviour for the wire upon substrate, whereas the density of states for the wireless slab shows linear jumps or increases. This can be regarded as characteristics of one-dimensional and two-dimensional behaviour respectively, indicating the addition of a wire has a noticeable effect on the density of states of the combined system. Also, the density of states for the wire-upon-slab shows a broader peak in the density of states in the low energy region than the wireless slab. This is because of the introduction of quantised modes in the wire which have low energy. It is also noted that the optical range does not change much between the two systems, suggesting that the high energy optical modes will be dominated by bulk effects and low lying energy modes are dominated

Table 3.2: Results for the highest and lowest non-zero zone-centre modes for different sizes and dimensionality of nanowire on a substrate. The size d is expressed in units of the cubic lattice constant a of silicon.

Substrate thickness (d/a)	Size of nanowire (d/a)	Size of vacuum (d/a)	ω_σ (cm^{-1})	$\omega_{optical}$ (cm^{-1})
1	1	1	117.15	510.45
1	1	2	108.44	510.38
2	1	1	89.81	520.82
2	2	1	74.15	520.35
2	2	2	64.88	520.86
2	2	3	62.90	521.42
3	1	1	72.19	523.45
4	1	1	60.27	524.64
5	1	1	50.88	525.37
5	1	2	46.94	525.41
5	2	2	42.54	525.37
6	1	1	44.22	525.76
6	2	2	37.59	525.73

by the quantised states that are introduced by the wire.

Figure 3.12 shows the typical dispersion curves of an ultrathin nanowire on a thin silicon substrate. The upper range of the dispersion curves shows that the optical modes are flattened, suggesting that the form of the optical modes are far more affected by the wire on the substrate than the form of the acoustic modes. It can be seen clearly in the $\Gamma - Y$ and $\Gamma - Z$ directions that the system has dispersive modes in the range 0 cm^{-1} to approximately 480 cm^{-1}. However, the ω_σ mode is lowered more in the combined wire-upon-slab system than in the isolated slab. It is also much lower than in a ultrathin nanowire. This shows that the key factor in determining the dependence of the lowest mode is the combined thickness of the substrate and the wire as opposed to the individual dimensions of either the wire of the slab.

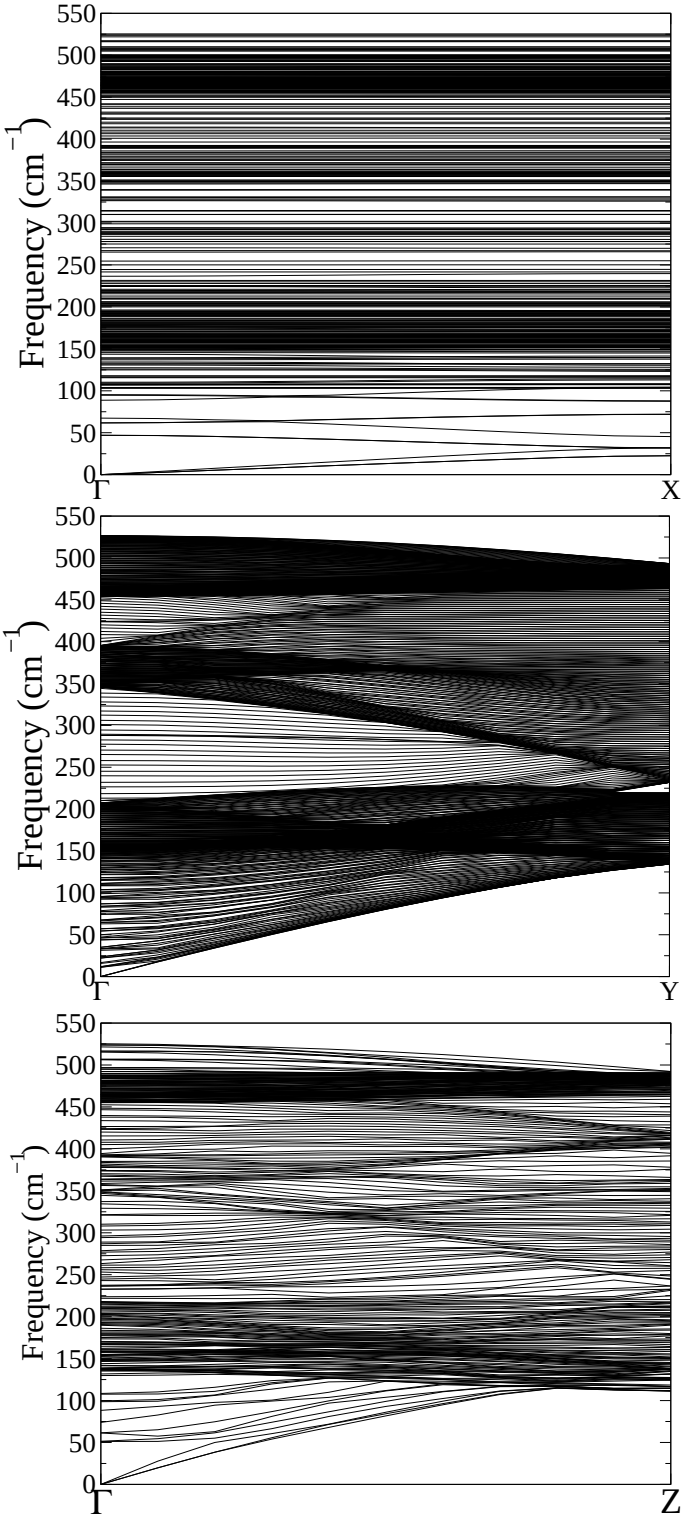

Figure 3.12: The phonon dispersion curves for an ultrathin silicon nanowire of cross section 0.543 nm × 0.543 nm on a 2.715 nm thick nanoslab. Γ-X is considered perpendicular to the surface of the slab, Γ-Y is perpendicular to the direction of propagation of the wire, and parallel to the direction of propagation of the slab, and Γ-Z is considered in the direction of propagation of both the wire and the slab.

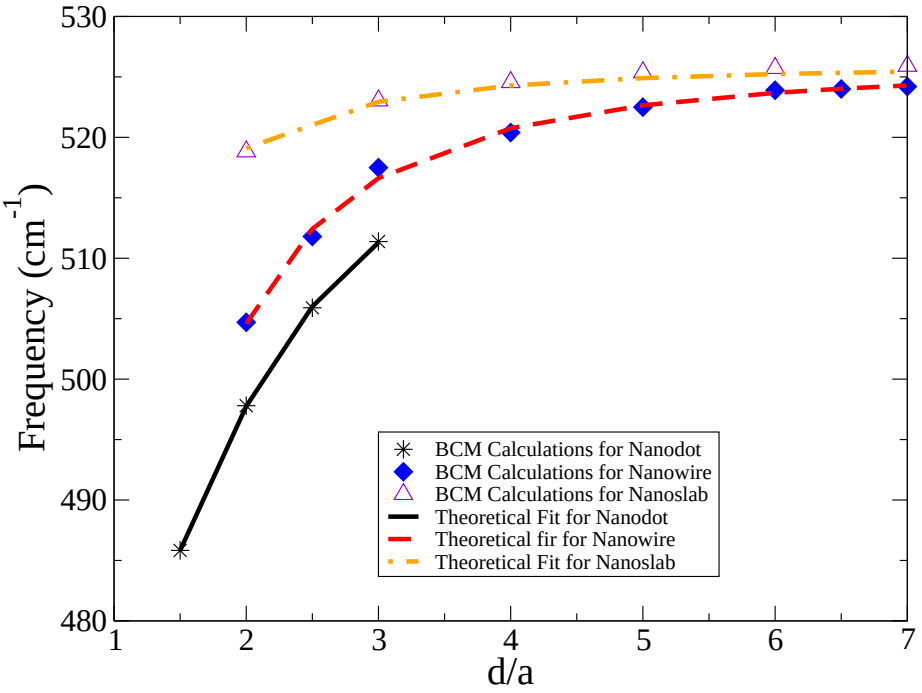

Figure 3.13: The variation of the highest mode with the size d of the nanostructure. a is the lattice parameter (0.543 nm).

Table 3.2 presents results for ω_σ and the highest optical mode for different thicknesses of the substrate and wire. These results show that for slab thicknesses of 3.801 nm and greater, the value of ω_σ saturates to a constant value of approximately 40 cm^{-1}. For thicker wires upon a given thickness of the substrate a similar trend was observed, but firm conclusions cannot be reached due to computational limitations. Similarly, the highest optical mode appears to be dominated by the substrate thickness rather than the wire thickness.

3.3.3.4 Behaviour of the Highest Optical mode

In all stand alone nanostructures, the frequency $\omega_{optical}$ of the highest optical mode shows a marked departure from the highest bulk frequency. This departure becomes more significant as the number of degrees' of quantisation increases (*i.e.* along the sequence nanoslab, nanowire, nanodot). Moreover, as shown in Fig. 3.13, for a given number of degree of confinement in a stand alone nanostructure, $\omega_{optical}$ increases with the size of the dimension d of confinement. The size dependence of

$\omega_{optical}$ was explained for superlattices and thin slabs in the 1980's by Jusserand *et al.* [126]. Using the diatomic linear chain model and considering only nearest neighbour interactions (that is interactions between all atoms within a distance $2a$, where a is the interatomic distance), Jusserand *et al.* obtained $\omega_{optical} \propto 1/d^2$. Here a brief description of their approach is presented and it is then extended to obtain expressions for the size dependence of $\omega_{optical}$ for the different types of nanostructures considered in this work. A detailed account is provided in Appendix C of the derivation of the expression for nanowires.

For a diatomic linear chain with masses m_1 and m_2, and interatomic separation a, the dynamical matrix [131] can be expressed as

$$\mathbb{D} = \begin{pmatrix} 2\Lambda_1/m_1 & (-2\Lambda_1/m_1)\cos qa \\ (-2\Lambda_1/m_2)\cos qa & 2\Lambda_1/m_2 \end{pmatrix}. \tag{3.18}$$

where Λ_1 is a force constant. In the long wavelength limit only the first-order term is retained in the expansion of the cosine term. The second item to recognise is that in the confinement direction $q \propto a$. Solving the dynamical equation $|\mathbb{D} - \omega^2\hat{\mathbb{I}}| = 0$ (where $\hat{\mathbb{I}}$ is the identity matrix) enables one to recover the result originally obtained by Jusserand *et al.*:

$$\Delta\omega^2 = \frac{\alpha}{d^2}, \tag{3.19}$$

where $\Delta\omega^2 = \omega_{bulk}^2 - \omega_{optical}^2$ and ω_{bulk} is the frequency of the highest optical mode in bulk. This result is applicable for nanoslabs. The above theory can be extended to calculate the effect of quantisation in two dimensions (for nanowires) as well as three dimensions (for nanodots).

Application of the model in two dimensions with the same condition as stated previously, *viz.* only interactions between all atoms within the distance $2a$ are considered (where a is the interatomic distance), and this requires three force constants. Let these be denoted as Λ_1, Λ_2, and Λ_3. Λ_1 is the m_1 - m_2 atomic interaction in the $< 100 >$ directions, and Λ_2, and Λ_3 are the m_1 - m_1 and m_2 - m_2 interactions respectively in the $< 110 >$ directions. Here the nanowire axis is considered along <001> direction, as stated earlier. Setting up a dynamical matrix as before and solving it in a similar manner it can be shown for confinement in two dimensions

that

$$\Delta\omega^2 = \frac{\beta_1}{d^2} + \frac{\beta_2}{d^3}, \tag{3.20}$$

where β_i are constants.

Similarly, for a nanodot with three-dimensional confinement, a three-dimensional diatomic structure is set up, using four force constants to account for interatomic interactions up to distances $2a$. The force constant Λ_1 accounts for the nearest neighbour interactions between m_1 - m_2 in the $< 100 >$ directions. Similarly, Λ_2 and Λ_3 account for second nearest neighbour interactions (i.e. between m_1-m_1 and m_2-m_2 in the $< 110 >$ directions). The fourth force constant, Λ_4 accounts for third nearest neighbour interactions (i.e. between m_1-m_2 in the $< 111 >$ directions). From this a dynamical matrix can be set up and solved as above, leading to the result;

$$\Delta\omega^2 = \frac{\eta_1}{d^2} + \frac{\eta_2}{d^3} + \frac{\eta_3}{d^4}, \tag{3.21}$$

where η_i are constants.

Figure 3.13 shows the fits of these equations to the results from the lattice dynamics calculations using the adiabatic bond charge model for the three fundamental types of nanostructure. As can be clearly seen, the simple analytical fits are in good agreement with the theoretical results obtained by the theory. These results can help explain Raman measurements on (ultra)small nanostructures. A suitable extrapolation of the results, using the analytical fits in Eqs. (3.19-3.21) can be expected to explain Raman measurements on thin-sized nanostructures grown, provided that such samples are clean i.e. not covered with any protective layers and are atomically smooth (no steps). These extrapolated results can also be expected to explain differences between grain-like and wire-like behaviour observed in Raman measurements in nanowires [92]. This is expected as systems which are made from a series of different nanocrystals will show greater quantisation than those which are pure crystalline structure (see Fig. 2.8 for further clarification).

In 1982 Iqbal *et al.* [133] carried out a series of measurements on nanodots of different sizes embedded in amorphous silicon. These results are shown in Fig. 3.14. The experimental trend is fitted very well by Eq. (3.21), though the dots are of a much

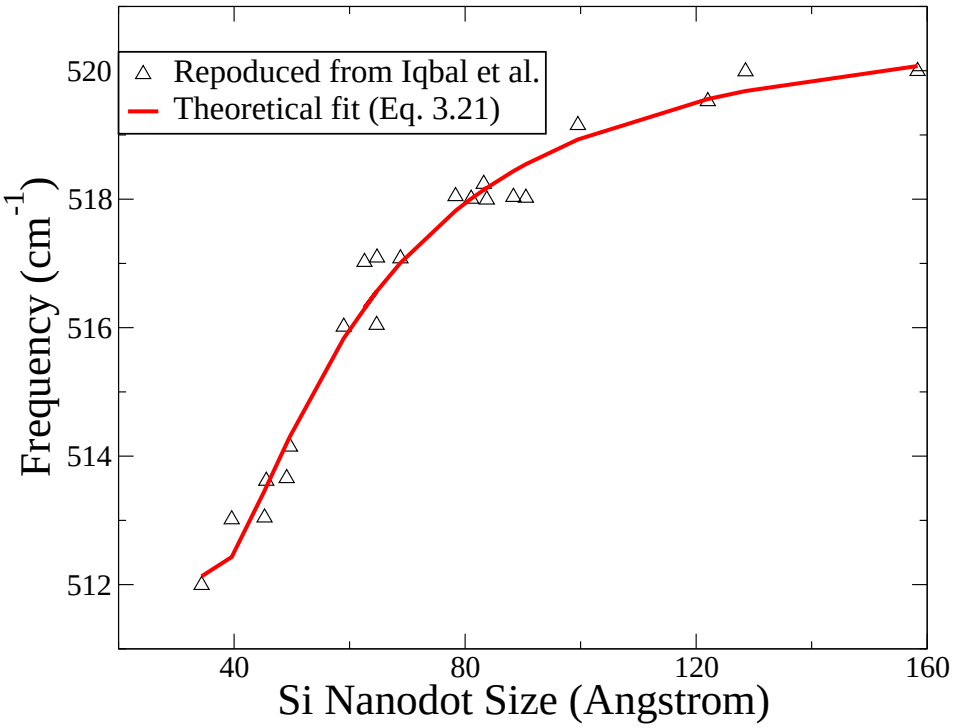

Figure 3.14: The experimental data of Iqbal *et al.* showing the variation of the highest optical mode with the size of the nanodot.

larger size than discussed in the previous sections. The maximum value for the highest optical frequency is lowered to the amorphous silicon as noted earlier, but the trend is in clear agreement with theory.

3.3.3.5 Summary of the results for silicon nanostructures

Silicon nanostructures have several common features in their lattice dynamics. It can be seen for the ultrasmall case of each structure that all branches except the acoustic are flat and dispersionless regardless of whether the system is zero-, one- or two-dimensional. As the size of these structures increases, these branches are seen to become dispersive in the direction of propagation. Eventually, as size increases, the branches in the direction of confinement start to follow a similar trend. In all systems studied, the characteristic lowest non-zero zone centre mode with frequency ω_σ is calculated and shown to decrease with the size of the nanostructure. An analytic fit has been presented for the size variation of this mode for simple structures of nanodots, nanowires and nanoslabs. It is also observed that in all systems the highest

optical mode is lowered and for simple systems this behaviour can be explained using a simple diatomic model. The calculated results for such variation have been fitted to analytic expressions.

These trends are also observed in the case of nanowires deposited on substrates. For this system the phonon dispersion is in general dominated by the substrate. In particular, the phonon branches in the $\Gamma - Y$ direction become more dispersive than in the stand alone nanowire, showing that the addition of the slab reduces quantisation in that plane. Also, the frequency ω_σ of a nanowire deposited upon a substrate is lower than that of either of the two stand alone systems.

All these silicon nanostructures show several interesting and important vibrational features. In the next section the lattice dynamics of carbon nanotubes are introduced. As can be seen, these structures have several features in common as well as some features which are different.

3.4 Lattice Dynamics of Carbon Nanotubes.

The lattice dynamics of carbon nanotubes show several interesting features. Some of these features are common with silicon nanostructures and some are not. For nanotubes, the lattice dynamics have been well studied on an atomistic level. In this section a review of the history and development of these novel and interesting structures is presented. A continuum model based upon research by Mahan [141] and Zhang *et al.* [142] is modified and presented. Results from this model are compared and contrasted with silicon nanostructures. These are presented here as Chapters 4, 5 and 6 make extensive use of the phonon dispersion relations derived in the following sections to derive and calculate the thermal properties of carbon nanotubes.

3.4.1 History

The lattice dynamics of carbon nanotubes have been studied extensively using several different models ranging from continuum [142] to *ab initio* [145]. This was first studied by Jishi *et al.* [134] in 1993 using a simple force constant model based upon the Born-von Kármán approach for graphene. In Jishi's model, the lattice dynamics was calculated for the two-dimensional unit cell of graphene consisting of two carbon atoms. From this, using a technique known as "zone-folding" (which is described in more detail in [13]) the lattice dynamics of carbon nanotubes can be constructed.

These early calculations revealed three key features of importance: (i) four acoustic modes, a longitudinal mode, two transverse modes and a twist mode; (ii) a low lying non-zero zone-centre mode, ω_σ (like observed in silicon nanostructures previously) and (iii) the presence of a second low lying zone-centre mode known as the breathing mode, ω_B. To improve agreement with the results that were emerging from Raman spectroscopy, as discussed in section 2.3.1.1, Jishi *et al.* modified the force constants [13] from the values applied to model the lattice dynamics of graphene to include other effects. From this, they showed that the tubes curvature also played an important role in determining the lattice dynamics of carbon nanotubes. However, this model is a not a true atomic model of the carbon nanotube. The calculations of Saito *et al.* were backed up and improved by Charlier *et al.* [135] in 1998 who applied the the De Launay model [136] to the carbon nanotube unit cell. This model involved no zone-folding techniques and showed similar results for the lattice dynamics using only six force constants. More importantly, this model showed that the zone-folding technique was a simple, but effective method for describing the lattice dynamics of carbon nanotubes.

The force constant models were then followed in 2001 by a continuum model for a nanotube presented by Kahn and Stroscio *et al.* [137]. This approach was based upon a previous project presented by Stroscio's group which used almost the same continuum approach to model a plant's micro-tubule [138]. Later in the same year, Stroscio's group presented a continuum model for the optical modes in a carbon nanotube [139]. These models where expanded upon and improved by two different

approaches in 2002 and 2003. Raichura and Stroscio *et al.* [140] introduced the effects of finite tube length and increased the sophistication of the model considerably. Their results showed that the initial model, whilst highly accurate for the acoustic modes, changed the interaction potential for the electrons when the tube length was less than 200 Å. However, as seen in section 2.2.4, nanotubes are now grown far beyond these lengths.

Mahan [141], in 2002, applied and adapted this continuum approach to provide analytic phonon dispersion relations for the low-frequency modes in carbon nanotubes. This technique produced good agreement with the previously reported form for the nanotubes presented by Stroscio *et al.* In 2003, Zhang *et al.* [142] applied Mahan's approach to also create analytic expressions for the dispersion relations for carbon nanotubes and applied them to the specific heat capacity. From this point onwards, continuum and force constant models were taken further to describe multi-wall systems [143], and to explore in detail the form of the flexural mode [144]. However, little new information was obtained regarding the acoustic and low lying optical modes of these structures.

In 2004 Ye *et al.* [145] applied *ab initio* techniques on the basis of density functional theory [26] and local density approximation to model the lattice dynamics of carbon nanotubes of various radii from first principles. In their calculations they showed that for the low lying phonon modes, the analytic expressions derived by Mahan and Zhang *et al.* were very accurate at low frequencies (less than twice the frequency of the breathing mode, ω_B), but the analytic expressions are still reasonably accurate for higher frequencies. The calculations of Ye *et al.* also agree with the earlier *ab initio* results of Agrawal *et al.* [49] which were for a (6,6) carbon nanotube.

As discussed in Chapter 1, the thermal properties of a covalently bonded crystal are heavily dependent on the acoustic branches of a nanostructure. Mahan and Zhang *et al.* have provided clear and effective analytic descriptions of the phonon dispersion relations of these modes and the lowest optical modes. The original method which Zhang *et al.* applied to using Mahan's analytic relations appears flawed (see the following section and section 4.3 for further details), but parts of their method are

still applicable and the original expressions provided by Mahan are an excellent basis for building a more detailed description of the thermal properties of carbon nanotubes on. The phonon dispersion expressions have a clear physical meaning and form the basis of expressions which are used in later chapters.

In the following sections the analytic expressions from Mahan and Zhang *et al.*'s approaches are re-derived. The original method is improved, with the reasoning for the changes in theory thoroughly explained and provided.

3.4.2 Phonon Dispersion Relations

To form analytic expressions for the phonon dispersion relations, Mahan and Zhang *et al.* modelled a single wall carbon nanotube as a cylindrical elastic thin shell. In their approach, the shell is assumed to have the carbon atoms equally distributed and hence, they may be treated as an isotropic medium of uniform mass density ρ. Thus, the vibration equation for the system is

$$\rho \frac{d^2 u_i}{dt^2} = \frac{\delta \sigma_{ik}}{\delta x_k}, \tag{3.22}$$

where $\mathbf{u}$ is the displacement, $\mathbf{x}$ the position and σ_{ik} is the stress tensor, which is determined [146] for an elastic shell from the strain tensor du_i/dr_k by

$$\sigma_{ik} = \frac{Y}{1+\sigma_P}[u_{ik} + \frac{\sigma_P}{1-2\sigma_P}(\sum_l u_{ll})\delta_{ik}], \tag{3.23}$$

where Y is the Young's modulus and σ_P is the Poisson's ratio of the material. For a carbon nanotube, $Y = 1.06$ TPa, σ_P =0.145 and ρ =2270 kg m^{-3} [138].

To simplify this equation, the tube's shell is assumed to be infinitely thin. This assumption is valid as the thickness of the shell is far less than the radius, Hence, the following condition may be applied

$$\sigma_{r\theta} = \sigma_{rz} = \sigma_{rr} = 0, \tag{3.24}$$

where θ, z and r are cylindrical coordinates. For a nanotube, a lattice wave may be separated into radial, transverse and longitudinal components. Thus the lattice

wave may be written as

$$\begin{bmatrix} u_r \\ u_\theta \\ u_z \end{bmatrix} = \begin{bmatrix} -iC_r \\ C_\theta \\ C_z \end{bmatrix} e^{i(m\theta + K_z z - \omega t)}, \tag{3.25}$$

where K_z is the longitudinal wave-vector and ω is the angular frequency of the lattice wave. C_r, C_θ and C_z are the amplitudes of the radial, transverse and longitudinal components respectively and m is the angular quantum number, which is an integer and defined by the the periodic condition in θ. Equation (3.22) may be expanded to provide three equations relating u_r, u_θ and u_z in terms of E, r, z, θ and σ_P . By applying Eq. (3.25) the phonon dispersion relations can be obtained from the equation

$$\begin{aligned} &\left(\frac{\omega^2}{\omega_B^2} - 1\right)\left(\frac{\omega^2}{\omega_B^2} - m^2 - \frac{1-\sigma_P}{2}k^2\right)\left(\frac{\omega^2}{\omega_B^2} - \frac{1-\sigma_P}{2}m^2 - k^2\right) \\ &-\sigma_P(1+\sigma_P)m^2k^2 - \sigma_P^2 k^2\left(\frac{\omega^2}{\omega_B^2} - m^2 - \frac{1-\sigma_P}{2}k^2\right) - m^2\left(\frac{\omega^2}{\omega_B^2} - \frac{1-\sigma_P}{2}m^2 - k^2\right) \\ &-\frac{(1+\sigma_P)^2}{4}m^2k^2\left(\frac{\omega^2}{\omega_B^2} - 1\right) = 0, \end{aligned} \tag{3.26}$$

where $k = K_z.R$ (where the longitudinal wave vector K_z is along the tube axis and R is the nanotube radius) and the breathing mode frequency is defined as

$$\omega_B = \frac{1}{R}\sqrt{\frac{Y}{\rho}(1-\sigma_P^2)}. \tag{3.27}$$

Equation (3.26) has two sets of solutions: (i) for m=0 and (ii) for $m \neq 0$.

For $m = 0$ the three solutions obtained are of the form

$$\omega_{1,\mathsf{WA}} = \omega_B\sqrt{\frac{1-\sigma_P}{2}k^2}, \tag{3.28}$$

$$\omega_{2,\mathsf{B}} = \frac{\sqrt{2}}{2}\omega_B\sqrt{(1+k^2) + \sqrt{(1+k^2)^2 - 4(1-\sigma_P^2)k^2}}, \tag{3.29}$$

and

$$\omega_{3,\mathsf{LA}} = \frac{\sqrt{2}}{2}\omega_B\sqrt{(1+k^2) - \sqrt{(1+k^2)^2 - 4(1-\sigma_P^2)k^2}}. \tag{3.30}$$

In case (ii), two more simplifications are required to enable simple analytic expressions to be determined. Firstly, the interaction between the longitudinal and

transverse stress may be ignored (i.e. $\sigma_{\theta z} = 0$) and secondly, that $\sigma^2 \ll 1$. With these considerations Eq. (3.26) becomes

$$\left(\frac{\omega^2}{\omega_B^2} - m^2 - \frac{1-\sigma_P}{2}k^2\right)\left[\left(\frac{\omega^2}{\omega_B^2} - 1\right)\left(\frac{\omega^2}{\omega_B^2} - m^2 - \frac{1-\sigma_P}{2}k^2\right) - m^2\right] = 0. \quad (3.31)$$

Hence for each value of $m > 0$ there are three corresponding solutions of the form

$$\omega_{\sigma,m} = \omega_B\sqrt{\frac{1-\sigma_P}{2}m^2 + k^2}, \quad (3.32)$$

$$\omega_{\sigma',m} = \frac{\sqrt{2}}{2}\omega_B\sqrt{(1 + m^2 + \frac{1-\sigma_P}{2}k^2) + \Omega(k)}, \quad (3.33)$$

and

$$\omega_{T,m} = \frac{\sqrt{2}}{2}\omega_B\sqrt{(1 + m^2 + \frac{1-\sigma_P}{2}k^2) - \Omega(k)}, \quad (3.34)$$

where

$$\Omega(k) = \sqrt{\left(1 + m^2 + \frac{1-\sigma_P}{2}k^2\right)^2 - 2(1-\sigma_P)k^2}. \quad (3.35)$$

From Eqs. (3.27-3.34), two features are apparent: (i) all modes are scaled by ω_B, which is defined by Eq. (3.27); (ii) Equation (3.34) is for a mixed acoustic mode. As discussed in section 3.4.1, *ab initio* calculations show that the carbon nanotube has a longitudinal branch (see Eq. (3.30)), a twist branch (see Eq. (3.28)) and two transverse or flexural modes which are doubly degenerate. Hence, to create a realistic consideration of the phonon dispersion relations, one should only consider the case of $m = 1$ for Eq. (3.34) and the branch should be considered doubly degenerate. Thus for Eq. (3.34), values of m greater than 1 are disregarded.

For a (n_1, n_2) nanotube, the radius R is calculated from Eq. (1.5) (i.e. $R = a_{gr}/(2\pi)\sqrt{n_2^2 + n_1^2 + n_1 n_2}$ [13]). Although the theory applies alike to $(n_1, 0)$ zigzag, (n_1, n_1) armchair, and (n_1, n_2) achiral nanotubes, the continuum model only distinguishes between nanotubes of different radii. Hence, only the case where $n_1 = n_2 = n$ is considered here, i.e. (n, n) armchair nanotubes. This is helpful for later as it enables a comparison with the discussion of Zhang *et al.* [142] and also allows an easy comparison of the specific heat capacity for (n, n) nanotubes of different radii as $n \propto R$.

3.4.3 Phonon Density of States

For a one-dimensional material, in order to find an analytic form for the density of states, one is required to calculate the number of K_z values in the range dK_z (or correspondingly the number of frequencies, $g(\omega)$ within a range of frequencies $d\omega$). It can be easily shown [131] that a unit of K_z-space contains $L_0/2\pi$ values of K_z where L_0 is the length of the one-dimensional structure (in this case the nanotube), as defined in section 1.3.4. Thus the total density of states for one-dimension may derived as

$$\begin{aligned}\sum_{\mathbf{q}} \rightarrow \int d\mathbf{q} &\equiv g(\omega)d\omega \\ &= \int_{L_0} \frac{L_0}{2\pi} dK_Z \\ &= \int \frac{L_0}{\pi} \frac{d\omega}{\nabla_{K_z}\omega}.\end{aligned} \tag{3.36}$$

Using this equation and Eqs. (3.28-3.34), an analytic form for the phonon density of states for a single wall nanotube can be obtained. For each value of m, there are three corresponding additional terms which are added to the total density of states. For $m = 0$ these are

$$g_1(\omega) = \frac{\sqrt{2}L_0}{\pi R\sqrt{1-\sigma_P}\omega_B}, \tag{3.37}$$

$$g_2(\omega) = \frac{L_0}{\pi R\omega_B} \frac{\left(\frac{\omega^2}{\omega_B^2} - 1 + \sigma_P^2\right)^2 + \sigma_P^2(1-\sigma_P^2)}{\left(\frac{\omega^2}{\omega_B^2} - 1 + \sigma_P^2\right)\sqrt{\left(\frac{\omega^2}{\omega_B^2} - 1\right)\left(\frac{\omega^2}{\omega_B^2} - 1 + \sigma_P^2\right)}}, \tag{3.38}$$

$$g_3(\omega) = \frac{L_0}{\pi R\omega_B} \frac{\left(1 - \frac{\omega^2}{\omega_B^2} - \sigma_P^2\right)^2 + \sigma_P^2(1-\sigma_P^2)}{\left(1 - \frac{\omega^2}{\omega_B^2} - \sigma_P^2\right)\sqrt{(1 - \frac{\omega^2}{\omega_B^2})(1 - \frac{\omega^2}{\omega_B^2} - \sigma_P^2)}}, \tag{3.39}$$

and summing all the contributions for $m \neq 0$ gives three more contributions to the total phonon density of states given by

$$g_4(\omega) = \frac{L_0\omega}{\pi R\omega_B^2} \sum_{m=1}^{m_1} \frac{1}{\sqrt{\frac{\omega^2}{\omega_B^2} - \frac{1-\sigma_P}{2}m^2}}, \tag{3.40}$$

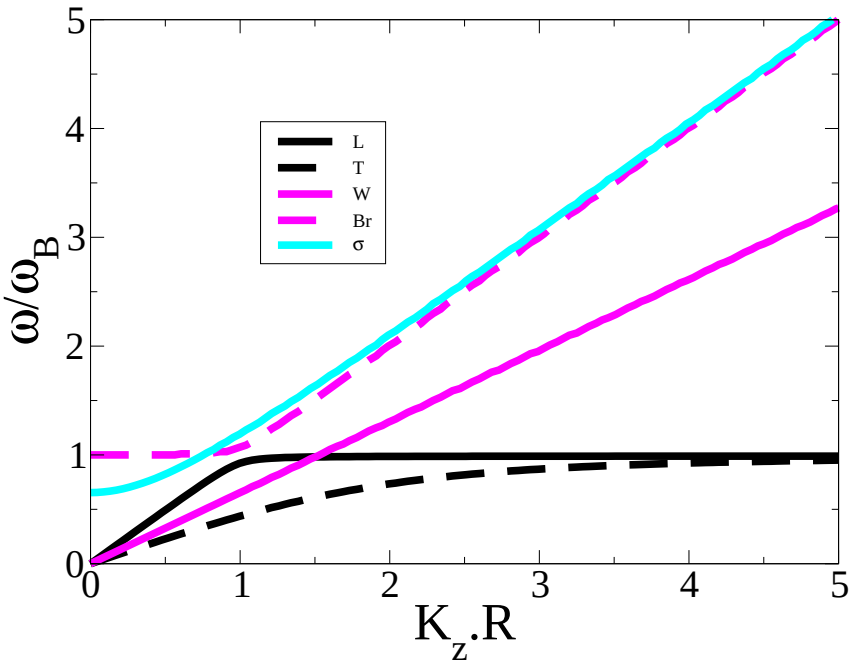

Figure 3.15: The phonon dispersion curves of the six lowest branches for a carbon nanotube of radius R. For a (10,10) nanotube, ω_B=170.76 cm^{-1}. Here the letter corresponds to the phonon branch: LA= Longitudinal, TA= (doubly degenerate) Transverse (or Flexure), WA= Twist, Br = Breathing and σ= σ (the lowest non-zero mode).

$$g_5(\omega) = \frac{\sqrt{2}L_0}{\sqrt{1-\sigma_P}\pi R\omega_B}\sum_{m=1}^{m_2}\frac{(\frac{\omega^2}{\omega_B^2}-1)^2+m^2}{(\frac{\omega^2}{\omega_B^2}-1)\sqrt{(\frac{\omega^2}{\omega_B^2}-1)(\frac{\omega^2}{\omega_B^2}-1-m^2)}}, \tag{3.41}$$

$$g_6(\omega) = \frac{\sqrt{2}L_0}{\sqrt{1-\sigma_P}\pi R\omega_B}\sum_{m=1}^{m_3}\frac{(1-\frac{\omega^2}{\omega_B^2})^2+m^2}{(1-\frac{\omega^2}{\omega_B^2})\sqrt{(1-\frac{\omega^2}{\omega_B^2})(1+m^2-\frac{\omega^2}{\omega_B^2})}}, \tag{3.42}$$

where m_1, m_2, and m_3 are the maximum values of the angular quantum number (with m_3 being set to 1 due to the discussion in the previous section).

3.4.4 Results

The lattice dynamics of a carbon nanotube is well documented as demonstrated in section 3.4.1. Instead, the focus here is on important results the analytic expressions reveal. Also, strong emphasis is being placed on the comparison with the lattice dynamics of silicon nanostructures discussed in section 3.3.

Carbon nanotubes show many vibrational properties which are similar to those of silicon nanostructures. Figure 3.15 shows that nanotubes, like silicon nanostructures, possess low-lying optical modes with energies comparable to those of the acoustic branches. Also, the group velocity of the acoustic phonon modes in a carbon nanotube are greater than those in bulk-diamond, which is a contributing factor to the unusual thermal properties of nanotubes. This is similar to the thinnest silicon nanowire where the zone-centre group velocity of the dilatational mode is much greater than that of longitudinal mode in bulk silicon. This would suggest that ultrathin structures will have much higher group-velocities than their corresponding bulk counterparts, but further work is needed to confirm this.

The group velocity of the acoustic modes does not change with nanotube size and this is a result of the simplified model presented. These results contrast with the results of Ye *et al.* [145] which show a slight variation in the acoustic modes zone centre velocity. This is because the Young's modulus Y [147], is found to change quite substantially with radius for the thinner tubes. However, it is known that the Young's modulus tends towards the value used here for tubes greater than the (9,9). However, no clear conclusion has been presented in the literature yet as to what factors control this variation. Comparison with Ye *et al.* shows that the difference this makes to the comparative velocities of these modes is no more than 5%. Also, a recent study by Lawler *et al.* [148] provides further evidence, using *ab initio* techniques, where they show that the elastic velocities of the acoustic modes and the Poisson's ratio change very little with tube size.

As the radius R decreases, it can be seen that the frequency of the two optical modes, ω_B and ω_σ, shown in Fig. 3.15, decrease as

$$\omega_{B/\sigma} \propto \frac{1}{R} \tag{3.43}$$

This is in good agreement with *ab initio calculations* and agrees with the data presented for the breathing mode shown in Table 2.1 in Chapter 2. This result contrasts with the silicon nanowire and is expected for two reasons: (i) strong carbon bonds result in a stronger confinement effect than the corresponding silicon bonds in the nanowire; (ii) a carbon nanotube consists of a single monolayer of atoms rolled

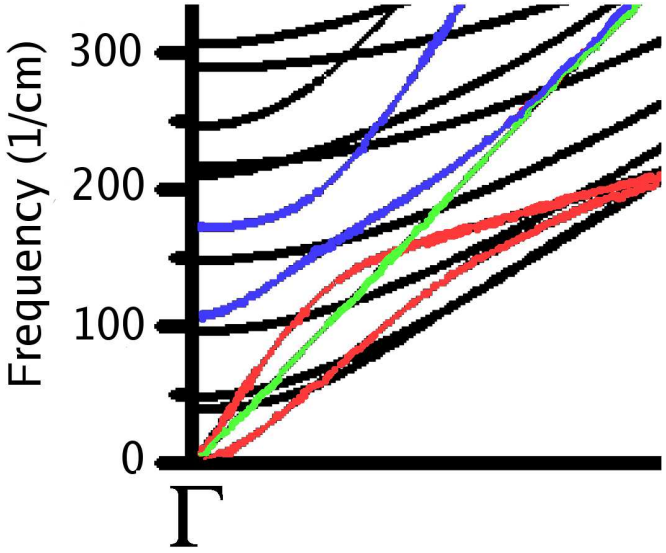

Figure 3.16: Reproduced from Ye *et al.* [145]. The low-lying phonon dispersion curves for a (10,10) carbon nanotube. The frequency of the zone-centre breathing mode ω_B is 170 cm^{-1}. Highlighted are the Longitudinal and doubly degenerate Transverse branch (red), the twist branch (purple) and the two optical branches (blue).

up to form a tube, whereas conversely, the thinnest nanowire considered is four monolayers thick. It can be clearly seen that this is a direct result of Eq. (3.27), which scales all the dispersion relations. Hence the breathing mode varies as Eq. (3.27) and the zone-centre ω_σ mode varies as

$$\omega_\sigma = \frac{1}{R}\sqrt{\frac{Y}{\rho}(1-\sigma_P^2)}\sqrt{\frac{1-\sigma_P}{2}}. \tag{3.44}$$

However, as Fig. 3.15 clearly shows, the turning point in the acoustic branches (i.e. where $d^2\omega/dK_z^2 \gg 1$) always occurs at $k = 1$. Hence as $w_B.R/k = A$ where A is constant for all values of $k < 1$. That is, within the continuum model the group velocity of each of the acoustic modes is constant regardless of radius for all carbon nanotubes.

The phonon dispersion relations obtained using the continuum model are in good agreement with *ab initio* calculations obtained by Ye *et al.* as shown in Fig. 3.16. Both show the turning points in the breathing mode and the longitudinal mode occur near the same frequency, though the continuum model finds this more pronounced. This is to be expected as a continuum model functions best in the long wave-length

limit (i.e. near the zone centre) and breaks down in the short-wavelength limit (i.e near the zone edge). However, the velocity of the modes is within 0.1 km s^{-1} of the results for the continuum model. It can be seen from *ab initio* calculations that there are other low-lying optical modes missing from the continuum approach, but the two Raman active modes, the ω_σ and the ω_B modes are present.

3.5 Summary

Nanostructures have several common features in their lattice dynamics. All structures show the appearance of low energy optical branches in their phonon dispersion curves, the branch associated with ω_σ in the silicon nanostructures and the carbon nanotube as well as the additional branch associated with ω_B in the carbon nanotube. Also, all of the thinnest structures have high zone-centre group velocity for their acoustic phonon branches, when compared to either bulk or larger nanostructures. For the silicon nanostructures, it can be seen for the ultrasmall case of each structure that all branches except the acoustic are flat and dispersionless regardless of whether the system is zero-, one- or two-dimensional. Conversely, the continuum model of the nanotube shows that the group velocity of the low optical modes is much larger for $k > 1$. As the size of the silicon structures increases, these branches are seen to become dispersive in the direction of propagation like the nanotube.

In all the materials studied here, the characteristic lowest non-zero zone centre mode with frequency ω_σ is calculated and shown to decrease with size of the nanostructure as $\omega_\sigma \propto 1/r^\alpha$ where α depends on the type of nanostructure. An analytic fit has been presented for the size variation of this mode for the silicon nanostructures (dots, wires and slabs) and the behaviour of low-lying modes in carbon nanotubes is explained from theory (see Eq. (3.27)). For the silicon systems considered, it is observed that the highest optical mode is lowered when compared with bulk and this behaviour can be predicted.

Having discussed the lattice dynamics of nanostructures, the focus moves now to the application of the phonon dispersion curves to calculating the thermal properties

of such structures. In the next chapter, the specific heat capacity of carbon nanotubes is explored in detail. After this, in Chapter 5 the lifetime of phonon modes undergoing three-phonon processes is discussed for silicon nanowires and carbon nanotubes. These sections make extensive use of the analytic expressions derived in the sections 3.4.2 and 3.4.3.

Chapter 4

Specific Heat Capacity Of Carbon Nanotubes

The final test of a theory is its capacity to solve the problems which originated it.

George B. Dantzig (November 1914 - May 2005)

4.1 Introduction

The heat capacity of a material is defined as the amount of energy per unit mass or per unit volume required to raises its temperature by one Kelvin. It is measured in $JK^{-1}kg^{-1}$ or $JK^{-1}m^{-3}$. This is because for solids these two quantities (mass and volume) are easily related through the mass density of the material, ρ. Specific heat capacity is generally defined to be measured at either constant volume or constant pressure. This is because for a gas these quantities can lead to quite different results. However, for a solid, the material's heat capacity does not change substantially with a change in pressure, except at high pressures where the external force to the system distorts the lattice. Hence, when discussing solids, one would normally refer to the specific heat capacity at constant volume.

In this chapter the previous calculations and measurements of specific heat capacity in carbon nanotubes that have been performed are introduced and described. The theory behind the the specific heat capacity of carbon nanotubes is presented followed by a discussion of the results. Theses results show the changeover between one-dimensional and two-dimensional behaviour in the specific heat capacity, as well as discussing the dependence this quantity has on the size of the nanotube and its temperature. Lastly, a summary is presented.

4.2 Background

Specific heat capacity, C_v, began to be understood in terms of vibrations when Einstein [2] proposed that each atom in a solid acted like a simple harmonic oscillator. This theory was expanded and refined by Debye [3] in 1912 when he described the phonon dispersion relations as a linear relationship between the wave-vector $\mathbf{q}$ and frequency ω for a system and applied this to covalently bonded semiconductors. The importance of specific heat capacity, especially in an early context, cannot be overstated. This is because before neutron and Raman scattering measurements were possible, the only easy and readily available method that was available for understanding the vibrational properties of a material was by measurement of a material's specific heat capacity. For carbon nanotubes, the specific heat capacity is a very interesting quantity as it can be used to differentiate between three-dimensional, two-dimensional and one-dimensional behaviour.

Benedict *et al.* [149] predicted that all single-wall nanotubes at low temperatures should show a linear relationship between specific heat capacity and temperature, T, i.e. $C_v \propto T$, which is a signature of a one-dimensional material. They also showed that at high temperatures this relationship would change to $C_v \propto T^2$ behaviour, which is two-dimensional-like behaviour. These dependencies were unusual as for bulk one would expect a T^3 relationship at low temperatures [131, 150]. Benedict *et al.* also showed that the electronic contribution to specific heat at all temperatures even for metallic tubes would be negligible. This was also later confirmed

by Klemens [151]. However, in Benedict's approach, they used simple dispersion relations and several adjustable parameters, suggesting that this approach may not be very accurate. Later, Benedict *et al.* [152] expanded this approach to multi-wall tubes and ropes of single wall tubes, where they showed that the tubes became more graphite-like in nature suggesting that intertube coupling may have a strong effect on the thermal properties of nanotubes.

In 1998 the linear dependence was confirmed by Yi *et al.* [154] who carried out measurements of the specific heat capacity of multi-wall tubes. However, Yi *et al.* were unable to measure single wall tubes and confirm the same behaviour. It was later in 2000, when Hone *et al.* showed evidence for the quantisation of phonon spectra in carbon nanotubes that the specific heat capacity of single-wall tubes was measured. The tubes in their sample were confirmed by scanning tunnelling microscopy to be single-wall, but these tubes occurred in bundles, forming ropes. These samples showed linear behaviour between 5 K and 300 K, but showed a deviation from this at ultralow temperatures. Popov, in 2002 [153], showed that this deviation may have been due to the transverse modes being damped due to tube interactions. This behaviour was confirmed by Zhang *et al.* [142] who discussed the behaviour of the specific heat capacity of a (10,10) nanotubes. Using the dispersion relations derived by Mahan [141], Zhang *et al.* derived analytic forms for the temperature dependence of the specific heat capacity of carbon nanotubes. In this approach, Zhang *et al.* showed that discluding the contribution from the mixed acoustic modes (which they had, in their approach, more than 10!) better agreement could be found between theory and experiment.

Of the theoretical approaches presented, none considers the effect of a variation in tube radius and the effect that this would have on the one-dimensional and two-dimensional behaviour of nanotubes, except the initial work of Benedict *et al.* It would be expected that a nanotube of infinite radius should show two-dimensional behaviour as in effect, it would be a single sheet of graphene. Also, as the ropes of tubes in the experiments of Hone *et al.* or the multi-wall tubes in the experiment of Ye *et al.* consisted of nanotubes which had a distribution of different radii, then these effects may prove important in explaining discrepancies between their results

and present theory.

4.3 Theory of Specific Heat Capacity

The specific heat capacity of a system is defined as:

$$C_v = \left(\frac{\delta E}{\delta T}\right)\Big|_{V_0} \tag{4.1}$$

where E is the thermal energy of the crystal with volume V_0 at temperature T. For phonons the total energy of a system in equilibrium is

$$E = \sum_{\mathbf{q}} \sum_{s} \hbar\omega_s(\mathbf{q})\bar{n}_s(\mathbf{q}), \tag{4.2}$$

where the symbols have their usual meanings as defined in Chapter 3. Here as the summation over $\mathbf{q}$ has to include all the independent phonon modes, the sum is replaced with an integral over all phonon modes using Eq. (3.36) such that $\sum_{\mathbf{q}s} \rightarrow \int g(\omega)\, d\omega$. Hence Eq. (4.1) becomes

$$C_v = \int_0^{w_D} k_B \left(\frac{\hbar\omega}{k_B T}\right)^2 \frac{e^{\hbar\omega/k_B T}}{(e^{\hbar\omega/k_B T}-1)^2} g(\omega) d\omega. \tag{4.3}$$

This equation can be evaluated using two different sets of dispersion relations: the more detailed analytic expressions presented by Mahan [141] and the simple dispersion relations from the Debye model.

4.3.1 Debye Model

In the Debye approach, the dispersion relations are modelled as linear, hence using Eq. (3.4) and Eq. (3.36) from Chapter 3 the density of states of a simple one-dimensional system is expected to be of the form

$$\begin{aligned} g_s(\omega)d\omega &= \int \frac{L_0}{2\pi}\frac{d\omega}{\nabla_{K_z}\omega} = \int \frac{L_0}{2\pi}\frac{d\omega}{c_s}, \\ g_{1D}(\omega) &= \frac{L_0}{2\pi c_s}, \end{aligned} \tag{4.4}$$

where the symbols have their usual meanings. Hence using the substitution $x = \frac{\hbar\omega}{k_B T}$, Eq. (4.3) becomes

$$C_{v,1D} = \frac{k_B^2 T L_0}{2\hbar\pi c_s} \int_0^{\omega_D} x^2 \frac{e^x}{(e^x - 1)^2} dx. \tag{4.5}$$

where ω_D is the Debye frequency [131], which is determined from the normalisation condition that the total number of vibrational modes is $2p$ (p being the total number of carbon atoms in the single wall nanotube). From this equation, it can be clearly seen that the specific heat capacity varies linearly with temperature in the low temperature limit. Similar analysis [131] reveals that for two-dimensional systems, the specific heat capacity varies as T^2 in the low temperature regime. Hence using this simple model, one can characterise systems of different dimensionality's. However, the phonon dispersion relations for a real system, like the carbon nanotube, are not linear and hence this model cannot provide either quantitative or accurate results for most realistic systems. However, in Chapter 3 analytic dispersion relations were obtained for carbon nanotubes and these are applied in the following section.

4.3.2 Dispersive Model

To model the specific heat capacity of a carbon nanotube more accurately than the simple Debye approach, one must apply the phonon dispersion relations obtained in section 3.4. Using the expressions from sections 3.4.2 and 3.4.3, it is possible to evaluate Eq. (4.3) by considering the two cases; $m = 0$ and $m \neq 0$. For $m = 0$, the phonon dispersion branches are the twist (W), longitudinal acoustic (LA), and breathing (B) modes. For $m \neq 0$ there are two mixed non-zero modes and one mixed acoustic mode (for $m = 1$ the transverse acoustic (TA) mode [142]). From these dispersion relations, analytic expressions for the density of states are easily produced (see Eqs. (3.37-3.42)). Hence, by using Eq. (4.3) the specific heat capacity can be calculated.

For carbon nanotubes, the specific heat capacity can be expressed as

$$C_v = \sum_j C_{v,j} \tag{4.6}$$

where

$$\begin{aligned} C_{v,j} &= \frac{k_B^2 T}{\hbar}\int_{x_{j,min}}^{x_{j,max}} dx x^2 g_j(x)\frac{e^x}{(e^x-1)^2} \\ &= D_j T\int_{x_{j,min}}^{x_{j,max}} dx x^2 f_j(x)\frac{e^x}{(e^x-1)^2} \end{aligned} \tag{4.7}$$

with $x = \hbar\omega/k_B T$, and

$$\begin{aligned} f_1(x) &= 1, \\ f_2(x) &= \frac{(\frac{x^2}{x_0^2}-1+\sigma_P^2)^2+\sigma_P^2(1-\sigma_P^2)}{(\frac{x^2}{x_0^2}-1+\sigma_P^2)\sqrt{(\frac{x^2}{x_0^2}-1)(\frac{x^2}{x_0^2}-1+\sigma_P^2)}}, \\ f_3(x) &= \frac{(1-\frac{x^2}{x_0^2}-\sigma_P^2)^2+\sigma_P^2(1-\sigma_P^2)}{(1-\frac{x^2}{x_0^2}-\sigma_P^2)\sqrt{(1-\frac{x^2}{x_0^2})(1-\frac{x^2}{x_0^2}-\sigma_P^2)}}, \\ f_4(x) &= T\sum_{m=1}^{m_1}\frac{x}{\sqrt{\frac{x^2}{x_0^2}-\frac{1-\sigma_P}{2}m^2}}, \\ f_5(x) &= \sum_{m=1}^{m_2}\frac{(\frac{x^2}{x_0^2}-1)^2+m^2}{(\frac{x^2}{x_0^2}-1)\sqrt{(\frac{x^2}{x_0^2}-1)(\frac{x^2}{x_0^2}-1-m^2)}}, \\ f_6(x) &= \sum_{m=1}^{m_3}\frac{(1-\frac{x^2}{x_0^2})^2+m^2}{(1-\frac{x^2}{x_0^2})\sqrt{(1-\frac{x^2}{x_0^2})(1+m^2-\frac{x^2}{x_0^2})}}. \end{aligned} \tag{4.8}$$

The contributions f_1 – f_3 originate from the $m = 0$ solutions and f_4 – f_6 originate from the $m \neq 0$ solutions. Here σ_P is the Poisson's ratio and $x_0 = \hbar\omega_B/k_B T$, with ω_B being the breathing mode frequency at the zone centre. The constants D_j (derived in the paper by Zhang *et al.* [142]) for (n, n) armchair single wall nanotubes are: $D_1 = 0.2468$ [J/kg/K^2], $D_2 = D_3 = 0.16137$ [J/kg/K^2], $D_4 = 6.5602 \times 10^{-5}$ [J/kg/K^3], $D_5 = D_6 = 0.02468$ [J/kg/K^2].

Before the integration limits, and the values for m_1 and m_2 are ascertained, one reminds the reader that ω_B varies with the tube radius R as $\omega_B = (1/R)\sqrt{Y/\rho(1-\sigma_P^2)}$, where Y is Young's modulus as seen from Eq. (3.27) in Chapter 3. Also, the reader is reminded that the tube radius varies linearly with the tube index n [13] as seen in Chapter 1. The upper integration limit, ω_{max}, and the values of m_1 and m_2 are determined from the normalisation condition that the total number of vibrational modes is $2p$ (p being the total number of carbon atoms in the single wall nanotube). The values of m_1 and m_2 are given in Table 4.1. The upper limits for $j = 3$ and $j = 6$ are are restricted by the cut-off point in the corresponding density of states

Table 4.1: The breathing mode frequency ω_B, the maximum vibrational frequency $\omega_{\max}$, and the limits of the summations m_1 and m_2 in Eq. (3) for carbon nanotubes of different radii R.

n	R (nm)	m_1	m_2	ω_B (rad/Ts)	$\omega_{\max}/\omega_B$
5	0.344	10	6	62.19	6.68
10	0.688	24	16	31.11	16.04
15	1.031	37	24	21.18	24.76
20	1.375	51	33	15.88	33.36

curve. For $j = 1, 3$ and 6 the lower limit is $x_{min} = 0$, whereas $x_{min} = \hbar\omega_B/k_BT$ for $j = 2$, $x_{min} = \hbar\omega_B m\sqrt{1-\sigma_P}/\sqrt{2}k_BT$ for $j = 4$ and $x_{min} = \hbar\omega_B(1+m^2)^{\frac{1}{2}}/k_BT$ for $j = 5$. The upper limit x_{max} is $\hbar\omega_{max}/k_BT$ for $j = 1, 2, 4$, and 5 and $\hbar\omega_B/k_BT$ for $j = 3$ and 6.

In the original approach, Zhang *et al.* evaluated Eqs. (4.7) and (4.8) poorly. In particular, some limits in Eq. (4.7) and the value of m_3 in Eq. (4.8) were adjusted to fit experiment without firm theoretical justifications or understanding of the vibrational characteristic of carbon nanotubes. Here, bearing in mind these considerations, the correct limits of integration for each term are presented. These are determined using the knowledge that $g(\omega)$ must be real for all values between the upper and lower limits. These limits must be less than or equal to $\hbar\omega_{max}/k_bT$. From this, it is possible to calculate the correct limits as shown above. It is important to note that the upper and lower limits of several integrals have to be approximated as they occur at singularity points in the density of states. This is taken into account by reducing (or increasing in the case of lower limits) the value of the limit by δ where δ is a

very small deviation. Zhang *et al.* used several different values for δ depending on the term and the fit to experiment. For the term $f_6(x)$ Zhang *et al.* used an experimental fit to set the upper limit and thus they ignored 75% of the total area of integration, which is highly unphysical. This was done to help fit experimental data, but has no physical basis and, as shown later, this is not necessary. In order to preserve consistency and to use the theory to its fullest, δ is set universally as $\delta = 0.004\omega_B$ to minimise numerical error.

Zhang *et al.* also incorrectly set $m_3 = 16$. This is done again to enable a better fit for the theory with experiment and is without any physical reasoning. Unfortunately, as mentioned in Chapter 3, this creates $m_3 + 2$ acoustic branches, which is unphysical for nanotubes. It has been shown by atomistic [13] and *ab initio* calculations [155, 145] that nanotubes have four acoustic branches: one longitudinal, one twist mode and two transverse mode. It can be shown from Eq. (4.8) that when $m_3 = 1$ the function $f_6(x)$ leads to a mixed acoustic mode which has the same form and zone-centre group velocity as the transverse or flexural mode obtained in *ab initio* calculations [155, 145]. Hence, here (as described in Chapter 3) m_3 is set to 1 and given double weighting to account for the doubly degenerate nature of the transverse mode.

4.4 Results of Calculations

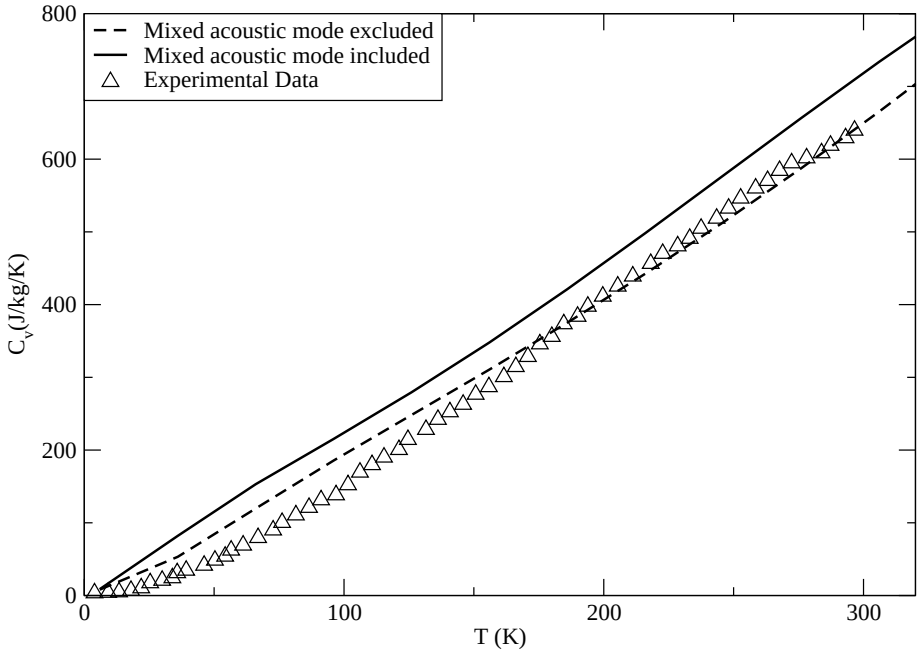

Figure 4.1: The specific heat capacity (C_v) of a (10,10) carbon nanotube as a function of temperature. Shown are the experimental data of Hone *et al.* and the theoretical results with and without the mixed acoustic mode contribution $C_{v,6}$.

Figure 4.1 shows the results obtained from the theory presented in section 4.3 for the (10,10) nanotube. It can be seen from the diagram that the effect of including the mixed acoustic mode is to increase the specific heat capacity C_v by an approximately constant amount. In the temperature range shown in the diagram, C_v varies linearly with temperature. Also shown in this figure is the experimental data from Hone *et al.* [66]. There is good agreement between theory without the inclusion of the mixed mode and experiment above 200 K. It has previously been discussed [153] that mixed acoustic modes are damped in bundles of nanotubes and the results presented here support this. As the experimental measurements by Hone *et al.* have been made for bundles of nanotubes, it is not surprising that there is better agreement between experiment and theory when the contribution from the mixed acoustic

mode is not included. As can be seen from closer examination of Fig. 4.1, there is a lack of good agreement in the C_v variation in the low temperature region between the presented results and experiment. This is likely to be due to a combination of several factors, notably the difference between single-wall nanotubes, multi-wall nanotubes, and bundle of nanotubes on the experimental side, and the simplicity of the theoretical model adopted here. In particular, the effect of multiple tubes creates a graphitic effect, with Van der Waals interactions between tubes dampening the one dimensional nature of the tubes. Hence it is expected (and commented on by Hone *et al.*) that disagreement in the lower range may occur as one dimensional effects and mixed acoustic modes are dampened. This has large implications for use of nanotubes as these interactions change their physical applicability's. In particular, it is not clear whether the Van de Waals interaction could occur with other surfaces, or what form this interaction may take, and thus isolated tubes placed on a substrate may not display as high a specific heat capacity as an isolated tube due to the surface dampening this mode of vibration.

The temperature variation of the specific heat capacity of nanotubes with different radii is shown in Fig. 4.2. Up to about 250 K, all nanotubes show a linear temperature variation, within an accuracy of 20 J/kg/K. This is a characteristic of one-dimensional behaviour, as can be expected from Eq. (4.5). Above room temperature a clear difference, both in the magnitude and temperature variation, can be seen for nanotubes with different radii. For example, at 400 K, the result for the (20,20) nanotubes is 12% higher than that for the (5,5) nanotubes. Also, it is possible to postulate a second reason for the disagreement between theory and experiment at low temperatures, shown in Fig. 4.1, that has not been considered before. Thinner nanotubes show a dip in their specific heat capacity at low temperatures. Hone *et al.* state clearly that the experimental data is for nanotubes with an average radius of 1.25 nm which corresponds to a $(10, 10)$ tube. On the basis of the results in Fig. 4.2 it can be suggest that whilst the average nanotube size is that of a $(10, 10)$ nanotube, the distribution is not normal and is biased towards thinner nanotubes, explaining the fit in the experimental data at low temperatures. If the distribution of radii for the nanotubes in the ropes could be found, then better fit

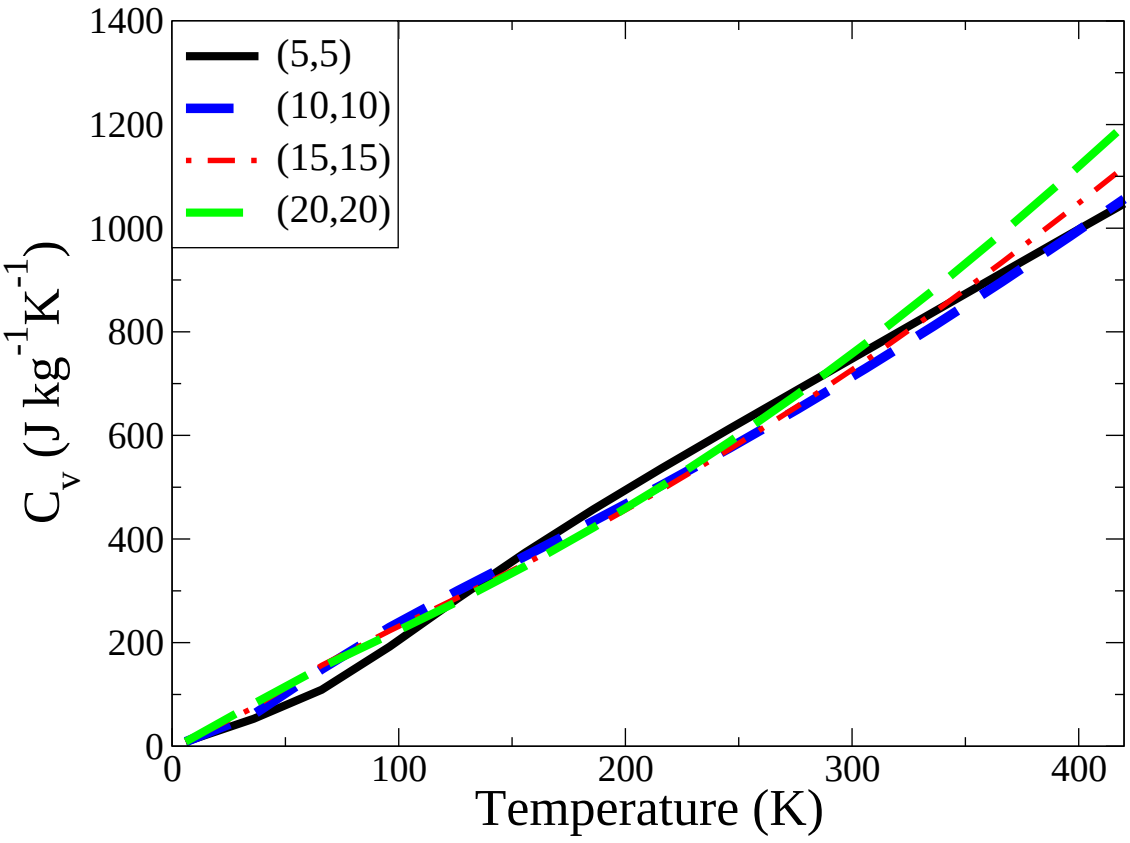

Figure 4.2: The variation of the specific heat capacity C_v of a series of (n,n) single wall nanotubes with temperature.

between theory and the experimental data in the lower temperature regimes could be achieved.

For a given radius, the temperature variation of C_v shows a departure from the linear towards quadratic dependence. Figure 4.3 shows the substantial deviation from the linear behaviour for the (15,15) nanotube beyond 190 K. The linear variation of C_v in Fig. 4.3 can be expressed as $C_v = bT + c$ with $b = 2.5642$ (J/kg/K^2) and $c = -61.7294$ (J/kg/K). As all tubes follow very similar linear temperature variation, this expression can be used to obtain an approximate value of C_v for a given low temperature. The departure from the linear variation in C_v is indicative of a change from the one-dimensional (1D) to two-dimensional (2D) behaviour. This is seen as a defining characteristic of all but the thinnest nanotube considered here [i.e.

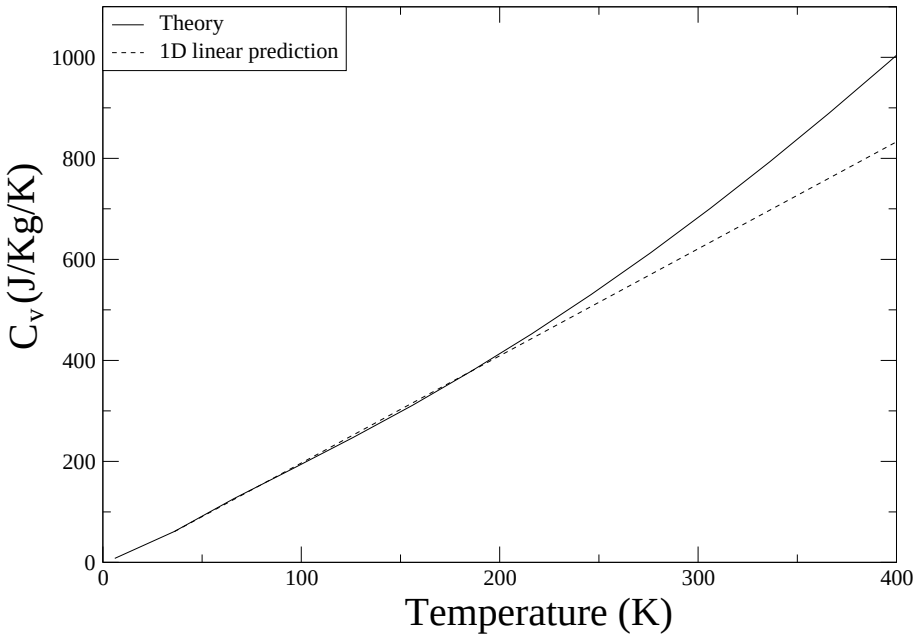

Figure 4.3: The specific heat capacity C_v of a (15,15) nanotube with a scaled linear one-dimensional Debye continuum prediction also shown.

(5,5)]. For very thin nanotubes the classical asymptotic limit is reached before the 2D-like behaviour sets in. In terms of the dispersion curves, it is the resultant density of states arising from the $\omega_{\sigma,m}$ modes which are the critical factor in determining this changeover. In small nanostructures, their are relatively few of these branches considered within the limits of integration as shown by the values of $m_{1,max}$ presented in Table 4.1. However, in larger tubes, which have a greater number of branches within the limits of integration have a larger contribution from these modes and hence the two-dimensional behaviour occurs at lower temperatures.

From numerical calculations, the change over from the one-dimensional-like to the two-dimensional-like behaviour as a function of the nanotube index n and temperature T has been obtained. This is shown in Fig. 4.4, where the numerical uncertainty in the data is also indicated. Previously Benedict *et al.* [149] have suggested a qualitative explanation for such a changeover. In their simple analysis, Benedict *et al.* had estimated the changeover as a function of n and T to be of the form $nT = \alpha$. Our numerical results suggest a modified form of the type $nT = A + B/T$, with the constants A and B calculated to be $A = 1146.27$ K and $B = 517267.0$ K^2. This provides quantitative values for the changeover and is in agreement with the

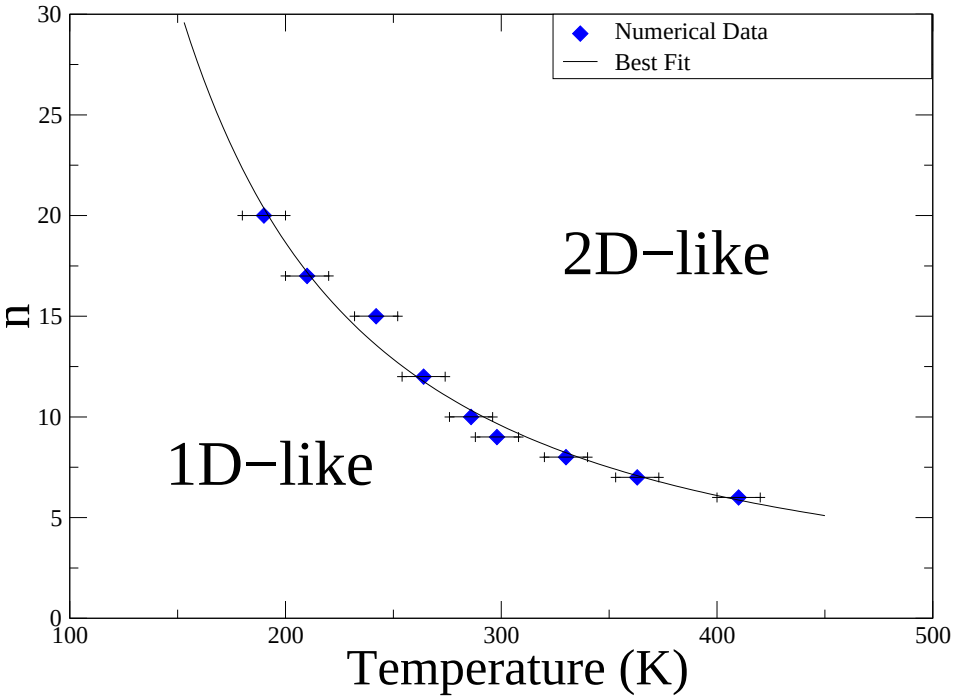

Figure 4.4: The change over in the specific heat capacity of (n, n) armchair carbon nanotubes from 1D-like to 2D-like behaviour as a function of n and T.

data from Hone *et al.* which shows mainly linear increase in the specific heat with temperature. Benedict *et al.*'s simple approach provides an estimate of α to be $\approx$1200 K. However, the data presented here shows that a more detailed and precise approach provides more accurate estimates of this behaviour. The quantitative estimates show that the changeover occurs at a much higher temperature than predicted from Benedict's theory and this is in better agreement with the experimental data. Hence, from the results presented, it is apparent that tubes with increasing radii show two-dimensional-like specific heat at decreasing temperatures. Eventually the specific heat of an infinitely thick tube (i.e. graphene-sheet like) would be purely two-dimensional in behaviour.

4.5 Summary

Using the one-dimensional tube continuum theory the variation of the specific heat capacity (C_v) of (n, n) arm-chair carbon nanotubes with temperature T and radius $R(n)$ has been investigated. In the very low temperature regime (less than 70 K) the majority of nanotubes ($n > 8$) show linear variation of C_v with T. However, the ultrathin nanotubes show a slight dip which accounts for discrepancies between theory and experiment. However, for temperatures greater than 70 K, but less than 200 K all nanotubes with n in the range 5-20 show linear variation of C_v with T. For these nanotubes a changeover occurs from the 1D-like to a 2D-like behaviour. For the range of n values considered here, such a changeover occurs between 180 K and 400 K. The crossover line can be expressed as $nT = A + B/T$, where A and B are constants. In the appropriate linear regime the variation of C_v for nanotubes of all sizes has been estimated, which hopefully would be helpful in analysing experimental measurements on single wall nanotubes. Whilst the tube continuum model may not be as rigorous as atomistic calculations, it nevertheless explains trends and key features for the temperature and size variation of the specific heat of single-wall carbon nanotubes as well as provides good agreement with experimental results.

Chapter 5

Phonon-Phonon Interactions In Nanostructures

Nows fills thy sleep with perturbations

Richard III, In Richard III by William Shakespeare, 1564 - 1616

5.1 Introduction

The interaction of phonons with other phonons is an extremely important scattering mechanism in most semiconducting materials. This scattering mechanism is vital in describing two thermal properties of system; these being the mean-free path of the phonons and the thermal conductivity. Phonon interactions occur due to the anharmonic regime of the crystal potential and because of this it is possible for phonons to be created and destroyed via these interactions. It is possible to have several different orders of phonon interactions. These can be three-phonon interactions, four-phonon interactions, five-phonon interactions and so on. However, it is three-phonon interactions that are the dominant mechanism in these thermal properties. In a real system, there are several further interactions to consider such as the interaction of phonons with electrons, phonon interactions with defects in the sample and the interaction of phonons with the boundaries of the system. In

semiconductors, however, it is the phonon-phonon interaction that dominates their thermal properties at room temperature.

Phonon-phonon interactions can be viewed as a perturbation on the harmonic system. As this perturbation is small, these interactions can be described using Fermi's Golden Rule. From the Golden Rule, one can calculate the lifetime of a phonon mode as a function of temperature. Hence the study of phonon-phonon interactions is the study of the lifetime of phonon modes. It is also important to note that the relaxation rate of a phonon mode (that is the rate at which phonons interact) is equal to the inverse of the phonon mode's lifetime and both terms are used when describing phonon-phonon interactions.

In this chapter the theory of three-phonon interactions is presented based on the dispersion relations presented in Chapter 3. The background of phonon-phonon interactions and the relaxation rate of phonon modes in bulk and nanostructures is discussed and motivation for this investigation explained. Using a well developed theoretical consideration, a detailed derivation of the three-phonon scattering relaxation rate is presented. From this important result, a qualitative analytic expression for the relaxation rate of all acoustic phonon modes and an exact analytic expression for the decay rate of the two zone-centre optical modes, ω_σ and ω_B in nanostructures are derived. These two modes are investigated for nanowires and nanotubes to assess whether, like bulk materials, such modes have such short lifetimes that they may be excluded from calculations of the relaxation rate of phonon modes, or whether they are important contributions which need to be considered for the total relaxation rate within these two nanostructures. Having assessed the contribution from these two mode's, the relaxation rate of phonon modes in carbon nanotubes is calculated and described precisely using numerical schemes. From these results the temperature and frequency dependence of the phonon modes lifetime are explained. These results also discuss the importance of particular phonon branches in the relaxation rates of the phonon modes and what effects a change in the size or temperature of the nanotube have on the relaxation rate. The results are then described using analytic expressions, based upon the qualitative equations for the acoustic modes derived earlier.

5.2 Background

The theory of phonon-phonon interactions has been studied for over half a century. The theoretical treatment of these interactions is linked to the modelling of the anharmonic potential, a complicated and difficult term which can be approximately determined using second-order and third-order elastic constants, which are exceptionally hard to measure experimentally. This applies especially for nanostructures. As such, there have been several different approaches to modelling these interactions in bulk materials, but only recently has there been any progress in nanostructures.

In 1954, Herring [156] was the among the first to use a relaxation time approach to understand and explore these interactions in bulk materials. In his approach, based loosely on Fermi's Golden Rule, and the linear Debye relations (reproduced in Eq. (3.4)), he showed that the relaxation rate of phonon modes undergoing three-phonon processes was directly proportional to the temperature. However, this approach relies on the condition that the temperature is higher than the Debye temperature [131] and uses a simplified form for the potential cubic anharmonic term V_3. This relaxation time approach was adopted by Liebfried and Schlomann [157] who had previously developed an anharmonic potential [158] as part of their specific heat calculations in 1952. This anharmonic potential was calculated using a Debye-like continuum approach to modelling the potential. Using their potential, Leibfried *et al.* were able to calculate the lifetime of the acoustic phonon modes undergoing three-phonon interactions for bulk semiconductors. This potential was advantageous in that it had only one adjustable parameter, but was disadvantageous in that it required linear dispersion relations. This theory was then applied to several semiconductors and showed good agreement with experiment [150], though in their results it was a necessity to vary at least one adjustable parameter with temperature to match high and low temperature experimental results.

Klemens, in 1958, proposed a second form for the anharmonic potential in bulk [159], which also only applied in the long wavelength limit to acoustic phonons, by applying symmetry arguments. The advantage of Klemens potential was that it applied to non-linear dispersion curves, which is the case in most real systems (though linear

is a very good approximation as discussed in Chapter 3). The disadvantage of this potential was that it required one to have knowledge of the average velocity of the phonon modes (with no clear definition of how to calculate this) and had two scalable parameters. Also, Klemen's expression, like Leibfried's, had an arbitrary coupling between the interacting phonon modes. However, Klemens and Liebfrieds models did not agree on the low temperature relaxation rates. Later, in 1966 Klemens [160, 161] improved and generalised this potential and the resultant expression for the relaxation rate of phonon modes by including the effects of optical modes, but still the two theories could not agree.

Hamilton and Parrott [162], in 1968, re-adapted and improved the form of the Leibfried's potential by expanding the potential in terms of the isotropic continuum model based upon the relations derived by Landau and Lifschitz [163]. By applying this approach, they showed that these scattering processes could explain the thermal conductance of germanium as a function of temperature using the Variational Principle. Later, on this basis, Parrott applied this potential using the knowledge gained from the variational approach to a *Relaxation time* approach [164, 165].

In 1974, Srivastava [166] presented a detailed description of the relaxation rate of phonon modes. Previous arbitrary parameters and coupling constants were replaced with measurable quantities and a clear description of the difference between *Class 1* and *Class 2* events was presented (*Class 1, Class 2* events and *Normal* and *Umklapp* processes are defined in the following section). Also, by removing arbitrary coupling parameters, Srivastava was able to show that at high temperatures, Umklapp processes would dominate in bulk materials and at low temperatures Normal processes would dominate. In his approach, he was able to discuss the exact contributions from different phonon modes, and only applied one semi-adjustable parameter, the Grüneisen constant, which did not need to change with temperature. Later, in 1976, Srivastava [167] improved upon the potential which Parrott had applied [165] by removing the necessity to use linear dispersion relations and correcting the potential to show a similar form to that of Klemens [159], but with only one semi-adjustable parameter (the Grüneisen constant) and no arbitrary coupling factor. Later, by applying this relaxation time approach to germanium, Srivastava [168] showed ex-

cellent agreement with experiment and explained the thermal conductivity in all regimes. This included the high temperature regime which is dominated completely by three-phonon events.

In 1981, Lax *et al.* [170] showed, using momentum and energy conservation conditions, that certain decay routes of phonon modes (such as a high energy transverse acoustic phonon mode decaying into two lower energy transverse acoustic phonon modes) were impossible due to momentum and energy conservation conditions. These conditions have been shown to apply to linear systems and also near the Brillouin zone centre for non-linear systems where the dispersion curves are approximately linear (see Chapter 3). This is especially interesting when one considers nanotubes.

In carbon nanotubes, as shown by Fig. 3.15, the dispersion curves are not linear across the entire Brillouin zone. This leads to the possibility of processes which are able to invalidate the condition proposed by Lax *et al.* In 2003, the relaxation rate of three-phonon processes in carbon nanotubes was explored by Xiao *et al.* [171]. In their approach, Xiao *et al.* do not include several features which are important to three-phonon scattering, such as Normal processes and low-lying non-acoustic branches in the phonon dispersions for the nanotubes. Also, their expression for phonon relaxation time due to three-phonon interactions does not explicitly differentiate between Class 1 events (two phonons merging into a third phonon) and Class 2 events (one phonon decaying into two phonons) and neither does it clearly state whether momentum conservation had been included, or whether the model relies on the assumptions of Lax *et al.* The expression for the anharmonic potential which Xiao *et al.* used is derived from the term which Klemens produced in the 1950's and does not appear to show any consideration of dimensionality effects and has a much weaker scattering rate than expected. Unfortunately, to the author's knowledge, though time-resolved Raman scattering can be performed to measure the lifetime of a phonon mode, there currently exists no such measurements available in the literature, though this would be highly beneficial to help clarify this further.

From the theoretical approaches described, there are several unanswered questions

concerning the nature of phonon modes in nanotubes and nanowires: What is their relaxation rate? How do they change with a change in radius and temperature? Can they be explained analytically? Are the low lying optical modes, ω_B and ω_σ important? What effect does dimensionality have and, perhaps most importantly, what effect will these factors have upon the thermal conductivity of carbon nanotubes? These and other questions are explored in the following sections.

5.3 Theory of Anharmonic Interactions

Three-phonon scattering is a consequence of the cubic anharmonic term within the crystal potential, V_3, which is shown in Eq. (3.2). The anharmonic part of the potential is considered to be a perturbation upon the harmonic potential which is applied to understand lattice dynamics, which are discussed in Chapter 3. As this is a perturbation, the lifetime of a phonon mode undergoing a three-phonon scattering event can be calculated by applying Fermi's Golden Rule.

5.3.1 General expression

Here a clear derivation of the lifetime of three-phonon processes for selected phonon modes are presented. The expression for the lifetime of phonon modes is formulated for a one-dimensional system, whilst the three-dimensional approach is also given to enable direct comparison. Such a derivation is very complicated and as such some simplifications are used, though these are kept to a minimum. These expressions are derived based upon an approach known as the *single mode relaxation time method* (*smrt*) [131]. In this approach one assumes that all modes except the scatterer are populated according to their Bose-Einstein equilibrium distribution $\bar{n}(\omega)$: $\bar{n}_{\mathbf{q}s} = \frac{1}{1-\exp(\hbar\omega/k_BT)}$. The three-phonon scattering lifetime is calculated using Fermi's Golden Rule. Fermi's Golden Rule describes the transition probability P_i^f of an event as

$$P_i^f(3ph) = \frac{2\pi}{\hbar}| < f|V_3|i > |^2\delta(E_f - E_i) \tag{5.1}$$

where E_i and E_f are the initial and final energy state of the system respectively, $|i>$ and $|f>$ are the initial and final states of the system respectively and V_3 is the lowest order anharmonic part of the crystal potential. Higher order anharmonic terms lead to multi-phonon processes involving more than three phonons. These processes are considered too weak to strongly change the relaxation rate.

Equation (5.1) requires one to evaluate the form of V_3, the cubic anharmonic part of the crystal potential. Within an elastic continuum approach, V_3 can be written as

$$V_3 = \frac{1}{3!}\int d^3r \sum_{lmn}\sum_{ijk} A_{ijk}^{lmn}\frac{\delta u_l}{\delta r_i}\frac{\delta u_m}{\delta r_j}\frac{\delta u_n}{\delta r_k}, \tag{5.2}$$

where A_{ijk}^{lmn} is the third order elastic tensor of the system, r_i is the position vector (component i) and u_l is the corresponding displacement at position r_i. For a three-dimensional continuum it can be readily shown [131] that the displacement vector is of the form

$$\mathbf{u}(\mathbf{r}) = \frac{1}{\sqrt{V_0}}(-i)\sqrt{\frac{\hbar}{2\rho}}\sum_{\mathbf{q}s}\sqrt{\frac{1}{\omega(\mathbf{q}s)}}\mathbf{e}_{\mathbf{q}s}(a_{\mathbf{q}s}^{\dagger} - a_{-\mathbf{q}s})e^{i\mathbf{q}.\mathbf{r}} \tag{5.3}$$

where ρ is the mass density per unit volume, s indicates the phonon branch and $\mathbf{q}$ is the wave vector. V_0 is the volume of the material and $a_{\mathbf{q}s}$ and $a_{\mathbf{q}s}^{\dagger}$ are the phonon creation and annihilation operators respectively. For a one-dimensional system, Eq. (5.3) is modified by $V_0 \rightarrow L_0$ and $\rho \rightarrow \rho'$ where L_0 is the length of the nanostructure and ρ' is the mass per unit length. It is important to note here that the vectors, $\mathbf{u}$, $\mathbf{q}$ and $\mathbf{e}$ are maintained irrespective of whether the system is one-, two- or three-dimensional.

Differentiating Eq. (5.3) with respect to r, and substituting into Eq. (5.2), the form of the potential becomes

$$\begin{aligned} V_3 = \frac{1}{3!}\int d^3r \left(\frac{\hbar}{2V_0\rho}\right)^{3/2} \sum_{\mathbf{q},\mathbf{q}',\mathbf{q}''}\sum_{s,s',s''} A_{ijk}^{lmn}\sqrt{\frac{1}{\omega(\mathbf{q}s)\omega(\mathbf{q}'s')\omega(\mathbf{q}''s'')}}\times \\ q_i\mathbf{e}_{\mathbf{q}s}^{l} q_j'\mathbf{e}_{\mathbf{q}'s'}^{m} q_k''\mathbf{e}_{\mathbf{q}''s''}^{n}(a_{\mathbf{q}s}^{\dagger} - a_{-\mathbf{q}s})(a_{\mathbf{q}'s'}^{\dagger} - a_{-\mathbf{q}'s'})\times \\ (a_{\mathbf{q}''s''}^{\dagger} - a_{-\mathbf{q}''s''})e^{i((\mathbf{q}+\mathbf{q}'+\mathbf{q}'').\mathbf{r})}, \end{aligned} \tag{5.4}$$

for three-dimensional systems, where q_i, q_j', and q_k' are the magnitudes of the wave vectors $\mathbf{q}$, $\mathbf{q}'$, and $\mathbf{q}''$ respectively and $\mathbf{e}_{\mathbf{q}s}^{l}$, $\mathbf{e}_{\mathbf{q}'s'}^{m}$ and $\mathbf{e}_{\mathbf{q}''s''}^{n}$ are the polarisation vectors

of the phonon mode. Similarly, for a one-dimensional system one obtains

$$V_3 = \int dr \left(\frac{\hbar}{2L_0\rho'}\right)^{3/2} \sum_{\mathbf{q},\mathbf{q}',\mathbf{q}''} \sum_{s,s',s''} A_{ijk}^{lmn} \sqrt{\frac{1}{\omega(\mathbf{q}s)\omega(\mathbf{q}'s')\omega(\mathbf{q}''s'')}} \times q_i \mathbf{e}_{\mathbf{q}s}^{l} q_j' \mathbf{e}_{\mathbf{q}'s'}^{m} q_k'' \mathbf{e}_{\mathbf{q}''s''}^{n} (a_{\mathbf{q}s}^{\dagger} - a_{-\mathbf{q}s})(a_{\mathbf{q}'s'}^{\dagger} - a_{-\mathbf{q}'s'}) \times (a_{\mathbf{q}''s''}^{\dagger} - a_{-\mathbf{q}''s''}) e^{i((\mathbf{q}+\mathbf{q}'+\mathbf{q}'').\mathbf{r})}. \tag{5.5}$$

It is now possible to solve the integration in Eqs. (5.4) and (5.5) using the Fourier theorem

$$\frac{1}{\mathcal{L}^D} \int d^D r e^{i([\mathbf{q}+\mathbf{q}'+\mathbf{q}''].\mathbf{r})} = \delta_{\mathbf{q}+\mathbf{q}'+\mathbf{q}'',\mathcal{G}} \tag{5.6}$$

where $\mathcal{G}$ is the reciprocal lattice vector for Umklapp processes and $\mathcal{G} = 0$ for Normal processes. D is the number of dimensions. For one dimensional systems $\mathcal{L}^1 = L_0$ and for three dimensional systems $\mathcal{L}^3 = V_0$. Using this identity, it is possible to rewrite Eq. (5.5) as

$$V_3 = \left(\frac{\hbar^3}{8L_0\rho'^3}\right)^{1/2} \sum_{\mathbf{q},\mathbf{q}',\mathbf{q}''} \sum_{s,s',s''} A_{ijk}^{lmn} \sqrt{\frac{1}{\omega(\mathbf{q}s)\omega(\mathbf{q}'s')\omega(\mathbf{q}''s'')}} \times q_i \mathbf{e}_{\mathbf{q}s}^{l} q_j' \mathbf{e}_{\mathbf{q}'s'}^{m} q_k'' \mathbf{e}_{\mathbf{q}''s''}^{n} (a_{\mathbf{q}s}^{\dagger} - a_{-\mathbf{q}s})(a_{\mathbf{q}'s'}^{\dagger} - a_{-\mathbf{q}'s'}) \times (a_{\mathbf{q}''s''}^{\dagger} - a_{-\mathbf{q}''s''}) \delta_{\mathbf{q}+\mathbf{q}'+\mathbf{q}'',\mathcal{G}}. \tag{5.7}$$

To simplify this expression further, one applies the following substitution to simplify A_{ijk}^{lmn}

$$A_{\mathbf{q},\mathbf{q}',\mathbf{q}''}^{s,s',s''} = \sum_{ijk} \sum_{lmn} \mathbf{e}_{\mathbf{q}s}^{l} v_i \mathbf{e}_{\mathbf{q}'s'}^{m} v_j' \mathbf{e}_{\mathbf{q}''s''}^{n} v_k'' A_{ijk}^{lmn} \tag{5.8}$$

where $\mathbf{v}$, $\mathbf{v}'$ and $\mathbf{v}''$ are the unit vectors along $\mathbf{q}$, $\mathbf{q}'$ and $\mathbf{q}''$ respectively.

Srivastava [131, 166, 167, 168], as described in the previous section, developed a good approximation for $A_{\mathbf{q},\mathbf{q}',\mathbf{q}''}^{s,s',s''}$ based upon the scheme originally developed by Hamilton and Parrot [162]. He suggested that for three-dimensional systems the expression would be

$$|A_{\mathbf{q},\mathbf{q}',\mathbf{q}''}^{s,s',s''}|^2 = \frac{40\rho^2(\gamma+1/2)^2}{3(a\omega_D)^2} \frac{\omega(\mathbf{q}s)^2\omega(\mathbf{q}'s')^2\omega(\mathbf{q}''s'')^2}{|\mathbf{q}|^2|\mathbf{q}'|^2|\mathbf{q}''|^2} \tag{5.9}$$

where a is the lattice constant, ω_D is the Debye frequency and γ is considered as a semi-adjustable mode-average Grüneisen's constant. For the calculations presented here, this value is set to 0.5, a value close to a recent choice for bulk diamond [172]. This expression is easily adapted for one-dimensional systems by substituting ρ' for ρ. Using Eqs. (5.9) and (5.7), one is finally able to perform a direct evaluation of Eq. (5.1), Fermi's Golden Rule.

In order to evaluate Eq. (5.1) it is necessary to consider the initial and final states of the system. For the initial state, one defines $|i>\equiv|n_{\mathbf{q}s}, n_{\mathbf{q}'s'}, n_{\mathbf{q}''s''}>$. There are two classes of three-phonon events which determine the final state of the system. These are *Class 1* and *Class 2*. Class 1 events are when two low energy phonons merge into a higher energy phonon. A Class 2 event is when a high energy phonon decays into two low energy phonons. Hence, for Class 1 events the final state is $|f>=|n_{\mathbf{q}s}-1, n_{\mathbf{q}'s'}-1, n_{\mathbf{q}''s''}+1>$ and for Class 2 events the final state is $|f>\equiv|n_{\mathbf{q}s}-1, n_{\mathbf{q}'s'}+1, n_{\mathbf{q}''s''}+1>$.

Class 1 and Class 2 events must obey momentum and energy conservation laws as expected and these are taken into account by the Kronecker delta and Dirac delta in Eqs. (5.7) and (5.1) respectively.

For energy conservation, one may state:

$$\omega(\mathbf{q}, s) + \epsilon\omega(\mathbf{q}', s') = \omega(\mathbf{q}'', s''), \tag{5.10}$$

where $\epsilon = 1$ for a Class 1 events and $\epsilon = -1$ for a Class 2 events. For momentum, the corresponding expression is

$$\mathbf{q} + \epsilon\mathbf{q}' = \mathbf{q}'' + \epsilon\mathbf{G} \tag{5.11}$$

where $\mathbf{G}$ is a finite reciprocal lattice vector for Umklapp processes and $\mathbf{G} = 0$ for Normal processes.

With these conditions considered, one can expand Eq. (5.1). For Class 1 events, Eq. (5.1) becomes

$$\begin{aligned} P^{\mathbf{q}''s''}_{\mathbf{q}s,\mathbf{q}'s'} &= \frac{2\pi}{\hbar^2}|<n_{\mathbf{q}s}-1, n_{\mathbf{q}'s'}-1, n_{\mathbf{q}''s''}+1|V_3|n_{\mathbf{q}s}, n_{\mathbf{q}'s'}, n_{\mathbf{q}''s''}>|^2\times \\ &\quad \delta(\omega(\mathbf{q}s)+\omega(\mathbf{q}'s')-\omega(\mathbf{q}''s'')). \end{aligned} \tag{5.12}$$

Likewise, for Class 2 events, Eq. (5.1) becomes

$$P_{\mathbf{q}s}^{\mathbf{q}'s',\mathbf{q}''s''} = \frac{2\pi}{\hbar^2}|<n_{\mathbf{q}s}-1,n_{\mathbf{q}'s'}+1,n_{\mathbf{q}''s''}+1|V_3|n_{\mathbf{q}s},n_{\mathbf{q}'s'},n_{\mathbf{q}''s''}>|^2\times \delta(\omega(\mathbf{q}s)-\omega(\mathbf{q}'s')-\omega(\mathbf{q}''s'')) \quad (5.13)$$

where $n_{\mathbf{q}s}$ is the non-equilibrium distribution function. Hence, substituting Eqs. (5.7) and (5.8) into Eq. (5.12) one obtains

$$P_{\mathbf{q}s,\mathbf{q}'s'}^{\mathbf{q}''s''} = \left(\frac{10\pi\hbar(\gamma+1/2)^2}{3(a\omega_D)^2L_0\rho'}\right) n_{\mathbf{q}s}n_{\mathbf{q}'s'}(n_{\mathbf{q}''s''}+1)\omega(\mathbf{q}s)\omega(\mathbf{q}'s')\omega(\mathbf{q}''s'')\times \delta(\omega(\mathbf{q}s)+\omega(\mathbf{q}'s')-\omega(\mathbf{q}''s''))\delta_{\mathbf{q}+\mathbf{q}'-\mathbf{q}'',\mathbf{G}}, \quad (5.14)$$

for Class 1 events. Similarly, Eq. (5.13) may be expanded to show

$$P_{\mathbf{q}s}^{\mathbf{q}'s',\mathbf{q}''s''} = \left(\frac{10\pi\hbar(\gamma+1/2)^2}{3(a\omega_D)^2L_0\rho'}\right) (n_{\mathbf{q}s}+1)n_{\mathbf{q}'s'}n_{\mathbf{q}''s''}\omega(\mathbf{q}s)\omega(\mathbf{q}'s')\omega(\mathbf{q}''s'')\times \delta(\omega(\mathbf{q}s)-\omega(\mathbf{q}'s')-\omega(\mathbf{q}''s''))\delta_{\mathbf{q}-\mathbf{q}'-\mathbf{q}'',\mathbf{G}}, \quad (5.15)$$

for Class 2 processes.

Having obtained the probabilities of transition, one now applies the linear Boltzmann equation which is described in Appendix D. Using the linear Boltzmann equation, one may apply the *single mode relaxation time* (*smrt*) approach to form an expression for the relation rate of a phonon mode $\mathbf{q}s$ as

$$\tau_{\mathbf{q}s}^{-1}(3ph,smrt) = \frac{1}{\bar{n}_{\mathbf{q}s}(\bar{n}_{\mathbf{q}s}+1)}\sum_{\mathbf{q}'s'}\sum_{\mathbf{q}''s''}(\bar{P}_{\mathbf{q}s,\mathbf{q}'s'}^{\mathbf{q}''s''}+\frac{1}{2}\bar{P}_{\mathbf{q}s,\mathbf{q}'s'}^{\mathbf{q}''s''}) \quad (5.16)$$

where $\bar{n}_{\mathbf{q}s}$ is the Bose-Einstein distribution for harmonic oscillators. Equation (5.16) is described in Appendix E. Substituting Eq. (5.14) and Eq. (5.15) into Eq. (5.16) reveals that the relaxation rate $\tau_{\mathbf{q}s}^{-1}$ may be expressed as

$$\tau_{\mathbf{q}s}^{-1}(3ph) = \left(\frac{10\pi\hbar(\gamma+1/2)^2}{3(a\omega_D)^2L_0\rho'}\right)\sum_{\mathbf{q}'s'}\sum_{\mathbf{q}''s''}\omega(\mathbf{q}s)\omega(\mathbf{q}'s')\omega(\mathbf{q}''s'')\times \left\{\frac{\bar{n}_{\mathbf{q}'s'}(\bar{n}_{\mathbf{q}''s''}+1)}{\bar{n}_{\mathbf{q}s}+1}\delta(\omega(\mathbf{q}s)+\omega(\mathbf{q}'s')-\omega(\mathbf{q}''s''))\delta_{\mathbf{q}+\mathbf{q}'-\mathbf{q}'',\mathbf{G}}+ \frac{1}{2}\frac{\bar{n}_{\mathbf{q}'s'}\bar{n}_{\mathbf{q}''s''}}{\bar{n}_{\mathbf{q}s}}\delta(\omega(\mathbf{q}s)-\omega(\mathbf{q}'s')-\omega(\mathbf{q}''s''))\delta_{\mathbf{q}-\mathbf{q}'-\mathbf{q}'',\mathbf{G}}\right\} \quad (5.17)$$

where the symbols have their usual meanings, and for bulk one replaces L_0 and ρ' with V_0 and ρ respectively.

5.3.2 Zone-centre optical modes

The first case of Eq. (5.17) which is considered is whether optical modes should be included in further considerations. In normal bulk materials the decay rate of the optical mode is very high and the lifetime of these modes is very small. This is due to these modes having high energies and low group velocities. This means that these modes generally contribute little to the thermal properties of a system. However, in nanostructures, this may not be the case as some of the optical modes, in particular, the ω_σ and ω_B modes, have low energies comparable to the acoustic modes. It is of great interest to compare the lifetime of these modes with their bulk counterparts. If these modes have a low decay rate, then it would indicate that such modes must be included in further considerations. To carry out a meaningful comparison, a three-dimensional approach is adopted here, to enable direct comparison with the lifetime of acoustic bulk modes. If one were to adopt a one-dimensional approach the lifetime of these low-lying optical modes would change substantially, and hence it would not be meaningful to compare these lifetimes with bulk acoustic modes.

For the comparative study presented here, it is the lifetimes of the zone-centre phonon modes, ω_σ and ω_B which are of primary interest. As these are zone-centre modes, one can immediately state $\mathbf{q} = 0$. As this is, in effect, a feasibility study, the Debye linear dispersion relations from Eq. (3.4) can be applied to the acoustic branches. The final assumption in these feasibility study is that only Normal decays of this phonon mode shall be calculated. The purpose of this is three-fold: (i) the relaxation rate of an optical mode should be dominated by the decay into acoustic modes; (ii) Normal processes allow a clear analytic expression to be developed; (iii) one avoids the necessity of defining a reciprocal lattice vector which cannot normally be defined for a continuum model. These assumptions change the form of Eq. (5.16) to

$$\tau_{\mathbf{q}s}^{-1} = \frac{1}{2\bar{n}[\bar{n}+1]} \sum_{\mathbf{q}',\mathbf{q}''} \sum_{s',s''} \bar{P}_{\mathbf{q}s}^{\mathbf{q}'s',\mathbf{q}''s''}, \tag{5.18}$$

and hence, Eq. (5.17) may be rewritten as

$$\tau_{\mathbf{q}s}^{-1} = \frac{\pi(\gamma+\frac{1}{2})^2\hbar}{2\rho\bar{c}^2V} \sum_{\mathbf{q}',\mathbf{q}''} \sum_{s',s''} \omega(\mathbf{q}s)\omega(\mathbf{q}'s')\omega(\mathbf{q}''s'') \frac{\bar{n}_{\mathbf{q}'s'}\bar{n}_{\mathbf{q}''s''}}{\bar{n}_{\mathbf{q}s}}$$

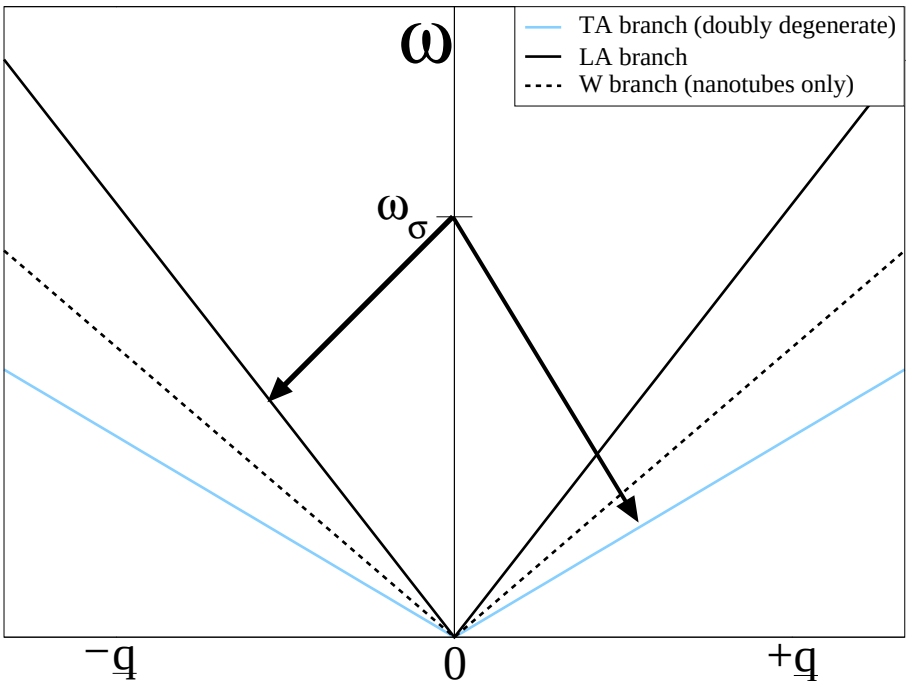

Figure 5.1: A schematic illustration of the decay of the low-lying zone-centre phonon mode ω_σ into two lower energy acoustic modes. The acoustic branches are modelled as linearly dispersive.

$$\delta_{\mathbf{q},\mathbf{q}'+\mathbf{q}''}\delta(\omega(\mathbf{q}s)-\omega(\mathbf{q}'s')-\omega(\mathbf{q}''s'')) \ , \qquad (5.19)$$

where $2\bar{c}^2$ is an approximation for $3(a\omega_D)^2/10$ and $\bar{c}$ is defined as $1/\bar{c}^3 = \sum_s 1/c_s$. This approximation agrees with the expression for the relaxation rate presented in [131] and enables a direct comparison with the bulk results for diamond presented in [172]. This expression can be reduced to an analytic expression using: (a) the linear Debye model for phonon dispersion relations (see Eq. (3.4)); (b) the $\mathbf{q} = 0$ condition; (c) changing the first summation over $\mathbf{q}'$ to an integration over $g(\omega')d\omega$ and (d) the energy and momentum conditions. By applying these, one may form an analytic expression of the form

$$\tau^{-1} = \frac{\gamma^2\hbar}{4\pi\rho\bar{c}^2}\sum_{s',s''} c_{s'}c_{s''}\frac{\omega^5}{[c_{s'}+c_{s''}]^5}\frac{\bar{n}'\bar{n}''}{\bar{n}}, \qquad (5.20)$$

where $c_{s'}$ and $c_{s''}$ are the speeds of the respective acoustic modes s' and s'' near the zone centre, and the equilibrium distribution functions $\bar{n}' = \bar{n}(\omega')$ and $\bar{n}'' = \bar{n}(\omega'')$ are defined with $\omega' = \omega c_{s'}/\{c_{s'}+c_{s''}\}$ and $\omega'' = \omega c_{s''}/\{c_{s'}+c_{s''}\}$.

In order to calculate the decay time, phonon dispersion relations and frequencies of such confined modes in the low energy range are required. These were obtained by

using the results presented in Chapter 3. In particular, for silicon nanowires, results from section 3.3.3.1 obtained using the adiabatic bond charge model were used and, for carbon nanotubes, the results presented in section 3.4 using an elastic continuum model were applied. It is important to note that the embedding technique which was used for the nanowire results in the loss of the fourth (rotational) acoustic mode. As the lowest non-zero confined mode (ω_σ) in both nanostructures, as well as the breathing mode ($\omega_{\rm B}$) in the nanotubes, is characterised by quite low energies, such modes can be expected to decay into two acoustic modes in the linear part of the dispersion curves, governed by the energy conservation $\omega_{\sigma/B} = \omega' + \omega''$ and the momentum conservation condition $\mathbf{q} = 0 = \mathbf{q}' + \mathbf{q}''$, as *schematically* presented in Fig. 5.1. The acoustic phonon speeds $c_{s'}$ and $c_{s''}$ were calculated from the linear regime of the dispersion curves. The material density ρ is set as 2329 kg/m^3 for silicon nanowires and 2020 kg/m^3 for carbon nanotubes. The value of Grüneisen's constant γ was set to 0.5 for both materials as its value is known to lie between 0.5 and 1.0 [131, 172] for most materials. The results of these calculations are presented in section 5.4.1.

5.3.3 Phonon-phonon interactions in Carbon Nanotubes

For carbon nanotubes, one wishes to evaluate Eq. (5.17) for a one-dimensional system. To do this, one replaces the summation over $\mathbf{q}'$ using Eq. (3.36) and hence also replace $\omega'(\mathbf{q}', s')$ and $\omega(\mathbf{q}'', s'')$ with $\omega'(s')$ and $\omega''(s'')$ respectively. Hence, due to the Dirac delta function the integration may be performed and the final expression for the lifetime of phonon mode $\omega(K_z, s)$ due to three phonon scattering in one dimension may be obtained. It has the form of

$$\begin{aligned}\tau^{-1}_{k_z,m,s}(3ph) &= \frac{10\pi\hbar(\gamma+1/2)^2}{3(a_{c-c}\omega_D)^2 L_0\rho'}\sum_{\mathbf{q}''s''}\omega(\mathbf{q}s)\omega(\mathbf{q}''s'')[\omega(\mathbf{q}''s'')-\omega(\mathbf{q}s)] \\ &\quad\times\Big\{\frac{\bar{n}'_{\epsilon=+1}[\bar{n}''+1]}{[\bar{n}+1]}g([\omega(\mathbf{q}'',s'')-\omega(\mathbf{q},s)],s')\delta_{K_z+K'_z-K''_z+G,0}\delta_{m+m'-m'',0} \\ &\quad-\frac{1}{2}\frac{\bar{n}'_{\epsilon=-1}\bar{n}''}{\bar{n}}g([\omega(\mathbf{q},s)-\omega(\mathbf{q}'',s'')],s')\delta_{K_z-K'_z-K''_z+G,0}\delta_{m-m'-m'',0}\Big\},\end{aligned} \tag{5.21}$$

Table 5.1: Phonon polarisation combinations allowed by the conservation of azimuthal quantum number for three-phonon processes in single wall nanotubes.

LA + (LA/WA/B)	$\leftrightarrow$	(LA/WA/B)
LA + (TA/σ)	$\leftrightarrow$	(TA/σ)
WA + (LA/WA/B)	$\leftrightarrow$	(LA/WA/B)
WA + (TA/σ)	$\leftrightarrow$	(TA/σ)
TA + (LA/WA/B)	$\leftrightarrow$	(TA/σ)
TA + (TA/σ)	$\leftrightarrow$	(LA/WA/B)
σ + (LA/WA/B)	$\leftrightarrow$	(TA/σ)
σ + (TA/σ)	$\leftrightarrow$	(LA/WA/B)
B + (LA/WA/B)	$\leftrightarrow$	(LA/WA/B)
B + (TA/σ)	$\leftrightarrow$	(TA/σ)

where $\bar{n} = 1/(e^{\hbar\omega(s)/k_BT}-1)$, $\bar{n}'' = 1/(e^{\hbar\omega''(s'')/k_BT}-1)$ and $\bar{n}'_\epsilon = 1/(e^{\epsilon\hbar(\omega''(s'')-\omega(s)/k_BT}-1)$, with k_B as the Boltzmann constant, T as the temperature. The wave-vector for the one-dimensional approach has now been expanded in terms of its two components; K_z, its wave-vector component along the $z-$axis, which corresponds to the direction of propagation of the nanotube, and m, the azimuthal quantum number. Hence, K'_z is a function of $\omega(K_z, s)$ and $\omega(K''_z, s'')$ and the integers m, m' and m'' are the azimuthal numbers of their respective phonon modes within a cylindrical coordinate system (see section 3.4 in Chapter 3 for further details). Here, $\epsilon = +1(-1)$ for Class 1 (Class 2) processes as described earlier, G is a reciprocal lattice vector along the tube axis and $g(\omega, s)$ is density of states for polarisation s and frequency ω. Also, a_{c-c} is the carbon-carbon bond length, ω_D is the Debye frequency, ρ' is the mass density per unit length, L_0 is the length of the tube, and γ is considered as a semi-adjustable mode-average Grüneisen's constant which, as in the previous section, is set to 0.5. Three-phonon processes, subject to azimuthal momentum conservation conditions only, are listed in Table 5.1. In this table the interaction with the two lowest optical branches, which correspond to the breathing mode and the σ mode are included as possibilities.

In order to calculate the lifetime of phonon modes undergoing three-phonon scat-

tering using Eq. (5.21), one requires knowledge of both the dispersion curves and the density of states of a given one-dimensional system. For the carbon nanotube, analytic expressions for the phonon dispersion relations and density of states for the six considered modes were taken from the approach presented in section 3.4 of Chapter 3. From this approach, the dispersion relations of the longitudinal mode (LA), twist mode (WA), doubly degenerate transverse mode (TA), breathing mode (B) and the lowest non-zero mode (σ) may be obtained. These dispersion curves are reproduced here to enable easy comparison and are plotted in Fig. 5.2.

With these relations obtained, it is important for lifetime calculations that one can ascertain the upper and lower limits for the allowed phonon frequencies for each branch. The maximum upper limit, ω_D (denoted the Debye frequency here) is determined from the normalisation condition that the total number of vibrational modes is $6N_C$, with N_C being the total number of unit cells in the carbon nanotube of length L_0 and 6 being the number of phonon branches. With all values obtained, one now considers calculating the lifetime of phonon modes using Eq. (5.21). This was achieved using a computational algorithm which finds the numerical solutions to Eq. (5.21) via the bisection technique. These results are presented in section 5.4.3.

5.3.4 Analytic model for relaxation rate in carbon nanotubes

For a *qualitative* analytic expression, it is necessary that one applies the linear Debye model to carbon nanotubes. As this is a simplistic model, for explaining trends and features of the relaxation rate of phonon modes undergoing three-phonon interactions, the effect of the optical modes shall be discarded immediately as their consideration should not change the form of the expressions derived. Thus, this leaves the acoustic branches TA, LA, and WA of the form $\omega(K_z) = c_s K_z$ where c_s is the group velocity of mode s. To simplify this model further let $m = 0$ for all modes. Using this relation, from Eq. (3.36) one obtains the density of states for each of these modes as:

$$g(\omega, s) = \frac{L_0}{\pi c_s}. \tag{5.22}$$

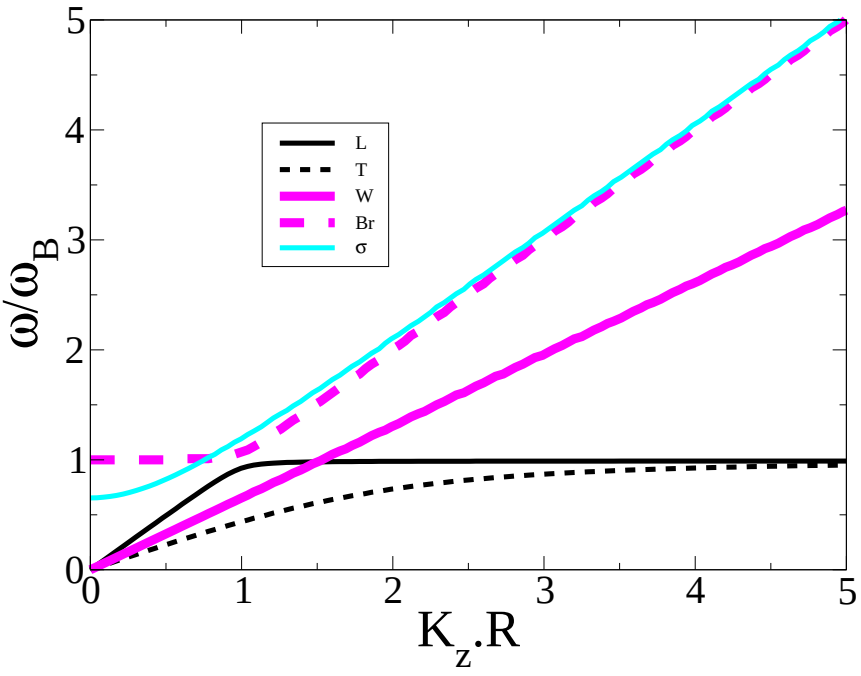

Figure 5.2: The phonon dispersion curves of the six lowest branches for a carbon nanotube of radius R. ω_B is the frequency of the breathing mode at the zone centre. Here the letter corresponds to the phonon branch: L = Longitudinal, T= (doubly degenerate) Transverse, W= Twist, Br = Breathing and σ= σ (the lowest non-zero mode).

Table 5.2: The allowed combinations of phonon polarisation branches within the simple analytic model.

Phonon branch with velocity c_{s_1}		Phonon branches with velocities c_{s_2} and c_{s_3}
LA	$\leftrightarrow$	WA + TA
LA	$\leftrightarrow$	TA + WA
WA	$\leftrightarrow$	LA + TA
WA	$\leftrightarrow$	TA + LA
TA	$\leftrightarrow$	LA + WA
TA	$\leftrightarrow$	WA + LA

The group velocities of these modes were obtained using the same method as outlined in section 5.3.2. Using these dispersion relations, an analytic evaluation of Eq. (5.21) is now possible using the conditions $c_s \neq c_{s'} \neq c_{s''}$ [170] and $k \geq 0$, $k' \geq 0$, and $k'' \geq 0$. These conditions allow only the processes shown in Table 5.2 and were introduced for three reasons: (i) Lax *et al.* show that interactions within the same phonon branch are not expected for the majority of the Brillouin zone for most real systems. (ii) This technique is to provide simple qualitative analytic expression for demonstration of the fundamental physics in simplified form. An analytic expression is possible without the condition that all wave-vectors are positive, but it is without elegance and lacks the clarity that the later derived equation possesses whilst not revealing any substantially new features or interesting details. (iii) A more comprehensive method is presented with the quantitative calculation in the previous section, but does not yield analytic expressions. With these considerations, one may evaluate Eq. (5.21) using the Debye dispersion relations.

Applying these considerations and the energy and momenta considerations one finds the following relations

$$\begin{aligned} \epsilon\omega'(s') &= \omega''(s'') - \omega(s) \\ \omega''(s'') &= \frac{c_{s'}}{c_{s'} - c_{s''}}(\omega\frac{c_{s'}}{c_s} - \omega - \epsilon G c_{s'}), \end{aligned} \tag{5.23}$$

where $\epsilon = +1(-1)$ for Class 1 (Class 2) events.

Using these relations and Eq. (5.21) the relaxation rate of a phonon mode in a carbon nanotube may be written as

$$\begin{aligned} \tau_{\omega s}^{-1}(3ph) &= \left(\frac{10\hbar(\gamma+1/2)^2}{3(a\omega_D)^2\rho'}\right) \\ &\sum_{s's''}\Big\{\frac{c_{s''}\omega}{(c_{s'}-c_{s''})^2}\left(\omega\frac{c_{s''}}{c_s} - \omega - Gc_{s''}\right)\left(\omega\frac{c_{s'}}{c_s} - \omega - Gc_{s'}\right) \\ &\times\left(\frac{\bar{n}'_1[\bar{n}''+1]}{[\bar{n}+1]} + \frac{\bar{n}'_{-1}\bar{n}''}{2\bar{n}}\right)\Big\}, \end{aligned} \tag{5.24}$$

where $\bar{n}'_{\pm 1}$ and $\bar{n}''$ are defined as:

$$\bar{n}'_\epsilon = 1/[\exp\Big\{\frac{\hbar}{K_b T}\frac{\epsilon c_{s'}}{c_{s'}-c_{s''}}\left(\omega\frac{c_{s''}}{c_s} - \omega - Gc_{s''}\right)\Big\} - 1],$$

$$\bar{n}'' = 1/[\exp\Big\{\frac{\hbar}{K_b T}\frac{c_{s''}}{c_{s'}-c_{s''}}\left(\omega\frac{c_{s'}}{c_s}-\omega-Gc_{s'}\right)\Big\}-1]. \tag{5.25}$$

These expressions can be simplified further by taking the high and low temperature approximations for $\bar{n}$.

In the high temperature limit, $\bar{n} \approx \alpha T/\omega$ where α is a constant. Thus Eq. (5.24) may be rewritten as

$$\tau^{-1}_{\omega s,HT}(3ph) \propto (A_1 + A_2\omega + A_3\omega^2)T. \tag{5.26}$$

Similarly, in the low temperature limit, $\bar{n} \approx \exp(-\beta\omega/T)$ where β is a constant. Also, in the low temperature limit, it is known from bulk results [172] that Normal processes dominate so G can be neglected. Hence Eq. (5.24) becomes

$$\tau^{-1}_{\omega s,LT}(3ph) \propto \omega^3 \exp(-\beta\omega/T). \tag{5.27}$$

This result compares favourably with Herring [156] who showed for three-dimensional systems that $\tau^{-1}_{\omega s,LT}(3ph) \propto \omega^{5-n}T^n \exp(-\hbar\omega/k_B T)$. The above expression may be re-expressed as $\tau^{-1}_{\omega s,LT}(3ph) \propto \omega^{3-n}T^n \exp(-\beta\omega/T)$ where $n = 0$. The reduction in maximum value of n is a direct consequence of dimensionality. These expressions are used to aid in understanding the results presented in the following sections.

5.4 Results

5.4.1 Lifetime of zone-centre optical modes in carbon nanotubes

For the feasibility study presented in section 5.3.2 calculations were performed for armchair (n, n) carbon nanotubes, with n ranging from 5 to 20. The nanotube radius r is related, for an (n, n) tube, to n by $r = 3a_{c-c}n$ where $a_{c-c} = 0.144$ nm according to Eq. (1.5). It was assumed that the confined modes ω_σ and ω_{B} can decay into the four acoustic modes (the longitudinal L, doubly degenerate transverse T and twist W). The frequencies of the confined modes (ω_σ) and (ω_{B}), and the speeds of the four acoustic modes were taken from the dispersion relations presented in Chapter

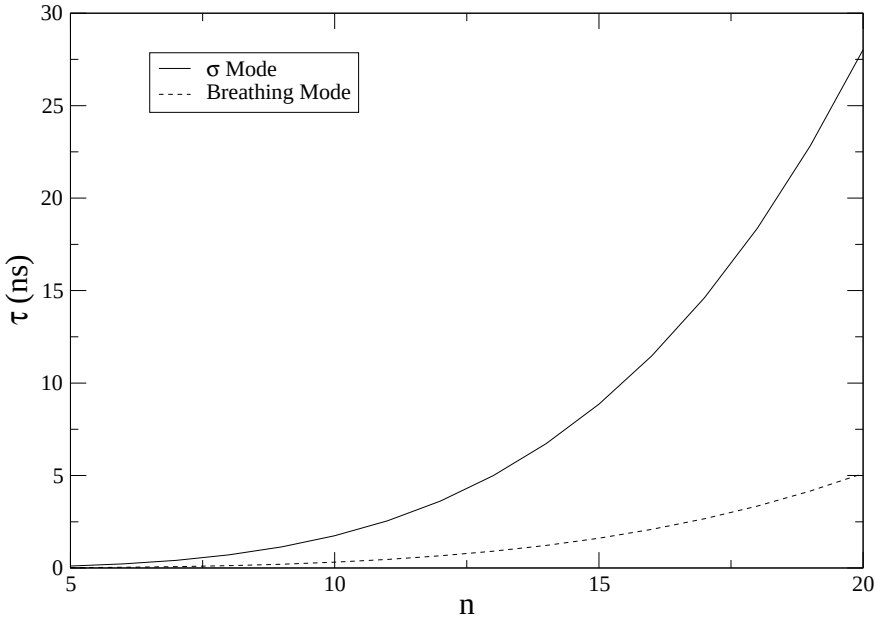

Figure 5.3: The variation of the lifetime of the lowest non-zero zone-centre confined mode and the breathing mode in (n, n) carbon nanotubes at 300 K.

3. The acoustic speeds for all n values are: $c_L = 21.6$ km/s, $c_T = 10.0$ km/s, $c_W = 14.5$ km/s. For the (10,10) nanotube $\omega_\sigma/(2\pi) = 3.43$ THz and $\omega_{\rm B}/(2\pi) = 5.25$ THz. For other sizes of the nanotubes both ω_σ and $\omega_{\rm B}$ scale as $1/n$. From Fig. 5.3 one observes a steady increase in the lifetime of both modes with an increase in the nanotube radius. The rate of increase for the lifetime of the mode ω_σ is greater than that of $\omega_{\rm B}$. This is because Eq. (5.20) shows that the lifetime is inversely proportional to the fifth power of the angular frequency of the confined mode, and the angular frequency $\omega_{\rm B}$ is much larger than ω_σ. Figure 5.4 shows the temperature dependence of the lifetime of the two modes for the (10,10) nanotube. Consistent with Eq. (5.20), the lifetime decreases with increase in temperature.

One observes from Fig. 5.4 that the relaxation rate (τ^{-1}) of these modes increases linearly with temperature in the entire presented range which is what would be expected for the high temperature behaviour of a phonon mode (see Eq. (5.27)). This is due to the very low frequencies of these modes, making $\hbar\omega/kT$ much smaller than unity for all the temperatures considered. This can be contrasted with the intrinsic lifetime of the zone-centre optical modes in bulk diamond, which due to their high frequency shows a linear variation only above the Debye temperature ($\sim$2000 K) [172].

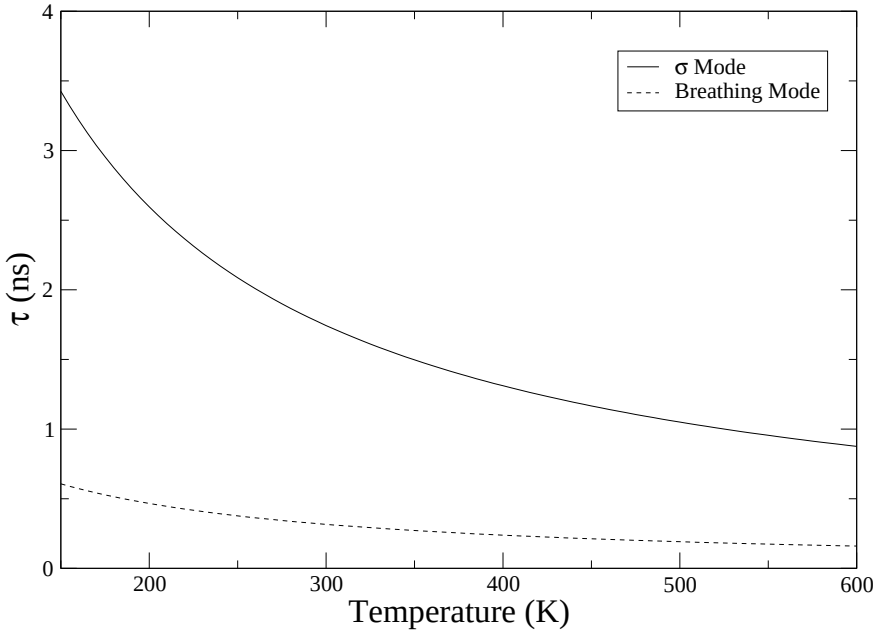

Figure 5.4: The lifetime of the lowest non-zero zone-centre confined mode and the breathing mode as a function of temperature for a (10,10) carbon nanotube.

While the trend in the variation of the lifetime of the two modes is correctly described by Figs. 5.3 and 5.4, the numerical results of the lifetimes are subject to the choice of the acoustic speeds and the frequencies of the modes. If instead of taking the speeds from the model described in section 3.4 in Chapter 3 one uses the values obtained from the classical elasticity theory used by Saito *et al.* [13] based upon Young's modulus and density of graphene, the calculated lifetime for the (10,10) nanotube is lowered by 22%. As Young's modulus of graphene is less than Young's modulus of the nanotube [173], the speeds obtained from Saito's model should be taken as limiting values, thus providing a minimum estimate for the lifetime.

It is interesting to compare the lifetimes of the ω_{B} mode in the nanotube and the lowest zone-centre longitudinal optical mode in graphite, both of which have comparable energies. An extension of the present calculations in the temperature range shown in Fig. 5.4 suggests a lifetime of the order of nanoseconds for the longitudinal optical mode in graphite. This contrasts with the lifetime of hundreds of picoseconds for the breathing mode in the (10,10) nanotube. This difference occurs mainly because of the presence of the twist mode which provides an additional channel for the decay of the breathing mode. However, the general trend shown by these results

Table 5.3: The frequencies of the lowest non-zero zone-centre confined mode and the acoustic speeds of the longitudinal and doubly transverse modes for a silicon nanowire of thickness d.

d (nm)	c_L (km/s)	c_T (km/s)	$\omega_\sigma/2\pi$ (THz)
0.543	24.43	20.27	4.737
1.086	11.86	8.50	3.199
1.629	10.69	7.58	2.628
2.172	9.88	6.67	2.126
2.715	9.10	6.50	1.782
3.258	8.91	6.18	1.520
3.801	8.71	6.11	1.344

---

is that these low lying optical modes in carbon nanotubes have lifetimes comparable with those of acoustic modes in bulk materials.

5.4.2 Lifetime of zone-centre optical modes in silicon nanowires

Calculations were made for square thin silicon nanowires whose cross section area varied in size from 0.543 nm × 0.543 nm to 3.801 nm × 3.801 nm. The frequency $\omega_\sigma/2\pi$ and the speeds of the acoustic modes (longitudinal and doubly transverse) obtained from Chapter 3 are given in Table 5.3. Except for the ultrathin wire (thickness 0.543 nm), the lifetime of the ω_σ mode increases with wire thickness, as shown in Fig. 5.5. By comparison, the lifetime of the ω_σ mode in the nanowire changes much more slowly with width than either of the two optical modes in the carbon nanotube. The calculations show that, at room temperature for the nanowire with thickness of 2.7 nm, the lifetime of the ω_σ mode is comparable to the lifetime

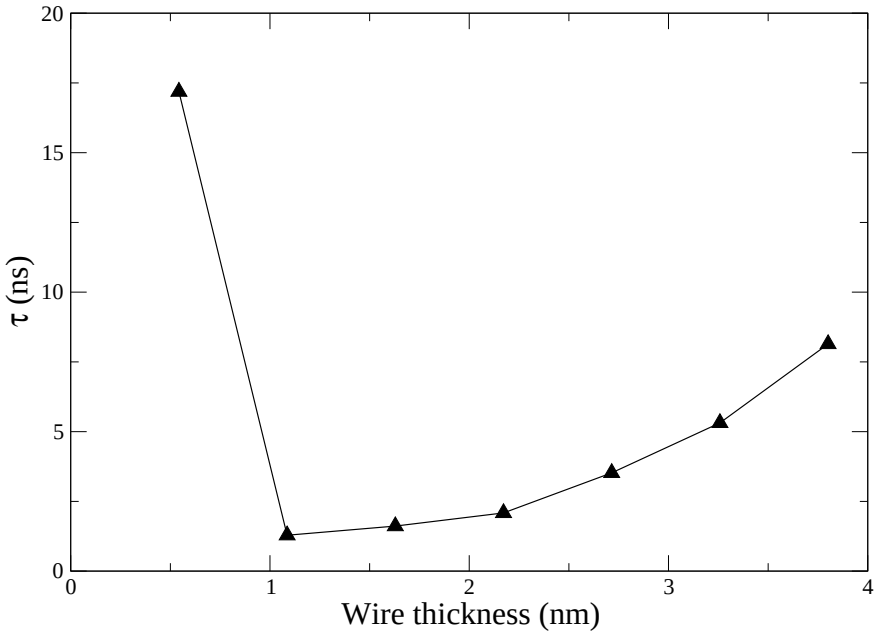

Figure 5.5: The variation of the lifetime of the lowest non-zero zone-centre confined mode with the thickness of the wire at 300 K. Symbols represent the numerical data and the line provides a guide for the variation of results.

of the breathing mode ω_{B} in the nanotube of similar diameter. In contrast, for the thickness 1.6 nm, the lifetime of the ω_σ mode is comparable for both the nanowire and the nanotube. The lifetime of the ω_σ mode in the nanotube becomes increasingly larger than in the nanowire for thicknesses larger than 1.6 nm. Figure 5.6 shows, the lifetime of this mode for nanowires varies linearly with temperature, which is similar to the nanotubes.

The ultrathin nanowire, with thickness 0.543 nm, is a special case and should be regarded as a new class of material as described in Chapter 3. As seen in Table 5.3, there is a sharp rise in the frequency $\omega_\sigma/2\pi$ due to increased confinement effect. Also, there is a sharper rise in the speeds of acoustic-like branches. These effects result in a dramatic increase in the lifetime of this mode; an order of magnitude larger than the trend extrapolated from the wires of other thicknesses considered here.

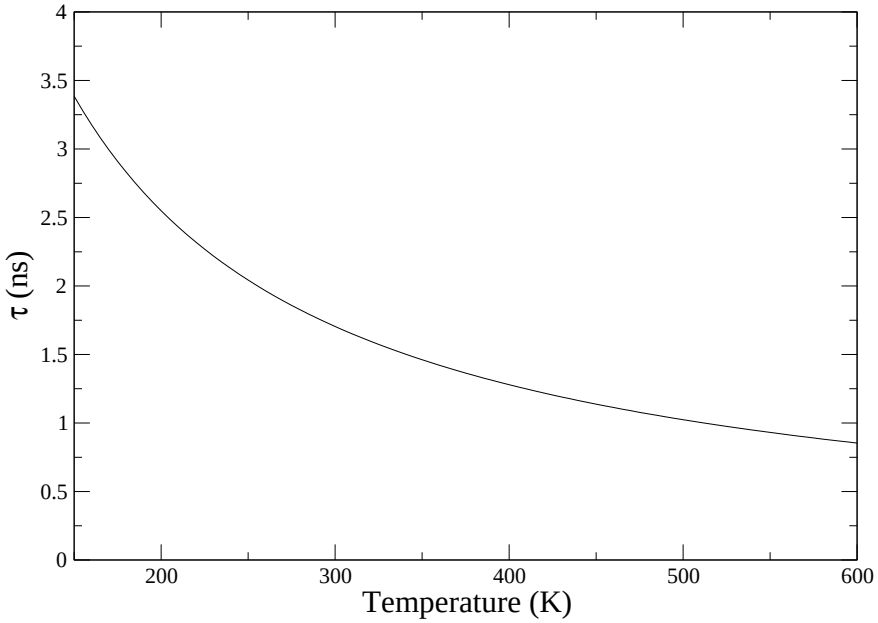

Figure 5.6: The lifetime of the lowest non-zero zone-centre confined mode as a function of temperature for a nanowire of thickness 2.172 nm.

5.4.2.1 Summary of relaxation rate of zone-centre optical modes

Lifetimes of low-lying confined phonon modes in carbon nanotubes and silicon nanowires have been estimated theoretically using a three-dimensional approach. It is found that these modes are very long-lived, with lifetimes of the order of nanoseconds and are comparable with bulk acoustic modes. These lifetimes are found to increase with size but decrease linearly with temperature above 150 K. An exception to the trend is the ultrathin silicon nanowire of thickness 0.543 nm, which shows a increase in the lifetime of the lowest confined mode, which is an order of magnitude larger than that expected from extrapolation of the results for other thicknesses. From these results one concludes that in the following analysis of the relaxation rate of phonon modes in carbon nanotubes, the two low lying optical modes, ω_B and ω_σ and their corresponding frequency branches must be considered. Also, these results show that for any calculation of the relaxation rate of silicon nanowires, these modes must be included.

5.4.3 The (10,10) Nanotube at Room Temperature

5.4.3.1 Frequency variation

The phonon dispersion curves for the (10,10) tube, based upon the continuum theory, are shown in Fig. 5.2. Figure 5.7 (a) displays the total lifetime of different phonon modes undergoing three-phonon processes for the (10,10) nanotube at 300 K as a function of frequency. In the low frequency regime (at least up to 0.5 ω_B) the relaxation rate (τ^{-1}) for each of the longitudinal, transverse, and twist (LA, TA, and WA) modes varies with frequency as ω^2. The relaxation rates of the longitudinal and transverse modes cut off beyond the frequency ω_B. Inclusion of the the two optical modes (σ and B) introduces fine structure not previously reported in the variation of the relaxation rate of the transverse mode. The first peak is due to the presence of the breathing and σ phonon branches. The relaxation rate of the σ mode starts to become effective beyond the frequency $\omega_B\sqrt{(1-\sigma_P)/2}$. The relaxation rate of this mode varies as ω^2 between this frequency and ω_B, beyond which there is a sudden increase due to interactions with the breathing mode. The relaxation rate of the breathing mode starts to be effective beyond the frequency ω_B and follows a ω^2 dependence. The ω^2 dependence of these modes is in agreement with Eq. (5.26) showing that the high temperature behaviour of these modes can approximated and explained very effectively with this simple expression. Also, the cut off points in the relaxation rate of these modes are direct results of the phonon dispersion curves of the corresponding modes. For example, above the frequency ω_B there are no valid frequencies for real K_z values for the longitudinal and transverse modes.

Figure 5.7 (b) displays the results of considering only Umklapp processes involving only the four acoustic branches (LA, doubly degenerate TA, and WA). This enables a comparison of these results (based upon the method presented in section 5.3) with those of Xiao *et al.* [171, 174]. The results indicate that the relaxation rate of the acoustic modes is much greater than those presented by Xiao *et al.* The author is unable to understand this difference except to speculate that their anharmonic potential is much weaker than that applied here and does not include one-dimensional effects which are vital. However, the results of the previous section and a com-

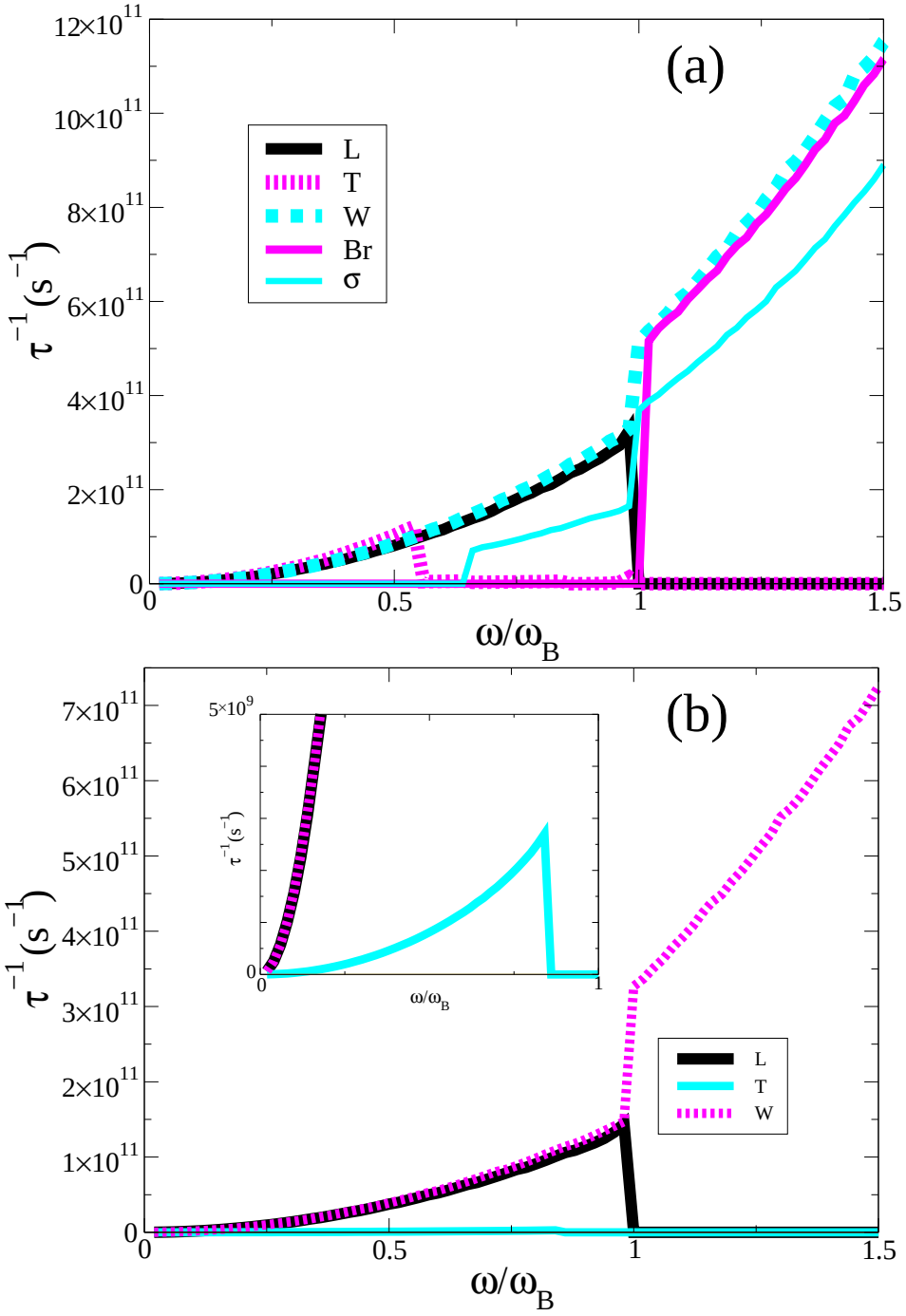

Figure 5.7: The inverse relaxation time of different phonon modes as a function of frequency ω for a (10,10) carbon nanotube at 300 K for: (a) σ and B modes with Normal processes included; (b) LA, TA and WA modes only undergoing Umklapp processes. ω_B is the frequency of the breathing mode at the zone centre. Here the letter corresponds to the mode (LA= Longitudinal, TA= (doubly degenerate) Transverse, WA= Twist, B= Breathing and σ= σ (the lowest non-zero mode)).

parison of the relaxation rates with bulk diamond [172] (which has a comparable thermal conductivity) shows good agreement and indicates that these results for the nanotube are more acceptable and correct. The general form of the frequency dependency in the low frequency region is in good agreement with Xiao *et al.* The difference between the results presented in Figs. 5.7 (a) and (b) is due to the inclusion of two factors: (i) the breathing and σ modes, and (ii) Normal processes. However, the main difference between Figs. 5.7 (a) and (b) arises due to the inclusion of the two optical modes, which has resulted in almost doubling of the total relaxation rate of the longitudinal and twist modes. The second point is less important because the contribution from Normal processes at room temperature is much smaller.

Figure 5.8 shows a comparison between the quantitative expression in Eq. (5.21) and the analytic expression from Eq. (5.24). Figure 5.8 (b) shows that the relaxation rates of both the LA and the WA modes vary with frequency as $\tau^{-1} \propto \omega^2$ for the range shown. This is as expected from Eq. (5.26). The TA mode also varies with frequency as $\tau^{-1} \propto \omega^2$ in the low frequency regime indicating that the A_1 and $A_2\omega T$ terms in Eq. (5.26) are negligible. However, the TA mode diverges from the ω^2 behaviour for the frequency $\omega = 0.5\omega_B$ and greater. For frequencies greater than this, the variation of the relaxation rate with frequency can be described as $\tau^{-1} \propto \omega^3 \exp(-A\omega)$ where A is an arbitrary constant. This is similar to Eq. (5.27).

5.4.3.2 Relative contributions from different processes

The room temperature relaxation rate of various phonon modes as a function of k, is shown in Figs. 5.9 and 5.10 for Normal and Umklapp processes, respectively. k is a dimensionless quantity related to the wave number K_z and tube radius R by $k = K_z R$. For low values of k (up to approximately $k = 2.8$) the total Umklapp contribution (Class 1 and Class 2) to the relaxation rate is larger than the total Normal contribution in general. For large values of k (typically $k > 6$), the Normal contribution is either comparable to the Umklapp contribution or dominates.

Here a discussion of relative importance of Class 1 and Class 2 events for Normal processes is presented. Closer examination of Fig. 5.9 reveals that the relaxation

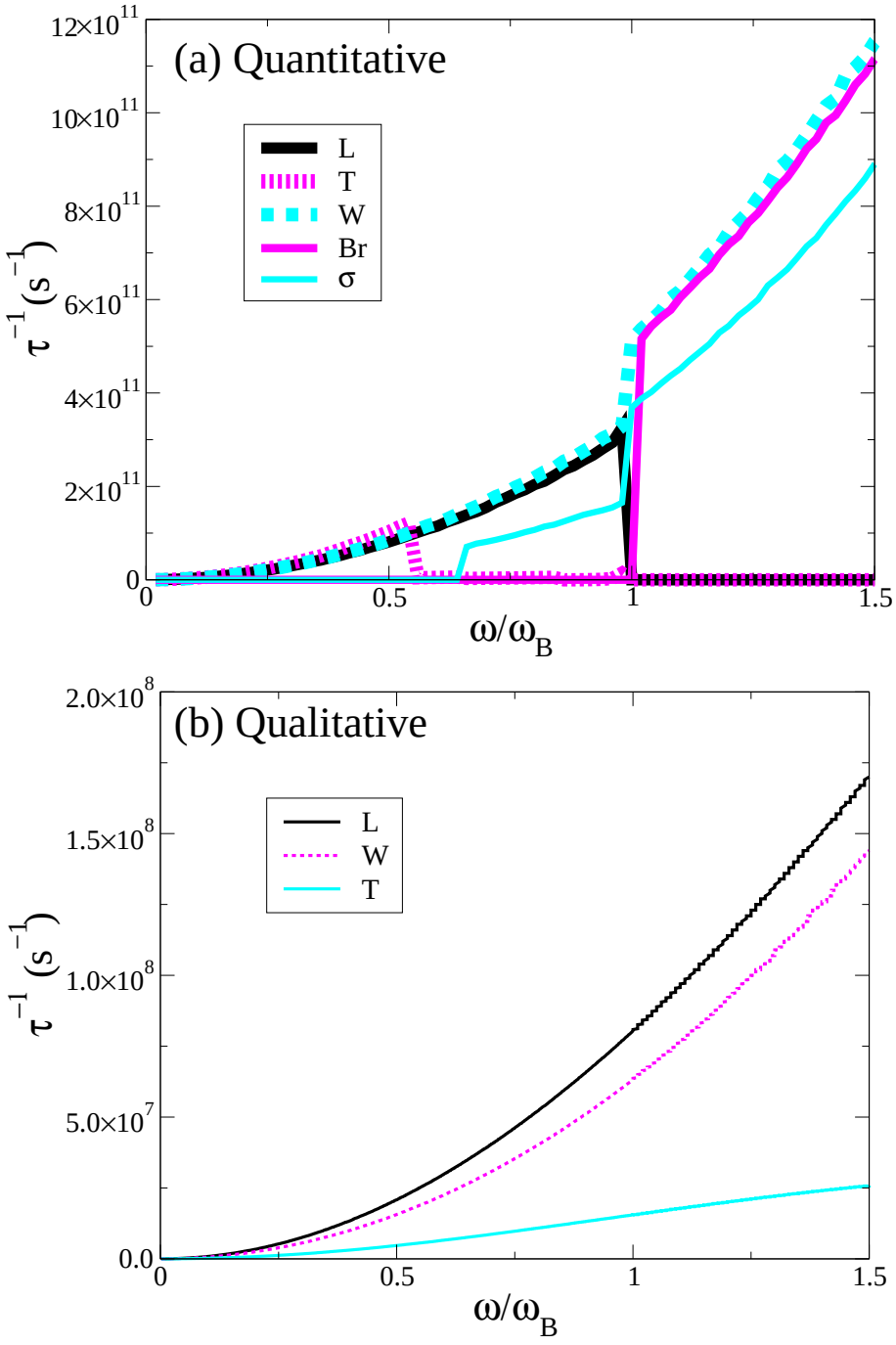

Figure 5.8: The inverse relaxation time of different modes across the Brillouin zone as a function of frequency ω for the (10,10) carbon nanotube at 300 K: (a) for the acoustic modes with σ and B modes and Normal Processes included, calculated using the quantitative method; (b) the acoustic modes (LA, TA and WA) calculated using the qualitative technique.

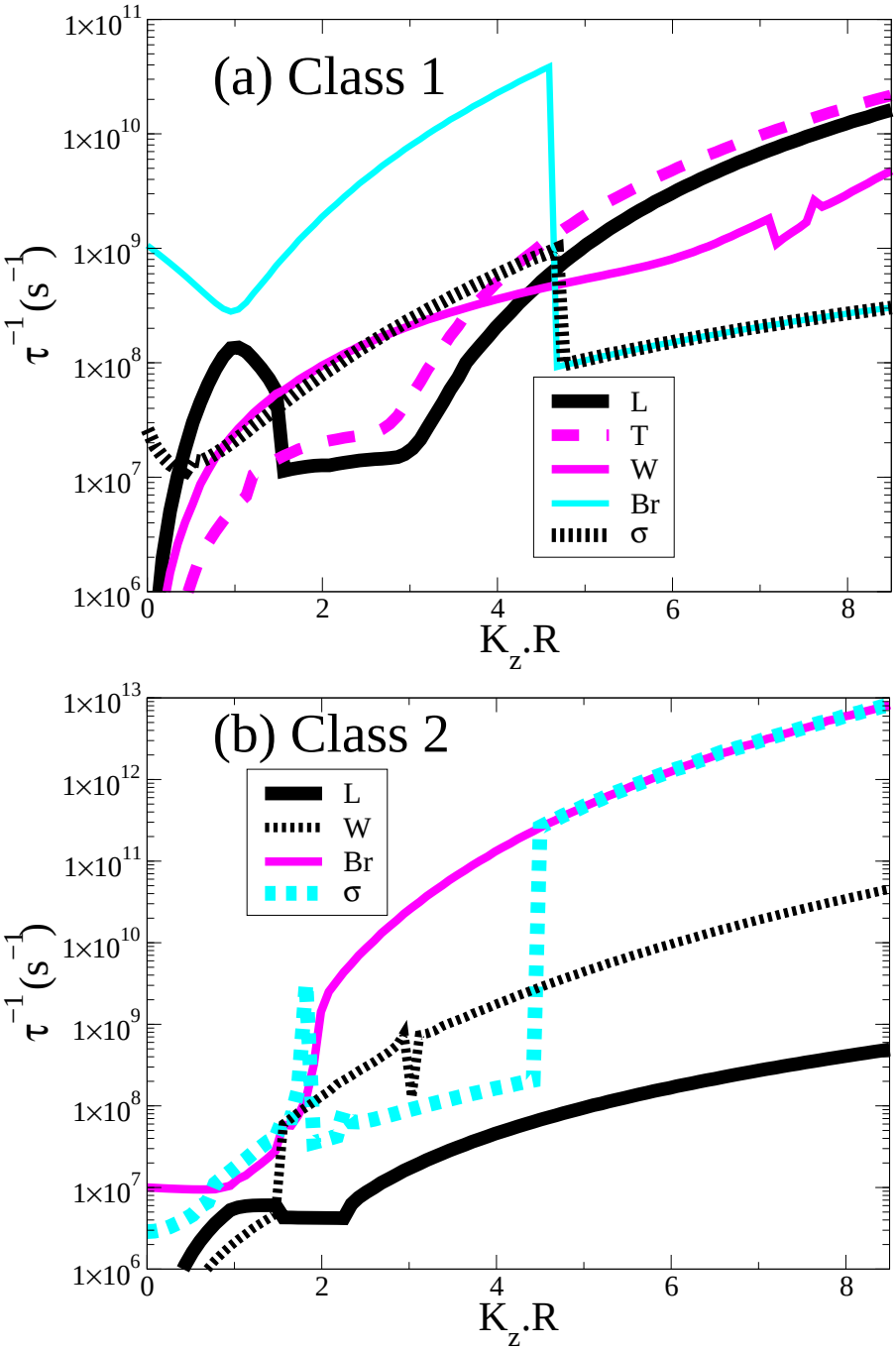

Figure 5.9: The relaxation rate of different modes undergoing Normal processes as a function of $K_z.R$ for a (10,10) carbon nanotube at 300 K. (LA= Longitudinal, TA= (doubly degenerate) Transverse, WA= Twist, B= Breathing and σ= σ (the lowest non-zero mode)).

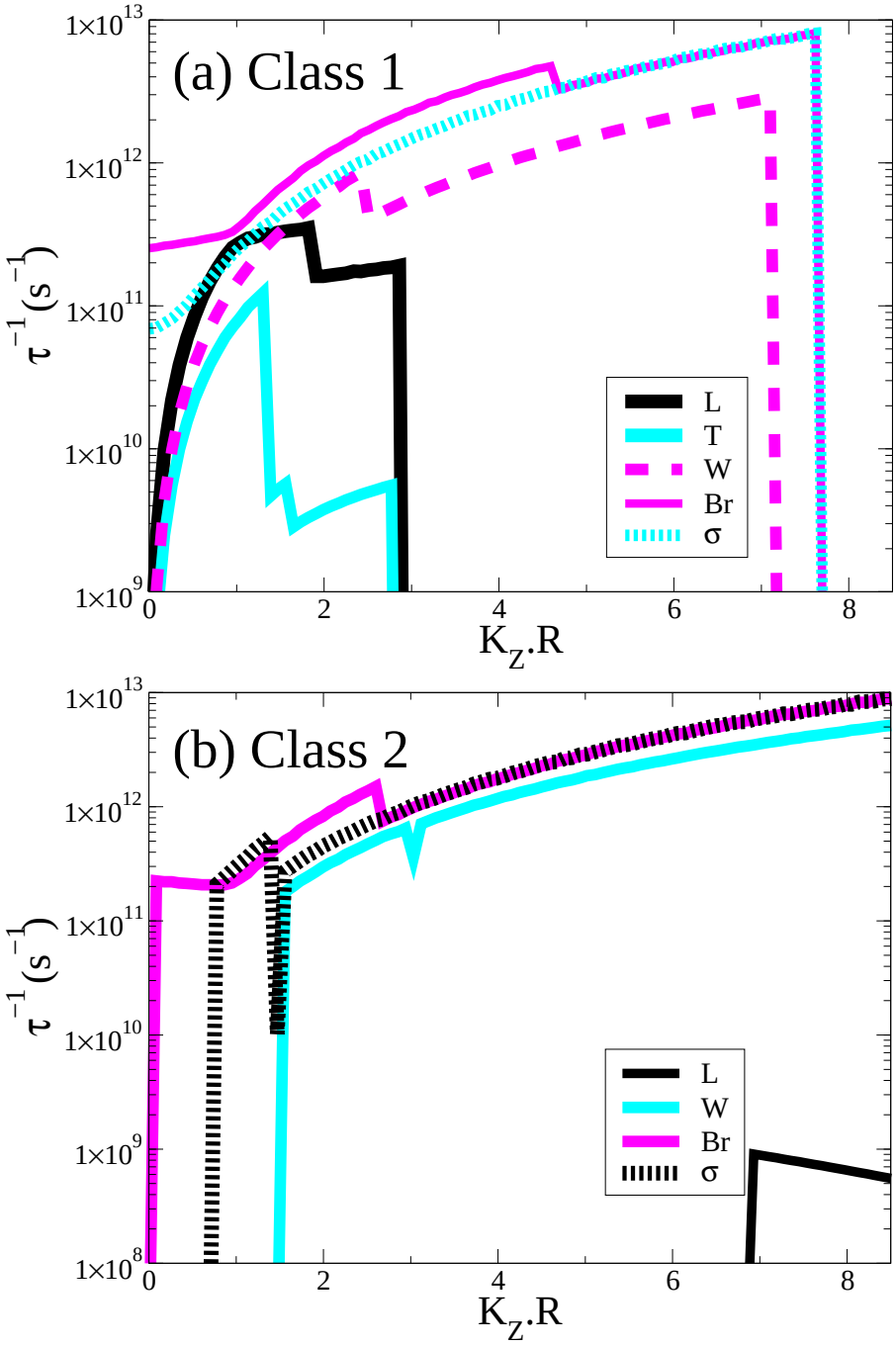

Figure 5.10: The relaxation rate of different modes undergoing Umklapp processes as a function of $K_z.R$ for a (10,10) carbon nanotube at 300 K. (LA= Longitudinal, TA= (doubly degenerate) Transverse, WA= Twist, B= Breathing and σ= σ (the lowest non-zero mode)).

rates of the acoustic modes LA and TA are dominated by Class 1 events. As expected, there is no contribution towards the Normal relaxation rate for transverse mode from Class 2 events. The peak near $k = 1$ for the longitudinal mode undergoing Class 1 events is due to its interaction with other acoustic modes and the flattening of the LA mode at $k = 1$. The rate of the fourth acoustic mode, WA, is mainly dominated by Class 1 events near the zone centre, but is contributed approximately equally by the two Classes of events beyond a critical point ($k = 1.6$). For the breathing mode, Class 1 events dominate near the zone centre and Class 2 events dominate for the rest of the zone. This is expected, as similar behaviour is observed in calculations of the relaxation rate in bulk systems. Correspondingly, the relaxation rate of the σ mode is dominated by Class 1 events near the zone centre and Class 2 events near the zone boundary, but shows subtle behaviour in the intermediate regime.

Now one discusses Umklapp processes and the relative importance of Class 1 and Class 2 events. Figure 5.10 shows that, as expected from previous calculations for bulk systems, the transverse branch does not participate in Class 2 events and, due to momentum conservation, it does not take part in Class 1 events beyond $k \approx 2.8$. Similarly, due to momentum conservation, longitudinal modes do not participate in Class 1 events beyond $k \approx 3$. Class 2 events only occur for $k > 5.8$ for the longitudinal modes. This is due to the group velocity of these modes being approximately zero and the phase velocity also being comparatively low. The relaxation rate of the twist mode undergoing Class 1 events shows a continuous increase until near $k \approx 2.8$ where there is a sudden drop caused by the cessation of the WA+LA$\rightarrow$ B and WA+TA$\rightarrow$ σ processes due to the conservation conditions. This is then followed by another increase in the rate until $k \approx 7.1$ beyond which there is no further contribution. The twist mode does not participate in Class 2 events until after $k \approx 1.4$. For the σ mode, both Classes contribute relatively equally except that Class 2 events do not contribute until after $k \approx 0.7$ and Class 1 events do not contribute beyond $k \approx 7.8$. The breathing mode also has equal contributions from Class 1 and Class 2 events, but there is no contribution from Class 1 events beyond $k \approx 7.8$.

Detailed investigation of the three-phonon events reveal that, subject to energy and

momentum conditions, all modes can interact with each other at different points across the Brillouin zone. For Normal processes, near the zone centre, Class 1 events of the type A+LA→WA (where A can be LA/WA/B) have the largest contribution to each mode's total relaxation rate. For the transverse mode's relaxation rate, the dominating Normal process is TA+σ→ B and for the σ mode's relaxation rate the dominating process is the Class 1 event σ+TA→ WA. Similarly, for Umklapp processes, Class 1 events of the form A+LA→ B (B can be WA or B) provide the largest contribution to the total relaxation rate for each of the three acoustic modes where $m = 0$. For the TA mode, the dominating process is TA+LA→σ. For the optical modes, the same process has a large contribution, but there is also a second contribution of comparative magnitude from the Class 2 process C+LA→ D where C can be B or σ and D is either LA or WA for $C =$ B or TA if $C = \sigma$.

Conversely, near the zone boundary, the dominant processes change substantially. For Normal processes, Class 1 events of the type D+LA→ B (where the symbols have the previously defined meanings) have the largest contribution to the acoustic mode's relaxation rate with the exception of the TA mode where the largest contribution arises from the TA+LA→σ process. Also, for the longitudinal mode, near the zone boundary there is a substantial contribution from the Class 2 event LA→TA+TA, which is a result of the flattening of the longitudinal branch. The twist mode has several large contributions to its relaxation rate (including the previously mentioned process). However, the largest contribution is from the Class 2 processes WA→LA+B. For the two optical modes, the largest contribution to each mode comes from the decay processes: B→LA+B and σ→LA+σ, for the breathing mode and the σ mode respectively. For Umklapp processes near the zone boundary, transverse modes are forbidden to take part in both classes of events due to energy and momentum conservation. Longitudinal modes are allowed to take part in Class 2 Umklapp processes of the type LA→TA+TA. However, the resulting relaxation rate is much smaller than the contribution made from Normal processes. For the twist mode, two Umklapp processes dominate the total relaxation rate, WA+LA→ WA and WA+LA→B. For the two optical modes, B and σ, the lifetime is dominated by the Umklapp events B+LA↔B and σ+LA↔σ, respectively.

These processes show that it is of critical importance to include the effects of the optical modes in three-phonon interactions for carbon nanotubes. This is due in part to three factors: (i) the flattening of the TA and LA modes, which leads to their dampening near the zone edge, (ii) the comparatively low energies of the B and σ modes, and their clear non-zero group velocities across the majority of the Brillouin zone, and (iii) the azimuthal momentum conservation conditions which restrict polarisations of participating phonons as listed in Table 5.1. Because of these factors, it is clear that different regions of the Brillouin zone allow only specific events, and this must be considered when three-phonon calculations are being carried out.

5.4.4 Lifetime Variation With Temperature

The temperature variation of relaxation rates is presented in Figs. 5.11 and 5.12. Generally, it is found that the shape of the τ^{-1} vs. $K_z.R$ curves remains unaltered over the temperature range of our study, as expected. However, the magnitudes and relative contributions from various processes to the relaxation rate change with temperature. To highlight the changes with temperature, Figs. 5.11 (a) and 5.11 (b) show the relaxation rate of the phonon modes undergoing selected processes at 10 K. These are presented here to enable a direct comparison with the results at 300 K in Figs. 5.9 and 5.10 respectively.

The relaxation rate of the two optical modes (B and σ) show two clear changes with a temperature drop. Firstly, there is comparatively little change (less than two orders of magnitude) in the relaxation rate due to Class 2 events. This is due to heavy contribution from spontaneous decay [175] which is expected to dominate the behaviour of these modes at low temperatures. Conversely, the relaxation rate contribution due to Class 1 events decreases by greater than four orders of magnitude with a decrease in temperature. This is because it becomes energetically unfavourable for two low energy phonons to merge and form a higher energy phonon at low temperatures. For the majority of phonon modes in the Brillouin zone the ratio of the contributions from Umklapp and Normal processes, $\tau^{-1}(U)/\tau^{-1}(N)$, decreases as

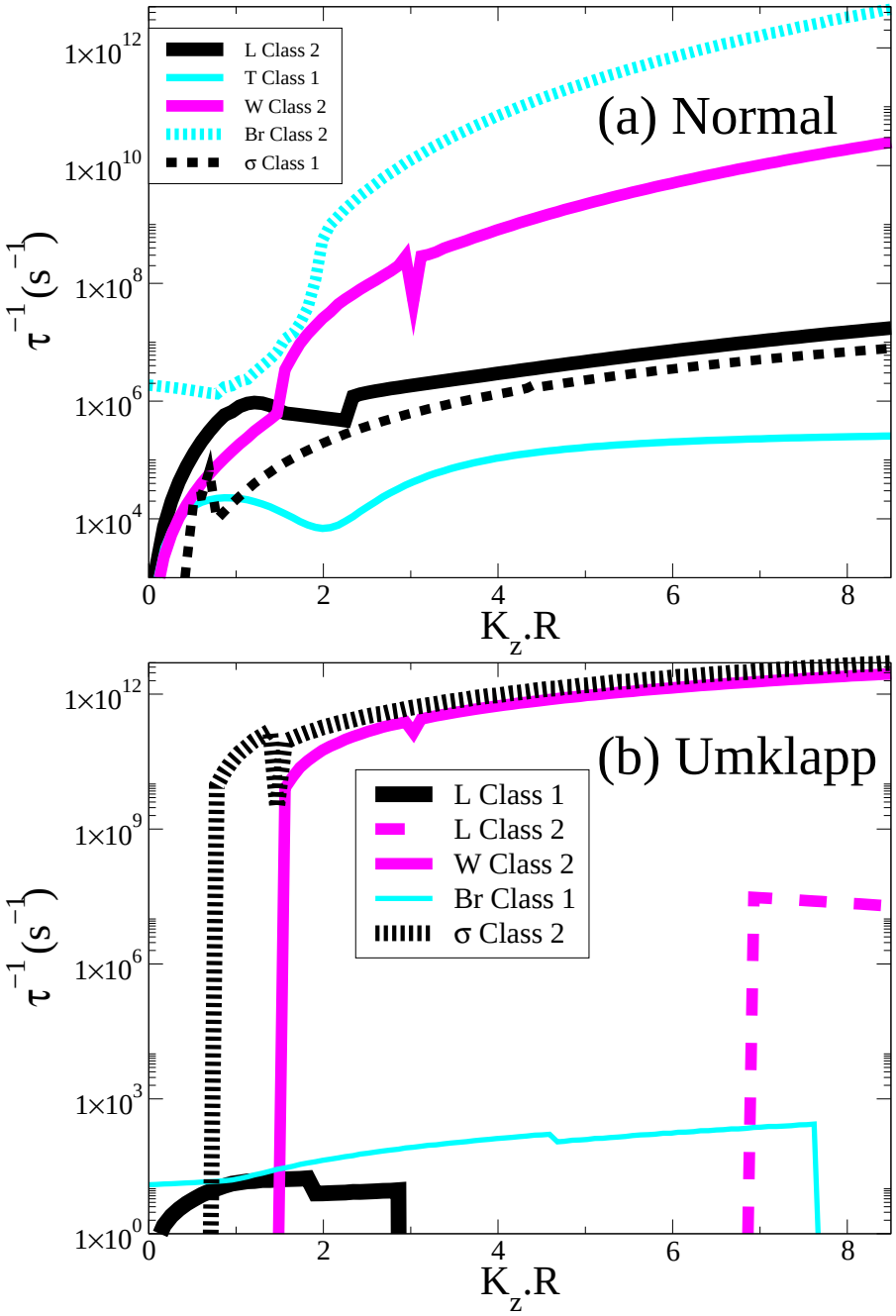

Figure 5.11: The relaxation rate of various modes undergoing selected processes for a (10,10) carbon nanotube at 10 K. (LA= Longitudinal, TA= (doubly degenerate) Transverse, WA= Twist, B= Breathing and σ= σ (the lowest non-zero mode)).

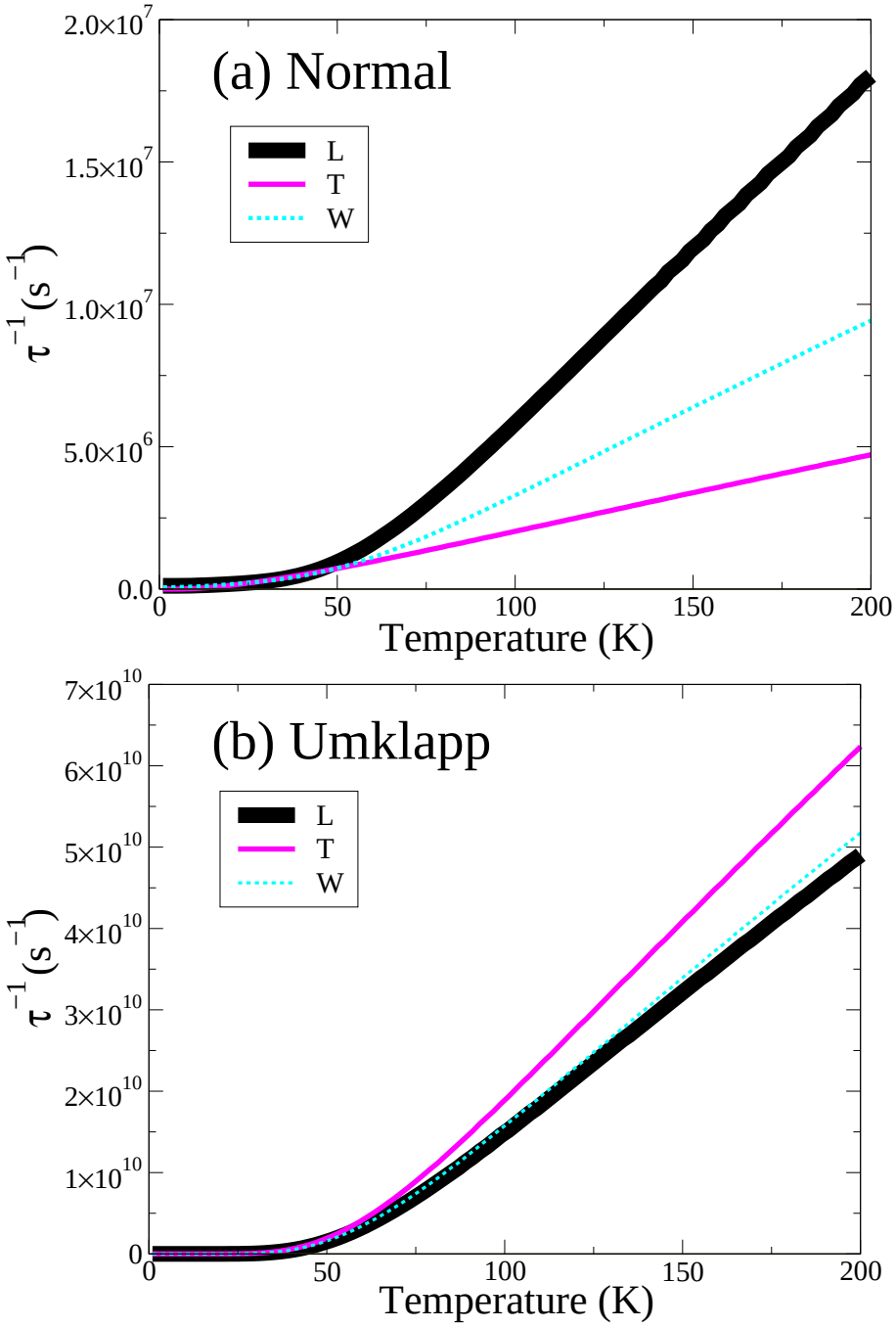

Figure 5.12: The relaxation rate of phonon modes with frequency $\omega = \omega_B/2$ as a function of temperature T for a (10,10) carbon nanotube. (LA= Longitudinal, TA= (doubly degenerate) Transverse, and WA= Twist),

the temperature decreases. However, $\tau^{-1}(U)$ is still greater than $\tau^{-1}(N)$ even at 10 K for these optical modes.

The two acoustic modes TA and LA show two major changes in their relaxation rate with a decrease in the temperature. The relaxation rate of Class 2 processes for the longitudinal mode show a decrease of approximately two orders of magnitude (the TA Class 2 events not being allowed due to conservation laws). The contribution to the total relaxation rates of the LA and TA modes from Class 1 Normal processes decreases much more quickly when they lie nearer the zone edge than the zone centre. However, the decrease in the Class 1 contribution from Umklapp processes is much greater. This means at low temperatures, near the centre of the Brillouin zone, Class 1 Normal events are the dominating contribution to the total relaxation time for both LA and TA modes. However, for $K_z.R > 0.4$ the dominating contribution to the total relaxation time for Longitudinal modes is the Class 2 Normal contribution. For the fourth acoustic mode, the twist mode (WA) two clear features can be observed: the contribution from Class 2 events has a lower decrease in magnitude than Class 1 events with temperature and the contribution to the total relaxation rate from Normal processes increases. It can be clearly seen from Figs. 5.9-5.11 that the Normal contribution is dominant at 10 K whereas Umklapp is dominant at room temperature.

Figure 5.12 shows the variation of the relaxation rate for the four acoustic modes as a function of temperature for the the frequency $\omega = \omega_B/2$. From Figs. 5.12 (a) and (b), it can be clearly observed that the decrease in relaxation rate of these modes undergoing Umklapp processes is far greater than those undergoing Normal processes with a corresponding decrease in temperature. This shows that contribution from Normal processes will dominate the relaxation rate of three-phonon interactions at low temperatures.

Figures 5.13 (a) and (b) show the temperature variation of relaxation rate for different phonon modes using the two different approaches from Eqs. (5.21) and (5.24) respectively. Figure 5.13 (a) shows the variation of the relaxation rate for the four acoustic modes as a function of temperature for the frequency $\omega = \omega_B/2$ calculated

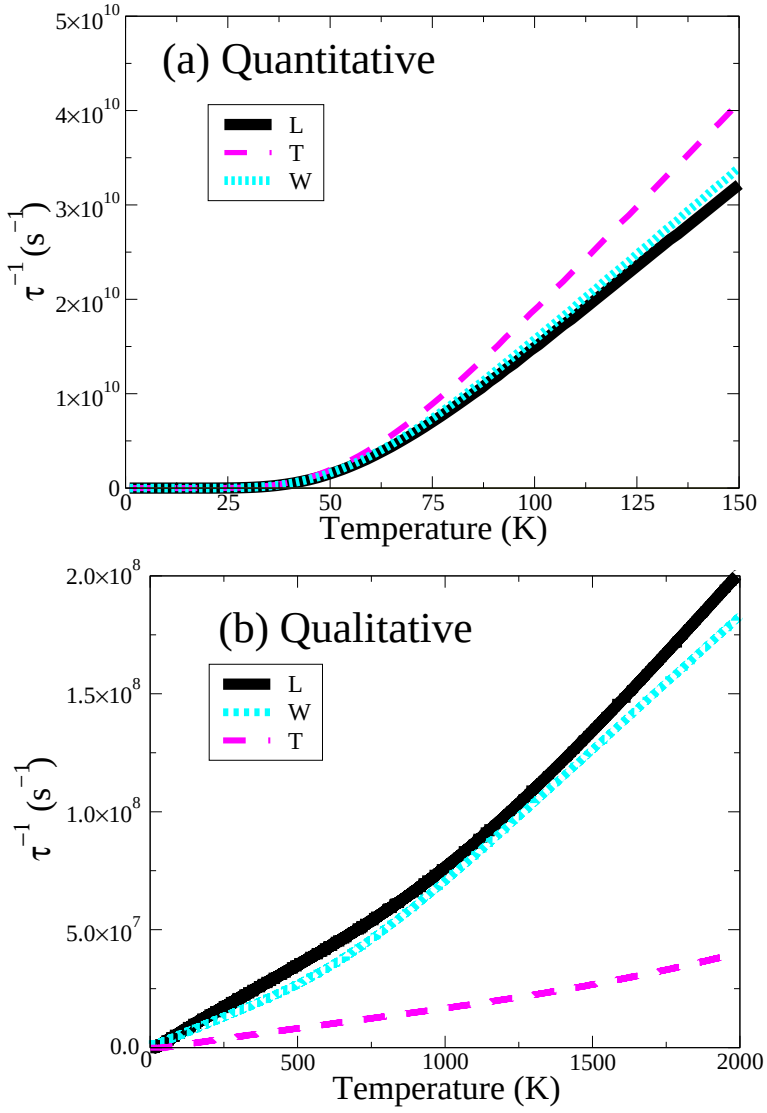

Figure 5.13: The inverse relaxation time (calculated using the (a) quantitative and (b) qualitative methods) of phonon modes with frequency $\omega = 0.5\ \omega_B$ as a function of temperature T for the (10,10) carbon nanotube.

from the precise quantitative method based upon Eq. (5.21). It can be seen clearly in the high temperature limit (see Eq. (5.27)) that $\tau^{-1} \propto \omega^2 T$ for the four acoustic modes. The results plotted in Fig. 5.13 (a) show this for temperatures greater than 80 K. For the two optical modes, the linear behaviour is observed for temperatures greater than 150 K. This is due to higher energy (and hence frequency) of these modes, and hence a higher temperature must be reached before the relaxation time becomes linear with temperature. The surprisingly low temperature (when compared with bulk diamond [172]) for which linear behaviour ensues is due to two factors: the quasi one-dimensional nature of the single-wall nanotube, and the flattening in the dispersion curves of the LA and TA modes (see Fig. 5.2). In the low temperature limit (less than 50 K), it can be seen that the four acoustic modes obey Eq. (5.26) as expected.

Figure 5.13 (b) shows the temperature dependence of the relaxation rate of the four acoustic modes calculated using Eq. (5.27). The linear relationship between the relaxation rate and temperature occurs at higher temperatures than in the quantitative approach. This is because the longitudinal mode and the two transverse modes do not flatten with an increase in the wave-vector. Figure 5.13 (b) shows good agreement with the predictions of Eqs. (5.26) and (5.27) for the appropriate high and low temperature regimes. The temperature where the behaviour changes from the low temperature approximation (Eq. (5.26)) to the high temperature approximation (Eq. (5.27)) is strongly dependent on the polarisation of the phonon acoustic branch as Fig. 5.13 (b) shows.

5.4.5 Lifetime Variation with Tube Size

To investigate the relaxation rate dependence on the nanotube size (i.e. radius) various selected phonon modes undergoing different processes at room temperature are presented in Tables 5.4-5.6 for the (5,5), (10,10) and (15,15) nanotubes respectively. These results have been presented at two values of the reduced wave-vector k ($= K_z.R$); $k = 1$ where the LA and TA branches flatten for all tubes (see Fig. 5.2), and near the zone edge ($k = 3, 7.5$ and 10 for the (5,5), (10,10) and (15,15) tubes

Table 5.4: Relaxation rates of different phonon modes undergoing various processes for the (5,5) nanotube at 300 K. The maximum value for $K_z.R$ is 4.33.

Normal or Umklapp	K_zR	Branch	Class 1 relaxation rate (s^{-1})	Class 2 relaxation rate (s^{-1})
N	1	LA	0.517×10^8	0.248×10^7
N	1	B	0.105×10^9	0.572×10^7
N	1	TA	0.128×10^7	N/A
N	1	WA	998×10^7	0.107×10^7
N	3	LA	0.683×10^7	0.876×10^7
N	3	B	0.188×10^8	0.159×10^{11}
N	3	σ	0.233×10^8	0.498×10^8
U	1	LA	0.939×10^{10}	N/A
U	1	B	0.863×10^{10}	0.170×10^{11}
U	1	TA	0.181×10^{10}	N/A
U	1	WA	0.566×10^{10}	N/A
U	3	LA	0.884×10^{10}	0.856×10^9
U	3	B	0.458×10^{11}	0.606×10^{11}
U	3	σ	0.473×10^{11}	$0.0.630 \times 10^{11}$

Table 5.5: Relaxation rates of different phonon modes undergoing various processes for the (10,10) nanotube at 300 K. The maximum value for $K_z.R$ is 8.66.

Normal or Umklapp	K_zR	Branch	Class 1 relaxation rate (s^{-1})	Class 2 relaxation rate (s^{-1})
N	1	LA	0.136×10^9	0.554×10^7
N	1	B	0.283×10^9	0.110×10^8
N	1	TA	0.257×10^7	N/A
N	1	WA	0.246×10^8	0.212×10^7
N	7.5	LA	0.926×10^{10}	0.335×10^9
N	7.5	B	0.236×10^9	0.335×10^9
N	7.5	σ	0.237×10^9	0.426×10^{13}
U	1	LA	0.270×10^{12}	N/A
U	1	B	0.346×10^{12}	0.224×10^{12}
U	1	TA	0.390×10^{11}	N/A
U	1	WA	0.144×10^{12}	N/A
U	7.5	LA	N/A	0.764×10^9
U	7.5	B	0.797×10^{13}	0.675×10^{13}
U	7.5	σ	0.782×10^{13}	0.683×10^{13}

Table 5.6: Relaxation rates of different phonon modes undergoing various processes for the (15,15) nanotube at 300 K. The maximum value for $K_z.R$ is 12.99.

Normal or Umklapp	K_zR	Branch	Class 1 relaxation rate (s^{-1})	Class 2 relaxation rate (s^{-1})
N	1	LA	0.216×10^9	0.828×10^7
N	1	B	0.327×10^8	0.257×10^8
N	1	TA	0.418×10^7	N/A
N	1	WA	0.385×10^8	0.318×10^7
N	10	LA	0.510×10^{11}	0.121×10^{10}
N	10	B	0.631×10^9	0.255×10^{14}
N	10	σ	0.633×10^9	0.269×10^{14}
U	1	LA	0.161×10^{13}	N/A
U	1	B	0.209×10^{13}	0.121×10^{13}
U	1	TA	0.203×10^{12}	N/A
U	1	WA	0.406×10^{12}	N/A
U	10	LA	N/A	N/A
U	10	B	0.849×10^{14}	0.147×10^{14}
U	10	σ	0.861×10^{14}	0.609×10^{14}

respectively).

The results show for all modes that an increase in tube radius leads to an increase in the Umklapp relaxation rate and a decrease in the Normal relaxation rate. Such size variations can be explained by examining Eq. (5.24). By considering the simplified case of linear dispersion and low temperature approximation (see Eq. (5.26)), and noting that $\omega_D \propto 1/R$, it can be shown that at a given temperature $\tau^{-1}(N) \propto \exp[-\alpha/R)/R]$ and $\tau^{-1}(U) \propto (aR + b + c/R)\exp(-\alpha/R)$ where a, b, c and α are constants. Thus, at a fixed temperature, the total relaxation rate for each mode will increase with an increase in radius. This condition applies for temperatures above approximately 200 K where Umklapp processes dominate the region. Conversely, for temperatures less than 200 K and for small radius nanotubes, an increase in the radius will lead to a decrease in the relaxation rate of phonon modes as Normal

processes will dominate.

Having discussed the magnitude of the variation of the Normal and Umklapp contributions to the relaxation rate, it is now prudent to consider the variation in the shape of the relaxation rate curves for Class 1 and Class 2 events with nanotube radius. The reader is advised to be familiar with the forms of Figs. 5.9 and 5.10 to gain best understanding of the following section. Firstly, the key features of the relaxation rate of the LA, TA, and WA modes with a change in radius are discussed. For the LA mode, the peaks observed in the relaxation rate curves for the Normal Class 1 and Class 2 events shift towards the zone centre and decrease in width with an increase in the radius of the nanotube. This is found to occur near $K_z.R = 1$ for all tube sizes as can be seen in Tables 5.4-5.6. This is due to the flattening of the LA branch which occurs at $K_z.R \approx 1$ (see Fig. 5.2). Beyond this peak, the relaxation rate decreases to a plateau, the width of which decreases with increase in tube radius. After the plateau region, the rise in the curves is much faster for larger radii. Also, as the nanotube radius increases, the ratio of contributions to the relaxation rate between Normal Class 1 and Class 2 events increases. This shows that Class 1 events become increasingly important for larger radii. This is expected as the two optical modes decrease in energy which makes these events more likely. For Umklapp processes, the form of the relaxation rate for LA modes changes very little, falling to zero at approximately $k = 2.8$ for all radii. Similarly, for TA modes the form of the relaxation rate as a function of wave vector for Normal Class 1 processes changes very little with radius except that the first point of inflexion tends towards the zone centre with increasing radius. The relaxation rate due to the TA Umklapp Class 1 process ceases at $k \approx 3.0$ for all radii, similar to the LA branch.

For the WA mode, the relaxation rate due to Normal processes near the zone centre remains of a similar form, with Class 1 events dominating. However, beyond the critical point of $k = 1.6$ the contribution of the Class 2 events rapidly increases and, for nanotubes of greater radius than the (10,10) nanotube, Class 2 events become increasingly dominant in their contribution. The relaxation rate for WA modes undergoing Umklapp processes is of a similar form to those shown in Fig. 5.10. Class 1 events do not occur for $k < 1.4$ for all radii and Class 2 events are prevented by

energy and momentum conservation conditions for $k > (G.R - 1.5)$. Also, like the LA mode, the ratio between the relaxation rate for Class 1 and Class 2 Normal processes increases with increasing radius, but to a lesser degree.

The changes in the relaxation rate of the two optical modes with an increase in radius show different behaviours. The relaxation rate due to Normal processes for the breathing mode is dominated by Class 1 events near the zone centre for all radii as shown in Tables 5.4-5.6 for $k = 1$. However, for k greater than 1.9, Class 2 events dominate the total relaxation time for all radii. As shown in Fig. 5.9, the contribution from Class 1 events does not become negligible until a critical point k_c within the Brillouin zone. In Fig. 5.9, the critical point k_c occurs at $k = 4.3$. For larger nanotubes, $k_c/(G.R)$ increases with radius. The σ mode shows comparatively less change in the form of its relaxation rate with an increase in radius. For Normal processes, the relaxation rate is dominated by Class 1 events until $k = 4.4$ for all radii beyond which Class 2 events dominate as Tables 5.4-5.6 indicate. Other than these features the general form remains the same as in Fig. 5.9. For both optical modes, the form of the relaxation rate across the Brillouin zone for Umklapp processes remains relatively unchanged when compared to the form shown in Fig. 5.10.

5.5 Summary of Carbon Nanotube Results

In summary, presented here has been a comprehensive study of the intrinsic lifetime of phonon modes undergoing three-phonon processes in carbon nanotubes. The previous sections have detailed the dependence of this lifetime on the phonon frequency at room temperature and shown that all the modes obey a variation of the type $\tau^{-1} \propto \omega^2$ to some degree. These results have also shown that the effect of not including the two lowest optical modes, σ and B, is to reduce the relaxation rate. This would lead to an over-estimation of the lifetime of phonon modes and thus also to an over-estimation of both the mean free path and the thermal conductivity. These results have shown that detailed analysis of the relaxation rate as a function of wave-vector enables a clear and precise understanding of which processes are allowed

and which dominate within the Brillouin zone. Within these results, one notes that there exist regions within the Brillouin zone where Normal and Umklapp processes are forbidden or dramatically reduced due to conservation conditions. The results also show where different processes (Normal and Umklapp, or Class 1 and Class 2) dominate the total relaxation rate of the phonon modes within the Brillouin zone. From the results one can show that, for long wavelength phonons (i.e. modes near the zone-centre) at room temperature, the relaxation rates due to Class 1 events are more dominant than Class 2 events. However, for optical modes towards the zone edge, Class 2 events become more dominant. The results have shown that the largest contribution to the relaxation rate of a mode undergoing allowed three-phonon interactions includes LA as one of the three participating phonon modes (i.e. $\alpha + \text{LA} \leftrightarrow \beta$ and $\alpha + \beta \leftrightarrow \text{LA}$). These results have also shown that three-phonon interactions involving either of the two lowest optical modes, σ and B, are of critical importance for nanotubes and must not be excluded from any considerations. This is mainly due to the low energy of these modes. As these modes in the carbon nanotube have velocities greater than 1 km/s for $k > 1$ (see Fig. 5.2), they are expected to make a significant contribution to thermal conductivity. This also shows that for all solid structures with low-lying non-zero phonon modes (such as nanowires), such modes must be included in calculating the total phonon relaxation time and thermal conductivity.

Section 5.4.4 has presented results of the variation of the relaxation rate for different phonon modes with temperature and shown that the rate of decrease of Normal contribution with decrease in temperature is much less than the rate of decrease of Umklapp contribution. This leads to Normal processes dominating the relaxation rate of three-phonon processes at low temperatures. These results have shown that the temperature dependence becomes linear at temperatures greater than 150 K for (10,10) nanotubes and that the lifetime in the high temperature approximation can be seen to obey a dependence of the form $\tau^{-1} \propto \omega^2 T$.

The effect of changing the radius of a carbon nanotube on its relaxation rate is discussed in detail and several interesting features are found. The most important result is that increasing the radius decreases the Normal contribution and in-

creases the Umklapp contribution to the total relaxation rate. Based upon the numerical results and analytic derivations in section 5.3.4, variations of the form $\tau^{-1}(N) \propto \exp(-\alpha/R)/R$ and $\tau^{-1}(U) \propto (aR + b + c/R)\exp(-\alpha/R)$ have been presented where a, b, c and α are constants. This shows that for consideration of nanotubes at low temperatures, especially those which have smaller radii than (10,10) nanotubes, Normal processes become increasingly important. It is also clear that the contribution from Class 1 events increases with increasing radii. This effect means that to accurately calculate the lifetime of phonon modes neither Normal processes nor the low-lying optical modes can be disregarded. This is because at small radii the effect of Normal processes becomes increasingly important and at large radii the effect of the two optical modes is vitally important.

5.6 Conclusion

In this Chapter, the lifetime of phonon modes undergoing various three-phonon processes has been derived for nanostructure. Both numerical and analytic expressions have been obtained for the variation of the relaxation rate of various modes as a function of radius, size and temperature.

The lifetimes of low-lying confined phonon modes in carbon nanotubes and silicon nanowires have been estimated theoretically using a three-dimensional approach and these modes were found to be very long-lived, with lifetimes of the order of nanoseconds which were comparable with bulk acoustic modes. It has been shown that for phonon-phonon calculations in all one-dimensional nanostructures, the low lying optical modes must not be excluded.

The relaxation rate of phonon modes in carbon nanotubes have been calculated using a one-dimensional approach. The detailed numerical study of three-phonon interaction reveals several features not noted before such as peaks in the relaxation rate and cut-off behaviours in particular phonon modes. The results suggest that three-phonon processes will set in at a lower temperature, and will have a larger effect on thermal conductivity, than had previously been predicted [174]. Also, the

present theoretical treatment allows modelling of larger nanotubes than previously considered [171], as the effect of the lowest optical modes are included and their contribution to three-phonon processes explained. These results have shown that neither Normal processes nor low-lying optical branches can be ignored in an accurate calculation of phonon lifetime.

Using the relatively simple qualitative theory presented in Section 5.3.4 the phonon relaxation rate can be explained analytically and good agreement in form between the two different approaches (numeric and analytic) can be shown. For nanotubes of fixed radius, these expressions have shown that the variation of relaxation rate can be approximated as $\tau^{-1} \propto \omega^3 \exp(-\beta\omega/T)$ at low temperatures and as $\tau^{-1} \propto \omega^2 T$ at high temperatures. These expressions have also shown the size variation as a function of temperature to be $\tau^{-1}(N) \propto \exp[(-\alpha/R)/R]$ and $\tau^{-1}(U) \propto (aR + b + c/R)\exp(-\alpha/R)$ where a, b, c and α are constants. Such expressions enable both experimentalists and theoreticians to understand three-phonon processes in simple terms without the need for heavy numerical analysis.

Chapter 6

Thermal Conductivity of Nanostructures

> "*I pass with relief from the tossing sea of Cause and Theory to the firm ground of Result and Fact.*"
>
> Winston Churchill, 1874-1965

6.1 Introduction

In the last chapter the subject of phonon-phonon interactions and the anharmonic potential was discussed. These interactions were said to have a strong effect on two thermal properties of nanostructures, namely the thermal conductivity and the mean free path of phonons. Of these two properties the former (the thermal conductivity) describes one of the most fundamental and important aspects of any material. In this chapter preliminary results of recent thermal conductivity calculations based on analytic theory are presented. These preliminary results for the thermal conductivity show some very exciting and new developments in theory and understanding.

Thermal conductivity in one-dimension is defined as the rate of flow of heat per unit length per kelvin and is normally measured in units of $\mathrm{Wm^{-1}K^{-1}}$. It is one of

the most complicated properties of a material and is dependent on several types of phonon interactions. In pure semiconductors and their nanostructures, its properties are determined by three types of interactions: (i) phonon-phonon interactions, as described in the previous chapter; (ii) phonon-mass defect interactions, i.e. phonons being scattered by a defect (normally a point defect) within the crystal's structure and (iii) phonon-boundary scattering where a phonon is scattered (either elastically or inelastically) by the boundary of a system. All three of these scattering mechanisms can be treated using the relaxation rate approach which was used for phonon-phonon interactions in Chapter 5 and Appendices D and E.

In the following Chapter, the theory of thermal conductivity for one-dimensional nanostructures is described. It is based upon results presented in the previous chapters. The theory is derived in terms of the single mode relaxation time approach and the linear Boltzmann equation (see Appendix E). It is then applied to carbon nanotubes, where preliminary results are calculated and presented.

6.2 Background to relaxation time theory of thermal conductivity

The origins of thermal conductivity can be traced as far back as the early 19th century, when Joseph Fourier expressed the flow of heat in an object as

$$\frac{dQ}{dt} = \kappa A_{Fo} \frac{\Delta T}{\Delta L} \tag{6.1}$$

where dQ/dt is the heat flow, A_{Fo} is the cross-sectional area, ΔT is the change in temperature and ΔL is the length of object in direction the heat flows. κ is the thermal conductivity of the object and in his original proposal, Fourier treated this as a constant. It was later shown that κ was dependent on material and its temperature. However, when one is first introduced to heat conductivity, it is usually via Fourier's Law that one is introduced.

It is with this approach in the early 1910's that Debye [176] formulated his theory of thermal conductivity. In his theory, Debye modelled phonons as an ideal gas or

as a cloud of quasi-particles to calculate the thermal conductivity of a crystal. This was performed on the basis of each phonon not interacting with anything in the crystal structure except other phonons. Debye used his linear dispersion relations to describe the phonons. This hybrid approach, of using a classical relation for the thermal conductivity (that he obtained from the ideal gas principle) and the quantum notion of a phonon proved to be a very effective starting point for the theory of thermal conductivity of a crystal.

In quantum mechanics, the definition of thermal conductivity was first developed in 1929 by Peierls [177, 178]. He defined thermal conductivity in quantum mechanics as

$$\mathbf{Q} = -\kappa \nabla T \tag{6.2}$$

where $\mathbf{Q}$ is the rate of heat energy flow per unit area, κ is the thermal conductivity and T is the temperature. The similarity to Eq. (6.1) is clear. However, this definition does not explicitly express how the thermal conductivity changes with temperature, which was tackled later. In his paper in 1929, Peierls describes thermal conductivity within the single mode relaxation time (*smrt*) approach as being chiefly due to Umklapp processes within the system. As was shown in the previous chapter, Normal processes also play an important role, as do other processes which are discussed later.

Later in 1951, Klemens [180] showed that it was possible to improve upon the *smrt* approach by considering a distribution function like the Bose-Einstein, but with an additional drifting term contribution in the exponential. Based upon this, Klemens showed using a series of intuitive arguments, rather than strict mathematical rigour, that the thermal conductivity predicted using the *smrt* approach was an underestimate and required an additional small term. However, in this approach, the contribution due to Normal processes was vastly underestimated and the additional term lacked clarity.

In 1960, Ziman redeveloped the theory to produce a simplified expression, based upon the various Variational approaches which were being developed [150, 179, 162].

His expression for the thermal conductivity was of the form

$$\kappa(T) = \frac{1}{3} C_v(T) \bar{v}_g \Lambda_{FP}(T) \tag{6.3}$$

where $C_v(T)$ is the specific heat capacity, $\bar{v}_g$ is the average group velocity and $\Lambda_{FP}(T)$ is defined as $v_g \tau(T)$ and is termed the mean free path of the phonon. Here, $\tau(T)$ is the mean scattering time of a phonon. The mean relaxation time was calculated from the three [159] contributing factors to phonon scattering in undoped semiconductors; (i) phonon-phonon scattering, (ii) mass-defect scattering and (iii) boundary scattering. The advantage of this early technique is that the scattering mechanism that Klemens [159] describes for a phonons boundary scattering is very effective, allowing for both elastic and inelastic scattering, and allows an easy estimate at low temperatures.

In 1959, Callaway [182] examined the problem more closely, using a more sophisticated and detailed approach than Klemens had in 1951. In his approach, he used a method which relied on a distribution function approach (like that described in Appendices D and E) with an additional drifting term that was similar in form to that which had been suggested by Klemens. In his approach, Callway showed that an additional contribution to the *smrt* thermal conductivity was needed. This additional term is due to Normal processes and he described it as $\kappa_{N-Drift}$ such that $\kappa_{total} = \kappa_{smrt} + \kappa_{N-Drift}$. This term clearly bared similarities to that of the Klemens description shown previously, but as can be seen, this process fails to include the contribution due to Umklapp processes. Never the less, this was a vast improvement. In 1976 the missing contribution due to Umklapp processes was evaluated by Srivastava [168]. Srivastava showed that the missing contribution was a small resistive force, which (whilst not as great as the additional contribution due to Normal processes) reduced the Callaway conductivity term and explained the thermal conductivity of bulk semiconductor materials very well.

In the following sections the *smrt* approach is followed. This approach is applied to calculate the thermal conductivity of carbon nanotubes using the information gained from the analytic terms described in Chapter 5.

6.3 Theory of Thermal Conductivity

The microscopic expression for heat current $\mathbf{Q}$ which can be seen from Eq. (6.2) is

$$\mathbf{Q} = \frac{1}{V_0}\sum_{\mathbf{q}s}\hbar\omega(\mathbf{q}s)n_{\mathbf{q}s}\mathbf{c}_s(\mathbf{q}) \tag{6.4}$$

where all the symbols retain their usual meanings and $\mathbf{c}_s(\mathbf{q})$ is the phonon group velocity of mode $\mathbf{q}s$. Using Eq. (D.3) from Appendix D, and noting that it is only the deviation that contributes to the heat current, one can re-expressed Eq. (6.4) as

$$\mathbf{Q} = \frac{1}{V_0}\sum_{\mathbf{q}s}\hbar\omega(\mathbf{q}s)\psi_{\mathbf{q}s}\bar{n}_{\mathbf{q}s}(\bar{n}_{\mathbf{q}s}+1)\mathbf{c}_s(\mathbf{q}) \tag{6.5}$$

where $\psi_{\mathbf{q}s}$ may be view as a deviation from the equilibrium system. Hence by manipulating Eqs. (6.2) and (6.5) one can show that

$$\begin{aligned}\kappa_{ij} &= -\frac{\mathbf{Q}_i.\nabla T_j}{|\nabla T|^2} \\ &= -\frac{1}{V_0|\nabla T|^2}\sum_{\mathbf{q}s}\hbar\omega(\mathbf{q}s)\psi_{\mathbf{q}s}\bar{n}_{\mathbf{q}s}(\bar{n}_{\mathbf{q}s}+1)\mathbf{c}_i(\mathbf{q}s).\nabla T_j \end{aligned}\tag{6.6}$$

This equation, for three-dimensional isotropic mediums and one-dimensional systems, can be simplified as $\kappa_{ij} = \kappa\delta_{ij}$ and hence Eq. (6.6) can be written as

$$\kappa = -\frac{1}{V_0|\nabla T|^2}\sum_{\mathbf{q}s}\hbar\omega(\mathbf{q}s)\psi_{\mathbf{q}s}\bar{n}_{\mathbf{q}s}(\bar{n}_{\mathbf{q}s}+1)\mathbf{c}_s(\mathbf{q}).\nabla T \tag{6.7}$$

However, it can be shown from Eq. (D.2) in Appendix D that

$$\psi_{\mathbf{q}s} = -\mathbf{c}_s(\mathbf{q}).\nabla T\tau_{\mathbf{q}s}\frac{\hbar\omega(\mathbf{q}s)}{k_BT^2}, \tag{6.8}$$

where $\tau_{\mathbf{q}s}$ is the phonon relaxation rate. It is important to note here that $\tau_{\mathbf{q}s}$ does not specify the process, and thus includes all scattering mechanisms, not just three-phonon as in the previous chapter. Hence, using Eqs. (6.7) and (6.8) from above and Eqs. (4.1) and (4.2) from Chapter 4 one can show that

$$\begin{aligned}\kappa &= \frac{1}{V_0k_BT^2}\sum_{\mathbf{q}s}\frac{(\mathbf{c}_s(\mathbf{q}).\nabla T)^2}{|\nabla T|^2}[\hbar\omega(\mathbf{q}s)]^2\bar{n}_{\mathbf{q}s}(\bar{n}_{\mathbf{q}s}+1)\tau_{\mathbf{q}s} \\ &= \frac{1}{\vartheta V_0k_BT^2}\sum_{\mathbf{q}s}c_s^2(\mathbf{q})[\hbar\omega(\mathbf{q}s)]^2\bar{n}_{\mathbf{q}s}(\bar{n}_{\mathbf{q}s}+1)\tau_{\mathbf{q}s} \\ &= \frac{1}{\vartheta}\sum_{\mathbf{q}s}c_s^2(\mathbf{q})C_v(\mathbf{q}s)\tau_{\mathbf{q}s} \end{aligned}\tag{6.9}$$

where ϑ is the number of degrees of freedom the system has. Here for ϑ-dimensional systems one can state

$$\frac{(\mathbf{c}_s(\mathbf{q}).\nabla T)^2}{|\nabla T|^2} = \frac{1}{\vartheta} c_s^2(\mathbf{q}) \tag{6.10}$$

where $\vartheta = 1$ for one-dimensional systems. In a three-dimensional system the average of $(\hat{\mathbf{c}}.\hat{\nabla T})^2$ is $1/3$ so $\vartheta = 3$.

Equation (6.9) is the *smrt* result for the thermal conductivity equation. It has three components: (i) the group velocity of phonon mode $\mathbf{q}s$, $c_s(\mathbf{q})$; (ii) the specific heat capacity, $C_v(\mathbf{q}s)$ and (iii) the lifetime of phonon mode $\tau_{\mathbf{q}s}$. Parts (i) and (ii) can be calculated from the results presented in Chapters 3 and 4 respectively. However, the lifetime of the phonon mode $\mathbf{q}s$ requires knowledge of the all scattering mechanisms in a one-dimensional system, not just the phonon-phonon interaction presented in Chapter 5. In the following sections it is prudent to examine these further with a view to calculate the thermal conductivity of a carbon nanotube.

6.3.1 Scattering mechanisms

In pure carbon nanotubes, the electronic contribution to thermal conductivity is negligible [151, 149]. This leaves three main scattering mechanisms for phonons: (i) boundary scattering; (ii) mass-defect scattering and (iii) phonon-phonon scattering. Using Matthiessen's rule one can state the total scattering rate as

$$\tau_{\mathbf{q}s}^{-1} = \tau_{\mathbf{q}s}^{-1}(bs) + \tau_{\mathbf{q}s}^{-1}(md) + \tau_{\mathbf{q}s}^{-1}(pp) \tag{6.11}$$

where $\tau_{\mathbf{q}s}^{-1}(bs)$ is the relaxation rate due to phonon-boundary scattering, $\tau_{\mathbf{q}s}^{-1}(md)$ is the relaxation rate due to phonon-mass-defect scattering and $\tau_{\mathbf{q}s}^{-1}(pp)$ is the relaxation rate due to phonon-phonon scattering. It is known from bulk [167, 168] that boundary scattering dominates the low temperature behaviour of the phonon relaxation rate, mass-defect scattering is often referred to determine maximum conductivity and phonon-phonon scattering reduces the thermal conductivity at high temperatures. Hence it is vital to evaluate each of these components.

6.3.1.1 Boundary Scattering

Boundary scattering is relatively the easiest of the scattering mechanisms to discuss. As carbon nanotubes are one-dimensional systems, it is expected that the phonons in the nanotube will undergo "ballistic" transport. If the tube is of length L_0 and the phonon has a velocity of $c_s(\mathbf{q})$ then one would expect its lifetime to be of the form

$$\tau_{\mathbf{q}s}(bs) = \frac{L_0}{c_s(\mathbf{q})}. \tag{6.12}$$

In carbon nanotubes, this length is of the order of hundreds of nanometers to tens of micrometers. The value of L_0 will be investigated further in section 6.4.

6.3.1.2 Mass Defect Scattering

Mass-defect scattering is a vital scattering mechanism in bulk materials. However, in carbon nanotubes, it is unknown how important this contribution is. In Appendix F, the derivation of the mass-defect relaxation rate is presented. Here, the final expression for the relaxation rate is quoted:

$$\tau^{-1}_{\mathbf{q}s}(md) = \frac{\pi \mathcal{G}_{md}}{2} \frac{|\mathbf{T}|}{L_0} \sum_{s'} g_{s'}(\omega(\mathbf{q}s))\omega^2(\mathbf{q}s), \tag{6.13}$$

where $\mathcal{G}_{md}$ is defined in Appendix F and $|\mathbf{T}|$ is the nanotubes translation vector arising from Eq. (1.6). It is important to note that for the carbon nanotube, $g(\omega) \propto L_0$ (see Eqs. (3.37-3.42)) and thus this eliminates the unknown variable L_0 and leaves only $|\mathbf{T}|$, the translation vector of the carbon nanotube in the numerator.

6.3.1.3 Anharmonic scattering

Chapter 5 discusses calculating the relaxation rate of phonon modes undergoing three-phonon processes in substantial detail. It was shown that the analytic expressions in the high temperature limit ($T > 200$ K) is a very good approximation for this process. Using the high temperature approximation one can write the lifetime

contribution from three-phonon processes as

$$\tau_{\mathbf{q}s}^{-1}(pp) = \mathcal{P} n \omega^2 T \tag{6.14}$$

where $\mathcal{P}$ is a measure of the strength of the anharmonic potential and n is the chiral number of an (n,n) nanotube (which is proportional to the radius). Thus, having evaluated all the contributing factors to the relaxation rate, one is left with two parameters L_0, the length of the nanotube, and $\mathcal{P}$, the strength of the phonon-phonon interaction. For these two parameters, two approaches are possible, $\mathcal{P}$ may be calculated from Chapter 5 and L_0 can be taken from experimental data or they may be treated as adjustable parameters to fit experiment.

6.4 Results Of Calculations

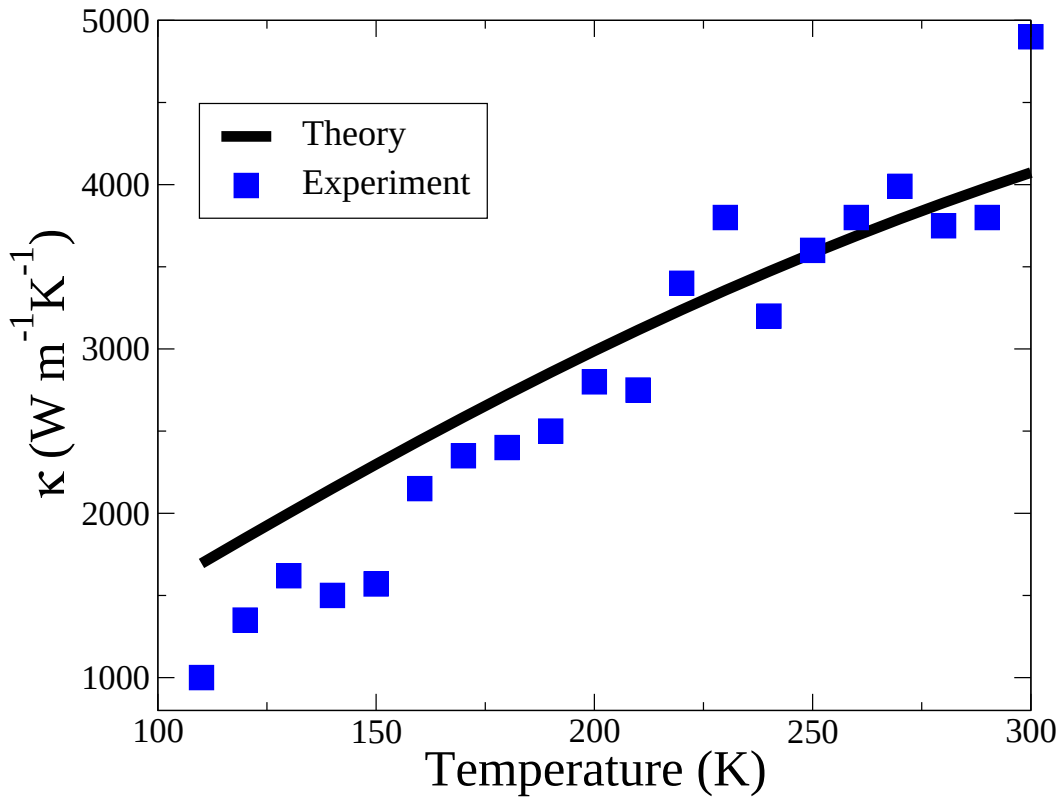

Figure 6.1: The thermal conductivity (κ) of an (8,8) carbon nanotube as a function of temperature. Shown are the experimental data of Yu *et al.* [184] and the theoretical results.

Figure 6.1 shows the results obtained from the theory presented in section 6.3 for the (8,8) nanotube. The length was taken to be 0.31 μm and the phonon scattering strength, $\mathcal{P}$, was taken to be 7.5×10^5 s/K. In the temperature range shown in the diagram, κ_{CNT} varies almost linearly with temperature. Also shown in this figure is the recent experimental data from Yu *et al.* [184]. There is good agreement between theory and experiment above 180 K. However, as can be seen from the report by Yu *et al.*, the uncertainty in the measurements is very large ($\pm$ 500 $\mathrm{Wm^{-1}K^{-1}}$). The regime presented is dominated by boundary scattering, with scattering due to phonon-phonon interactions only coming into effect near 300 K. In the report presented, Yu *et al.* are unable to explain why their apparent calculated length (using a very simple theory) for the nanotube is much smaller than the distance between the two contacts (2.76 μm), which should be the nanotube's length. However, closer examination of their results and their scanning electron microscopy images reveal that the measured nanotube does not lie straight across the gap between the source and drain, but has numerous kinks and deviations. Because of these, the mean free-path due to boundary scattering will be less. The results presented here for a tube with a ballistic path-length of 0.31 μm are in good agreement with this statement. This has important implications for nanotube usage in electronics. If a tube cannot be grown smoothly and not applied to a system without kinks forming in its structure, then applications using the nanotubes for thermal management will be limited to lower than the ideal conductivity predicted by some earlier theoretical reports [185]. This is backed up by the preliminary calculations presented here, where increasing the length parameter L_0 by a factor of two can lead to an almost doubling of the thermal conductivity at 200 K. At 300 K this is also observed, but phonon-phonon interactions have a greater effect with longer lengths of tubes and reduce the maximum value obtainable.

Figure 6.2 shows the thermal conductivity, (κ), of an (8,8) carbon nanotube as a function of temperature, T. It also shows the components from individual phonon branches. It is surprising to see that the doubly degenerate transverse branches and the σ branch contribute comparatively little to the total thermal conductivity at all temperatures greater than 20 K. The reason for this behaviour is thought to be

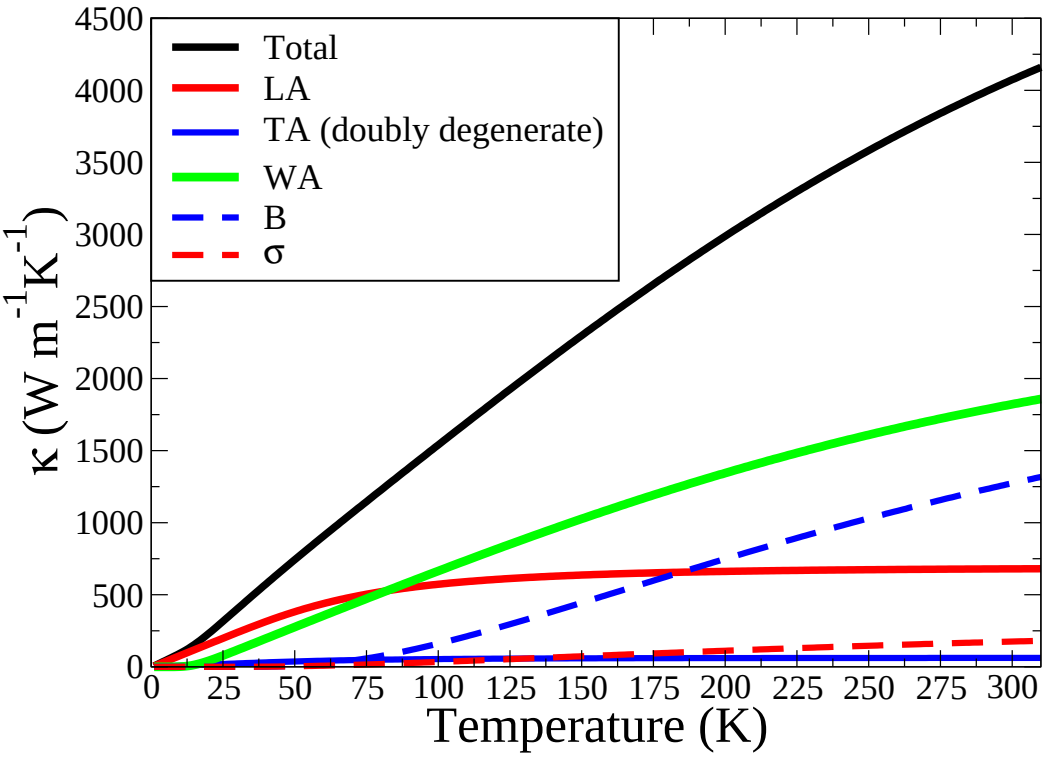

Figure 6.2: The thermal conductivity (κ) of an (8,8) carbon nanotube as a function of temperature. The total thermal conductivity and its component breakdown are presented. Here the letter corresponds to the mode (LA= Longitudinal, TA= (doubly degenerate) Transverse, WA= Twist, B= Breathing and σ= σ (the lowest non-zero mode)).

mainly a result of the comparatively low speeds of these phonon modes, though the flattening in the transverse branch is also thought to be a contributing factor (See Fig. 5.2). The largest contribution for temperatures greater than 85 K comes from the twist mode, which contributes to 45% of the total thermal conductivity at room temperature (300 K). The next two largest contributions are from the breathing mode (31%) and the longitudinal mode (16%). This result echos the statement made in the previous chapters that the low lying optical modes must not be discarded from the calculations, as without the breathing mode, theory and experiment would not agree.

From Fig. 6.2, it can be seen that the contribution from the twist mode starts to flatten out at 280 K, and this effect is due to phonon-phonon scattering. Simi-

larly, the breathing mode contribution starts to flatten at 300 K. For temperatures greater than this, phonon-phonon scattering starts to reduce the thermal conductivity. However, due to the simplified form of the phonon scattering rate presented here, the results are not presented for higher temperatures until a more rigorous calculation can confirm the effectiveness of Eq. (6.14).

In Appendix F, the mass-defect scattering term was derived for one-dimensional systems. However, unlike in bulk, the term has shown to have little effect on the scattering time presented here. The results presented have used the naturally occurring ratios of carbon-12 and carbon-13 (99.9% and 0.1%) in the formulation of $\mathcal{G}_{md}$. It is found that even if this value ($\mathcal{G}_{md}$) is increased artificially by a factor of 10, the thermal conductivity does not change by more than 200 $\mathrm{Wm^{-1}K^{-1}}$ at room temperature. This artificially large change corresponds to heavy doping or a high presence of point defects, but the thermal conductivity is relatively unresponsive to this. This is related to the one-dimensional density of states term being approximately constant (this is seen in Eq. (5.22) in Chapter 5). This contrasts with bulk where the density of states varies as ω^2. Hence, the decreased importance of this term is due to two factors: (i) the reduced frequency dependence, and (ii) the greater effect of the boundary scattering in the one-dimensional tube. The result of these changes is that the mass-defect scattering rate is much weaker in one-dimensional systems than in either three-dimensional or two-dimensional systems. This could have strong implications for doping which traditionally is seen to reduce the thermal conductivity due to mass-defect and electron-phonon scattering. Hence for one-dimensional nanostructures, in simple theories one may ignore mass-defect scattering. However, for more comprehensive calculations, Eq. (6.13) may be used.

6.5 Conclusion

In this chapter preliminary results for the thermal conductivity of a carbon nanotube have been presented. It has been shown that for temperatures between 75 K and 225 K the thermal conductivity is linearly dependent on temperature. These results

have also shown that the most important consideration in any theoretical calculation or experimental measurement is how perturbed the nanotube is from an ideal linear one-dimensional line. It has been observed from scanning electron microscopy and confirmed using the theory here that the thermal conductivity is highly sensitive to any kinks or bends in the tube. This will have a strong effect on thermal applications of nanotubes. It has also been noted in this chapter that the optical modes normally not considered in thermal conductivity calculations must be included to obtain a correct temperature dependence. It has also been shown that these modes contribute sizable amounts to the total thermal conductivity. Also in this chapter, results for the mass-defect scattering in carbon nanotubes have been presented. These results have shown that one-dimensional systems are far more robust to mass-defect scattering than their higher dimensional counter-parts. This has strong implications for the manufacture of both doped systems and other future thermal applications for nanotubes, nanowires and other one-dimensional systems.

Chapter 7

Conclusion

" Though much is taken, much abides; and though
We are not now that strength which in old days
Moved earth and heaven, that which we are, we are
One equal temper of heroic hearts,
Made weak by time and fate, but strong in will
To strive, to seek, to find, and not to yield."

Alfred Tennyson, Ulysses, 1842

7.1 Summary

In this work, the nature of phonons in nanostructures has been explored in detail, and several exciting features have been revealed and discussed. Chapter 1 introduced nanostructures, and defined some of their basic properties. In particular, the size of silicon nanostructures is defined in terms of the parameter d, the width of the confining dimension. Similarly, for nanotubes, the radius of a nanotube R is defined and it is connected to the tube's Chiral numbers (n_1,n_2). In Chapter 2, a summary of some of the available measured experimental data is presented. Methods for fabrication, and measuring the properties of phonons in nanostructures are described. Also, information concerning the thermal properties of nanostructures

has been discussed.

In Chapter 3 the lattice dynamics of nanostructures is discussed. Silicon nanostructures have several common features with regards to their lattice dynamics. It has been shown that for the ultrasmall case of each structure that all branches except the acoustic branch are flat and dispersionless regardless of whether the system is zero-, one, or two-dimensional. As the size of these structures increases, these branches are seen to become dispersive in the direction of propagation. Eventually, as size increases, the branches in the direction of confinement start to follow a similar trend. In all systems studied, the characteristic lowest non-zero zone centre mode with frequency ω_σ is calculated and shown to decrease with the size of the nanostructure. An analytic fit has been presented for the size variation of this mode for nanodots, nanowires and nanoslabs. It is also observed that in all systems the highest optical mode is lowered and for simple systems this behaviour can be explained using a simple diatomic model, as shown in Appendix C. The calculated results for such variation have been fitted to these analytic expressions.

The previously mentioned trends are also observed in the case of nanowires deposited on substrates. For this system the phonon dispersion is in general dominated by the substrate. In particular, the phonon branches in the $\Gamma - Y$ direction become more dispersive than in the stand alone nanowire, showing that the addition of the slab reduces quantisation in that plane. Also, the frequency ω_σ of a nanowire deposited upon a substrate is lower than that of either of the two stand alone systems.

A continuum model for the phonon dispersion relations in carbon nanotubes is also presented in Chapter 3. In this model, several similarities between the nanotube and nanowire were described. Both systems show low-lying optical branches with energies comparable to the acoustic modes. These modes are shown to vary with size of the nanotube (like the nanowire) and this behaviour was explained using Eq.(3.43). Also, the group velocity of the acoustic modes in the nanotube was shown to be very high, which helps explain some of the unusual thermal properties associated with nanotubes.

In Chapter 4, using the one-dimensional tube continuum theory, the variation of the

specific heat capacity (C_v) of (n, n) arm-chair carbon nanotubes with temperature T and radius was discussed. In the very low temperature regime the majority of nanotubes showed a linear variation of their specific heat capacity with temperature. However, ultrathin nanotubes show a slight dip in this variation which helps account for discrepancies between theory and experiment. It was also shown that, for carbon nanotubes, a changeover from the 1D-like to a 2D-like behaviour occurs in the variation of the specific heat with temperature. For the range of n values, such a changeover occurs between 180 K and 400 K. The crossover line can be expressed as $nT = A + B/T$, where A and B are constants.

Chapter 5 discusses in detail the lifetime of phonon modes undergoing various three-phonon processes in nanotubes. The lifetimes of low-lying confined phonon modes in carbon nanotubes and silicon nanowires have been estimated theoretically using a three-dimensional approach and these modes were found to be very long-lived, with lifetimes of the order of nanoseconds. This is comparable to the lifetime of bulk acoustic modes. It has been shown for one-dimensional nanostructures the low lying optical modes must not be excluded from any correct calculation of the relaxation rate of phonon modes.

The relaxation rate of phonon modes in carbon nanotubes have been calculated using a one-dimensional approach. This model clearly includes momentum conservation and also describes the important azimuthal conservation condition which must be included. The detailed numerical study of three-phonon interactions reveals several features not noted before such as peaks in the relaxation rate and cut-off behaviours in particular phonon modes. The results suggest that three-phonon processes will set in at a lower temperature, and will have a larger effect on thermal conductivity, than had previously been predicted [174]. Also, the present theoretical treatment allows modelling of larger nanotubes than previously considered [171], as the effect of the lowest optical modes are included and their contribution to three-phonon processes explained. These results have shown that neither Normal processes nor low-lying optical branches can be ignored in an accurate calculation of phonon lifetime.

Using a relatively simple qualitative theory the phonon relaxation rate can be

explained analytically and good agreement in form between the two different approaches (numeric and analytic) can be shown. For nanotubes of fixed radius, these expressions have shown that the variation of relaxation rate can be approximated as $\tau^{-1} \propto \omega^3 \exp(-\beta\omega/T)$ at low temperatures and as $\tau^{-1} \propto \omega^2 T$ at high temperatures. These expressions have also shown the size variation as a function of temperature to be $\tau^{-1}(N) \propto \exp[-\alpha/R)/R]$ and $\tau^{-1}(U) \propto (aR + b + c/R)\exp(-\alpha/R)$ where a, b, c and α are constants. Such expressions enable both experimentalists and theoreticians to understand three-phonon processes in simple terms without the need for heavy numerical analysis.

Chapter 6 introduces the theory of thermal conductivity. In this chapter, preliminary results for the thermal conductivity of a carbon nanotube were presented. It has been shown that for temperatures between 75 K and 225 K the thermal conductivity is linearly dependent on temperature. These results have also shown that the most important consideration in any theoretical calculation or experimental measurement is how perturbed the nanotube is from an ideal linear one-dimensional system. It has been observed from scanning electron microscopy and confirmed using the theory presented in Chapter 6 that the thermal conductivity is highly sensitive to any kinks or bends in the tube. This will have a strong effect on thermal applications of nanotubes. It has also been noted that the optical modes normally not considered in thermal conductivity calculations must be included for one to calculate a correct temperature dependence. It has also been shown that these modes contribute sizable amounts to the total thermal conduction. Also, in this chapter, results for the mass-defect scattering in carbon nanotubes have been presented. These results have shown that one-dimensional systems are far more robust to mass-defect scattering than their higher dimensional counter-parts.

7.2 Future Work

There are several areas presented within this thesis that warrant further investigation. A calculation of the thermal conductivity of carbon nanotubes using the

full three-phonon lifetime calculations presented in Chapter 5 would be of interest. This would explore in detail the effects of a change of temperature and nanotube radii on the thermal conductivity and would possibly present new information not previously noted in Chapter 6. Using these calculations the effects of the optical modes could be investigated further and a study in particular of the effect of the σ mode on thermal conductivity at high temperature would be of great interest as this mode is expected to have a strong effect on the behaviour of $\kappa(T)$ at ultrahigh temperatures. It would also be of interest to exclude from the calculations transverse modes contribution to the thermal conductivity. These are damped due to intertube interactions and this might explain the results of Hone *et al.* presented in Chapter 2. Furthermore, it would be of great use and practicality to use the detailed analytic expressions presented within Chapter 5 to create analytic expressions for the thermal conductivity of a carbon nanotube. These expression should be both a function of temperature and of radius. This may help experimentalists when designing systems known exactly how much heat the system will channel across its elements and may help with future electronic applications.

It would also be thought-provoking, based on the preliminary evidence in Chapter 6, to carry out full thermal conductivity calculations for the silicon nanowires, whose phonon dispersion relations were calculated in Chapter 3. Like the nanotube, the effects of changing the size of the nanowire, or its temperature, would change the its thermal conductivity. To model such a system, boundary effects would have to be examined very carefully using a more sophisticated model than that presented in Chapter 6. This is because the amorphous layer found coating most silicon nanowires would be expected to provide a high level of inelastic boundary scattering and also the phonons would not be expected to under go ballistic transport.

A second area where further information would lead to new and exciting physics is *ab initio* calculations of the electronic band structure of silicon nanowires. In particular, these calculations could be used to examine what form the relaxed structure would take. Once the relaxed structure is known, one could examine further the phonon dispersion relations and find how the change in structure effects the phonon dispersion curves presented in Chapter 3. However, such changes are expected to be

slight. Furthermore, it would be of appealing to see if the analytic relation for the highest optical mode presented in Chapter 3 could be refined further for cylindrical wires and non-uniform wires, but this would be a very long undertaking (with the strong possibility that very little new knowledge would be gained).

If such calculations of the electronic band structure of silicon nanostructures were performed in detailed, then it would also be possible to calculate the phonon-electron interaction and examine how this interaction would change both the thermal conductivity and the electrical conductivity. These effects, combined with the effects of the amorphous coating which several structures have, could lead to new and novel physics. However, the difficulty in modelling a non-uniform system on the surfaces of nanostructures would limit such models at the present time to either continuum or simple Born-von Kármán models. In the future, when the computational power has increased further, then it is expected that such calculations may be performed.

In the case of carbon nanotubes, there are still several fascinating qualities of these systems which remain untouched. In particular, the current emphasis in the research community is on single tubes, be they multi-wall or single wall. However, the interaction between carbon nanotubes is very poorly understood, and their interaction with other systems even less understood. Carbon nanotubes have shown substantially poorer qualities when not isolated, and this feature has not been explored in detail to the author's knowledge to date. From an experimental point of view, if two tubes of the same radius could be isolated, and then slowly brought into contact with each other, then a clearer understanding of the forces between these tubes might be gained. Similarly, on a theoretical front, whilst a substantial amount of research was performed in the 1980's into graphite, and the interaction between its layers and the Van-der Waals force has still not been fully understood.

Another area of unexplored research is that of doping either nanowires or nanotubes. Both systems could benefit from doping, be it controlled via scanning tunnelling manipulation, or via evaporation concentration methods. These procedures could substantially change the properties of either nanostructure and have the potential to create further nanostructures, with unknown properties. Also, doping in both sys-

tems has the potential to create electrically conducting systems, but at the expense of the thermal conduction of these systems (due to an increased interaction between electrons and phonons). The advantage of using doping if it could be achieved well, is that it may be possible to tailor nanostructures further, and introduce a clear method of tailoring their properties for use.

7.3 Final word

In this Thesis, the physics of phonons in silicon nanostructures and carbon nanotubes has been discussed. The fundamental quantity, the phonon dispersion relation, which is necessary for considering phonons in any structure has been obtained in Chapter 3. The results for nanostructures of various sizes have been discussed and the effects of dimensionality on their lattice dynamics has been presented. Based upon these phonon dispersion relations, the specific heat capacity of carbon nanotubes has been calculated in Chapter 4. The change over from one-dimensional behaviour to two-dimensional behaviour has been explained and a relationship for this occurrence, which is dependent on the nanotube size and temperature, has been obtained. Using the dispersion relations obtained in Chapter 3, detailed calculations of the lifetime of phonon modes in nanostructures have been performed using an approach based on Fermi's Golden Rule. In Chapter 5 the lifetime of the low-lying zone-centre optical modes has been calculated and shown to be comparable with that of bulk acoustic modes. Hence, it has been shown that these modes must be included for accurate calculations of the lifetime of phonon modes undergoing phonon-phonon interactions. Upon this basis the lifetime of phonon modes in carbon nanotubes were calculated and this lifetime has been shown to be of the order of nanoseconds. A correct one-dimensional model was described for the carbon nanotube, which considered the important angular momentum conditions which limit phonon-phonon interactions that had not been noted before. This model was adapted using Debye dispersion relations to provide analytic expressions for the relaxation rate of phonon modes. This analytic expression was shown to be in good agreement with numerical calculations based upon fully dispersive phonon dispersion relations. It was shown in Chapter 6 that the thermal conductivity is linearly dependent on temperature for between 75 K and 225 K. It was also shown that mass-defect scattering has substantially less effect in one-dimensional systems than in three-dimensional systems. Using the theory for boundary scattering, the reason for the vast number of different theoretical results is described as being a result of the ballistic free-path distance, L_0. These results are expected to be of great use to anyone who is researching into the theory or applications of nanotubes

or semiconducting nanostructures.

Appendix A

The Brillouin zone

A.1 Definition

It is conventional when defining a real structure in terms of its atomic co-ordinates in realspace to also define a set of vectors which correspond to reciprocal space. The unit cell (also known as the Wigner-Sietz Cell [27]) in reciprocal space is called the Brillouin zone. Reciprocal space is also described as momentum space.

The reciprocal lattice vectors are defined using their real space cousins by the following relations

$$\mathbf{a_1^*} = 2\pi \frac{\mathbf{a}_2 \wedge \mathbf{a}_3}{\mathbf{a}_1.(\mathbf{a}_2 \wedge \mathbf{a}_3)}, \tag{A.1}$$

$$\mathbf{a_2^*} = 2\pi \frac{\mathbf{a}_3 \wedge \mathbf{a}_1}{\mathbf{a}_1.(\mathbf{a}_2 \wedge \mathbf{a}_3)}, \tag{A.2}$$

$$\mathbf{a_3^*} = 2\pi \frac{\mathbf{a}_1 \wedge \mathbf{a}_2}{\mathbf{a}_1.(\mathbf{a}_2 \wedge \mathbf{a}_3)}. \tag{A.3}$$

Thus for the face centred cubic lattice (such as needed for the silicon structure) whose realspace vectors are described by Eq. (1.9) one generates the following lattice vectors

$$\mathbf{a_1^*} = \frac{2\pi}{a_{Si}}(-\hat{\mathbf{i}} + \hat{\mathbf{j}} + \hat{\mathbf{k}}), \tag{A.4}$$

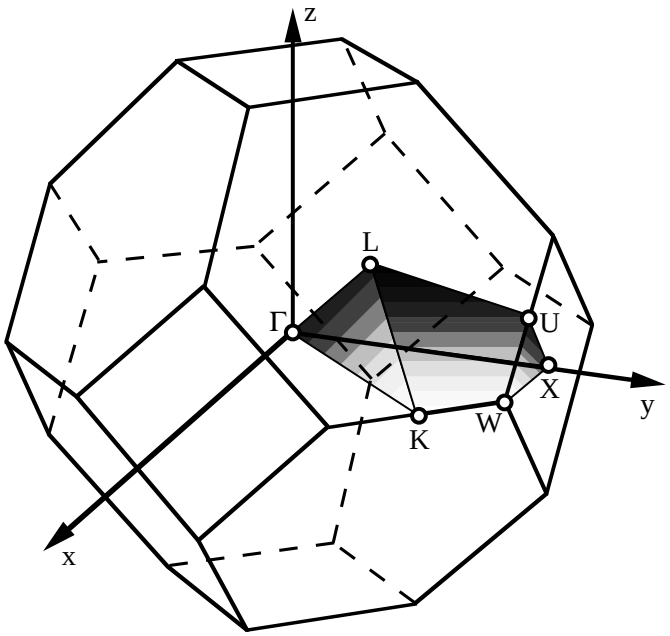

Figure A.1: The Brillouin zone for the face centred cubic lattice.

$$\mathbf{a_2^*} = \frac{2\pi}{a_{Si}}(\hat{\mathbf{i}} - \hat{\mathbf{j}} + \hat{\mathbf{k}}), \tag{A.5}$$

$$\mathbf{a_3^*} = \frac{2\pi}{a_{Si}}(\hat{\mathbf{i}} + \hat{\mathbf{j}} - \hat{\mathbf{k}}), \tag{A.6}$$

where the symbols have their usual meanings. This produces the central Brillouin zone of the form of a rhombic dodecahedron, which is shown in Fig. A.1.

A.2 Silicon Nanostructures

The nanostructures modelled in Chapter 3 are modelled within a super cell technique. Each of these supercells is a large cubic cell of dimensions $n_x a_{Si} \times n_y a_{Si} \times n_z a_{Si}$. Thus for this system, the reciprocal lattice vectors can be defined as

$$\begin{aligned} \mathbf{a}_1^* &= \frac{2\pi}{n_x a_{Si}}\hat{\mathbf{i}} \\ \mathbf{a}_2^* &= \frac{2\pi}{n_y a_{Si}}\hat{\mathbf{j}} \\ \mathbf{a}_3^* &= \frac{2\pi}{n_z a_{Si}}\hat{\mathbf{k}} \end{aligned} \tag{A.7}$$

where n_x, n_y and n_z are integers and a_{Si} is the cubic lattice constant of silicon. In this modelling technique, the Z direction is always considered the direction of

propagation of the system and the X direction is always considered the direction of confinement for the system.

It is important to define important points within the Brillouin zone which are labelled on Figs 3.4-3.12. These are

$$\begin{aligned} \Gamma &= (0,0,0) \\ X &= \frac{2\pi}{n_x a_{Si}}(1,0,0) \\ Y &= \frac{2\pi}{n_y a_{Si}}(0,1,0) \\ Z &= \frac{2\pi}{n_z a_{Si}}(0,0,1) \\ K &= \frac{2\pi}{a_{Si}}(1/n_x, 1/n_y, 0) \end{aligned} \tag{A.8}$$

A.3 Carbon nanotube

In the one-dimensional model used for the carbon nanotube, there is only one direction of propagation, the $\Gamma - Z$, which lies along the tube's axis. The length of the tube's unit cell is defined by the translation vector $\mathbf{T}$. Thus its reciprocal is

$$\mathbf{G} = \frac{2\pi}{|\mathbf{T}|}\hat{\mathbf{z}} \tag{A.9}$$

which for any (n,n) nanotube may be written as

$$\mathbf{G} = \frac{2\pi}{a_{c-c}}\hat{\mathbf{z}}. \tag{A.10}$$

and one defines two points within the Brillouin zone

$$\begin{aligned} \Gamma &= (0) \\ Z &= \frac{2\pi}{\sqrt{3}a_{c-c}}(1) \end{aligned} \tag{A.11}$$

where the symbols retain their usual meanings.

Appendix B

The $\mathbb{C}$-Matrix in the adiabatic bond charge model

B.1 The $\mathbb{C}$-Matrix

As shown in section 3.2.2.2 in Chapter 3, the $\mathbb{C}$-matrix for the adiabatic bond charge model takes the form

$$\mathbb{M}\omega^2\mathbf{e}_{ion} = [\mathbb{C}_{ion-ion} - \mathbb{C}_{ion-bc}\mathbb{C}_{bc-bc}^{-1}\mathbb{C}_{bc-ion}]\mathbf{e}_{ion}. \tag{B.1}$$

where $\mathbb{C}_{ion-ion}$, $\mathbb{C}_{ion-bc}$, $\mathbb{C}_{bc-bc}$, and $\mathbb{C}_{bc-ion}$ are the matrices for ion-ion, ion-bc (bond charge), bc-bc and bc-ion interaction respectively and have sizes $3N \times 3N$, $6N \times 3N$, $6N \times 6N$ and $6N \times 3N$ where N is the number of atoms in the unit cell. Each of these matrices may be separated into Coulomb and non-Coulomb parts. These can be expressed as

$$\begin{aligned}
\mathbb{C}_{ion-ion} &= \mathbb{R} + \frac{4Z^2}{\epsilon}\mathbb{R}_C \\
\mathbb{C}_{ion-bc} &= \mathbb{T} + \frac{2Z^2}{\epsilon}\mathbb{T}_C \\
\mathbb{C}_{bc-bc} &= \mathbb{S} + \frac{Z^2}{\epsilon}\mathbb{S}_C
\end{aligned} \tag{B.2}$$

where $\mathbb{C}_{ion-bc} = \mathbb{C}^{\dagger}_{bc-ion}$, Z is the charge of the bond charge, ϵ is the static dielectric constant, $\mathbb{R}$, $\mathbb{S}$ and $\mathbb{T}$ are the non-coulomb parts of the ion-ion, bc-bc, and ion-bc interaction matrices respectively and $\mathbb{R}_C$, $\mathbb{S}_C$ and $\mathbb{T}_C$ are the corresponding coulombic matrices.

Hence it is now appropriate to consider the form of each of these matrices.

B.2 The Coulomb interaction

The elements of the Coulomb force matrix between two charges, Q_b and $Q_{b'}$ at a distance r apart is given by

$$\Phi^{C}_{\alpha\beta}(\mathbf{lb};\mathbf{l'b'}) = \frac{1}{4\pi\epsilon_0}\frac{\delta^2}{\delta x_\alpha \delta x_\beta}\frac{Q_b Q_{b'}}{r}\bigg|_{\mathbf{r}=\mathbf{x}(lb;l'b')} \tag{B.3}$$

given that $(\mathbf{lb}) \neq (\mathbf{l'b'})$. Using Ewald's summation technique, one may obtain the Fourier component of Eq. (B.3) [115]. This technique yields an expression of the form

$$\begin{aligned}\mathbb{X}_{\alpha\beta}(bb'|\mathbf{q}) \;=\; & \frac{1}{4\pi\epsilon_0}\frac{-4\pi e^2}{V_{uc}}\times \\ & \Bigg(\sum_{\mathbf{G}}\frac{(\mathbf{q}+\mathbf{G})_\alpha(\mathbf{q}+\mathbf{G})_\beta}{(\mathbf{q}+\mathbf{G})^2}\exp\left[-\frac{(\mathbf{q}+\mathbf{G})^2}{4\eta}\right]\exp\left[i\mathbf{q}.(\mathbf{x}(\mathbf{lb})-\mathbf{x}(\mathbf{l'b'}))\right] \\ & +\eta^{\frac{3}{2}}V_{uc}\sum_{l'}\mathbb{H}_{\alpha\beta}(\sqrt{\eta}|\mathbf{x}(\mathbf{lb})-\mathbf{x}(\mathbf{l'b'})|)\exp\left[i\mathbf{q}.(\mathbf{x}(\mathbf{l'b'})-\mathbf{x}(\mathbf{lb}))\right]\Bigg),\end{aligned} \tag{B.4}$$

where η is a convergence parameter and V_{uc} is the unit cell volume. $\mathbf{G}$ is the reciprocal lattice vector (defined in Appendix A), and $\mathbb{X}$ represents one of the coulombic terms from the $\mathbb{C}-$matrix, $\mathbb{R}_C$, $\mathbb{S}_C$ and $\mathbb{T}_C$. The function $\mathbb{H}$ is given by

$$\mathbb{H}_{\alpha\beta}(\mathbf{x}) = \frac{\delta^2}{\delta x_\alpha \delta x_\beta}\left[\frac{2}{\sqrt{\pi}}\frac{1}{|\mathbf{x}|}\int_{|\mathbf{x}|}^{\infty}\exp(-s^2)ds\right], \tag{B.5}$$

and

$$\mathbb{H}_{\alpha\beta}(\mathbf{0}) = \frac{4}{3}\sqrt{\pi}\delta_{bb'}. \tag{B.6}$$

It is important to note that $\mathbb{H}_{\alpha\beta}$ is related to the complementary error function by

$$xH(x) = \mathrm{erfc}(x) = \frac{2}{\sqrt{\pi}}\int_{x}^{\infty}\exp(-s^2)ds. \tag{B.7}$$

By examining Eq. (B.2), it can be seen that the coulomb contribution to the $\mathbb{C}$ matrix has only one adjustable parameter Z^2/ϵ where Z is the charge of the bond-charge and ϵ is the dielectric constant.

B.3 The central short-range interaction

The central force acts directly between atoms. It is attractive in nature when the atoms are further apart than their equilibrium positions and repulsive when the atoms are closer than their equilibrium positions. It can be compared to the force between objects connected via a spring. This simplistic spring model is the basis of the monotonic chain model. In the adiabatic bond charge model, the central force is described in terms of the potential energy of the crystal similar to that of the Born Von Karman force. In this approach, one assumes that the potential energy of the crystal may be written as a sum of pair potentials $\phi(r(\mathbf{lb};\mathbf{l'b'}))$ where $r(\mathbf{lb};\mathbf{l'b'})$ is the instantaneous distance between the particles located at $(\mathbf{lb})$ and $(\mathbf{l'b'})$. Hence

$$\Phi = \frac{1}{4}\sum_{\mathbf{lb}}\sum_{\mathbf{l'b'}}\phi_{\mathbf{bb'}}(r(\mathbf{lb};\mathbf{l'b'})) \tag{B.8}$$

with the condition that $(\mathbf{lb}) \neq (\mathbf{l'b'})$ (so this term is omitted) and the factor of a half to ensure that each term is counted only once. Here $\mathbf{r}(\mathbf{lb};\mathbf{l'b'})$, $\mathbf{x}(\mathbf{lb};\mathbf{l'b'})$ and $\mathbf{u}(\mathbf{lb};\mathbf{l'b'})$ are defined as

$$\begin{aligned}
\mathbf{r}(\mathbf{lb};\mathbf{l'b'}) &= \mathbf{r}(\mathbf{lb}) - \mathbf{r}(\mathbf{l'b'}) \\
\mathbf{x}(\mathbf{lb};\mathbf{l'b'}) &= \mathbf{x}(\mathbf{lb}) - \mathbf{x}(\mathbf{l'b'}) \\
\mathbf{u}(\mathbf{lb};\mathbf{l'b'}) &= \mathbf{r}(\mathbf{lb};\mathbf{l'b'}) - \mathbf{x}(\mathbf{lb};\mathbf{l'b'}) \\
&= \mathbf{u}(\mathbf{lb}) - \mathbf{u}(\mathbf{l'b'})
\end{aligned} \tag{B.9}$$

where $\mathbf{u}(\mathbf{lb})$ is the displacement of atom lb, $\mathbf{x}(\mathbf{lb})$ is its mean (or original) position and $\mathbf{x}(\mathbf{lb})$ is the atoms current (or displaced) position. The potential can be expanded using Taylor's theory about $\mathbf{u}(\mathbf{lb};\mathbf{l'b'})$ as was done in Eqs. (3.2) and (3.3).

Thus Φ_2 can be written as

$$\begin{aligned}\Phi_2 &= \frac{1}{4}\sum_{\mathbf{lb}\alpha}\sum_{\mathbf{l'b'}\beta}\phi_{\alpha\beta}(\mathbf{lb};\mathbf{l'b'})u_\alpha(\mathbf{lb};\mathbf{l'b'})u_\beta(\mathbf{lb};\mathbf{l'b'})) \\ &= \frac{1}{2}\sum_{\mathbf{lb}\alpha}\sum_{\mathbf{l'b'}\beta}\phi_{\alpha\beta}(\mathbf{lb};\mathbf{l'b'})[u_\alpha(\mathbf{lb})u_\beta(\mathbf{lb}) - u_\alpha(\mathbf{lb})u_\beta(\mathbf{l'b'})], \qquad \text{(B.10)}\end{aligned}$$

where

$$\begin{aligned}\phi_{\alpha\beta}(\mathbf{lb};\mathbf{l'b'}) &= \frac{\delta^2}{\delta x_\alpha \delta x_\beta}\phi_{bb'}(r)\bigg|_{\mathbf{r}=\mathbf{x}(\mathbf{lb};\mathbf{l'b'})} \\ &= \left\{\frac{x_\alpha x_\beta}{r^2}\left[\phi''_{bb'}(r) - \frac{1}{r}\phi'_{bb'}(r)\right] + \frac{\delta_{\alpha\beta}}{r}\phi'_{bb'}(r)\right\}\bigg|_{\mathbf{r}=\mathbf{x}(\mathbf{lb};\mathbf{l'b'})}, \qquad \text{(B.11)}\end{aligned}$$

with $\phi' = d\phi/dr$ and $\phi'' = d^2\phi/dr^2$. These may be regarded as a set of six constants which consist of ϕ'_{i-i}, ϕ'_{i-bc}, ϕ'_{bc-bc}, ϕ''_{i-i} ϕ''_{i-bc} and ϕ''_{bc-bc}. However, of these force constants, ϕ'_{bc-bc} and ϕ''_{bc-bc} are tiny forces and are set to zero, leaving only four force constants. Comparing Eq. (B.10) with Eq. (3.3) reveals that one can show the force constants are related to the pair potential by

$$\begin{aligned}\Phi_{\alpha\beta}(\mathbf{lb};\mathbf{l'b'}) &= -\phi_{\alpha\beta}(\mathbf{lb};\mathbf{l'b'}) \\ \Phi_{\alpha\beta}(\mathbf{lb};\mathbf{lb}) &= \sum_{\mathbf{l'b'}\neq\mathbf{lb}}\phi_{\alpha\beta}(\mathbf{lb};\mathbf{l'b'}) \qquad \text{(B.12)}\end{aligned}$$

and from these relations it is possible to calculate the central components of the dynamical matrix.

B.4 Bond-bending Keating-type interaction

The central short range force is insufficient for describing the lattice dynamical behaviour of covalently bonded semiconductors and an additional indirect (or non-central) force is required. This force can be viewed as a bond-bending force or anti-compressive force that resists the distortion of the bonds between the atoms. The force is simulated by considering a Keating-style potential [111] between an ion

and two of its bond charges of the form

$$V_K(b) = \frac{B_b}{2}\frac{(\mathbf{r}_{b\Upsilon}.\mathbf{r}_{b\Upsilon'} + a_b^2)^2}{4a_b^2}, \tag{B.13}$$

where B_b is a measure of the potential strength, $\mathbf{r}_{b\Upsilon}$ and $\mathbf{r}_{b\Upsilon'}$ are the instantaneous distance vectors between ion b and its two neighbouring bond charges Υ and Υ' and

$$a_b^2 = -\mathbf{x_{b\Upsilon}}.\mathbf{x_{b\Upsilon'}}. \tag{B.14}$$

Hence, one writes the corresponding force constant matrix as

$$\Phi_{ij}^K(b;\Upsilon) = \frac{B_b}{4a_b^2}\sum_{\Upsilon'}(r_j(\Upsilon') - r_j(b))(r_i(\Upsilon) + r_i(\Upsilon') - 2r_i(b)). \tag{B.15}$$

As these interactions are only ever considered over nearest neighbours this contributes one additional force constant $B_b = B_1$ which bring the total number of parameters to six.

B.5 Reducing parameters

The six parameters presented are all physical meaningful. Six is consider an acceptable number of parameters for many phenomenological models, but it is preferable to reduce this number further it is possible. One can reduce this number by relating different parameters using the Madelung energy [113].

This energy shows that the total energy per atom of the system may be written as

$$E = \sum_n c_n\phi_n(r) - \frac{1}{2}\alpha_M\frac{4Z^2}{\epsilon}\frac{e^2}{r}\frac{1}{4\pi\epsilon_0} \tag{B.16}$$

where c_n are the appropriate prefactors from the interaction matrices for the short range potentials ϕ_n and α_M is the Madelung constant (which is dependent on the crystal structure).

For IV-IV semiconductors the equilibrium condition ($\frac{\delta E}{\delta r} = 0$) is

$$\begin{aligned}\frac{\delta E}{\delta r} &= 0 \\ &= 2\phi_{i-i}(r_0) + 2\phi'_{i-b}(\frac{r_0}{2}) + r_0V'_K(-\frac{1}{12}r_0^2) + \alpha_M\frac{4Z^2e^2}{\epsilon r_0^2}\frac{1}{8\pi\epsilon_0}\end{aligned} \tag{B.17}$$

However, for IV-IV semiconductors, the off-diagonal term ϕ'_{i-b} is zero. This is because: (i) its magnitude is very small and (ii) of the conditions arising from rotational invariance [183, 111] first-neighbour non-central terms disappear. Also, one can see from Eq. (B.13) that V'_K=0 in equilibrium. Thus, ϕ_{i-i} can be obtained in terms of the Madelung constant (a known measurable quantity) which reduces the total number of parameters to four for IV-IV systems.

Appendix C

Highest optical mode in nanostructures

Note. In this chapter, the notation used is independent of all other chapters and appendices. As such several symbols previously used are given different definitions here. The reader is asked to ignore the meaning of any notation presented elsewhere in this thesis and to see the Table of Notation presented at the end of this Appendix.

Due to quantisation, the frequency of the highest optical mode in nanostructures is decreased. It can be observed that the smaller a nanostructure is, the greater this decrease is. This behaviour can be explained using a diatomic spring constant model. This approach was first developed by Jusserand *et al.* [126] for superlattices. Here the method is expanded and refined for nanostructures.

In superlattices, which are a series of alternating layers of two different materials, it was observed that the highest optical mode of each material was lower than the bulk

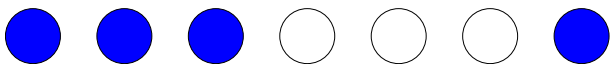

Figure C.1: The diatomic model for a superlattices used by Jusserand *et al.* [126]. Here the blue atoms correspond to atoms of mass m_1 and the white atoms correspond to atoms of mass m_2.

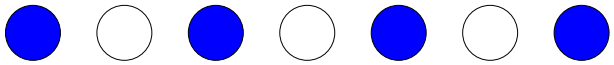

Figure C.2: A schematic showing the simple diatomic chain model. Here the blue atoms correspond to atoms of mass m_1 and the white atoms correspond to atoms of mass m_2.

value. It is expected that Jusserand's relations would also hold true for isolated thin slabs of materials. The reason for this similarity is because each layer has different forces between the atoms and also has different mass density. The original model conceived to show this effect for superlattices is shown in Fig. C.1. This figure shows a linear chain of atoms. At first glance, this model appears to be a one-dimensional model. However, it can be assumed that the quantisation behaviour that occurs in superlattices is due to the alternating layers which lie in one axis of motion. The other two directions are free to propagate naturally and thus no quantisation effects will occur in these directions. Here, these alternating layers of materials are classed as material 1, and material 2 for ease of description. From this model, Jusserand *et al.* showed that the highest optical mode of each material varies as

$$\omega^2_{op,(1,2)} = \omega_{bu(1,2)} - v^2_{L,(1,2)} \left(\frac{i'\pi}{(N_{(1,2)}+1)a} \right)^2, \tag{C.1}$$

where $\omega_{optical}$ is the frequency of the optical mode of the material in the superlattice, $\omega_{optical-bulk(1,2)}$ is the frequency of the optical mode in the bulk material 1 or 2 and $N_{1,2}$ is the number of atoms thickness in layer 1 or 2. a is the bond-length and i' corresponds to an integer number between 1 and $N_{1,2}$, which represents the zone-folding effect [126]. $v^2_{L,(1,2)}$ is the group velocity of the optical mode. There are two important assumptions used within the Jusserand model: (i) $|\mathbf{q}| = q \propto \frac{1}{d}$ where $\mathbf{q}$ is the wave-vector and d is thickness of the layer and (ii) only atomic interactions within $2a$ of each atom are considered (i.e. only nearest neighbours in the linear chain model).

Figure C.2 shows the the simple diatomic lattice. This is a well known system which consists of two atoms of masses m_1 and m_2 where one considers the distance between each of these atoms as a. If one considers the chain infinitely long and defines atom m_1 as the $2n^{th}$ atom and atom m_2 as the $(2n+1)^{th}$ atom, then one may describe the forms of the standard equations of motion for these atoms, which are given in

most solid state text books [27]. These are

$$m_1 \frac{d^2 u_{2n}}{dt^2} = \Lambda_1[(u'_{2n+1} - u_{2n}) + (u'_{2n-1} - u_{2n})] \tag{C.2}$$

$$m_2 \frac{d^2 u'_{2n+1}}{dt^2} = \Lambda_1[(u_{2n+2} - u'_{2n+1}) + (u_{2n} - u'_{2n+1})] \tag{C.3}$$

where Λ_1 is the nearest neighbour force constant and u_{2n} and u'_{2n+1} are the displacements of the $2n^{th}$ and $(2n+1)^{th}$ atom.

Here one uses trial solutions of the form

$$u_{2n} = A_1 \exp[i(2nqa - \omega t)], \tag{C.4}$$

$$u'_{2n+1} = A_2 \exp[i((2n+1)qa - \omega t)]. \tag{C.5}$$

These expressions when applied to Eqs. (C.2) and (C.3) produce a pair of coupled eigenvalue equations which can be written in the form

$$\omega^2 A_i = \sum_{j=1}^{2} \mathbb{D}_{ij} A_i \tag{C.6}$$

where $i = 1, 2$ and $\mathbb{D}$ is a two by two dynamical matrix of the form

$$\mathbb{D} = \begin{pmatrix} \frac{2\Lambda_1}{m_1} & \frac{2\Lambda_1}{m_1}\cos(qa) \\ \frac{2\Lambda_1}{m_2}\cos(qa) & \frac{2\Lambda_1}{m_2} \end{pmatrix}. \tag{C.7}$$

The resulting solutions are of the form

$$\omega^2 = \Lambda_1 \left(\frac{1}{m_1} + \frac{1}{m_2}\right) \pm \Lambda_1 \left[\left(\frac{1}{m_1} + \frac{1}{m_2}\right)^2 - \frac{4}{m_1 m_2}\sin^2(qa)\right]^{\frac{1}{2}}. \tag{C.8}$$

This is a standard and well known solution, but it can be applied to produce a Jusserand-like result. To this end, one assumes the long wavelength limit and applies the same condition as Jusserand, i.e. $q \propto 1/d$. By expanding Eq. (C.8) and replacing $\sin(qa)$ with a'/d one can show

$$\omega^2 = \Lambda_1 \left[\left(\frac{1}{m_1} + \frac{1}{m_2}\right) + \frac{1}{2}\left[\left(\frac{1}{m_1} + \frac{1}{m_2}\right)^2 - \frac{4a'^2}{m_1 m_2 d^2}\right]\right] \tag{C.9}$$

or

$$\omega^2 = \omega_{bulk}^2 - \frac{B_1}{d^2} \tag{C.10}$$

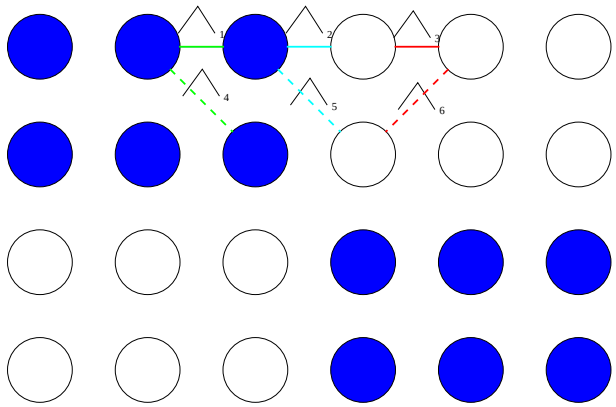

Figure C.3: A schematic showing the ideal method for modelling a nanowire using an identical Jusserand technique. Blue atoms have mass m_1 and white atoms have mass m_2. Also shown are all the force constants that must be considered within this approach.

where a' and B_1 are constants. The second result is implied from Eq. (C.8) as when the sine term is zero, then the positive solution must equal the value of the zone centre optical mode.

For a nanowire or nanodot, this procedure can be extended to take into account confinement in two- or three-dimensions. In an ideal case, one would prefer to consider a two-dimensional system such as that shown in Fig. C.3. However, this is a very complicated system which generates a very large matrix. This limits its applicability. Secondly, as shown by the previous example for superlattices and nanoslabs, the result can be predicted from a more simple model; that of a diatomic grid of atoms.

Here, the approach used above is applied to nanowires, and can be applied to nanodots to show the results described in section 3.3.3.4 in Chapter 3. The diatomic grid is shown in Fig. C.4. In this approach, the same condition of only considering neighbours within a distance of $2a$ of selected atom is considered. Thus one considers nearest neighbour interactions, which lie along the $x-$ and $y-$axis, and the next nearest neighbour, which lies along the lines denoted by $y = x$ and $y = -x$ as indicated in Fig. C.4.

Hence following the above approach, one can state equations of motion for the two

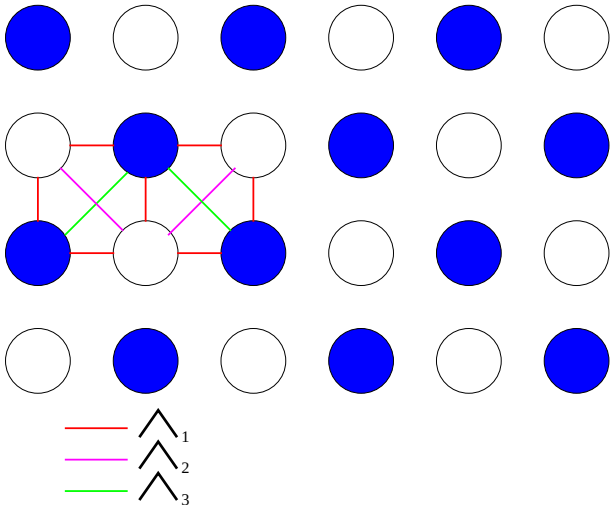

Figure C.4: A schematic showing the adopted method for modelling a nanowire confinement effects on the optical mode. Blue atoms have mass m_1 and white atoms have mass m_2. Also shown are all the force constants that must be considered within this approach. Here A corresponds to Λ_1, B corresponds to Λ_2 and C corresponds to Λ_3 used in the text.

atoms of m_1 and m_2 which are denoted as the $(2n, 2m)^{th}$ atom and $(2n+1, 2m)^{th}$. These take the form of

$$\begin{aligned} m_1\frac{d^2u_{2n,2m}}{dt^2} &= \Lambda_1[u_{2n+1,2m} + u_{2n-1,2m} + u_{2n,2m+1} + \\ &\quad u_{2n,2m-1} - 4u_{2n,2m}] + \\ &\quad \Lambda_2[u_{2n+1,2m+1} + u_{2n+1,2m-1} + u_{2n-1,2m+1} + \\ &\quad u_{2n-1,2m-1} - 4u_{2n,2m}], \end{aligned} \tag{C.11}$$

and

$$\begin{aligned} m_2\frac{d^2u_{2n+1,2m}}{dt^2} &= \Lambda_1[u_{2n+2,2m} + u_{2n,2m} + u_{2n+1,2m+1} + \\ &\quad u_{2n+1,2m-1} - 4u_{2n+1,2m}] + \\ &\quad \Lambda_3[u_{2n+2,2m+1} + u_{2n+2,2m-1} + u_{2n,2m+1} + \\ &\quad u_{2n,2m-1} - 4u_{2n+1,2m}], \end{aligned} \tag{C.12}$$

where Λ_1, Λ_2 and Λ_3 are force constants. Like previously, one assumes trial wave functions.

$$u_{2n,2m,x(y)} = A_{1,x(y)}exp[i(\mathbf{q}.\mathbf{r_1} - \omega t)] \tag{C.13}$$

$$u_{2n+1,2m,x(y)} = A_{2,x(y)}exp[i(\mathbf{q}.\mathbf{r_2} - \omega t)] \tag{C.14}$$

where $\mathbf{q}.\mathbf{r_1} = 2q_x na + 2q_y ma$ and $\mathbf{q}.\mathbf{r_2} = 2q_x(n+1)a + 2q_y ma$.

Equations (C.11) and (C.12) are expanded using Eqs. (C.13) and (C.14), which yield expressions of the form

$$\begin{aligned} \mathbf{A_1}\omega^2 &= \Lambda_1[\mathbf{A_2}cos(q_x a) + \mathbf{A_2}cos(q_y a) - 4\mathbf{A_1}] + \\ &\quad \Lambda_2[\mathbf{A_1}cos(q_x a + q_y a) + \mathbf{A_1}cos(q_x a - q_y a) - 4\mathbf{A_1}] \end{aligned} \tag{C.15}$$

and

$$\begin{aligned} \mathbf{A_2}\omega^2 &= \Lambda_1[\mathbf{A_1}cos(q_x a) + \mathbf{A_1}cos(q_y a) - 4\mathbf{A_2}] + \\ &\quad \Lambda_3[\mathbf{A_2}cos(q_x a + q_y a) + \mathbf{A_2}cos(q_x a - q_y a) - 4\mathbf{A_2}] \end{aligned} \tag{C.16}$$

From these two the $\mathbb{D}$ matrix may be formed. This is diagonalised and solved for ω^2 like previously. The positive solution from the quadratic equation is obtained and expanded using the small angle identities. This yields, after some algebraic manipulation, the following relation

$$\omega^2 = C_1 + \frac{C_2}{d^2} + \frac{C_3}{d^3} + \textit{2nd order and greater terms} \tag{C.17}$$

for nanowires where C_{1-3} are constants. For nanodots, the above approach is expanded to three-dimensions to reflect three-dimensional confinement. In this approach a fourth force constant, Λ_4 is necessary. This force constant acts along the lines $y = x = z$, $x = -y = z$, $x = y = -z$ and $x = -y = -z$ between third nearest neighbours. This yields a relation of the form

$$\omega^2 = D_1 + \frac{D_2}{d^2} + \frac{D_3}{d^3} + \frac{D_4}{d^4} + \textit{2nd order and greater terms} \tag{C.18}$$

where D_{1-4} are constants.

C.1 Table Of Notation

a	The bond length.
$A_{1,2}$	The amplitude of atom 1 or 2.
B_1	The parameter in Eq. (C.10).
C_{1-2}	The parameters in Eq. (C.17).
D_{1-3}	The parameters in Eq. (C.18).
d	The width of confinement of the nanostructure.
$\mathbb{D}$	The dynamical matrix.
$\mathbf{q}$	The wave-vector.
Λ_{1-4}	The nearest neighbour, next nearest etc. force constants.
$m_{1,2}$	The mass of atom 1 or 2.
$N_{1,2}$	The number of atoms thickness that layer 1 or 2 is in the superlattice.
t	The time co-ordinate.
u_j	The displacement of atom i.
$u_{j,k}$	The displacement of atom.
$v^2_{L,(1,2)}$	The group velocity of the optical mode.
ω	The angular frequency.
ω_{bu}	The angular frequency of the highest optical mode in bulk.
ω_{op}	The angular frequency of the highest optical mode.
x, y, z	The x, y and z co-ordinates.

Appendix D

Linearised Boltzmann equation

The linearised Boltzmann equation is a simplified form of the generalised Boltzmann equation [131] for phonons. This equation takes the form

$$-\mathbf{c}_s(\mathbf{q}).\nabla T\frac{\delta n_{\mathbf{q}s}}{\delta T}+\left.\frac{\delta n_{\mathbf{q}s}}{\delta t}\right|_{scatt}=0, \tag{D.1}$$

where $\left.\frac{\delta n_{\mathbf{q}s}}{\delta t}\right|_{scatt}$ represents the rate of change due to the various scattering events. ∇T represents the temperature gradient, where $T\equiv T(\mathbf{r})$ and $\mathbf{c}_s(\mathbf{q})$ is the group velocity of the phonon.

To change the generalised form to the linear form of this equation, one notes that the equilibrium distribution, $\bar{n}_{\mathbf{q}s}$, does not change with time, and replaces $n_{\mathbf{q}s}$ in the second term with the linear Taylor expansion in $n_{\mathbf{q}s}-\bar{n}_{\mathbf{q}s}$. Furthermore, if one assumes that a steady state exists, and that the temperature gradient is small, then one replaces $n_{\mathbf{q}s}$ in the first term of Eq. (D.1) with $\bar{n}_{\mathbf{q}s}$. Hence one can write Eq. (D.1) as

$$\begin{aligned}-\mathbf{c}_s(\mathbf{q}).\nabla T\frac{\delta \bar{n}_{\mathbf{q}s}}{\delta T} &= \left.\frac{\delta n_{\mathbf{q}s}}{\delta t}\right|_{scatt}\\ &= \frac{n_{\mathbf{q}s}-\bar{n}_{\mathbf{q}s}}{\tau_{\mathbf{q}s}},\end{aligned} \tag{D.2}$$

where $\tau_{\mathbf{q}s}$ is the total relaxation time for phonon $\mathbf{q}s$.

To evaluate Eq. (D.2), one must introduce a new function $\psi_{\mathbf{q}s}$ which is defined by

$$\begin{aligned} n_{\mathbf{q}s} &= [\exp(\hbar\omega(\mathbf{q}s)/k_BT - \psi_{\mathbf{q}s}) - 1]^{-1} \\ &\simeq \bar{n}_{\mathbf{q}s} - \psi_{\mathbf{q}s}\frac{\delta\bar{n}_{\mathbf{q}s}}{\delta(\hbar\omega(\mathbf{q}s))} \\ &= \bar{n}_{\mathbf{q}s} + \psi_{\mathbf{q}s}\bar{n}_{\mathbf{q}s}(\bar{n}_{\mathbf{q}s}+1) \end{aligned} \tag{D.3}$$

Hence $\psi_{\mathbf{q}s}$ may be viewed as a deviation from the equilibrium distribution for phonons in mode $\mathbf{q}s$. Thus one may rewrite Eq. (D.2) as

$$\begin{aligned} \left.\frac{\delta n_{\mathbf{q}s}}{\delta T}\right|_{scatt} &= \frac{n_{\mathbf{q}s} - \bar{n}_{\mathbf{q}s}}{\tau_{\mathbf{q}s}} \\ &= \frac{\psi_{\mathbf{q}s}\bar{n}_{\mathbf{q}s}(\bar{n}_{\mathbf{q}s}+1)}{\tau_{\mathbf{q}s}}, \end{aligned} \tag{D.4}$$

To understand $\psi_{\mathbf{q}s}$ further, one considers the general inelastic event of the type

$$(\mathbf{q}s) + (\mathbf{q}'s') \rightarrow (\mathbf{q}''s'') + (\mathbf{q}'''s''') \tag{D.5}$$

Hence, the transition probability for this process is

$$P^{\mathbf{q}''s'',\mathbf{q}'''s'''}_{\mathbf{q}s,\mathbf{q}'s'} = n_{\mathbf{q}s}n_{\mathbf{q}'s'}(n_{\mathbf{q}''s''}+1)(n_{\mathbf{q}'''s'''}+1)Q^{\mathbf{q}''s'',\mathbf{q}'''s'''}_{\mathbf{q}s,\mathbf{q}'s'} \tag{D.6}$$

where $Q^{\mathbf{q}''s'',\mathbf{q}'''s'''}_{\mathbf{q}s,\mathbf{q}'s'}$ is the intrinsic transition probability. This transition rate is the same in either direction (i.e. $Q^{\mathbf{q}''s'',\mathbf{q}'''s'''}_{\mathbf{q}s,\mathbf{q}'s'} = Q^{\mathbf{q}s'',\mathbf{q}'s'}_{\mathbf{q}''s'',\mathbf{q}'''s'''}$) due to the principle of microscopic reversibility. Thus one can write

$$\begin{aligned} \left.\frac{\delta n_{\mathbf{q}s}}{\delta T}\right|_{scatt} &= \sum_{\mathbf{q}'s'}\sum_{\mathbf{q}''s''}\sum_{\mathbf{q}'''s'''}\left(P^{\mathbf{q}''s'',\mathbf{q}'''s'''}_{\mathbf{q}s,\mathbf{q}'s'} - P^{\mathbf{q}s,\mathbf{q}'s'}_{\mathbf{q}''s'',\mathbf{q}'''s'''}\right) \\ &= \sum_{\mathbf{q}'s'}\sum_{\mathbf{q}''s''}\sum_{\mathbf{q}'''s'''}[n_{\mathbf{q}''s''}n_{\mathbf{q}'''s'''}(n_{\mathbf{q}s}+1)(n_{\mathbf{q}'s'}+1) - \\ &\quad n_{\mathbf{q}s}n_{\mathbf{q}'s'}(n_{\mathbf{q}''s''}+1)(n_{\mathbf{q}'''s'''}+1)]Q^{\mathbf{q}''s'',\mathbf{q}'''s'''}_{\mathbf{q}s,\mathbf{q}'s'} \end{aligned} \tag{D.7}$$

which using Eq. (D.3) may be rewritten as

$$-\frac{\delta n_{\mathbf{q}s}}{\delta T} = \sum_{\mathbf{q}'s'}\sum_{\mathbf{q}''s''}\sum_{\mathbf{q}'''s'''}\left(\psi_{\mathbf{q}s} + \psi_{\mathbf{q}'s'} - \psi_{\mathbf{q}''s''} - \psi_{\mathbf{q}'''s'''}\right)\bar{P}^{\mathbf{q}''s'',\mathbf{q}'''s'''}_{\mathbf{q}s,\mathbf{q}'s'} \tag{D.8}$$

To derive this, one must use the relation

$$\bar{n}_{\mathbf{q}''s''}\bar{n}_{\mathbf{q}'''s'''}(\bar{n}_{\mathbf{q}s}+1)(\bar{n}_{\mathbf{q}'s'}+1) = \bar{n}_{\mathbf{q}s}\bar{n}_{\mathbf{q}'s'}(\bar{n}_{\mathbf{q}''s''}+1)(\bar{n}_{\mathbf{q}'''s'''}+1) \tag{D.9}$$

which maintains balance between forward and backward directions and can be verified using the energy conservation condition $\omega(\mathbf{q}s) + \omega(\mathbf{q}'s') = \omega(\mathbf{q}''s'') + \omega(\mathbf{q}'''s''')$.

Appendix E

Single-mode relaxation time approach (*smrt*)

For three-phonon processes, using Appendix D, one can write the scattering rate as

$$\left.\frac{\delta n_{\mathbf{q}s}}{\delta t}\right|_{3\ ph} = \sum_{\mathbf{q}'s'}\sum_{\mathbf{q}''s''}\left[(P^{\mathbf{q}'s'}_{\mathbf{q}s,\mathbf{q}''s''} - P^{\mathbf{q}s,\mathbf{q}''s''}_{\mathbf{q}'s'}) + \frac{1}{2}(P^{\mathbf{q}'s',\mathbf{q}''s''}_{\mathbf{q}s} - P^{\mathbf{q}s}_{\mathbf{q}'s',\mathbf{q}''s''})\right] \tag{E.1}$$

where the symbols have their usual meanings. The 1/2 factor is to avoid double counting within the summations. Following the approach outlined in Appendix D one can linearise Eq. (E.1) and express

$$\begin{aligned}\left.\frac{\delta n_{\mathbf{q}s}}{\delta t}\right|_{3\ ph} = & \sum_{\mathbf{q}'s'}\sum_{\mathbf{q}''s''}\Bigg[\bar{P}^{\mathbf{q}'s'}_{\mathbf{q}s,\mathbf{q}''s''}(\psi_{\mathbf{q}s} + \psi_{\mathbf{q}'s'} - \psi_{\mathbf{q}''s''}) \\ & + \frac{1}{2}\bar{P}^{\mathbf{q}'s',\mathbf{q}''s''}_{\mathbf{q}s}(\psi_{\mathbf{q}s} - \psi_{\mathbf{q}'s'} - \psi_{\mathbf{q}''s''})\Bigg].\end{aligned} \tag{E.2}$$

In the single-mode relaxation time approach, one assumes that only the phonons in mode $\mathbf{q}s$ have a non-equilibrium distribution, i.e. $\psi_{\mathbf{q}s} \neq 0$ and $\psi_{\mathbf{q}'s'} = \psi_{\mathbf{q}''s''} = 0$. Hence one can rewrite Eq. (E.2) using Eq. (D.4) as

$$\tau^{-1}_{\mathbf{q}s} = \frac{1}{\bar{n}_{\mathbf{q}s}(\bar{n}_{\mathbf{q}s}+1)}\sum_{\mathbf{q}'s'}\sum_{\mathbf{q}''s''}\left(\bar{P}^{\mathbf{q}''s''}_{\mathbf{q}s,\mathbf{q}'''s'''} + \frac{1}{2}\bar{P}^{\mathbf{q}''s'',\mathbf{q}'''s'''}_{\mathbf{q}s}\right) \tag{E.3}$$

Appendix F

Mass Defect Scattering

Let

$$\bar{M} \equiv \sum_i f_i M_i = \frac{N}{p} \sum_j M_j \tag{F.1}$$

be the average mass of the material, with f_i the fraction of unit cells having mass M_i and N/p be the number of unit cells in the solid. For a carbon nanotube this ratio is related to translation vector. Using Eq. (1.6) from Chapter 1 one can show that $N/p = |\mathbf{T}|/L_0$. From this approach, the crystal Hamiltonian can be written as

$$\begin{aligned} H &= \sum_j \frac{1}{2} M_j \dot{u}_j^2 + V_2 \\ &= H_0 + H_{md} \end{aligned} \tag{F.2}$$

where $H_0 = \sum_j \frac{1}{2}\bar{M}\dot{u}_j^2 + V_2$ is the unperturbed part of the system. The perturbed term due to the mass difference takes the form

$$\begin{aligned} H_{md} &= \sum_j \frac{1}{2}(M_j - \bar{M})\dot{u}_j^2 \\ &= \sum_j \frac{1}{2}\Delta M_j \dot{u}_j^2 \end{aligned} \tag{F.3}$$

Using Eq. (5.3) with Eq. (F.3) one can show that

$$\begin{aligned} H &= \frac{\hbar}{4\rho' L_0} \sum_{\mathbf{q}s\mathbf{q}'s'} \sqrt{\omega(\mathbf{q}s)\omega(\mathbf{q}'s')}\mathbf{e}^*_{\mathbf{q}s}.\mathbf{e}_{\mathbf{q}'s'}(a^\dagger_{\mathbf{q}s} - a_{-\mathbf{q}s})(a^\dagger_{\mathbf{q}'s'} - a_{-\mathbf{q}'s'})\mathcal{M}_{\mathbf{q}\mathbf{q}'} \\ &= \sum_{\mathbf{q}s\mathbf{q}'s} H_{md}(\mathbf{q}s, \mathbf{q}'s') \end{aligned} \tag{F.4}$$

where

$$\mathcal{M}_{\mathbf{q}\mathbf{q}'} = \sum_j \Delta M_j e^{[i(\mathbf{q}-\mathbf{q}').\mathbf{r}_j]}, \tag{F.5}$$

and

$$\begin{aligned} |\mathcal{M}_{\mathbf{q}s\mathbf{q}'s'}|^2 &= \sum_{j,j'} \Delta M_j \Delta M_{j'} e^{[i(\mathbf{q}-\mathbf{q}').(\mathbf{r}_j-\mathbf{r}_{j'})]} \\ &= \sum_j (\Delta M_j)^2 + \sum_{j\neq j'} \Delta M_j \Delta M_{j'} e^{[i(\mathbf{q}-\mathbf{q}').(\mathbf{r}_j-\mathbf{r}_{j'})]} \\ &= \sum_j (\Delta M_j)^2 \\ &= \sum_j \frac{p}{N} \sum_i (\Delta M_i)^2, \end{aligned} \tag{F.6}$$

where it is assumed the isotopes are randomly distributed. Using Fermi's Golden Rule (see Eq. (5.1)) and Eq. (F.4) one can calculate the transition probability $P_{\mathbf{q}s}^{\mathbf{q}'s'}$, which has an inital state $|i>=|n_{\mathbf{q}s}, n_{\mathbf{q}'s'}>$ with $E_i = \hbar\omega(\mathbf{q}s)$ and a final state $|f>=|n_{\mathbf{q}s}-1, n_{\mathbf{q}'s'}+1>$ with $E_f = \hbar\omega(\mathbf{q}'s')$. Thus one can write the transition probability (using Eq. (F.6)) as

$$\begin{aligned} P_{\mathbf{q}s}^{\mathbf{q}'s'} &= \frac{2\pi}{\hbar}\left|_{\pi} < f|H_{md}|i > \right|^2 \delta(E_f - E_i) \\ &= \frac{}{2(\rho' L_0)^2} n_{\mathbf{q}s}(n_{\mathbf{q}'s'}+1)\omega(\mathbf{q}s)\omega(\mathbf{q}'s')(\mathbf{e}^*_{\mathbf{q}s}.\mathbf{e}_{\mathbf{q}'s'})^2 |\mathcal{M}_{\mathbf{q}\mathbf{q}'}|^2 \delta(E_f - E_i) \\ &= \frac{\pi}{2\rho' L_0}\frac{N}{p} n_{\mathbf{q}s}(n_{\mathbf{q}'s'}+1)\omega(\mathbf{q}s)\omega(\mathbf{q}'s')(\mathbf{e}^*_{\mathbf{q}s}.\mathbf{e}_{\mathbf{q}'s'})^2 \delta(\omega(\mathbf{q}s) - \omega(\mathbf{q}'s')) \\ &= \frac{\pi \mathcal{G}_{md}}{2}\frac{N}{p} \sum_{\mathbf{q}s\mathbf{q}'s} n_{\mathbf{q}s}(n_{\mathbf{q}'s'}+1)\omega(\mathbf{q}s)\omega(\mathbf{q}'s')\delta(\omega(\mathbf{q}s) - \omega(\mathbf{q}'s')), \end{aligned} \tag{F.7}$$

where the product of the unit vectors $(\mathbf{e}^*_{\mathbf{q}s}.\mathbf{e}_{\mathbf{q}'s'}) = 1$ for a carbon nanotube and

$$\begin{aligned} \mathcal{G}_{md} &= \sum_i f_i \frac{\Delta M_i}{\rho' |\mathbf{T}|} \\ &= \sum_i f_i \left(\frac{\Delta M_i}{\bar{M}}\right). \end{aligned} \tag{F.8}$$

From a similar discussion to that in Appendix D one can show

$$\left.\frac{\delta n_{\mathbf{q}s}}{\delta t}\right|_{md} = \bar{P}_{\mathbf{q}s}^{\mathbf{q}'s'}(\psi_{\mathbf{q}'s'} - \psi_{\mathbf{q}s})$$

$$= \frac{\pi \mathcal{G}_{md}}{2} \frac{N}{p} \sum_{\mathbf{q}s\mathbf{q}'s} \bar{n}_{\mathbf{q}s}(\bar{n}_{\mathbf{q}'s'}+1)\omega(\mathbf{q}s)\omega(\mathbf{q}'s')\times (\psi_{\mathbf{q}'s'}-\psi_{\mathbf{q}s})\delta(\omega(\mathbf{q}s)-\omega(\mathbf{q}'s')). \quad \text{(F.9)}$$

This equation is simplified using the *smrt* assumption such that $\psi_{\mathbf{q}'s}=0$. Hence

$$\left.\frac{\delta n_{\mathbf{q}s}}{\delta t}\right|_{md} = \frac{-\pi \mathcal{G}_{md}}{2} \frac{N}{p} \sum_{\mathbf{q}s\mathbf{q}'s} \bar{n}_{\mathbf{q}s}(\bar{n}_{\mathbf{q}'s'}+1)\omega(\mathbf{q}s)\omega(\mathbf{q}'s')(\psi_{\mathbf{q}s})\delta(\omega(\mathbf{q}s)-\omega(\mathbf{q}'s'))$$
$$= -\bar{n}_{\mathbf{q}s}(\bar{n}_{\mathbf{q}s}+1)\psi_{\mathbf{q}s}\tau_{\mathbf{q}s}(md). \quad \text{(F.10)}$$

Thus rearranging, and using the identity $\sum_{\mathbf{q}} \rightarrow g(\omega)d\omega$ the relaxation rate due to mass scattering may be written as

$$\tau^{-1}_{\mathbf{q}s}(md) = \frac{\pi \mathcal{G}_{md}}{2} \frac{N}{p} \sum_{\mathbf{q}s} \omega(\mathbf{q}s)\omega(\mathbf{q}'s')\frac{(\bar{n}_{\mathbf{q}'s'}+1)}{(\bar{n}_{\mathbf{q}s}+1)}\delta(\omega(\mathbf{q}s)-\omega(\mathbf{q}'s'))$$
$$= \frac{\pi \mathcal{G}_{md}}{2} \frac{|\mathbf{T}|}{L_0} \sum_{s'} \int g(\omega(\mathbf{q}'s'))\omega(\mathbf{q}s)\omega(\mathbf{q}'s')\frac{(\bar{n}_{\mathbf{q}'s'}+1)}{(\bar{n}_{\mathbf{q}s}+1)}\delta(\omega(\mathbf{q}s)-\omega(\mathbf{q}'s'))$$
$$= \frac{\pi \mathcal{G}_{md}}{2} \frac{|\mathbf{T}|}{L_0} \sum_{s'} g_{s'}(\omega(\mathbf{q}s))\omega^2(\mathbf{q}s). \quad \text{(F.11)}$$

Bibliography

[1] D. Bernoulli, *Hydrodynamica*, (1738).

[2] A. Einstein, *The Planck theory of radiation and the theory of specific heat*, Ann. Phys., Lpz. **22**, 180 (1907).

[3] P. Debye, *The theory of specific warmth*, Ann. Phys., Lpz. **39**, 789 (1912).

[4] H. Y. Chu and W. L. Fang, *Bulk micromachining fabrication platform using the integration of DRIE and wet anisotropic etching*, Microsystem Technologies-Micro-And Nanosystems-Information Storage and Processing Systems **11**, 141 (2005).

[5] J. Albuschies, M. Baus, O. Winkler, B. Hadam, B. Spangenberg and H Kurz, *High-density silicon nanowire growth from self-assembled Au nanoparticles*, Microelectronic Eng. **83**, 1530 (2006).

[6] P. Mishra and K. P. Jain, *Raman, photoluminescence and optical absorption studies on nanocrystalline silicon*, Mat. Sci. and Eng. B **95**, 202 (2002).

[7] J. H. Lee, Zh. M. Wang, Z. Y. Abuwaar, N. W. Strom and G. J. Salamo, *Evolution between self-assembled single and double ring-like nanostructures*, Nanotechnology **17**, 3973 (2006).

[8] S. Iijima and T. Ichihashi, *Single-shell carbon nanotubes of 1-nm diameter*, Nature **363**, 603 (1993).

[9] H. W. Kroto, J. R. Heath, S. C. O'Brien, R. F. Curl and R. E. Smalley, C_{60}*: Buckminsterfullerene*, Nature **318**, 162 (1985).

[10] A. Oberlin, M. Endo and T. Koyama, *Filamentous growth of carbon through benzene decomposition*, J. Cryst. Growth **32**, 335 (1976).

[11] S. Iijima, *Helica microtubules of graphitic carbon*, Nature **354**, 56 (1991).

[12] M. Monthioux and V. L. Kuznetsov, *Who should be given the discovery of carbon nanotubes?* Carbon, **44**, 1621 (2006).

[13] R. Saito, G. Dresselhaus, M.S. Dresselhaus, *Physical Properties of Carbon Nanotubes* (Imperial College Press, 1998).

[14] S. Bandow, G. Chen, G. U. Sumanasekera, R. Gupta, M. Yudasaka, S. Iijima and P. C. Eklund, *Diameter-selective resonant Raman scattering in double-wall carbon nanotubes*, Phys. Rev. B **66**, 075416 (2002).

[15] M. Simeoni, S. Santucci, S. Picozzi and B. Delly, *Defective aluminium nitride nanotubes: a new way for spintronics? A density functional study*, Nanotechnology **17**, 3166 (2006).

[16] P. Saxena and S. P. Sanyal, *Phonon structure and dynamics of boron nitride single wall nanotube*, Physica E **24**, 244 (2004).

[17] R. Q. Zhang, S. T. Lee, C. K. Law, W. K. Li, and B. K. Teo, *Silicon nanotubes: Why not?*, Chem. Phys. Lett. **364**, 251 (2002).

[18] Y. H. Tang, L. Z Pei, Y. W. Chen and C. Guo, *Self-assembled silicon nanotubes under supercritically hydrothermal conditions*, Phys. Rev. Lett. **95**, 116102 (2005).

[19] R. Songmuang, N. Y. Jin-Phillipp, S. Mendach and O. G. Schmidt, *Single rolled-up SiGe/Si microtubes: Structural and thermal stability*, Appl. Phys. Lett. **88**, 021913 (2006).

[20] J. Hu, M. Ouyang, P. Yang, C. M. Liebers, *Controlled growth and electrical properties of carbon nanotubes and silicon nanowires*, Nature **399**, 48 (1999).

[21] H. W. Kroto, *The stability of the fullerenes C_n, with n = 24, 28, 32, 36, 50, 60 and 70*, Nature **329**, 529 (1985).

[22] K. Nagata, E. Dejima, Y. Kikuchi and M. Hashiguchi, *Kilogram-scale [60]Fullerene Separation from a Fullerene Mixture: Selective Complexation of Fullerenes with 1,8-Diazabicyclo[5.4.0]undec-7-ene (DBU)*, Chem. Lett. **34**, 178 (2005).

[23] G. Tegos, T. Demidova, D. Arcila-Lopez, H. Lee, T. Wharton, H. Gali and M. Hamblin,*Cationic Fullerenes Are Effective and Selective Antimicrobial Photosensitizers*, Chemistry & Biology **12,** 1127 (2005).

[24] E. Oberdorster, S. Q. Zhu, T. M. Blickley, P. McClellan-Green and M. L. Haasch, *Ecotoxicology of carbon-based engineered nanoparticles: Effects of fullerene (C_{60}) on aquatic organisms*, Carbon **44**, 1112 (2006).

[25] M. Ardnt, O. Nairz, J. Voss-Andreae, C. Keller, G. van der Zouw and A. Zeilinger, *Wave-particle duality of* C_{60}, Nature **401**, 680 (1999).

[26] G. P. Srivastava, *Theoretical modelling of semiconductor devices: Microscopic studies of electrons and phonons.* (World Scientific Publishing Co. Pte. Ltd. 1999).

[27] C. Kittel, *Introduction to solid state physics*, Seventh Edition. (John Wiley and Sons, Inc, New York, Chichester, Brisbane, Toronto, Singapore, 1996).

[28] H. Ohnishi, Y. Kondo and K. Takayanagi, *Quantized conductance through individual rows of suspended gold atoms*, Nature **395**, 780 (1998).

[29] D. P. Yu, C. S. Lee, I. Bello, X. S. Sun, Y. H. Tang, G. W. Zhou, Z. G. Bai, Z. Shang and S. Q. Feng, *Synthesis of nano-scale silicon wires by excimer laser ablation at high temperature*, Solid State Comm. **105**, 403 (1998).

[30] M. K. Sunkara, S. Sharma, R. Miranda, G. Lian and E. C. Dickey, *Bulk synthesis of silicon nanowires using a low-temperature vapor-liquid-solid method*, Appl. Phys. Lett. **79**, 1546 (2001).

[31] S. Hofmann, C. Ducati, R. J. Neill, S. Piscanec and A. C. Ferrari, *Gold catalyzed growth of silicon nanowires by plasma enhanced chemical vapor deposition*, J. Appl. Phys. **94**, 6005 (2003).

[32] Y. F. Zhang, Y. H. Wang, C. S. Lee, I. Bello and S. T. Lee, *Germanium nanowires sheathed with an oxide layer*, Phys. Rev. B **61**, 4158 (1999).

[33] Z. H. Wu, X. Y. Mei, D. Kim, M. Blumin and H. E. Ruda, *Growth of Au-catalyzed ordered GaAs nanowire arrays by molecular-beam epitaxy*, Appl. Phys. Lett. **81**, 5177 (2002).

[34] T. Stelzner, G. Andrä, E. Wendler, W. Wesch, R. Scholz, U. Gösele and S. Christiansen, *Growth of silicon nanowires by chemical vapour deposition on gold implanted silicon substrates*, Nanotechnology **17**, 2895 (2006).

[35] T. Hiosugi, T. Hashizume, S. Heike, H. Kajiyama, Y. Wada, S. Watabe, T. Hasegawa and K. Kitazawa, *Scanning tunneling microspy/spectroscopy of dangling-bond wires fabricated on the Si(100)-2 × 1-H surface*, Appl. Surf. Sci. **130-132**, 340 (1998).

[36] A. Yajima, M. Tsukada, S. Watabe, M. Ichimura, Y. Suwa, T. Onogi and T. Hashizume, *First-principles calculation of As atomic wires on a H-terminated Si(100) surface*, Phys. Rev. B **60**, 1456 (1999).

[37] P. Sutter and M. G. Lagally, *Quantitative determination of dislocation-induced strain at the surface of (001) silicon-on-insulator*, Phys. Rev. Lett. **82**, 1490 (1999).

[38] S. J. Sque, R. Jones, J. P. Goss, P. R. Briddon, and S. Oberg, *First-principles study of C_{60} and $C_{60}F_{36}$ as transfer dopants for p-type diamond.* J. Phys.: Cond. Matt. **17**, L21 (2005).

[39] R. H. Miwa, W. Orellana and A. Fazzio, *Substrate-dependent electronic properties of an armchair carbon nanotube adsorbed on H/Si(001)*, Appl. Phys. Lett. **86**, 213111 (2005).

[40] H. M. Tütüncü and G. P. Srivastava, *Calculation of phonon dispersion on the ZnSe(110) surface*, Phys. Rev. B **57**, 3791 (1998).

[41] R. D. Smardon, G. P. Srivastava, and S. J. Jenkins, *Electronic structure of a stepped semiconductor surface: Density functional theory of Si(114)-(2×1)*, Phys Rev B **69**, 085303 (2004).

[42] K. Chuasiripattana, R. H. Miwa, and G. P. Srivastava, *Atomic geometry and electronic states on GaAs(111)A-Se($2\sqrt{3}\times 2\sqrt{3}$)*, Surf Sci **966-968**, 909 (2004).

[43] R. D. Smardon and G. P. Srivastava, *Ab initio surface reaction energetics of H_2X (X=O or S) on Si(001)-(2×1)*, Surf. Sci. **584**, 161 (2005).

[44] K. Chuasiripattana and G. P. Srivastava, *Rotation of ad-dimers in the initial stages of Bi and Si deposition on the Si(001) surface*, Phys. Rev. B **71**, 153312 (2005).

[45] H. G. Craighead and G. A. Niklasson, *Characterization and optical properties of arrays of small gold particles*, Appl. Phys. Lett. **44**, 1134 (1984).

[46] M. Jung, S. I. Mho, H. L. Park, *Long-range-ordered CdTe/GaAs nanodot arrays grown as replicas of nanoporous alumina masks*, Appl. Phys. Lett. **88**, 133121 (2006).

[47] I. H. Park, J. W. Lee, C. W. Chung, *Formation of silicon nanodot arrays by reactive ion etching using self-assembled tantalum oxide mask*, J. Ind. Eng. Chem **11**, 590 (2005).

[48] S. Reich, C. Thomsen and P. Ordejon, *Electronic band structure of isolated and bundled carbon nanotubes*, Phys. Rev. B **65**, 155411 (2002).

[49] B. K. Agrawal, S. Agrawal and R. Srivastava, *Ab initio study of small diameter (6,6) armchair carbon nanoropes: orientational dependent properties*, J. Phys.: Cond. Matt. **15**, 6931 (2003).

[50] M. F. Lin and K. W.-K. Shung, *Plasmons and optical properties of carbon nanotubes*, Phys. Rev. B **50**, 17744 (1994).

[51] S. J. Tans, M. H. Devoret, H. Dai, A. Thess, R. E. Smalley, L. J. Geerligs and C. Dekker, *Individual single-wall carbon nanotubes as quantum wires*, Nature **386**, 474 (1997).

[52] A. Bezryadin, A. R. M . Verschueren, S. J. Tans and C. Dekker, *Multiprobe Transport Experiments on Individual Single-Wall Carbon Nanotubes*, Phys. Rev. Lett. **80**, 4036 (1997).

[53] L. Langer, V. Bayot, E. Grivei, J.-P. Issi, J. P. Heremans, C. H. Olk, L. Stockman, C. Van Haesendonck and Y. Bruynseraed, *Quantum Transport in a Multiwalled Carbon Nanotube*, Phys. Rev. Lett. **76**, 479 (1997).

[54] H. D. Jensen and J. M. Martinis, *Accuracy of the electron pump*, Phys. Rev. B **46**, 13407 (1993).

[55] L. T. Canham, *Silicon quantum wire array fabrication by electrochemical and chemical dissolution of wafers*, Appl. Phys. Lett. **57**, 1046 (1990).

[56] R. Rurali and N. Lorente, *Metallic and semimetallic silicon* $< 100 >$ *nanowires*, Phys. Rev. Lett. **94**, 026805 (2005).

[57] R. Rurali and N. Lorente, *On the properties of surface reconstructed silicon nanowires*, Nanotechnology **16**, S250 (2005).

[58] J. Hu, M. Ouyang, P. Yang and C. M. Lieber, *Controlled growth and electrical properties of heterojunctions of carbon nanotubes and silicon nanowires*, Nature **399**, 48 (1999).

[59] N. G. Shang, U. Vetter, I. Gerhards, H. Hofsäss, C. Ronning and M. Seibt, *Luminescence centres in silica nanowires*, Nanotechnology **17**, 3215 (2006).

[60] A. Tanaka, S. Onari and T. Arai, *Low-frequency Raman scattering from CdS microcrystals embedded in germanium dioxide glass matrix*, Phys. Rev. B **47**, 1237 (1993).

[61] M. E. Eames and J. C. Inkson, *Interface scattering and the tunneling magnetoresistance of Fe(001)/MgO(001)/Fe(001) junctions*, Appl. Phys. Lett. **88**, 252511 (2006).

[62] S. Ladak and R. J. Hicken, *Evidence for hot electron magnetocurrent in a double barrier tunnel junction device*, Appl. Phys. Lett. **87**, 232504 (2005).

[63] B. Nagabhirava, T. Bansai, G. U. Sumanasekera, B. W. Alphenaar and L. Liu, *Gated spin transport through an individual single wall carbon nanotube*, Apll. Phys. Lett. **88**, 023503 (2006).

[64] E. Pop, D. Mann, Q. Wang, K. Goodson and H. Dai, *Thermal conductance of an individual single-wall nanotube aove room temperature*, Nano Lett. **6**, 96 (2005).

[65] D. Li, Y. Wu, P. Kim, L. Shi, P. Yang, A. Majumdar, *Thermal conductivity of individual silicon nanowires*, Appl. Phys. Lett. **83**, 2934 (2003).

[66] J. Hone, B. Batlogg, Z. Benes, A.T. Johnson, J.E.Fischer, *Quantised phonon spectrum of single wall carbon nanotubes*, Science **289**, 1730 (2000).

[67] M. Born, *The crystal lattice theory of diamonds*, Ann. Phys.,Lpz **44**, 605 (1914).

[68] M. A. Stroscio, M. Dutta, *Phonons in Nanostructures* (Cambridge University Press, 2001).

[69] N. Nishiguchi, T. Ando and M. N. Wybourne, *Acoustic phonon modes of rectangular quantum wires*, J. Phys:. Cond. Mat. **9**, 5751 (1997).

[70] H. Fang, Y. Wu, J. Zhao and J. Zhu, *Silver cataysis in the fabrication of silicon nanowire arrays*, Nanotechnology **17**, 3768 (2006).

[71] W. Han, S. Fan, Q. Li and Y. Hu, *Synthesis of Gallium Nitride Nanorods Through a Carbon Nanotube-Confined Reaction*, Science **277**, 1287 (1997).

[72] H. Dai, E. W. Wong, Y. Z. Lu, S. Fan and C. Lieber, *Synthesis and characterization of carbide nanorods*, Nature **375**, 769 (1995).

[73] See the Proceedings of the International Conference of Nanoscience and Technology, Institute of Physics Conference Series (2006) for more details (to be published).

[74] T. Saif, E. Alaca and H. Sehito, *Nano wires by self assembly*, IEEE, 1-7803-7744-3/03 (2003).

[75] G. Binning, H. Rohrer, Ch. Gerber, and E. Weibel, *Surface studies by scanning tunnneling microscopy*, Phys. Rev. Lett. **49**, 57 (1982).

[76] J. D. Baird, O. P. Hartree and R. Phillips, *Transmission Electron Microscopy Of Beryllium*, Nature **182**, 1660 (1958).

[77] E. Hartmann, M. Enachescu, M. Schwartzkopff and F. Kock, *Imaging and manipulation properties of nanoparticles in scanning tunneling microscopy*, Nanotechnology **7**, 376 (1996).

[78] T. Hashizume, S. Heike, M. Lutwyche, S. Watanabe, K. Nakajima, T. Nishi, and Y. Wada, *Interaction of Ga adsorbants with dangling bonds on the hydrogen terminated Si(100) surface*, Jpn. J. Appl. Phys. **35**, L1085, (1996).

[79] D. Huang and Y. Yamamoto, *Si dimer chain on Si(100)-2 × 1:H surface fabricated by scanning tunneling microscope*, Jpn. J. Appl. Phys, **35**, 3734 (1996).

[80] Ch. Ossadnik, S. Vespek and I. Gregora, *Applicability of Raman scattering for the characterization of nanocrystalline silicon*, Thin Sol. Films **337**, 148 (1999).

[81] A. Thess, R. Lee, P. Nikolaev, H. Dai, P. Petit, J. Robert, C. Xu, Y. H. Lee, S. G. Kim, A. G. Rinzler, D. T. Colbert, G. E. Scuseria, D. Tománek, J. E. Fischer and R. E. Smalley, *Crystalline Ropes Of Metallic Carbon Nanotubes*, Science **273**, 483 (1996).

[82] T. Guo, P. Nikolaev, A. Thess, D. T. Colbert, R. E. Smalley, *Catalytic growth of single-wall nanotubes by laser vaporization*, Chem. Phys. Lett. **243**, 49 (1995).

[83] C. Journet, W. K. Maser, P. Bernier, A. Loiseau, M. Lamy de la Chapelle, S. Lefrant, P. Deniard, R. Lee and J. E. Fischer, *Large-scale production of nanotubes by the electric-arc technique*, Nature **388**, 756 (1997).

[84] Y. Saito and M. Inagaki, *Optical emission studies on in an arc flame of fullerene/metallofullerene generator*, Jpn. J. Appl. Phys. **32**, L954 (1993).

[85] M. Endo, K. Takeuchi, K. Kibori, K. Takahashi, H. W. Kroto and A. Sarkar, *Pyrolytic carbon nanotubes from vapor-grown carbon fibres*, Carbon **33**, 873 (1995),

[86] G. Burns, *Solid state physics, International Edition*, (Academic Press, 1985).

[87] A. M. Rao, E. Richter, Shunji Bandow, Bruce Chase, P. C. Eklund, K. A. Williams, S. Fang, K. R. Subbaswamy, M. Menon, A. Thess, R. E. Smalley, G.

Dresselhaus and M. S. Dresselhaus, *Diameter-Selective Raman Scattering from Vibrational Modes in Carbon Nanotubes*, Science **275**,187 (1997).

[88] A. Jorio, C. Fantini1 M. S. S. Dantas, M. A. Pimenta, A. G. Souza Filho, Ge. G. Samsonidze, V. W. Brar, G. Dresselhaus, M. S. Dresselhaus, A. K. Swan, M. S. Ünlü, B. B. Goldberg and R. Saito, *Linewidth of the Raman features of individual single-wall carbon nanotubes*, Phys. Rev. B **66**, 115411 (2002).

[89] M. J. O'Connell, S. Sivaram and S. K. Doorn, *Near-infrared resonance Raman excitation profile studies of single-walled carbon naotube intertube interactions: A direct comparison of bundled and individually dispersed HiPco nanotubes*, Phys. Rev. B **69**, 235415 (2004).

[90] M. Paillet, T. Michel, J. C. Meyer, V. N. Popov, L. Henrard, S. Roth and J.-L. Sauvajol, *Raman active phonons of identified semiconducting single-wall carbon nanotubes*, Phys. Rev. Lett. **96**, 257401 (2006).

[91] B. Li, D. Yu and S-.L. Zhang, *Raman spectral study of silicon nanowires*, Phys. Rev. B **59**, 1645 (1999).

[92] W. Ding, L. Li, B. Li, S. Zhang, *Abnormal Raman spectral phenomenon of silicon nanowires*, Chin. Sci. Bull. **45**, 1351 (2000).

[93] J. Qi, J. M. White, A. M. Belcher and Y. Masumoto, *Optical spectroscopy of silicon nanowires*, Chem. Phys. Lett. **372**, 763 (2003).

[94] S. Piscanec, M. Cantoro, A. C. Ferrari, J. A. Zapien, Y. Lifshitz, S. T. Lee, S. Hofmann and J. Robertson, *Raman spectroscopy of silicon nanowires*, Phys. Rev. B **68**, 241312 (2003).

[95] S. Bhattacharyya and S. Samui, *Phonon confinement in oxide-coated silicon nanowires*, Appl. Phys. Lett. **84**, 1564 (2004).

[96] C. Meier, S. Lüttjohann, V. G. Kravets, H. Nienhaus, A. Lorke, and H. Wiggers, *Raman properties of silcion nanoparticles*, Physica E, **32**, 155 (2006).

[97] D. Bersani, P. P. Lottici, X-. Z. Ding, *Phonon confinement in the Raman scattering by TiO_2 nanocrystals*, Appl. Phys. Lett. **72**, 73 (1998).

[98] J. L. Liu, G. Jin, Y. S. Tang, Y. H. Luo, K. L. Wang and D. P. Yu, *Optical and acoustic phonon modes in self-organized Ge quantum dot superlattices*, Appl. Phys. Lett. **76**, 586 (2000).

[99] S. Rols, Z. Benes, E. Anglaret, J. L. Sauvajol, P. Pananek, J. E. Fischer, G. Coddens, H. Schrober, and A. J. Dianoux, *Phonon density of states of single-wall carbon nanotubes*, Phys. Rev. Lett. **85**, 5222 (2000).

[100] H. D. Young, R. A. Freedman, T. R. Sandin and A. L. Ford, *University physics, Ninth edition*, (Addison-Wesley Publishing Company, 1996).

[101] J. S. Hwang, K. J. Lin, and C. Tien, *Measurement of heat capacity by fitting the whole temperature response of a heat-pulse calorimeter*, Rev. Sci. Instr. **68**, 94 (1996).

[102] J. Hone, M. Whitney, C. Piskoti and A. Zettl, *Thermal conductivity of single-wall carbon nanotubes*, Phys. Rev. B **59**, R2514 (1998).

[103] P. Kim, L. Shi, A. Majumdar and P. L. McEuen, *Thermal transport measurements of individual multwall nanotubes*, Phys. Rev. Lett. **87**, 215502 (2001).

[104] H. Dai, J. H. Hafner, A. G. Rinzler, D.T. Colbert and R. E. Smalley, *Nanotubes as nanoprobes in scanning probe microscopy*, Nature **384**, 147 (1996).

[105] J. Ihm, A. Zunger and M. L. Cohen, *Momentum-space formalism for the total energy of solids*, J. Phys. C. Solid State Phys. **12**, 4409 (1979).

[106] K. Klunc and R. M. Martin, *Ab Initio Force Constants of GaAs: A New Approach to Calculation of Phonons and Dielectric Properties*, Phys. Rev. Lett. **48**, 406 (1982).

[107] M. Born and K. Huang, *Dynamical Theory of Crystal Lattices* (Oxford: Oxford University Press, 1954).

[108] H. M. J. Smith, *The theory of the vibrations and raman spectrum of the diamond lattice*, Phil. Trans. R. Soc. Lon. **241**, 105 (1948).

[109] F. J. Herman, *Lattice vibrational spectrum of germanium*, J. Phys. Chem. Solids **8**, 405 (1959).

[110] M. J. P. Musgrave and J. A. Pople, *General valence force field for diamond*, Proc. R. Soc. A **268**, 474 (1962).

[111] P. N. Keating, *Effect of invariance requirements on the elastic strain energy of crystals with application to the diamond structure*, Phys. Rev, **145**, 637 (1966).

[112] W. Cochran, *Theory of the lattice vibrations if germanium*, Proc. R. Soc. A **253**, 260 (1959).

[113] W. Weber, *Adiabatic bond charge model for phonons in diamond, Si, Ge, and α-Sn*, Phys. Rev. B **15**, 4789 (1977).

[114] K. C. Rustagi and W. Weber, *Adiabatic bond charge model for phonons in A3B5 semiconductors*, Sol. Stat. Comm. **18**, 673 (1976).

[115] A. A. Maradudin, W. E. Montroll, G. H. Weiss and I. P. Ipatova, *Solid State Physics Supplement 3* (Academic, New York, 1971).

[116] H. M. Tütüncü, *Lattice Dynamics of semiconductors and their surfaces*, Thesis, University of Exeter (1998).

[117] G. Dolling, *Inelastic Scattering of Neutrons in Solids and Liquids*, (IAEA, Vienna, 1963), Vol. I, p. 37.

[118] G. Nilsson and G. Nelin, *Study of the Homology between Silicon and Germanium by Thermal-Neutron Spectrometry* , Phys. Rev. B **6**, 3777 (1972).

[119] N. Bannov, V. Aristov, V. Mitin and M. A. Stroscio, *Electron relaxation times due to the deformation-potential interaction of electrons with confined acoustic phonons in a free-standing quantum well*, Phys. Rev. B **51**, 9930 (1995).

[120] M. A. Stroscio, K. W. Kim, S. Yu, and A. Ballato, *Theoretical calculation of longitudinal-optical-phonon lifetime in GaAs*, J. Appl. Phys. **76**, 4670 (1994).

[121] G. Kanellis, J. F. Morhange, and M. Balkanski, *Effect of dimensions on the vibrational frequencies of thin slabs of silicon*, Phys. Rev. B **21**, 1543 (1980).

[122] Hu X H and Zi. J, *Reconstruction of phonon dispersion in Si nanocrystals*, J. Phys.: Condens. Matter **14**, L671 (2002).

[123] N. Mingo and L. Yang, *Phonon transport in nanowires coated with an amorphous material: An atomistic Green's function approach*, Phys. Rev. B **68**, 245406 (2003).

[124] N. Mingo, *Calculation of Si nanowire thermal conductivity using complete phonon dispersion relations*, Phys. Rev. B **68**, 113308 (2003).

[125] T. Thonhauser and G. D. Mahan, *Phonon modes in Si [111] nanowires*, Phys. Rev. B, **69**, 075213 (2004).

[126] B. Jusserand, D. Paquet, F. Mollot, F. Alexandre and G. Le Roux, *Influence of the supercell structure on the folded acoustic line in Raman line intensities in superlattices*, Phys. Rev. B **35**, 2808 (1987).

[127] H. Lamb, *On the vibrations of an elastic sphere*, Proc. London Math. Soc. **13**, 189 (1882).

[128] S. M. Rytov, *Acoustical properties of a thinly laminated medium*, Akust. Zh. **2**, 71 (1956) [Sov. Phys. Acoust. **2**, 68 (1956)].

[129] C. Q. Sun, L. K. Pam, C. M. Li, and S. Li, *Size-induced acoustic hardening and optic softening of phonons in InP, CeO_2, SnO_2, CdS, Ag, and Si nanostructures*, Phys. Rev. B **72**, 134301 (2005)

[130] H. M. Tütüncü and G. P. Srivastava, *Surface phonons on InP(110) with the adiabatic bond-charge model* Phys. Rev. B **53**, 15675 (1996).

[131] G. P. Srivastava, *The Physics of Phonons* (Adam Hilger, Bristol; 1990).

[132] M. Fujii, Y. Kanzawa, S. Hayashi and K. Yamamoto, *Raman scattering from acoustic phonons confined in Si nanocrystals*, Phys. Rev. B **54**, R8373, (1996).

[133] Z. Iqbal and S. Veprek, *Raman scattering from hydrogenated microcrystalline and amorphous silicon*, J. Phys. C **15**, 377 (1982).

[134] R. A. Jishi, L. Venkataraman, M. S. Dresselhaus and G. Dresselhaus, *Phonon modes in carbon nanotubules*, Chem. Phys. Lett. **209**, 77 (1993).

[135] A. Charlier, E. McRae and M.-F. Charlier, A. Spire and S. Forster, *Lattice dynamics study of zigzag and armchair carbon nanotubes*, **57**, 6689 (1998).

[136] J. De. Launay, *Solid State Physics* **3** 203 (Academic Press, Inc, New York, 1957).

[137] D. Kahn, K. W. Kim and M. A. Stroscio, *Quantized vibrational modes of nanospheres and nanotubes in the elastic continuum model*, J. Appl. Phys. **89**, 5107 (2001).

[138] Y. M. Sirenko, M. A. Stroscio and K. W. Kim, *Elastic vibrations of microtubules in a fluid*, Phys. Rev. E **53**, 1003 (1996).

[139] M. A. Stroscio, M. Dutta, D. Kahn and K. W. Kim, *Continuum model of optical phonons in a nanotube*, Superlattices and microstructures —bf 29, 405 (2001).

[140] A. Rachura, M. Dutta and M. A. Stroscio, *Quantized acoustic vibrations of single-wall carbon nanotube*, J. Appl. Phys. **94**, 4060 (2003).

[141] G. D. Mahan, *Oscillations of a thin hollow cylinder: Carbon nanotubes*, Phys. Rev. B **65**, 235402 (2002).

[142] S. Zhang, M. Xia, S. Zhao, T. Xu and E. Zhang, *Specific heat of single-wall carbon nanotubes*, Phys. Rev. B **68**, 075415 (2003).

[143] M. Xia, S. Zhang, E. Zhang, S. Zhao and X. Zuo, *Vibrational spectra of double-wall carbon nanotubes*, Phys. Rev. B **69**, 233407 (2004).

[144] G. D. Mahan and G. S. Jeon, *Flexure modes in carbon nanotubes*, Phys. Rev. B **70**, 075405 (2004).

[145] L.-H. Ye, B.-G. Liu, D.-S. Wang, and R. Han, *Ab initio phonon dispersions of single-wall carbon nanotubes*, Phys. Rev. B **69**, 235409 (2004).

[146] L. D. Landau and E. M. Lifshitz, *Theory of Elasticity*, (Pergamon, Oxford, 1986).

[147] N. Yao and V. Lordi, *Young's modulus of single-walled carbon nanotubes*, J. Appl. Phys. **84**, 1939 (1998).

[148] H. M. Lawler, J. W. Mintmire and C. T. White, *Helical strain in carbon nanotubes: Speed of sounds and the Poisson ratio from first principles*, Phys. Rev. B **74**, 125415 (2006).

[149] L. X. Benedict, S. G. Louie, and M. L. Cohen, *Heat Capacity of carbon nanotubes*, Sol. State. Comm. **100**, 177, (1996).

[150] J. M. Ziman, *Electrons and Phonons* (Oxford University Press, Clarendon, 1960).

[151] P. G. Klemens, *Graphite, graphene, and carbon nanotubes*, In Thermal Conductivity 26/ Thermal Expansion 14 (Ed. R. Dinwiddie, Publ: DEStech, 2004).

[152] A. Mizel, L. X. Benedict, M. L. Cohen, S. G. Louie, A. Xettl, N. K. Budraam and W. P. Beyerman, *Analysis of the low-temperature specific heat of multiwalled carbon nanotubes and carbon nanotube ropes*, Phys. Rev. B. **60**, 3264 (1999).

[153] V. N. Popov, *Low-temperature specific heat capacity of nanotube systems*, Phys. Rev. B **66**, 153408 (2002).

[154] W. Yi, L. Lu, Z. Dina-lin, Z. W. Pan and S. S. Xie, *Linear specific heat capacity of carbon nanotubes*, Phys. Rev. B **59**, R9015 (1998).

[155] D. Sánchez-Portal, E. Artacho, J. M. Soler, *Ab initio structural, elastic, and vibrational properties of carbon nanotubes*, Phys. Rev. B **59**, 12678 (1999).

[156] C. Herring, *Role of low-energy phonons in thermal conduction*, Phys. Rev. **95**, 954 (1954).

[157] G. Leibfried and G. Schlömann, *Wärmeleitung in elekrisch isolierenden kristallen*, Nach. Akad. Wiss. Göttingen Math. Phys. K1 II(a) **4** 71 (1954).

[158] G. Leibfried and W. Brenig, *Zur spezifischen wärme fester körper*, Zeitschrift für Physik **134**, 451 (1952).

[159] P. G. Klemens. *Thermal conductivity and lattice vibrational modes*, Solid State Phys. **7**, 1 (1958).

[160] P. G. Klemens, *Anharmonic decay of optical phonons*, Phys. Rev. —bf 148, 845 (1966).

[161] P. G. Klemens, *Decay of high-frequency longitudinal phonons*, J. Appl. Phys. **38**, 4573 (1967).

[162] R. A. H. Hamilton and J. E. Parrott, *Variational calculation of the thermal conductivity of germanium*, Phys. Rev. **178**, 1284 (1969).

[163] L. D. Landau and E. M. Lifschitz, *Theory of elasticity*, (Pergamon Press, Inc., New York, 1959).

[164] J. E. Parrott, *Generalization of the Callaway thermal conductivity equation*, phys. stat. (b) **48**, K159 (1971).

[165] J. E. Parrott, Proc. Int. Cong. on Phonon Scattering in Solids (Paris), p 27 (1972).

[166] G. P. Srivastava, *Anharmonic relaxation of phonons*, Pramäna, **3**, 209 (1974).

[167] G. P. Srivastava, *Calculations of anharmonic phonon relaxation times*, Pramäna, **6**, 1 (1976).

[168] G. P. Srivastava, *Calculation of lattice thermal conductivity of Ge from 4 to 900 K*, Phil. Mag. **34**, 795 (1976).

[169] G. P. Srivastava, *Phonon conductivity of insulators and semiconductors*, J. Phys. Chem. Solids **41**, 357 (1980).

[170] M. Lax, P. Hu and V. Narayanamurti, *Spontaneous phonon decay selection rule: N and U processes*, Phys. Rev. B **23**, 3095 (1981).

[171] Y. Xiao, X. H. Cao, and J. W. Ding, *Three-phonon Umklapp process in zigzag single-walled carbon nanotubes*, J. Phys.: Condens. Matter **15**, L341 (2003).

[172] S. Barman and G. P. Srivastava, *Quantitative estimate of phonon scattering rates in different forms of diamond*, Phys. Rev. B **73**, 073301 (2006).

[173] N. Yao and V. Lordi, *Young's modulus of single-walled carbon nanotubes*, J. Appl. Phys. **84**, 1939 (1998).

[174] J. X. Cao, X. H. Yan, Y. Xiao, and J. W. Ding, *Thermal conductivity of zigzag single-walled carbon nanotubes: Role of the umklapp process*, Phys. Rev. B **69**, 073407 (2004).

[175] S. I. Tamura, *Spontaneous decay rates of LA phonons in quasi-isotropic solids*, Phys. Rev. B **31**, 2574 (1985).

[176] P. Debye, *Vorträge über die kinetische Theorie der Materie und Elektrizität*, Edited by M. Planck (B. G. Teubner, Leipzig, 1914).

[177] R. Peierls, *The kinetic theory of thermal conduction in crystals*, Ann. Physik **3**, 1055 (1929).

[178] R. Peierls, *Quantum Theory of Solids*, (Oxford University Press, 1955).

[179] J. M. Ziman, *Principles of the theory of solids*, (Cambridge University Press, 1960).

[180] P. G. Klemens, *The thermal conductivity of dielectric solids at low temperatures*, Proc. Roy. Soc. **A208**, 108 (1951).

[181] C. Kittel, *Interpretation of the thermal conductivity of glasses*, **75**, 972 (1949).

[182] J. Callaway, *Model for Lattice Thermal Conductivity at Low Temperatures*, Phys. Rev. **113**, 1046 (1959).

[183] M. Lax, *Lattice Dynamics*, (Pergamon Press Ltd, New York, 1965).

[184] C. Yu, L. Shi, Z. Yao, D. Li and A. Majumdar, *Thermal conductance and thermopower of an individual single-wall carbon nanotube*, Nano Lett. **5**, 1842 (2005).

[185] S. Berber, Y-.K. Kwon and D. Tománek, *Unusually high thermal conductivity of carbon nanotubes*, Phys. Rev. Lett. **84**, 4613 (2000).